NASA Contractor Report 4517

NASA-UVa Light Aerospace Alloy and Structure Technology Program Supplement: Aluminum-Based Materials for High Speed Aircraft

E. A. Starke, Jr.
University of Virginia
Charlottesville, Virginia

Prepared for
Langley Research Center
under Grant NAG1-745

National Aeronautics and
Space Administration
Office of Management
Scientific and Technical
Information Program
1993

TABLE OF CONTENTS

Introduction

Current marketing analyses have indicated that a significant market would exist for an HSCT even today, provided that the fare premium can be kept below about 15%. The key critical development issue for an economically viable HSCT airframe will be the development of materials and processes which allow a complex, highly-stressed, extremely weight-efficient airframe to be fabricated and assembled for a dollar-per-pound cost not greatly different than today's mature airframes. Considering challenges in environmental control, propulsion, and materials technologies, it is believed that an acceptable aircraft could be certified for airline service in 2006. Current NASA/Industry plans are keyed to this service date. In order to meet this certification date, program go-ahead will be required in the 1998 time frame, with mature material allowables and accumulated exposure behavior for the selected environment in hand.

The cost and weight issues suggest that there is the need for an aluminum-based materials program to support the HSCT. The primary arena for high-temperature aluminum-based alloys in the HSCT airframe will be the desirable replacement of titanium for general high specific strength and damage tolerance critical applications. While titanium has many attractive features, it remains a very expensive option. In addition, although great advances have been made in organic composites in recent years, many airframe applications will benefit from the low cost processing and inherently isotropic stress response of metallic materials, either in I/M or P/M forms. Current Douglas HSCT baseline studies indicate that approximately half of a successful HSCT airframe will be metallic. Based on this philosophy, low cost and durability and damage tolerance issues must be emphasized in the materials development program.

With the structural design and the speed of the HSCT still not established, it is impossible to choose one class of materials

for development. If a Mach 2.0 aircraft is selected, there is a good probability that an I/M 2XXX, 6XXX, or Al-Cu-Li-Mg-Ag alloy meeting the strength/toughness goals and stability requirements can be developed for the fuselage and lower wing. If a Mach 2.4 aircraft is chosen, the dispersion strengthened Al-Fe-X alloys may be more suitable than the I/M candidates unless other new I/M alloys are developed. Regardless of speed, a discontinuously reinforced metal matrix composite will probably be needed in order to meet the stiffness requirements of the upper wing. The matrix, which could be either a 2XXX, 6XXX or Al-Fe-X alloy, would then be determined by the speed of the aircraft.

The High Speed Civil Transport (HSCT) is continually evolving with respect to cruise Mach Number, structural and manufacturing concepts, and potential materials of construction. Until firm decisions can be made on certain issues, it will be necessary to explore a large number of materials options. The major objective of this program is to explore and develop candidate I/M, P/M and MMC aluminum alloys that may be suitable for use on the HSCT.

TASK 1. I/M 2XXX and 6XXX ALLOY DEVELOPMENT

Principal Investigator, Alcoa:	Dr. L.M. Angers
Principal Investigator, Boeing:	Dr. W.E. Quist
Principal Investigator, Douglas:	Mr. R. Kahandal
UVa Contact:	Dr. E.A. Starke, Jr.

Subtask 1A. I/M 2XXX Alloy Development (Alcoa)

Principal Investigator:	Dr. L.M. Angers
Senior Engineer:	Dr. G. Dixon

Objective. The primary objective of this task is to develop a damage tolerant aluminum based material for the lower wing and fuselage of a Mach 2.0 aircraft. This material must first meet preliminary strength and toughness targets at room temperature and then several criteria associated with elevated temperature service, (e.g., retention of room temperature properties after exposure, performance at the operating temperature and resistance to creep deformation).

The ingot metallurgy (I/M) 2XXX alloys are under consideration here because existing Al-Cu-Mg alloys combine relatively high strengths with good thermal stability.

Background and Alloy Selection. The most up-to-date Alcoa data on 2XXX exploratory alloys, archival Alcoa data on 2XXX alloys and external literature were reviewed in order to arrive at a set of 2XXX alloys and a detailed experimental plan for the current program. These alloy compositions were discussed with Professor E. A. Starke of UVa and Barry Lisagor and Tom Bales of NASA-Langley.

Five alloys were selected. Their nominal compositions in weight percent are:

1. Al-5.85 Cu-0.20 Mg-0.30 Mn-0.15 Zr-0.10 V
2. Al-5.85 Cu-0.20 Mg-0.30 Mn-0.15 Zr-0.10 V-0.25

3. Al-5.85 Cu-0.50 Mg-0.30 Mn-0.15 Zr-0.10 V
4. Al-5.85 Cu-0.50 Mg-0.30 Mn-0.15 Zr-0.10 V-0.50 Ag
5. Al-4.2 Cu-1.2 Li-0.08 In-0.15 Zr.

Alloys 1 through 4 were designed to study the effects of Mg, Si and Ag on precipitation in 2519-type alloys. Note that alloy 1 is the 2519 control, alloy 2 contains excess Si, alloy 3 contains excess Mg and alloy 4 contains combined additions of Mg and Ag. Alloy 2519 was chosen as the baseline since recent data suggest that it has a promising strength/plane stress toughness combination when compared to 2024-T3 and 6013-T6 (see Fig. 1). Here, crack resistance is plotted as a function of crack extension for 2024-T3, 6013-T6 and 2519-T87. All data are from 16 inch wide by 44 inch long panels. Based on the data which was obtained from these 16" wide panels, 2519-T87 look favorable when compared to the other alloys. Furthermore, 2519-T87 has a significantly higher tensile yield strength than either of the other two alloys. In order to make this argument more conclusively, one would need to test wider panels.

The interest in these additions relied heavily on prior Alcoa investigations. Firstly, there are many studies which would support the use of higher Mg levels than those in 2519. During the late 1940's and early 1950's, Alcoa carried out extensive alloy development work surrounding the compositions which eventually became 2219 and 2618. One alloy, called M237, contained 0.5% Mg and exhibited significantly higher strengths than 2219. This higher strength alloy was not pursued at the time, and later, when 2519 was developed, Mg levels were kept low in order to maintain weldability.

The effects of Si level were also explored in the early days; however, those results were very difficult to interpret without the benefit of original raw data. An investigation carried out much later in conjunction with Alcoa's forging plant in Cleveland, however, was more conclusive. Si additions served as nucleation

aids for the Θ' precipitates, thereby increasing the peak aged yield strengths which could be achieved in T6-type tempers. This discovery, which is particularly useful for product forms like forgings which cannot be stretched prior to artificial aging, led to the development of the forging alloy C197. It may also have potential for HSCT materials. If high strengths can be achieved without the use of cold work, the thermal stability may be improved.

Recent Alcoa research on small ingots has shown that combined additions of Ag and Mg to 2519 can lead to a 10% increase in the peak aged tensile yield strength of the T8-type temper. This strength advantage, which has been attributed to the replacement of Θ' by the more potent plate-like Ω phase, is maintained after short exposures at temperatures up to 400°F (see Fig. 2). Alloy 4 was selected so that this promising alloy could be explored further.

Alloy 5, which was designed by Professor E. A. Starke, is a modified version of alloy 2020. This alloy utilizes In additions as nucleation aids for the relatively stable T1 plates and Zr additions for recrystallization control. By replacing the Mn in 2020 with Zr, a strength/toughness advantage was expected and realized in the Al-Cu-Li-Cd-Zr alloy (1). The potential for developing even higher strengths by replacing Cd with In was also demonstrated (2).

Material Fabrication. Four alloys have been cast as 6" thick x 16" wide x 60" long ingots (e.g., the non-Li bearing alloys) and stress relieved in an 850°F furnace. Actual and nominal compositions are compared in Table I.

Table I. Nominal and Actual Chemical Compositions of the I/M 2XXX Alloys of the Present Investigation.

Alloy	Composition (wt. %)									
	Cu	Mg	Mn	Ag	Zr	V	Fe	Si	Li	In
689245										
nominal	5.85	0.20	0.30	-	0.15	0.10	0.05	0.04		
actual	5.71	0.18	0.29		0.15	0.09	0.05	0.06		
689246										
nominal	5.85	0.20	0.30	-	0.15	0.10	0.05	0.25		
actual	5.78	0.22	0.29		0.14	0.09	0.06	0.25		
689247										
nominal	5.85	0.50	0.30	-	0.15	0.10	0.05	0.04		
actual	5.83	0.52	0.30		0.14	0.10	0.05	0.05		
689248										
nominal	5.85	0.50	0.30	0.50	0.15	0.10	0.05	0.04		
actual	5.75	0.52	0.30	0.49	0.16	0.09	0.06	0.05		
689XXX										
nominal	4.20				0.15		0.05	0.04	1.20	0.08
actual										

Results and Discussion. Ingot slices were taken from each alloy for preheating studies using optical metallography and thermal analysis. These studies revealed that the actual compositions are slightly beyond the maximum solubility for Cu and Mg at 985°F. A small endothermic reaction, identified as the eutectic reaction $L \rightarrow Al(ss) + \Theta$, was present in all preheated samples. The onset temperature and area under the peak varied slightly, depending on how much Mg and Si was present in the alloy. Onset temperatures and areas are summarized below. These onset temperatures will not be exceeded during subsequent heat treatments.

Alloy	Description	Onset Temperature (°F)	Area (J/g)
689245-P2	2519 control	1000	2.75
689246-P2	2519 + Si	995	2.00
689247-P2	2519 + Mg	989	1.16
689248-P2	2519 + Ag,Mg	992	2.10

Four rolling sections 14" wide and 14" long were machined from each ingot. Two were preheated at 985°F and air cooled.

References.

1. W.X. Feng, F.S. Lin and E.A. Starke, Jr., "The Effect of Minor Alloying Elements on the Mechanical Properties of Al-Cu-Li Alloys," *Met. Trans. 15A*, p. 1209-1220 (1984).

2. L.B. Blackburn and E.A. Starke, Jr., "Effect of In Additions on Microstructure Mechanical Property Relationships for an Al-Cu-Li Alloy," in *Aluminum-Lithium Alloys*, eds. T.H. Sanders, Jr., and E.A. Starke, Jr., MCE Publications Ltd., Birmingham, UK, p. 751-766 (1989).

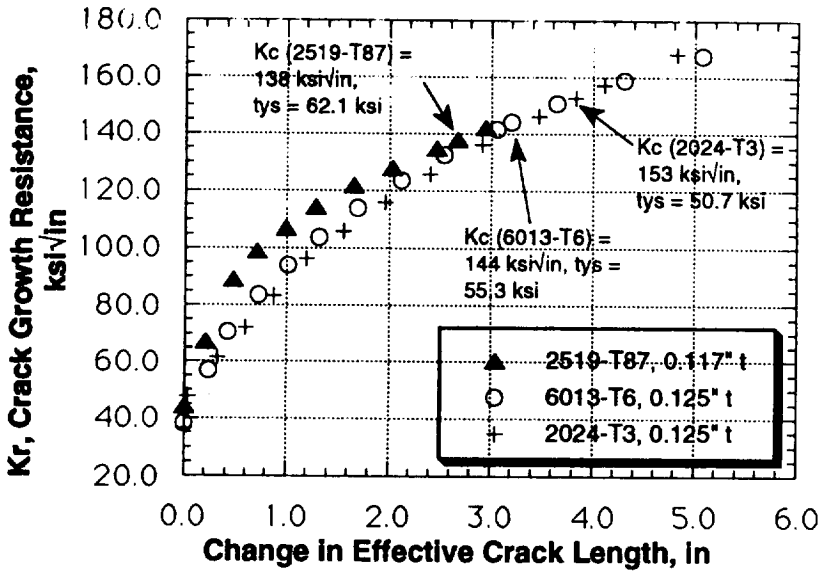

Figure 1. Crack growth resistance as a function of change in effective crack length for 2024-T3, 6013-T6 and 2519-T87 sheet.

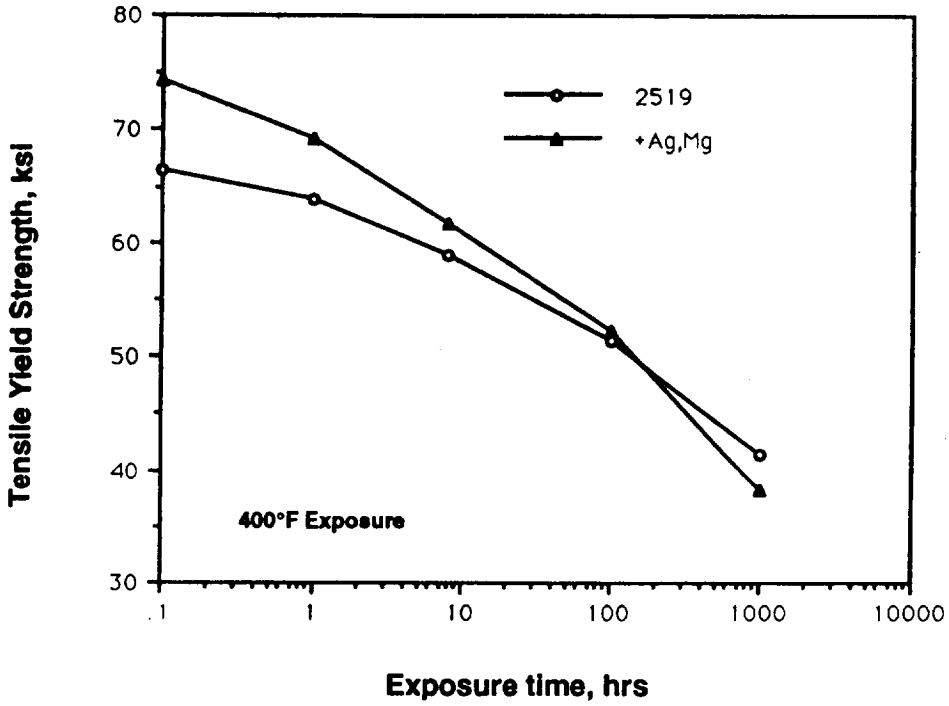

Figure 2. Room temperature tensile yield strength as a function of exposure time at 400°F for alloy 2519-T87 and a modified version of the same alloy containing Ag and higher levels of Mg.

Subtask 1A(i). I/M 2XXX Alloy Development (Boeing)

Principal Investigator: Dr. W.E. Quist

Progress for Report Period. There was little activity in support of this contract during the subject time period. The contract for this effort between the Boeing Co. and the University of Virginia was signed and approved on March 4, 1992. No alloys were received by Boeing for evaluation during the January through June time period, either from the materials suppliers or the University of Virginia.

Subtask 1A(ii). I/M 2XXX Alloy Development (Douglas)

Principal Investigator: Dr. R. Kahandal

No progress to report to date.

Subtask 1B. I/M 6XXX Alloy Development (Alcoa)

Principal Investigator: Dr. L.M. Angers
Senior Engineer: Dr. G. Dixon

Objective. The primary objective of this task is to develop a damage tolerant aluminum based material for the lower wing and fuselage of a Mach 2.0 aircraft. This material must first meet preliminary strength and toughness targets at room temperature and then several criteria associated with elevated temperature service, (e.g., retention of room temperature properties after exposure, performance at the operating temperature and resistance to creep deformation).

The I/M 6XXX alloys, or Al-Mg-Si-Cu alloys, are under consideration here because alloy 6013-T6 exhibits a strength/toughness combination equivalent to 2024-T3, but with significantly greater thermal stability.

Background and Alloy Selection. A set of alloys representing modifications to 6013 was selected. Alcoa-funded thermodynamic modeling by Joanne L. Murray (Scientific Associate in Alloy Technology Division) was used to select compositions which would utilize the maximum amount of Mg, Si and Cu which can be put into solution during heat treatment. Alloys 1 through 5 represent total weight percents of solute of 2.7, 3.5, 4.4, 5.1 and 5.8, respectively. These compositions also roughly explore the Cu, Mg and Si levels of compositions intermediate to 2519 and 6013 (e.g., if these commercial compositions are corrected for their losses of Cu, Mg and Si to form constituent and dispersoid). During aging, these compositions are expected to produce Mg_2Si, Q and Θ' phases in various proportions. Zr was chosen as the dispersoid forming element in all alloys.

1. Al-0.8 Cu-1.05 Mg-0.85 Si-0.15 Zr
2. Al-1.85 Cu-0.90 Mg-0.70 Si-0.15 Zr
3. Al-3.1 Cu-0.75 Mg-0.58 Si-0.15 Zr
4. Al-3.9 Cu-0.65 Mg-0.53 Si-0.15 Zr
5. Al-5.3 Cu-0.20 Mg-0.25 Si-0.15 Zr.

Several compositions exploring the effects of certain elevated temperature dispersoid-forming elements and Ag effects on the Θ' precipitates were also selected.

6. Al-1.2 Cu-1.05 Mg-0.85 Si-0.15 Zr-0.5 Mn-0.1 V
7. Al-0.8 Cu-1.05 Mg-0.85 Si-0.15 Zr-0.5 Ag
8. Al-3.1 Cu-0.75 Mg-0.58 Si-0.15 Zr-0.5 Ag.

Alloy 6 is designed to contain the same strengthening phases as alloy 1 but with additional high temperature dispersoids. In this alloy, Cu levels were increased from 0.85 wt% in alloy 1 to 1.2 wt% to account for the loss of Cu expected as a result of formation of $Al_{20}Cu_2Mn_3$ in alloy 6.

Alloys 7 and 8 were selected to determine whether there is any advantage to having Ω phase, rather than Θ', in these alloys. By analogy to the work done on Ag additions to 2519, we might expect that any Θ' would be replaced by Ω in these alloys. During aging, these compositions are expected to produce Mg_2Si, Q and Ω.

Material Fabrication. Book mold ingots approximately 6" x 2.75" x 1.25" in size were cast. Nominal and actual compositions are compared in Table I.

The alloys were preheated, rolled to 0.125" thick sheet and heat treated and aged. Severe blistering occurred on the surfaces of all of the alloys.

Results and Discussion. Slices were taken from each ingot

for optical metallography and thermal analysis on preheated samples. Optical metallography revealed relatively clean microstructures and thermal analyses showed less than 0.5 J/g of melting reaction in any sample, suggesting that solubilities were not substantially exceeded in any of the alloys.

Table I Nominal and Actual Chemical Compositions of the I/M 6XXX Alloys of the Present Investigation

Alloy	Composition (wt. %)							
	Cu	Mg	Si	Zr	Mn	V	Ag	Fe
715670								
nominal	0.80	1.05	0.85	0.15				
actual	0.80	1.01	0.84	0.14	0.00	0.00	n.m.	0.00
715671								
nominal	1.85	0.9	0.70	0.15				
actual	1.81	0.86	0.69	0.15	0.00	0.00	n.m.	0.00
715672								
nominal	3.10	0.75	0.58	0.15				
actual	3.16	0.75	0.60	0.15	0.00	0.00	n.m.	0.00
715673								
nominal	3.90	0.65	0.53	0.15				
actual	3.93	0.66	0.55	0.15	0.00	0.00	n.m.	0.00
715674								
nominal	5.30	0.20	0.25	0.15				
actual	5.17	0.21	0.25	0.16	0.00	0.00	n.m.	0.00
715675								
nominal	1.20	1.05	0.85	0.15	0.5	0.1		
actual	1.18	1.02	0.83	0.18	0.50	0.09	n.m.	0.01
715676								
nominal	0.8	1.05	0.85	0.15			0.5	
actual	0.81	1.03	0.85	0.14	0.00	0.00	0.51	0.00
715677								
nominal	3.10	0.75	0.58	0.15			0.5	
actual	3.13	0.78	0.60	0.17	0.00	0.00	0.55	0.00

Subtask 1B(i). I/M 6XXX Alloy Development (Boeing)

No progress to report to date. See Subtask 1A(i).

Subtask 1B(ii). I/M 6XXX Alloy Development (Douglas)

No progress to report to date.

TASK 2. I/M Al-Cu-Li-Mg-Ag ALLOY DEVELOPMENT

Principal Investigator, Reynolds: Dr. A. Cho
Principal Investigator, UVa: Dr. J.M. Howe
Principal Investigator, Boeing: Dr. W.E. Quist
Principal Investigator, Douglas: Mr. R. Kahandal

Objectives. The objective of Task 2 is to optimize a precipitate strengthened ingot metallurgy alloy, based on the Al-Cu-Li-Mg-Ag system, to meet the property and thermal stability requirements of the High Speed Civil Transport Research Program. A concurrent goal is to understand the effects of thermal exposure on the microstructural/property evolution of the alloy as a function of time and temperature in order to help composition optimization and to develop techniques for predicting the evolution of the alloy during long-term service environments.

Property Goals. Boeing Aircraft Company proposed several ambitious property goals for ingot metallurgy aluminum alloys for damage tolerant HSCT applications. It is desired that the combination of tensile yield strength and $K_{app.}$ fracture toughness fall within the range between 70/140/ ksi/ksi-inch$^{1/2}$ to 80/100 ksi/ksi-inch$^{1/2}$ after exposure to an anticipated elevated temperature service environment of about 275°F (135°C).

Background. Successful development of the high speed civil transport system (HSCT) depends on the availability of high performance elevated temperature materials. Among the conventional aluminum alloy systems, 2XXX series alloys are commonly used for elevated temperature applications because Cu bearing particles exhibit greater thermal stability. For example, alloys 2618 and 2519 contain a large volume fraction of coarse intermetallic particles, which not only enhance thermal stability, but also contribute to alloy strength. Unfortunately, coarse intermetallic particles are only marginally effective as

strengthening agents while being deleterious on fracture toughness. Therefore, conventional 2XXX alloys offer limited strength and fracture toughness capability.

Among conventional aluminum alloy systems, only 7XXX series alloys could potentially meet the proposed property goals, but only prior to any thermal exposure. 7XXX series alloys are strengthened by a combination of metastable GP zones and $MgZn_2$ precipitates which provide a good combination of high strength and fracture toughness. However, these precipitate phases are not stable above 100°C. Therefore, 7XXX series alloys are not suitable for elevated temperature applications.

Recent work at Reynolds Metals Company has demonstrated that a new proprietary Al-Cu-Li-Mg-Ag alloy (RX818) could potentially meet Boeing's requirements for high combination of strength and fracture toughness. RX818 is mainly strengthened by thermodynamically stable phases which form an extremely fine distribution of precipitates (i.e., T_1 and S'-like phases). These are effective in providing high combination of strength and fracture toughness because the formation of large intermetallic particles is avoided. A high level of property stability in RX818 has been established in thermal exposure studies at Reynolds. Further improvement of thermal stability of the alloy could be achieved by adding optimum amounts of dispersoids in addition to the precipitate distribution. In the Task 2 program, the optimum amounts of precipitates and dispersoids will be established to improve the mechanical properties and thermal stability of the RX818 alloy.

Approach. To accomplish the above objectives, the Task 2 program consists of the following subtasks:

Subtask 2A: Evaluate RX818 Variation Alloys as Model Materials to Understand the Role of Various Strengthening Phases During Thermal Exposure (Reynolds Metals Company)

Subtask 2A.1 : Evaluate the three variants of RX818 alloy with modified Mg and Ag content to examine the effect of T_1 and S'-like phases on thermal stability of RX818 alloy.

Subtask 2A.2: Examine the effect of dispersoids on thermal stability and mechanical properties of RX818 alloy - moderate level of dispersoids for conventional casting.

Subtask 2A.3: Examine the effect of dispersoids on thermal stability and mechanical properties of RX818 alloy - high level of dispersoids by Spray Deposition Technique.

Subtask 2B: A study of the microstructural evolution of the Al-Li-Cu-Mg-Ag System with RX818 alloy (University of Virginia)

Subtask 2C: Al-Cu-Li-Mg-Ag Alloy Development (Boeing)

Subtask 2D: Al-Cu-Li-Mg-Ag Alloy Development (Douglas)

Subtask 2A. Evaluate RX818 Variation Alloys as Model Materials to Understand the Role of Various Strengthening Phases During Thermal Exposure (Reynolds Metals Company)

Principal Investigator: Dr. A. Cho

Subtask 2A.1: Evaluate the three variants of RX818 alloy with modified Mg and Ag content to examine the effect of T_1 and S′-like phases on thermal stability and mechanical properties during long-term thermal exposure.

1. Composition selection and casting. The RX818 alloy is mainly strengthened by thermodynamically stable phases which form extremely fine distributions of plate-shaped precipitates (T_1 phases) and lath-shaped precipitates (S′-like phases). Depending on the alloy compositions, different volume fractions of T_1 (Al_2CuLi) and S′-like (Al_2CuMg) phases would precipitate according to thermodynamic requirements. As a result, the overaging characteristics of the RX818 alloy would be determined not only by diffusion controlled coarsening kinetics of the two strengthening phases but also by the solute partitioning between the two phases according to their solvus temperatures. Therefore, this work will examine the effect of different volume fractions of the T_1 phase and S′-like phase by varying the amount of Mg and Ag content. Within the composition range of RX818, the volume fraction of the S′-like phase will increase with higher Mg content. The effect of Ag content in this alloy is more complicated. However, it appears that higher Ag content increases the volume fraction of T_1 phase particles.

For this work, three levels of Mg and Ag contents are selected with fixed Cu and Li contents as three RX818 variant alloys. To meet the material requirement, four ingots were cast.

Compositions:

	Cu	Mg	Li	Zr	Ag	Si	Fe
(target)	3.6	.8	1.0	.14	.4	<.08	<.08
64627(actual)	3.8	.8	.9	.13	.4	.06	.06
(target)	3.6	.8	1.0	.14	.8	<.08	<.08
64641(actual)	3.6	.76	.8	.14	.8	.06	.07
(target)	3.6	.4	1.0	.14	.4	<.08	<.08
64653(actual)	3.6	.4	.8	.14	.4	.05	.07
64667(actual)	3.4	.4	.8	.14	.5	.04	.07

2. Fabrication

The ingots were homogenized, scalped and hot rolled to 0.125" gauge sheet. Sheet products were solution heat treated at 990°F for 1 hour followed by cold water quench and 5% stretch. The sheet product were aged at 320°F for 16 hours as a standard age practice for all the RX818 variant alloys.

3. Microstructural Examination

Optical metallographic examination revealed that all the sheet gauge products are completely unrecrystallized grain structures in T8 temper condition.

Further microstructural examinations will be conducted by Prof. J. Howe at UVA. (Three alloy samples were shipped to UVA)

4. Mechanical Properties

Tensile test results and plane stress fracture toughness test results by 16" wide center notched panel tests in longitudinal direction are shown in Table 1. All four compositions met the tensile yield strength requirement proposed by Dan Fager from Boeing Aircraft Company. Tensile yield stress vs. fracture toughness values by K_c from 64641 and 64667 are plotted in Fig. 1

to compare to the typical values for other alloys. It is encouraging that both alloys are substantially superior to other aircraft alloys. Figure 2 illustrates that fracture toughness values by $K_{app.}$ from both 64641 and 64667 alloys meet the BAC's proposed TYS/$K_{app.}$ requirement.

5. Long Term Thermal Stability

The long term thermal exposure experiments will be conducted at 275°F. Sample blanks in T8 temper from the three alloys have been exposed to temperatures at 275°F for 100h, 500h, 1,000h and 2,500h. No test results are available to date.

TABLE 1

Tensile Test and Plane Stress Fracture Toughness Test Results for Four RX818 Type Alloys.

S.No.	UTS(ksi)	TYS(ksi)	El.(%)	K_c	$Ka_{pp.}$
64627-T8	84.7	82.3	6.3		
64641-T8	87.8	85.4	6.3	116.9	98.2
64653-T8	82.1	78.9	8.0		
64667-T8	85.4	82.1	8.0	131.0	102.8

Note:

All the tensile property values are averaged from duplicate test results.

K_c and $K_{app.}$ values were tested by 16" wide center notched and fatigue precracked specimens.

K_c and $K_{app.}$ values are from single tests.

K_c and $K_{app.}$ values are in ksi-(inch)$^{1/2}$.

Subtask 2A.2. Examine the effect of dispersoids on thermal stability and mechanical properties of RX818 alloy - moderate level of dispersoids for conventional casting.

1. Composition selection and casting. The strength of the RX818 alloy is based on precipitate strengthening. Further improvement of thermal stability of the alloy could be achieved by introducing optimum amount of dispersoids in addition to the precipitate distribution. The addition of dispersoids will improve thermal stability but could be deleterious to fracture toughness if too much of dispersoids are added. The key to the further improvement, therefore, would be identifying the optimum combination of precipitation strengthening and dispersoid strengthening. Two considerations were given in selecting alloying elements to form dispersoids: the first, its ability to form a thermally stable coherent phase to maximize strengthening effect, and the second, its cost to be economical enough for commercial scale production.

In this work, Zirconium, Vanadium and Manganese additions are being examined among the peritectic elements. For the initial five compositions of 30 lbs. permanent mold ingots were selected and cast. The target and actual compositions are as follows:

Compositions:

	Cu	Li	Mg	Ag	Zr	V	Mn	Hf	Sc
65836(target)	3.5	1.0	.4	.4	.17	.1	.3		
(actual)	3.4	.99	.52	.34	.15	.12	.3		
65837(target)	3.5	0.8	.4	.4	.17	.1	.3		
(actual)	3.5	.86	.39	.22	.18	.12	.3		
65638(target)	3.0	1.2	.4	.4	.17	.1	.3		
(actual)	3.1	1.21	.4	.36	.15	.12	.29		
65839(target)	3.5	1.0	.4	.4	.17	.1	--		
(actual)	3.35	1.04	.4	.34	.17	.12	--		
65840(target)	3.5	1.0	.4	.4	.17	--	--		
(actual)	3.5	1.0	.39	.36	.16	.01	--		

2. Fabrication

The ingots were homogenized, scalped and hot rolled to 0.125" gauge sheet. The hot rolled sheet was then, cold rolled to .090" gauge sheet. The final gauge sheet products were solution heat treated at 990°F for 1 hour followed by cold water quench. T8 temper sheets were stretched by 5% and aged at 320°F for 16 hours as a standard T8 temper practice. T6 temper sheets were straightened by stretching nominally 1% then aged at 350°F for 12 hours.

3. Microstructural Examination

Optical metallographic examinations were conducted in T8 temper sheet (Fig. 3). The results revealed that S. Nos. 65836, 65837 and 65838 are completely recrystallized. S. No. 65839 is partially recrystallized, and S. No. 65840 is not recrystallized. The degree of recrystallization was reflected in the strength of the material as discussed below.

4. Mechanical Properties.

Tensile test results for the T8 temper samples and the T8 temper after thermal exposure are shown in Tables 2, 3, 4 and 5. Tensile test results for the T6 temper samples after thermal exposure are shown in Tables 6, 7 and 8. Tensile test results for the T6 temper samples without thermal exposure are still being tested.

Figure 4 and Fig. 5 show the tensile yield stresses and elongation in longitudinal direction of the 5 alloys in T8 temper after thermal exposure up to 1,000 hours at 275°F. The baseline alloy 65840 shows the highest strength, due to the unrecrystallized structure. Among the recrystallized sheet materials, low solute alloys (low Li and low Ag for 65837 and low Cu for 65838) show low strengths. The decrease in strength during the thermal exposure at 275°F is not significant. The strengths of all 5 alloys become stable after 500 hours at 275°F.

In Figure 5, tensile ductility appears to be decreasing during the thermal exposure except S. No.65837.

Figure 6 and Fig. 7 show the tensile yield stresses and elongation in long transverse direction of the 5 alloys in T8 temper after thermal exposure up to 1,000 hours at 275°F. Both strengths and ductilities become stable after 500 hours at 275°F. Again, the unrecrystallized sheet, S.No.65840, shows the highest strength among the five alloys.

Figure 8 and Fig. 9 show the tensile yield stresses and elongation in longitudinal direction of the 5 alloys in T6 temper after thermal exposure up to 1,000 hours at 275°F.

Figure 10 and Fig. 11 show the tensile yield stresses and elongation in long transverse direction of the 5 alloys in T6 temper after thermal exposure up to 1,000 hours at 275°F.

The strengths in both longitudinal and long transverse direction of the five alloys increase during the thermal exposure at 275°F. The ductility variation during the thermal exposure are too much scattered to draw meaningful conclusions.

In order to compare T6 vs. T8 material, Fig. 12 shows the long transverse tensile yield stresses after thermal exposure for fully recrystallized S. No.65836 and unrecrystallized S. No. 65840. As expected, the unrecrystallized structure and T8 temper show higher strengths. In Fig. 13, long transverse ductility of T6 and T8 temper show no difference after 500 hours at 275°F. Unrecrystallized S. No.85840 in T6 and T8 tempers shows no difference in ductility after 500 hours at 275°F. However, fully recrystallized S. No.65836 in T6 condition shows higher ductility than in T8 temper material. Significance of these observations will be confirmed by notch tensile tests.

TABLE 2
Tensile test results from T8 temper material aged at 320°F/16 hrs.

S. No.	Age	Dir.	UTS(ksi)	TYS(ksi)	El.(%)
65836A	320F/16h	L	73.5	70.7	10.0
		45	72.5	65.7	10.5
65836B	320F/24h	L	74.9	72.6	7.5
		45	75.3	69.0	10.5
65837A	320F/16h	L	68.3	64.8	10.5
		45	68.3	62.6	12.0
65837B	320F/24h	L	69.5	66.0	11.0
		45	69.2	62.8	10.0
65838A	320F/16h	not tested due to material defect			
65838B	320F/24h	not tested due to material defect			
65839A	320F/16h	L	75.5	72.7	7.0
		45	72.6	66.4	11.0
65839B	320F/24h	L	74.6	71.1	8.0
		45	70.9	63.9	12.0
65840A	320F/16h	L	79.5	75.3	11.0
		45	71.1	65.9	13.5
65840B	320F/24h	L	79.4	74.9	10.0
		45	72.2	67.0	12.0

Note: All the property values are averaged from duplicate test results.

TABLE 3

Tensile test results from T8 temper material aged at 320°F/16hrs., then exposed to 100 hours at 275°F

S. No.	Dir.	UTS(ksi)	TYS(ksi)	El.(%)
65836-1A	L	78.5	78.5	8.0
	45	76.2	76.2	9.5
	LT	78.6	72.3	7.0
65837-1A	L	72.6	68.4	8.0
	45*			
	LT*			
65838-1A	L	72.3	68.3	9.0
	45	69.7	63.6	10.5
	LT	73.5	69.5	6.0
65839-1A	L	79.3	76.3	6.5
	45	74.5	68.8	12.0
	LT	78.7	73.7	7.0
65840-1A	L	83.6	79.8	10.0
	45	74.0	68.8	14.5
	LT	79.2	75.3	13.0

Note: All the property values are averaged from duplicate test results.

* Due to the material defects, tests were not conducted.

TABLE 4

Tensile test results from T8 temper material aged at 320°F/16hrs., then exposed to 500 hours at 275°F

S. No.	Dir.	UTS(ksi)	TYS(ksi)	El.(%)
65836-1B	L	76.8	74.5	8.5
	45	75.0	69.1	11.0
	LT	75.9	71.0	5.0
65837-1B	L	70.6	67.1	10.0
	45	69.3	63.7	10.5
	LT	71.8	66.2	8.0
65838-1B	L	71.8	69.0	10.0
	45	68.8	63.6	11.0
	LT	73.6	68.8	7.5
65839-1B	L	77.7	75.0	10.0
	45	72.3	66.9	11.5
	LT	76.9	71.6	7.0
65840-1B	L	80.4	76.9	9.0
	45	72.1	67.4	12.5
	LT	78.6	74.6	10.0

Note: All the property values are averaged from duplicate test results.

TABLE 5

Tensile test results from T8 temper material aged at 320°F/16hrs., then exposed to 1,000 hours at 275°F

S. No.	Dir.	UTS(ksi)	TYS(ksi)	El.(%)
65836-1C	L	77.6	75.3	7.5
	45	76.1	70.2	9.5
	LT	76.3	71.2	5.0
65837-1C	L	70.4	67.0	10.0
	45	71.3	66.0	10.0
	LT	71.8	66.7	6.0
65838-1C	L	74.6	71.4	8.0
	45	71.4	66.1	10.0
	LT	74.0	69.7	6.0
65839-1C	L	78.4	75.8	7.5
	45	72.4	67.2	11.5
	LT	77.0	72.2	7.0
65840-1C	L	81.2	77.6	8.0
	45	74.9	70.6	12.0
	LT	78.3	74.6	10.0

Note: All the property values are averaged from duplicate test results.

TABLE 6

Tensile test results from T6 temper material aged at 350°F/12hrs., then exposed to 100 hours at 275°F

S. No.	Dir.	UTS(ksi)	TYS(ksi)	El.(%)
65836-4A	L	73.2	67.9	10.0
	45	70.8	63.4	11.0
	LT	74.0	66.8	8.0
65837-4A	L	69.8	64.5	9.5
	45	67.0	60.0	11.0
	LT	68.7	61.4	9.5
65838-4A	L	70.9	65.7	9.0
	45	67.2	60.5	12.0
	LT	71.0	65.3	9.0
65839-4A	L	76.6	70.9	9.5
	45	68.1	62.0	14.0
	LT	73.6	67.5	12.0
65840-4A	L	76.5	71.1	8.0
	45	72.9	72.9	12.0
	LT	75.6	70.0	7.0

Note: All the property values are averaged from duplicate test results.

TABLE 7

Tensile test results from T6 temper material aged at 350°/12hrs., then exposed to 500 hrs at 275°/F

S. No.	Dir.	UTS(ksi)	TYS(ksi)	El.(%)
65836-4B	L	70.8	68.0	9.5
	45	72.5	65.6	9.5
	LT	74.3	68.0	7.0
65837-4B	L	71.5	67.1	10.0
	45	69.1	63.0	10.5
	LT	70.0	63.6	9.0
65838-4B	L	73.1	69.1	8.5
	45	67.7	61.8	11.5
	LT	72.1	66.3	8.0
65839-4B	L	75.6	71.2	8.0
	45	72.3	66.1	10.0
	LT	75.9	70.9	7.0
65840-4B	L	80.8	76.3	8.0
	45	71.6	65.7	12.0
	LT	76.6	71.7	10.0

Note: All the property values are averaged from duplicate test results.

TABLE 8

Tensile test results from T6 temper material aged at 350°F/12hrs., then exposed to 1,000 hours at 275°F

S. No.	Dir.	UTS(ksi)	TYS(ksi)	El.(%)
65836-4C	L	77.6	71.3	6.5
	45	72.1	65.0	10.0
	LT	75.3	68.7	7.0
65837-4C	L	72.9	68.8	10.0
	45	69.6	62.3	9.5
	LT	71.9	65.4	7.5
65838-4C	L	73.9	69.4	9.0
	45	68.6	61.7	10.5
	LT	72.5	66.3	7.0
65839-4C	L	76.9	70.8	7.0
	45	73.0	65.5	10.5
	LT	76.1	70.0	6.0
65840-4C	L	82.0	77.0	8.0
	45	72.7	67.0	12.5
	LT	76.9	72.0	9.5

Note: All the property values are averaged from duplicate test results.

Subtask 2A.3: Examine the effect of dispersoids on thermal stability and mechanical properties of RX818 alloy - high level of dispersoids by Spray Deposition Technique.

1. Composition selection and casting by Spray Deposition:

The dispersoid particles formed by Zr, V and Mn are coherent phases which are effective strengthening agents. However, addition of too much of these elements would result in coarse incoherent particles which are extremely deleterious to fracture toughness.

Therefore, the total amount of these coherent dispersoid particles is very limited compared to the precipitate particles in RX818 alloy. One way to increase the amount of these coherent dispersoid particles is to employ a casting technique with a faster solidification rate.

In this work, RX818 variation alloys with high volume fracture of dispersoids will be evaluated with the billet cast by Spray Deposition Technique. Spray Deposition Technique was selected for its enhanced solidification rate and its economic feasibility for commercial scale production. Five compositions of 30 lbs. permanent mold ingots were cast as starting stock material for Spray Deposition casting. The compositions are as follows:

Compositions:

S.No.		Cu	Li	Mg	Ag	Zr	V	Mn
65831	(target)	3.5	1.0	.4	.4	.3	.2	--
	(actual)	3.45	1.0	.43	.29	.29	.18	.01
65632	(target)	3.5	1.0	.4	.4	.3	.2	.5
	(actual)	3.6	1.04	.43	.38	.28	.18	.44
65833	(target)	3.5	1.0	.4	.4	.25	.2	.3
	(actual)	3.6	1.1	.43	.44	.26	.17	.32
65834	(target)	3.5	1.0	.4	.4	.25	.1	.3
	(actual)	3.39	1.02	.41	.43	.22	.09	.3
65835	(target)	3.0	1.2	.4	.4	.3	.2	--
	(actual)	3.58	1.21	.42	.46	.27	.17	--

2. Spray Deposition:

University of California at Irvine completed casting of five spray deposited billets.

The billets were machined to 3" diameter for extrusion.

FRACTURE TOUGHNESS OF RX818-T8 TYPE ALLOYS

Center Notched 16" Wide Panel(Fatigue Precrack)

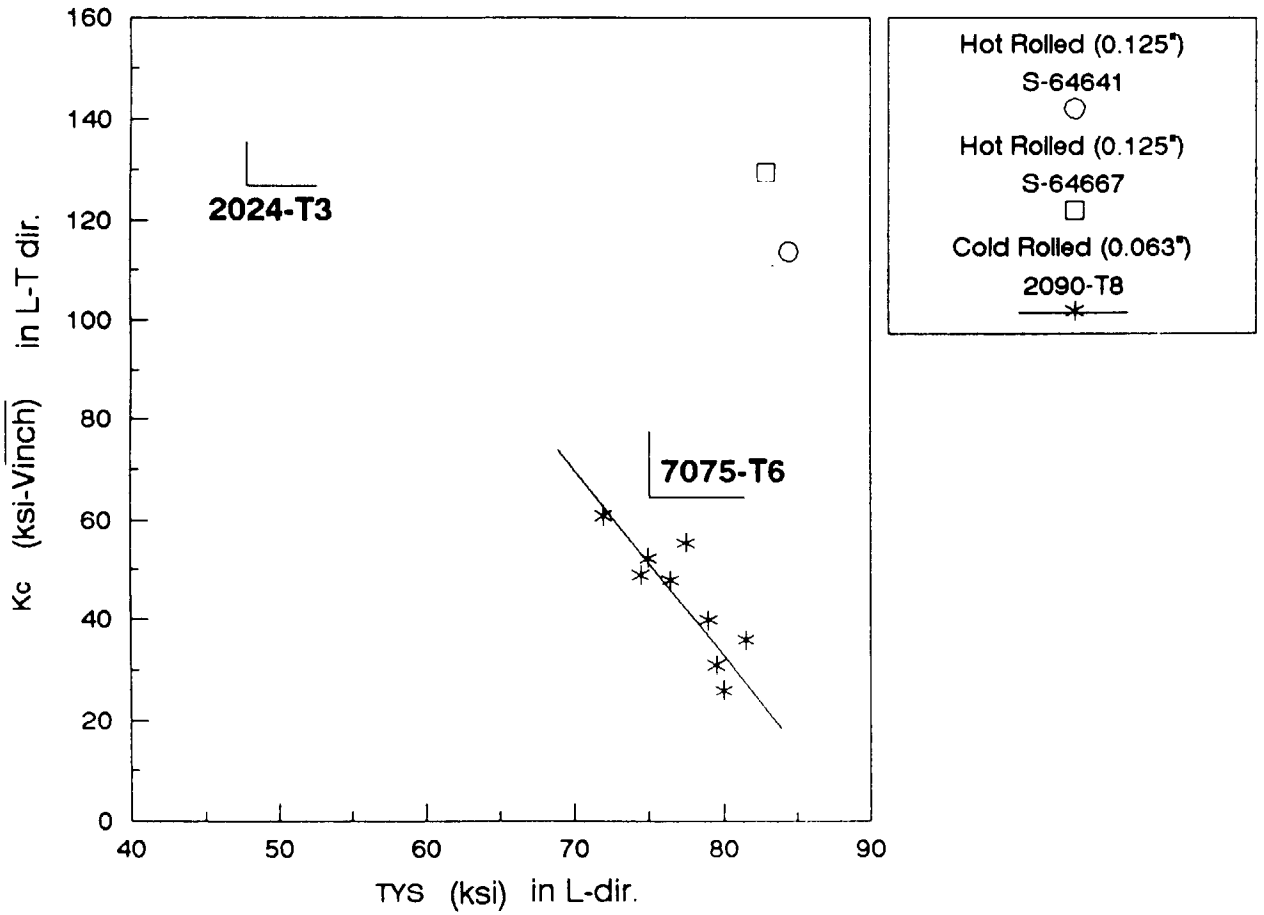

8/4/92

Alex Cho;Reynolds

Figure 1

FRACTURE TOUGHNESS OF RX818-T8 TYPE ALLOYS

Center Notched 16" Wide Panel(Fatigue Precrack)

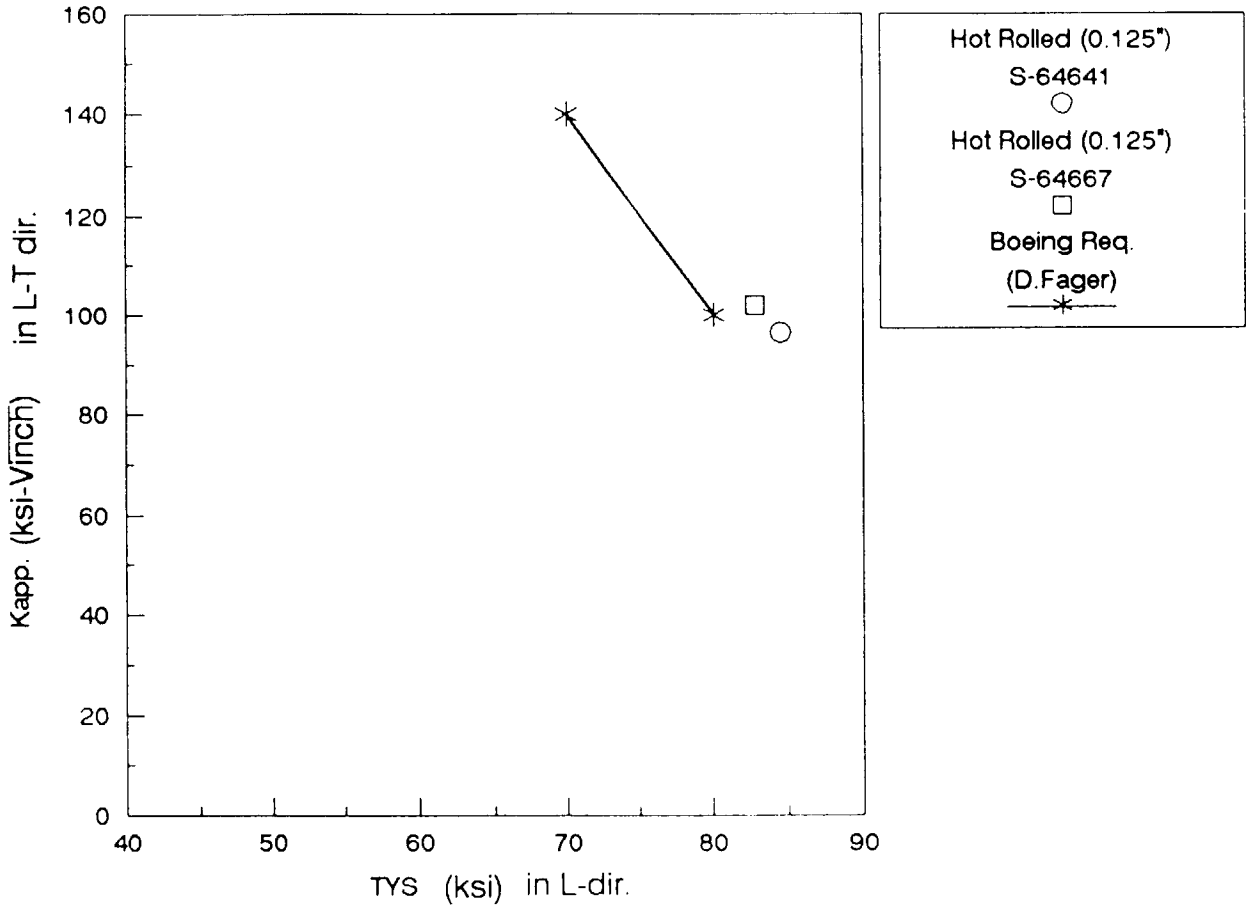

8/4/92

Alex Cho;Reynolds

Figure 2

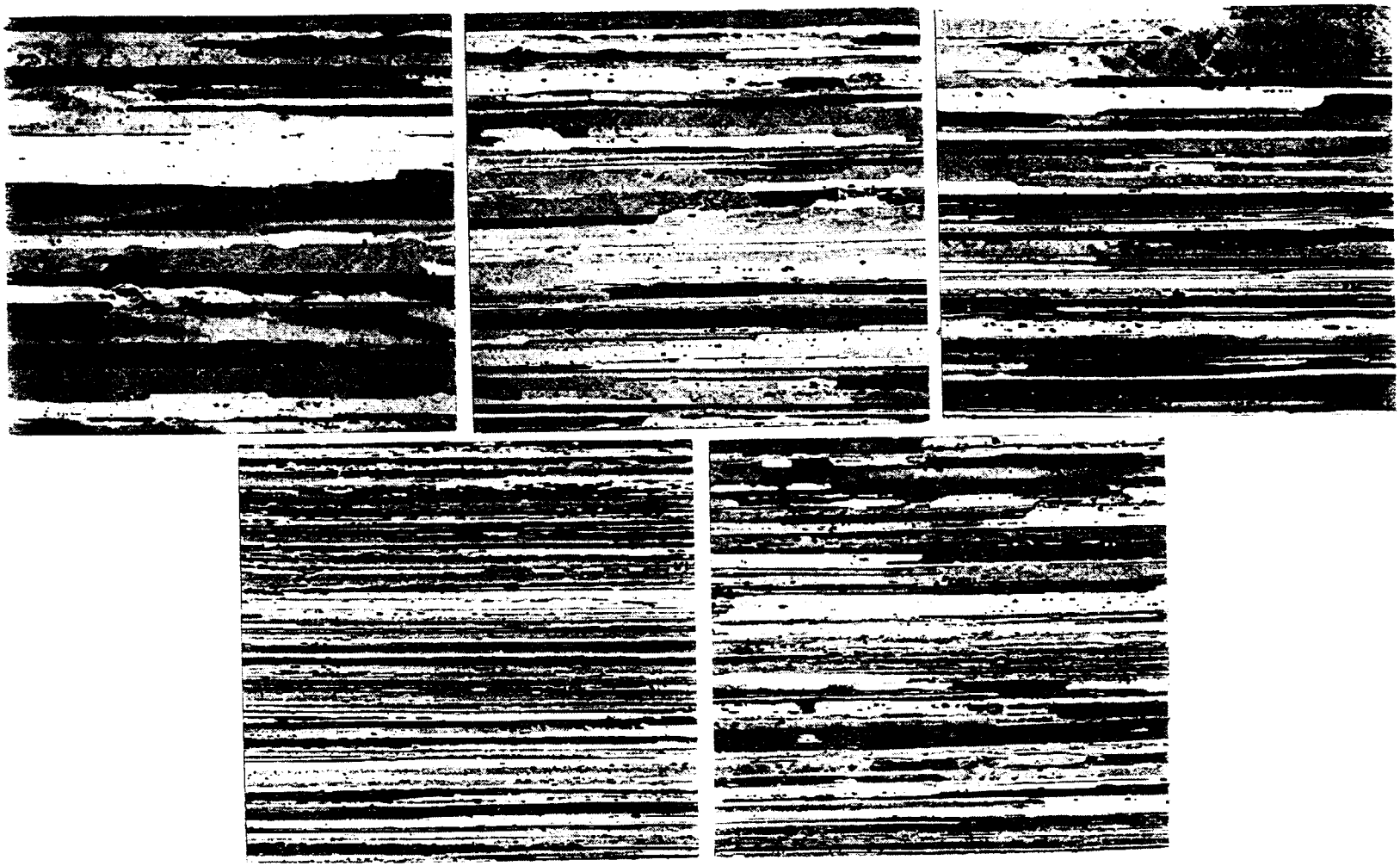

Figure 3. Photomicrographs of metallographically prepared longitudinal cross-sections of the submitted Weldalite samples (Lot #65836A-#65840A) showing the typical grain structure observed just below the surface to near center.
Etch: Electrolytic 3% HBF_4 35 DC $Volts_3$ - 70°C

Magnification: 100X

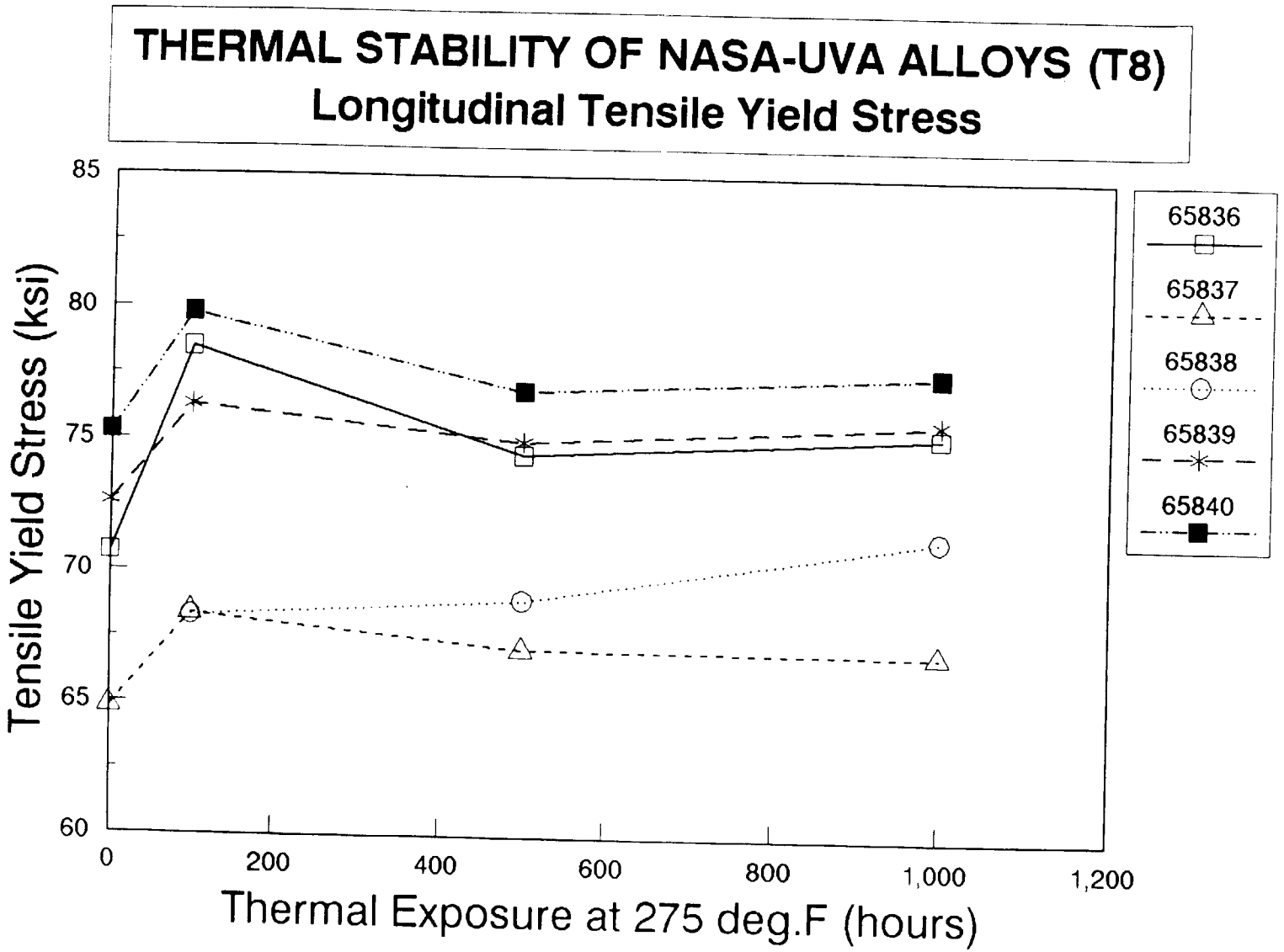
THERMAL STABILITY OF NASA-UVA ALLOYS (T8)
Longitudinal Tensile Yield Stress
Tensile Yield Stress (ksi)
85
80
75
70
65
60
0
200
400
600
800
1,000
1,200
Thermal Exposure at 275 deg.F (hours)
65836
65837
65838
65839
65840

Figure 4

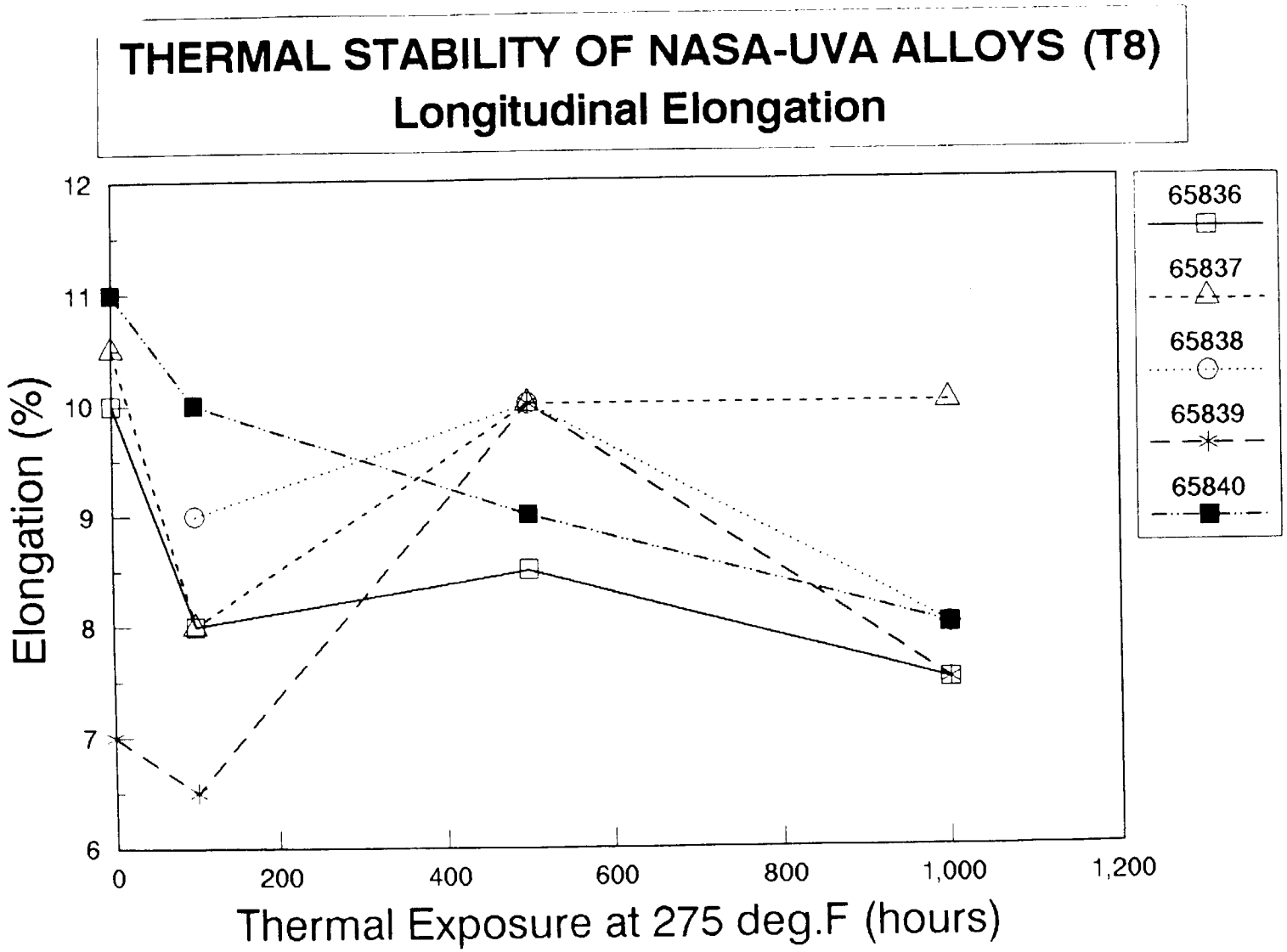
THERMAL STABILITY OF NASA-UVA ALLOYS (T8)
Longitudinal Elongation
Elongation (%)
12
11
10
9
8
7
6
0
200
400
600
800
1,000
1,200
Thermal Exposure at 275 deg.F (hours)
65836
65837
65838
65839
65840

Figure 5

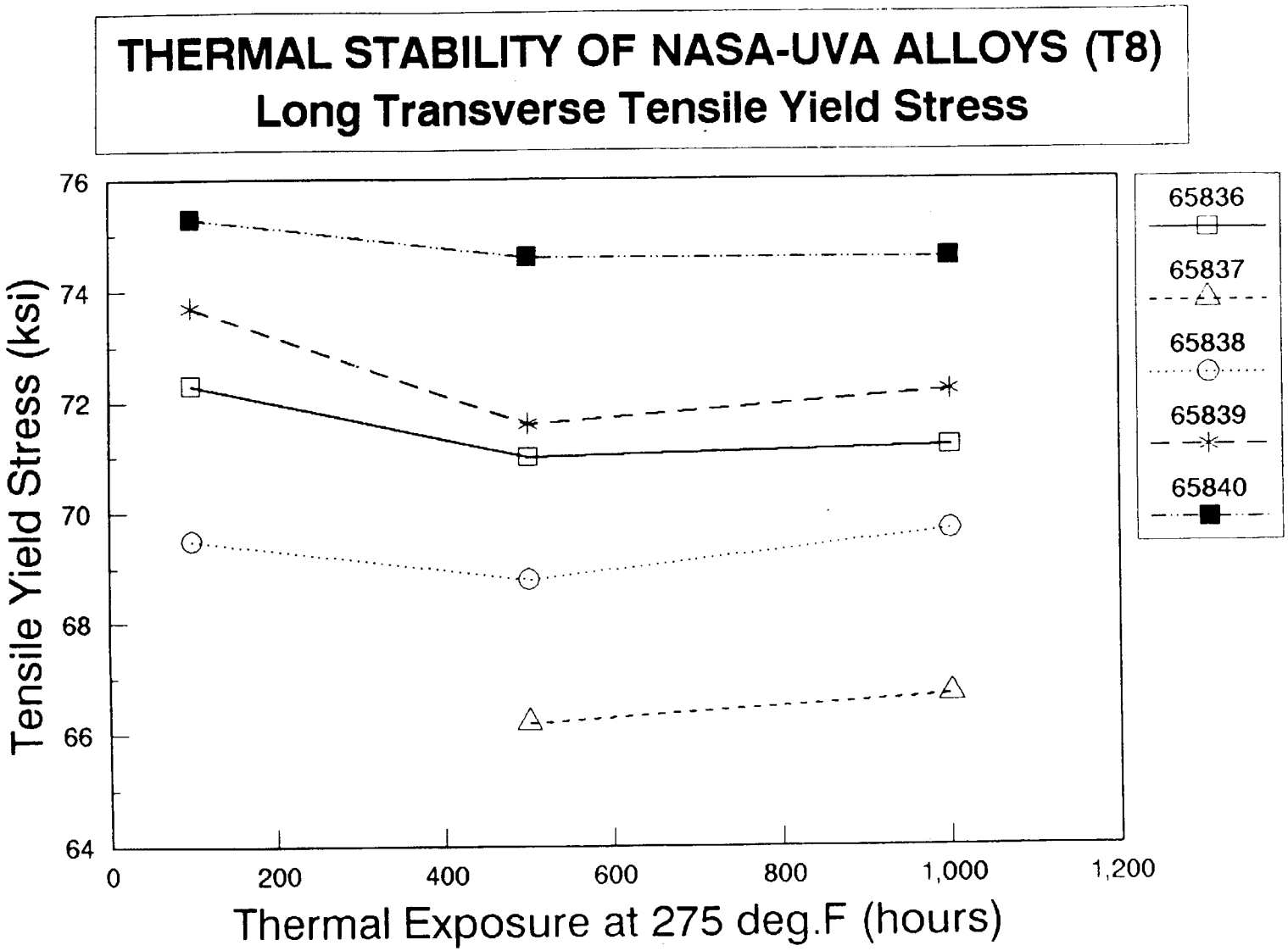
THERMAL STABILITY OF NASA-UVA ALLOYS (T8)
Long Transverse Tensile Yield Stress
Tensile Yield Stress (ksi)
76
74
72
70
68
66
64
0
200
400
600
800
1,000
1,200
Thermal Exposure at 275 deg.F (hours)
65836
65837
65838
65839
65840

Figure 6

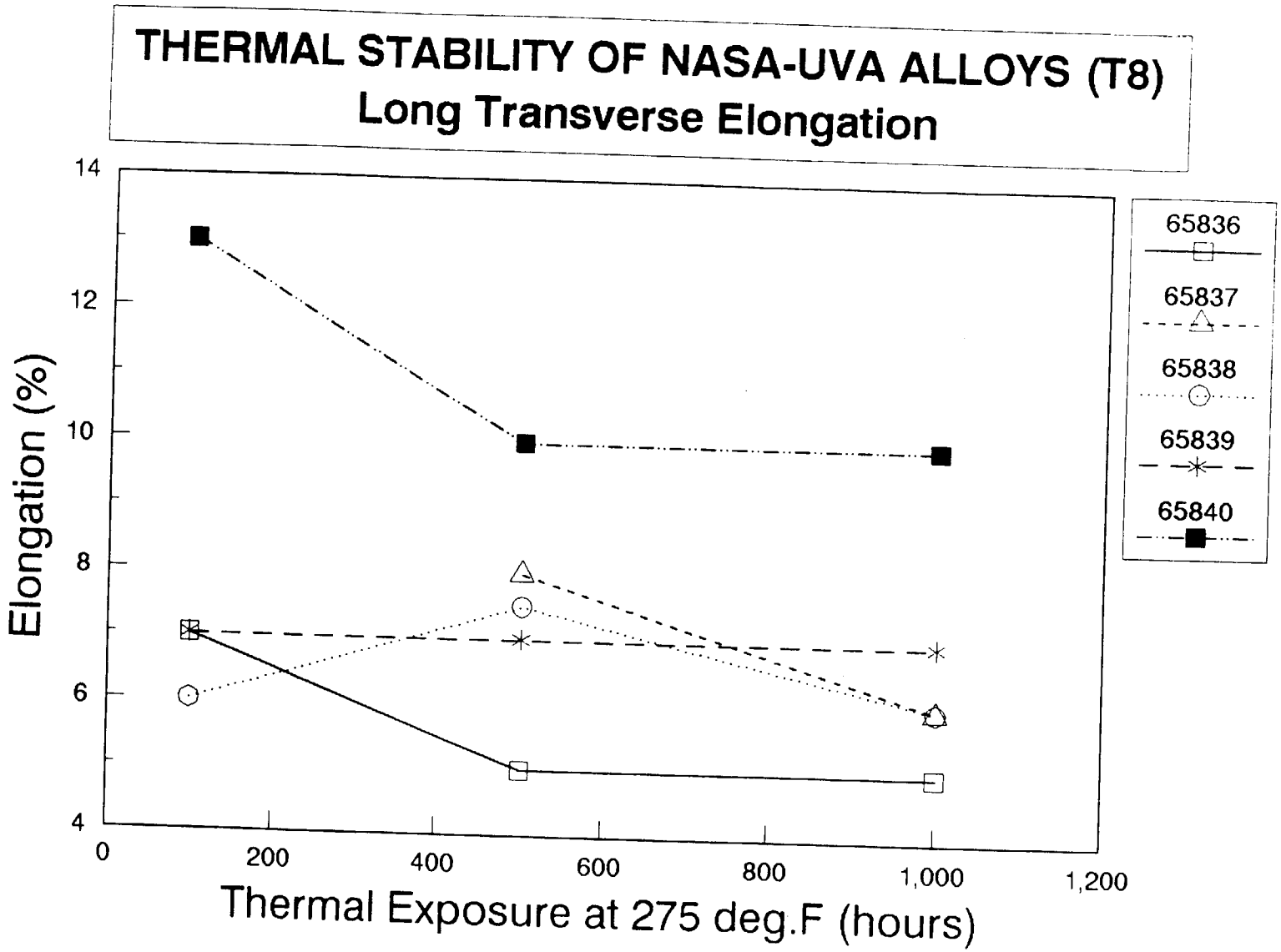
THERMAL STABILITY OF NASA-UVA ALLOYS (T8)
Long Transverse Elongation
Elongation (%)
14
12
10
8
6
4
0
200
400
600
800
1,000
1,200
Thermal Exposure at 275 deg.F (hours)
65836
65837
65838
65839
65840

Figure 7

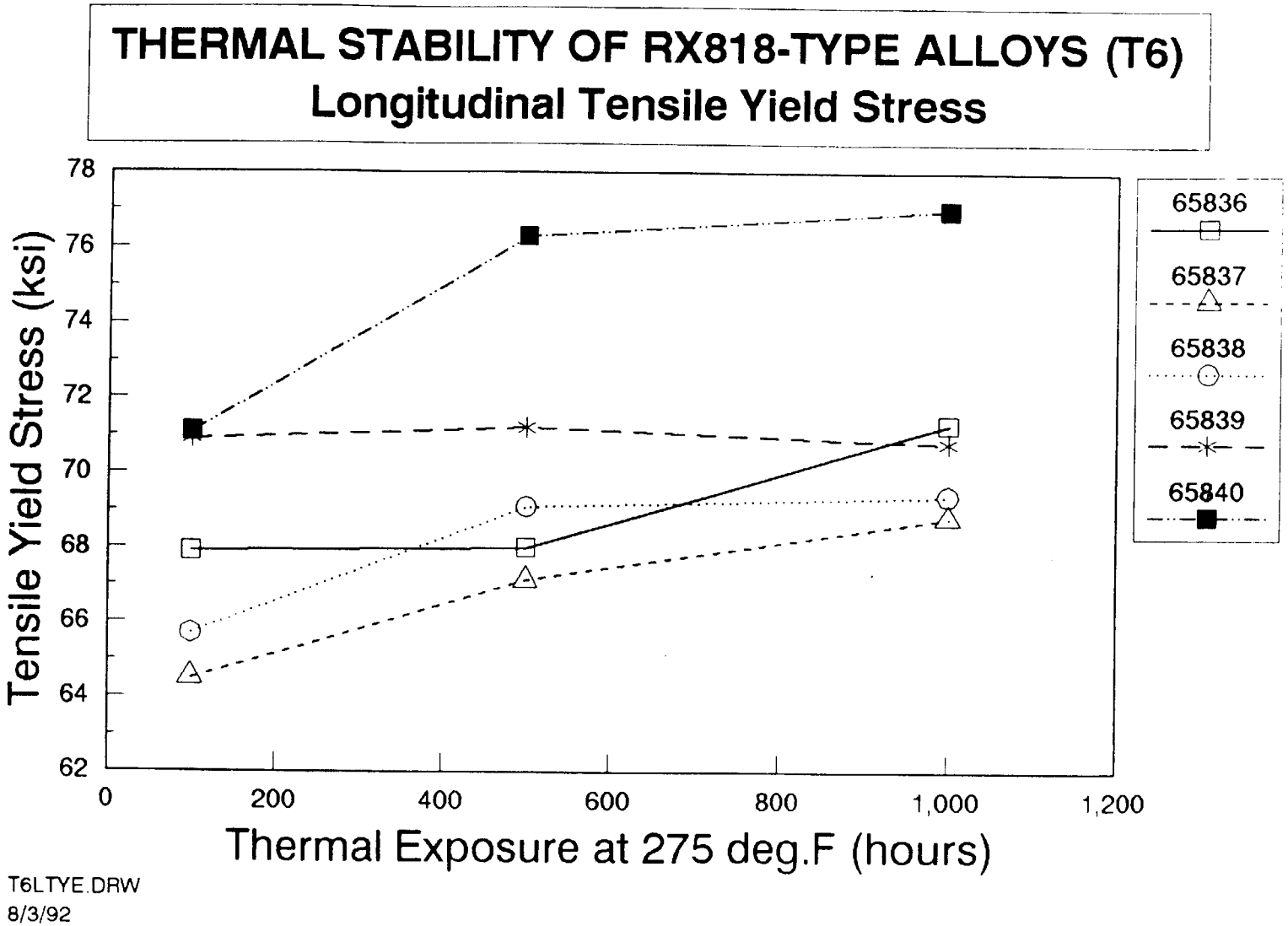
THERMAL STABILITY OF RX818-TYPE ALLOYS (T6)
Longitudinal Tensile Yield Stress
Tensile Yield Stress (ksi)
78
76
74
72
70
68
66
64
62
0
200
400
600
800
1,000
1,200
Thermal Exposure at 275 deg.F (hours)
65836
65837
65838
65839
65840
T6LTYE.DRW
8/3/92

Figure 8

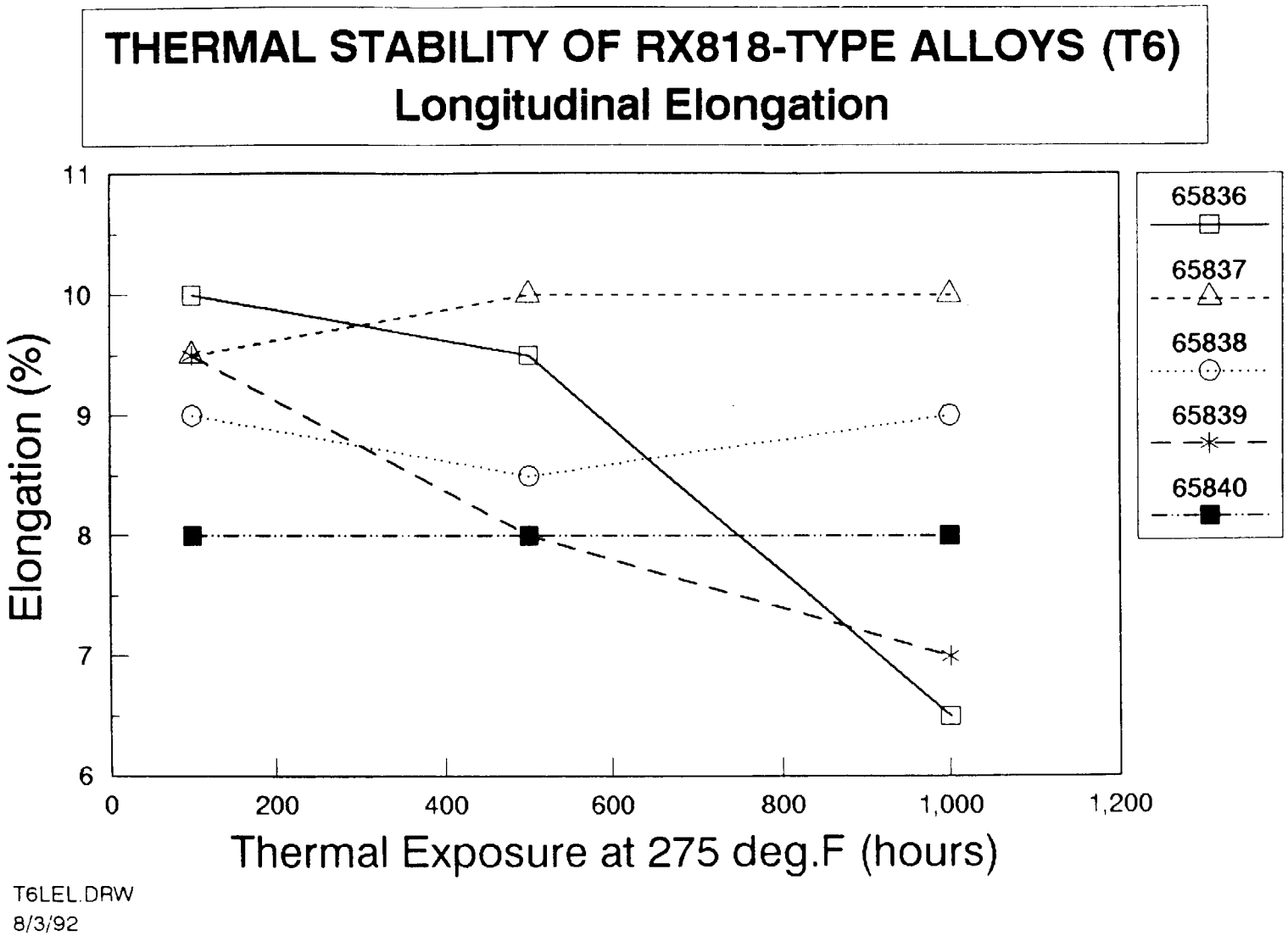
THERMAL STABILITY OF RX818-TYPE ALLOYS (T6)
Longitudinal Elongation
Elongation (%)
11
10
9
8
7
6
0
200
400
600
800
1,000
1,200
Thermal Exposure at 275 deg.F (hours)
65836
65837
65838
65839
65840
T6LEL.DRW
8/3/92

Figure 9

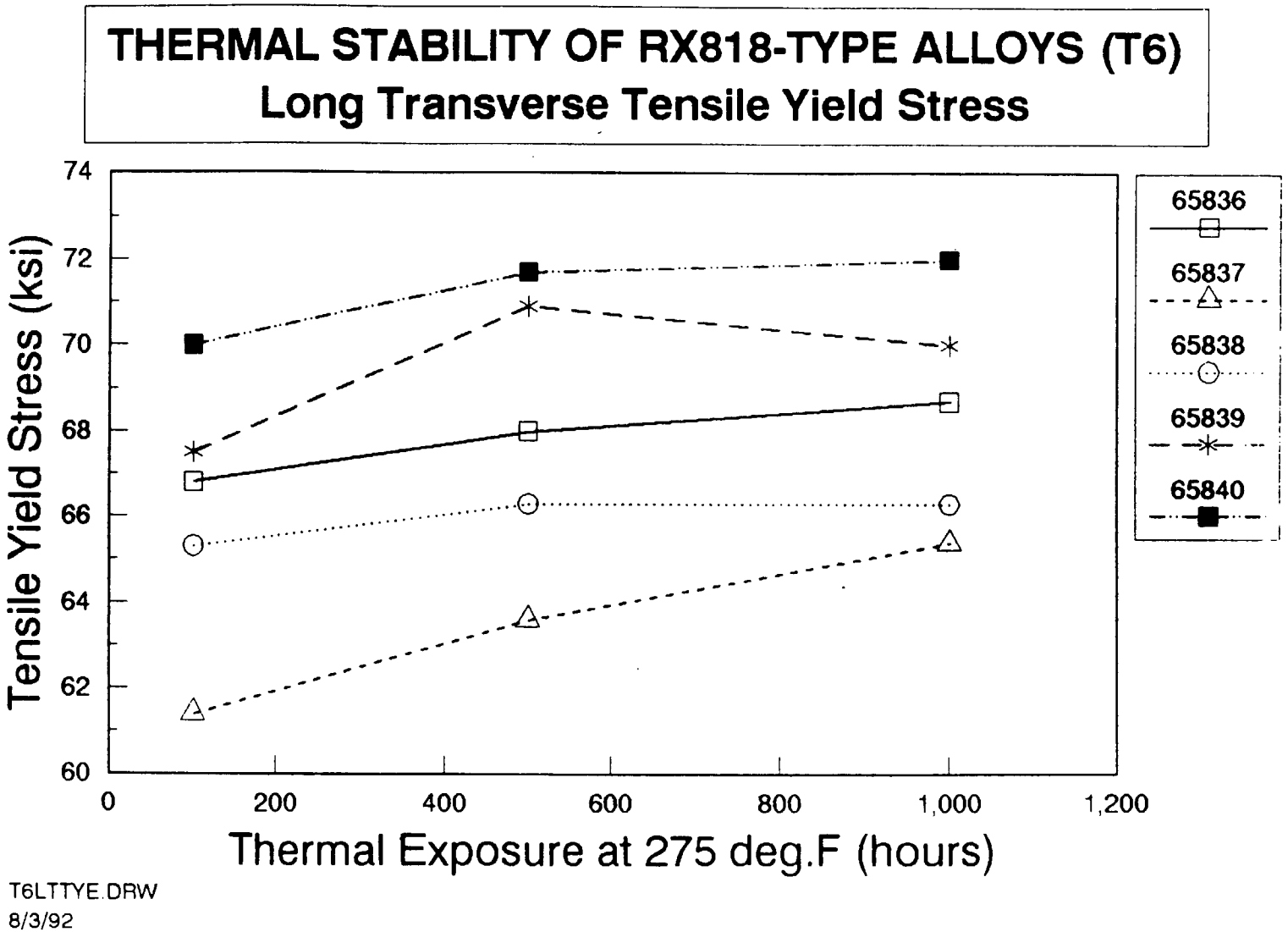
THERMAL STABILITY OF RX818-TYPE ALLOYS (T6)
Long Transverse Tensile Yield Stress
Tensile Yield Stress (ksi)
74
72
70
68
66
64
62
60
0
200
400
600
800
1,000
1,200
Thermal Exposure at 275 deg.F (hours)
65836
65837
65838
65839
65840
T6LTTYE.DRW
8/3/92

Figure 10

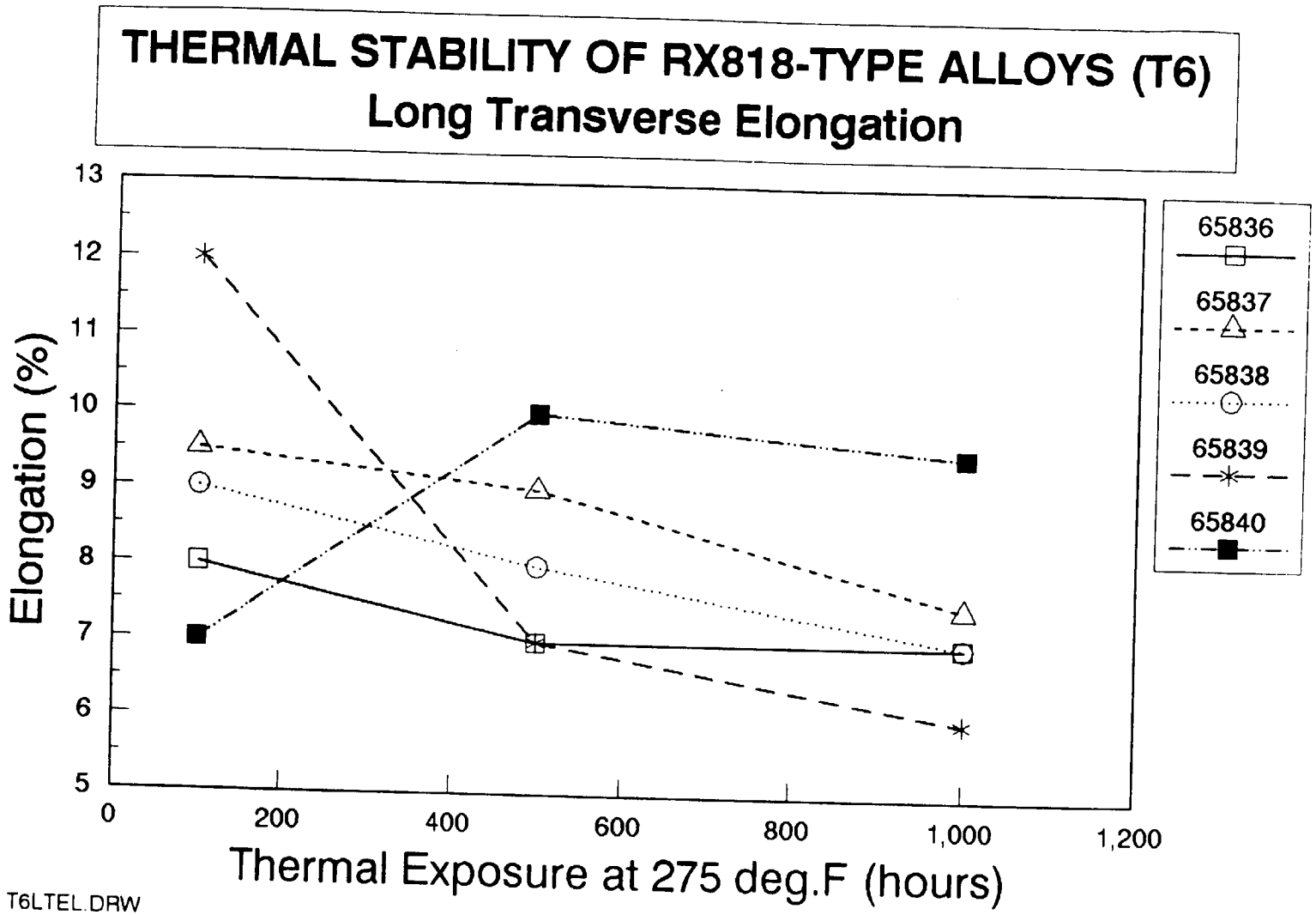
THERMAL STABILITY OF RX818-TYPE ALLOYS (T6)
Long Transverse Elongation
Elongation (%)
13
12
11
10
9
8
7
6
5
0
200
400
600
800
1,000
1,200
Thermal Exposure at 275 deg.F (hours)
65836
65837
65838
65839
65840
T6LTEL.DRW
8/3/92

Figure 11

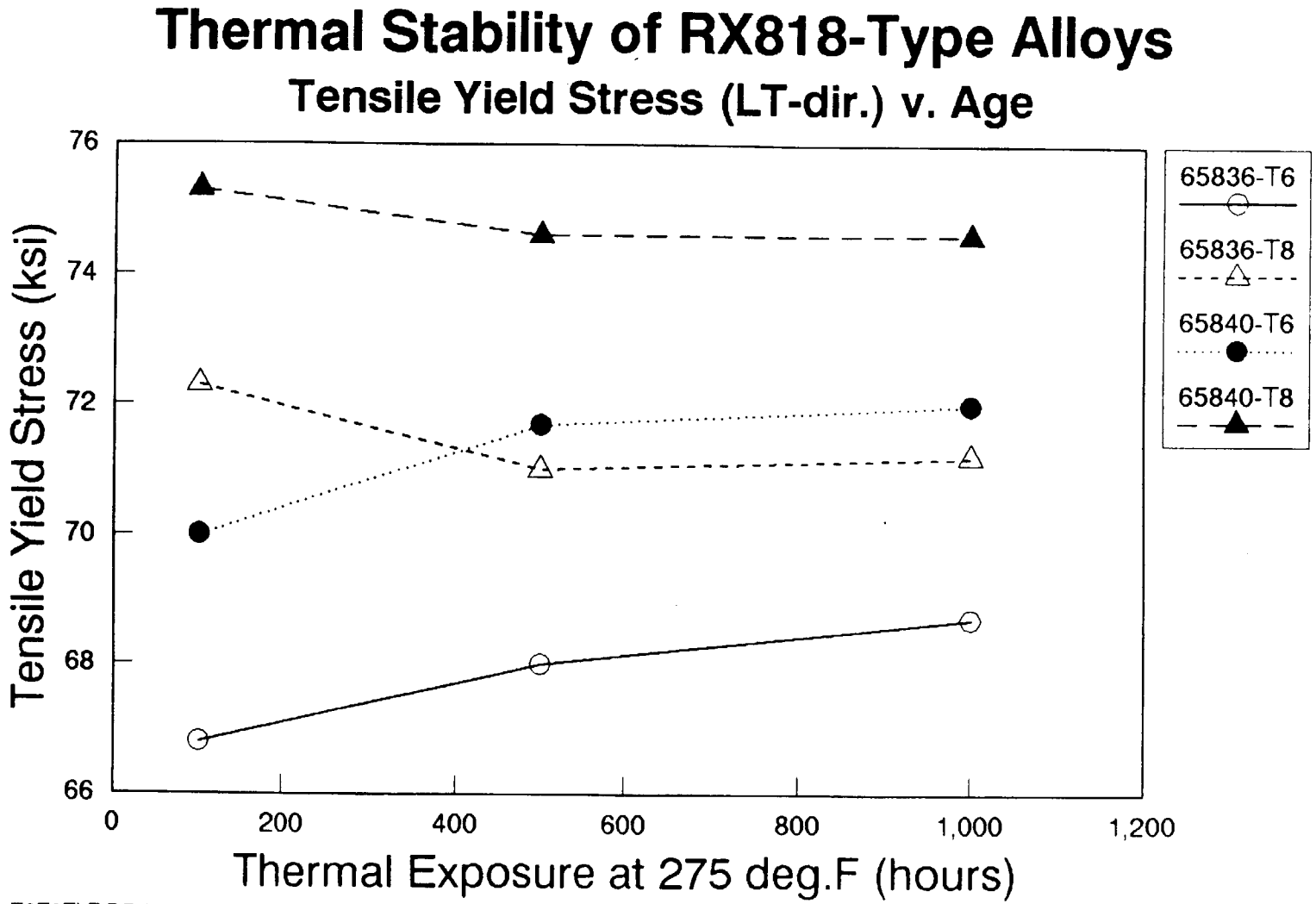
Thermal Stability of RX818-Type Alloys
Tensile Yield Stress (LT-dir.) v. Age
Tensile Yield Stress (ksi)
76
74
72
70
68
66
0
200
400
600
800
1,000
1,200
Thermal Exposure at 275 deg.F (hours)
65836-T6
65836-T8
65840-T6
65840-T8
T6T8TLT.DRW
8/3/92

Figure 12

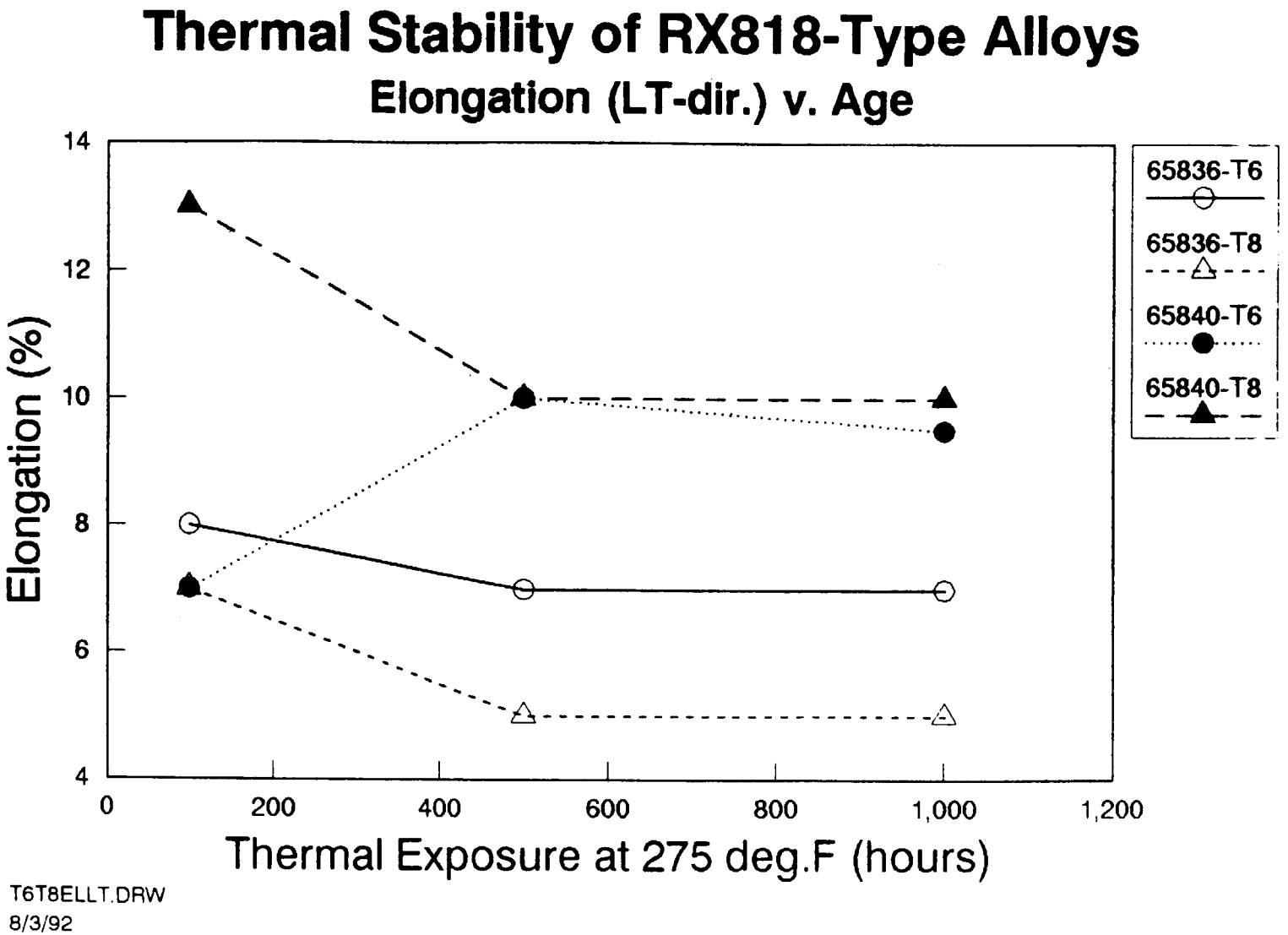
Thermal Stability of RX818-Type Alloys
Elongation (LT-dir.) v. Age
Elongation (%)
14
12
10
8
6
4
0
200
400
600
800
1,000
1,200
Thermal Exposure at 275 deg.F (hours)
65836-T6
65836-T8
65840-T6
65840-T8
T6T8ELLT.DRW
8/3/92

Figure 13

Subtask 2B. A Study of the Microstructure/Property Evolution Characteristics of the Al-Li-Cu-Mg-Ag System with RX818 (UVa)

Principal Investigator: Dr. J.M. Howe
Research Associate: Dr. Y. Mou

During the first six months, we examined the microstructure of Reynolds RX818-T8 alloy sheet received from NASA-Langley (Lot No. 64667 shown in Subtask 2A.1) in both the -T8 condition and after additional aging treatments for longer times at the same or higher aging temperatures. The purpose of these experiments was to obtain initial insight into the effects of time and temperature on the microstructure of the base RX818 alloy. The RX818 sheet had been solution heat treated, stretched 5% and aged for 16 hrs. at 160°C (320°F) to a -T8 temper prior to our examination. Samples of this sheet were then aged for an additional 990 hrs. at 160°C (320°F) at NASA-Langley and also for 168 hrs. at 250°C (482°F) at UVa. In addition, three other variations of RX818 alloy (Lot Nos. 64627, 64641 and 64653 shown in Subtask 2A.1) in a -T8 temper were received from Reynolds and the microstructures of these alloys were examined to assess the effects of increasing levels of Mg and Ag on the microstructure of the base RX818 alloy. Thin foils were prepared by electropolishing 3 mm disks in a 25% HNO_3 - methanol solution and the thin foils were examined in a Philips EM400T microscope at 120 kV.

Microstructure of RX818 Lot. No. 64667. Figures 1 (a-c) show three bright-field (BF) transmission electron microscope (TEM) images and corresponding selected-area diffraction (SAD) patterns of the -T8 material in <110>, <112> and <100> matrix zone axes, respectively. In the -T8 condition, the alloy contains mostly T_1 phase in the form of plates on the {111} matrix planes and a minority of S' phase in the form of laths along the <100>

matrix directions. Two variants of the T_1 phase are edge on in the <110> image in Fig. 1(a), one variant is edge on in the <112> image in Fig. 1(b) and all of the variants are inclined in the <100> image in Fig. 1(c). The largest T_1 plates and S' laths in the BF images were about 110 nm and these precipitates are indicated in Figs. 1(a) and (b). Several variants of S' laths are oriented end on in a <100> matrix orientation and a few of these precipitates are arrowed in Fig. 1 (c). Note the small volume fraction of S' precipitates. No other phases were observed in this condition.

The corresponding <110> and <112> SAD patterns in Figs. 1(a) and (b) display streaks along the <111> directions with prominent spots at 1/3 and 2/3 of the <220> matrix direction and these are characteristic of the T_1 phase. Faint streaking along the <420> matrix direction is also evident in the <112> zone axis in Fig. 1(b) (arrow) and this is due to the relatively small volume fraction of S' phase present. Faint reflections are also present along the <100> directions in the <110> SAD pattern in Fig. 1(c) (arrowed) due to the S' phase. Additional faint reflections at the 1/2 of the <220> matrix positions may be due to the ß' phase since the alloy contains 0.13 wt.% Zr, but this has not yet been confirmed.

Figures 2(a) and (b) show bright-field TEM images and corresponding diffraction patterns for the sample aged for an additional 990 hrs. at 160°C (total aging of 1006 hrs. at 160°C) in <110> and <112> zone axes, respectively. Comparison with Figs. 1(a) and (b) shows that the microstructure has changed due to this extra heat treatment. Qualitatively, there appears to be more S' phase (labelled in Fig. 2(b)) and somewhat less of the T_1 phase, and the T_1 plates have begun to thicken (coarsen), as can be seen for the arrowed plates in Fig. 2(b) and by Fig. 2(c). Figure 2(c) is a higher magnification TEM image of T_1 plates in a <110> zone axis which illustrates how the thickness of one particular T_1 plate

has thickened to four or five times that of the initial precipitates. The strength of the S' precipitate reflections in Figs. 2(a) and (b) is much stronger than in Figs. 1(a) and (b) and distinct spots are visible rather than diffuse streaks, as indicated by the arrow in Fig. 2(b).

Figures 3(a) and (b) show TEM images and corresponding diffraction patterns in <110> and <100> zone axes, respectively, for the -T8 sample aged for an additional 168 hrs. at 250°C (482°F). The magnification of these images is slightly less than that in Figs. 1 and 2 and it is evident that the microstructure has changed dramatically with this additional heat treatment. The precipitate density is much lower than before and the existing precipitates are much larger. Some T_1 phase is still present, as seen in the <110> bright-field TEM image in Fig. 3(a), where a T_1 precipitate is indicated. The T_1 reflections at 1/3 and 2/3 of the <220> direction are present in the SAD pattern in Fig. 3(a) and the streaks along the <111> matrix directions have become a series of discrete spots due to the increased thickness of the T_1 plates. Some weak ß' reflections are also visible in the diffraction pattern in Fig. 3(a). Fig. 3(b) shows an additional image and diffraction pattern in a <100> orientation. The large plates in Fig. 3(b) appear to be Θ' phase on the {100} planes, as identified both from their morphology in the bright-field image and from the diffraction spots at 1/3 and 2/3 of the <200> matrix reflections arrowed in the corresponding SAD pattern. ß' reflections are also visible in the SAD pattern. Since the precipitates are widely spaced in this sample, the reflections present in the diffraction pattern depend on the position of the selected-area aperture.

Lastly, Figures 4(a) and (b) show TEM images and corresponding SAD patterns in <110> and <112> orientations, respectively, of grain-boundary precipitates in a sample aged for an additional 234 hrs. at 160°C (320°F). Both boundaries are low-angle grain boundaries (angle of misorientation less than 5°) as

evident from the nearly parallel orientations of the T_1 plates in the two grains. Precipitation has occurred on the boundaries and a number of the precipitates in Fig. 4(a) display strong Moire contrast, similar to the precipitates in Figs. 2(c), indicating that they may be the same phase. Other plate-shaped precipitates that cause puckering of the grain boundary are visible in Fig. 4(b). Since these precipitates are not parallel to the T_1 plates in the matrix, they are probably not T_1 phase. The diffraction patterns from the grain-boundary regions contain many extra reflections due to the precipitates and these will be identified in future work.

Microstructures of Lot Nos. 64627 and 64641. Figures 5 and 6 show the effects of increasing the Mg and Ag contents on the microstructure of the base RX818 alloy. Figures 5(a-c) show BF TEM images and corresponding diffraction patterns in the <110>, <112> and <100> zone axes for the higher Mg alloy (Lot. No. 64627). Increasing the Mg content to 0.7wt.% increases the amount of S' phase, and this is particularly evident by the strong S' reflections which appear as crosses (arrowed) in the <100> SAD pattern in Fig. 5(c). The S' precipitates appeared to nucleate in sheets, as indicated by arrows in several of the BF TEM images.

Increasing both the Ag and Mg contents to about 0.8wt.% caused relatively coarse S' plates to form in the matrix rather than the thin sheets seen in Fig. 5. This is evident in the <112> BF TEM images in Figs. 6(a-b). The diffraction pattern in this orientation (Fig. 6(c)) contains many spots due to the twelve different variants of S' phase in addition to the T_1 precipitates, and we have begun to simulate the diffraction pattern (Fig. 6(d)) in order to distinguish the different spots in the pattern.

Summary. The microstructure of the base RX818-T8 alloy contains mostly T_1 plates with a small amount of S' phase. Aging of the -T8 material for an additional 990 hrs. at 160°C (320°F) leads to some coarsening of the T_1 plates and the formation of more S' phase. Aging at 250°C leads to dramatic changes in the phases in the microstructure. Increasing the Mg content of the base RX818 alloy increases the amount of fine S' phase while increasing both the Mg and Ag concentrations causes coarse S' phase to form in the microstructure rather than fine laths.

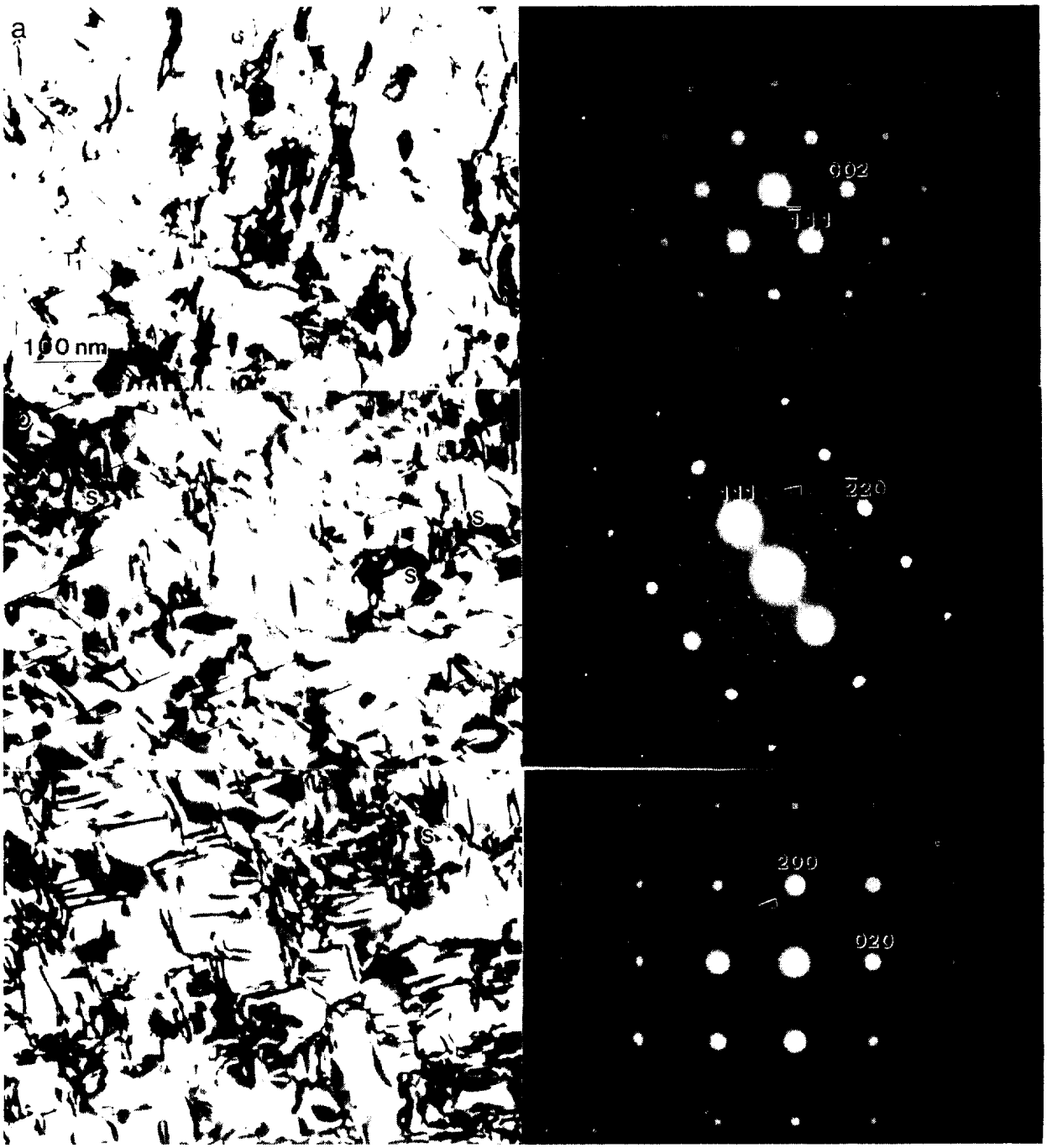

Figure 1. Bright-field TEM images and corresponding diffraction patterns from RX818-T8 alloy containing 0.4Mg and 0.4Ag (wt.%) in (a) <110>, (b) <112> and (c) <100> zone axis orientations.

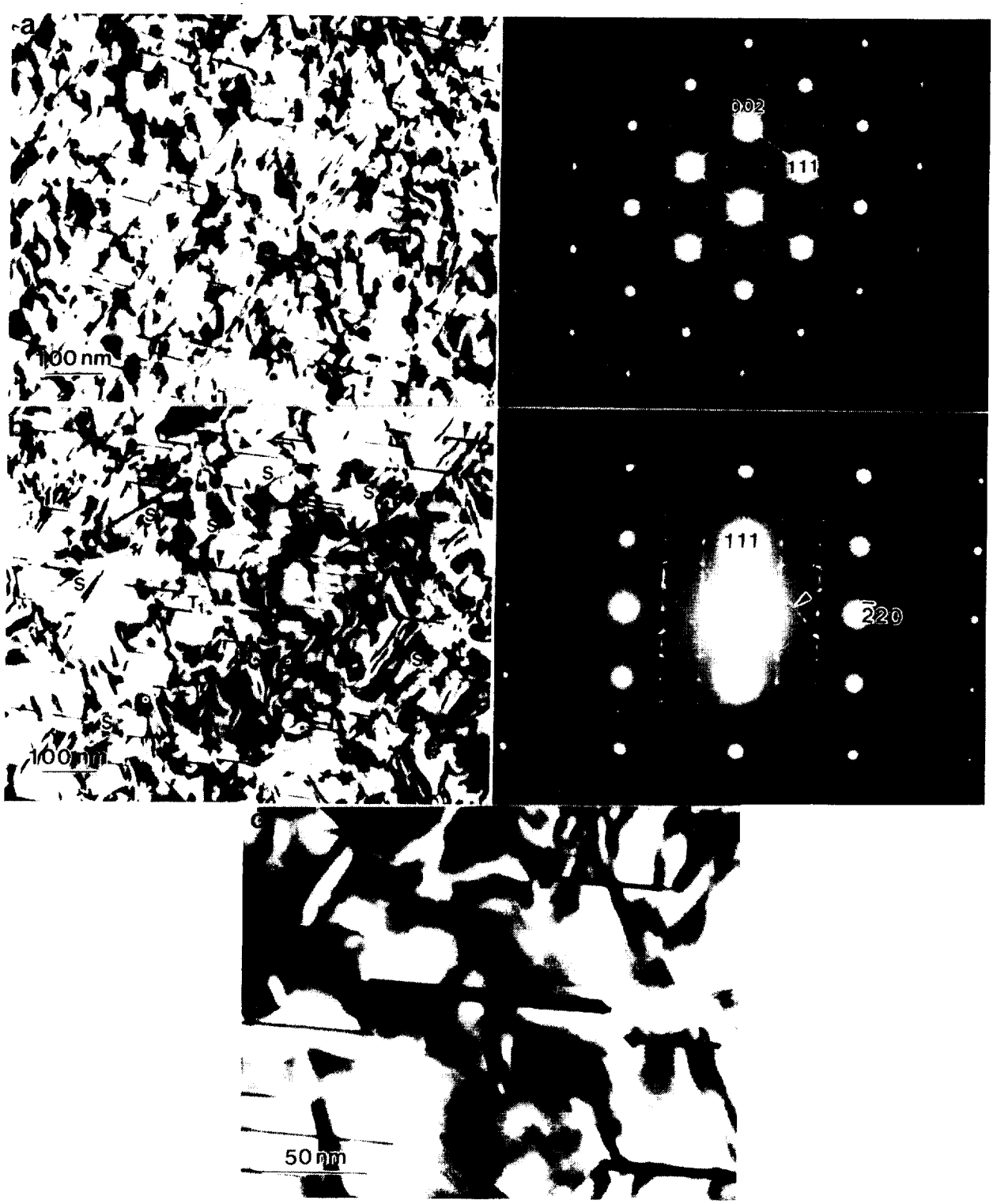

Figure 2. Bright-field TEM images and corresponding diffraction patterns from RX818-T8 alloy aged for an additional 990 hrs. at 160°C (320°F) in (a) <110> and (b) <112> zone axis orientations. (c) An unusually thick T_1 precipitate plate.

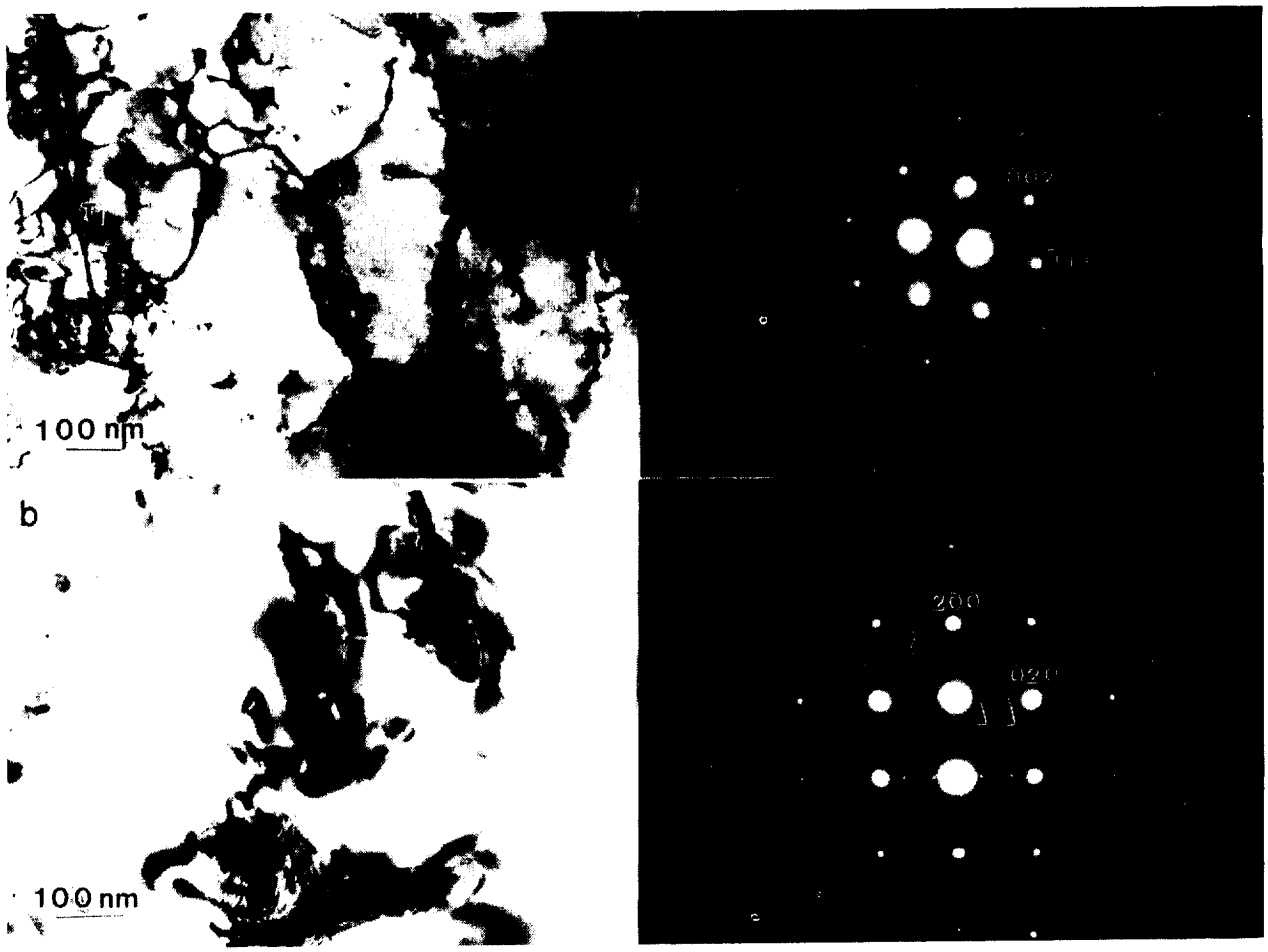

Figure 3. Bright-field TEM images and corresponding diffraction patterns from RX818-T8 alloy aged for an additional 168 hrs. at 250°C (482°F) in (a) <110> and (b) <100> zone axis orientations.

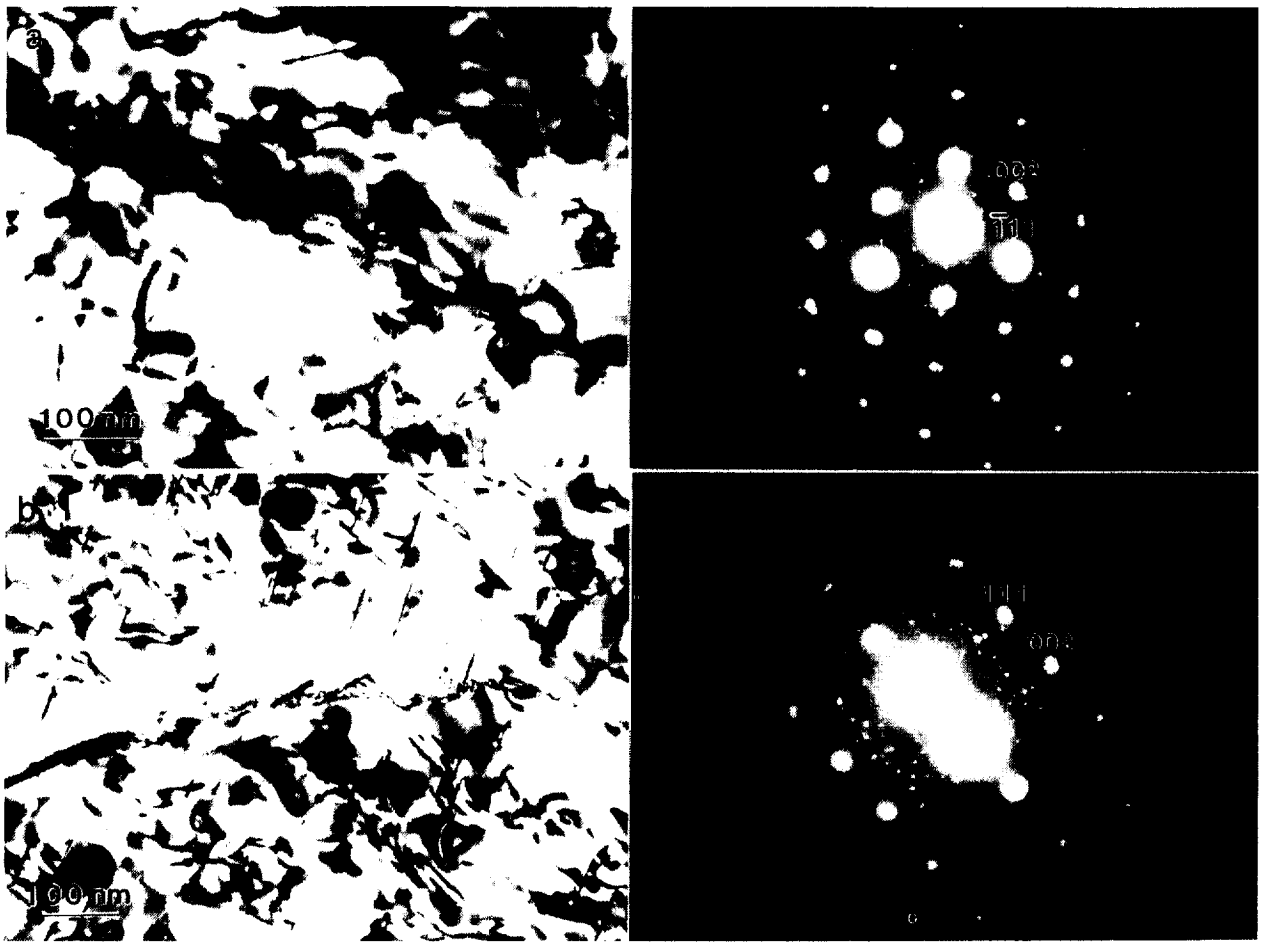

Figure 4. Bright-field TEM images and corresponding diffraction patterns from low-angle grain-boundaies in RX818-T8 alloy aged for an additional 234 hrs. at 160°C (320°F) in (a) <110> and (b) <112> zone axis orientations.

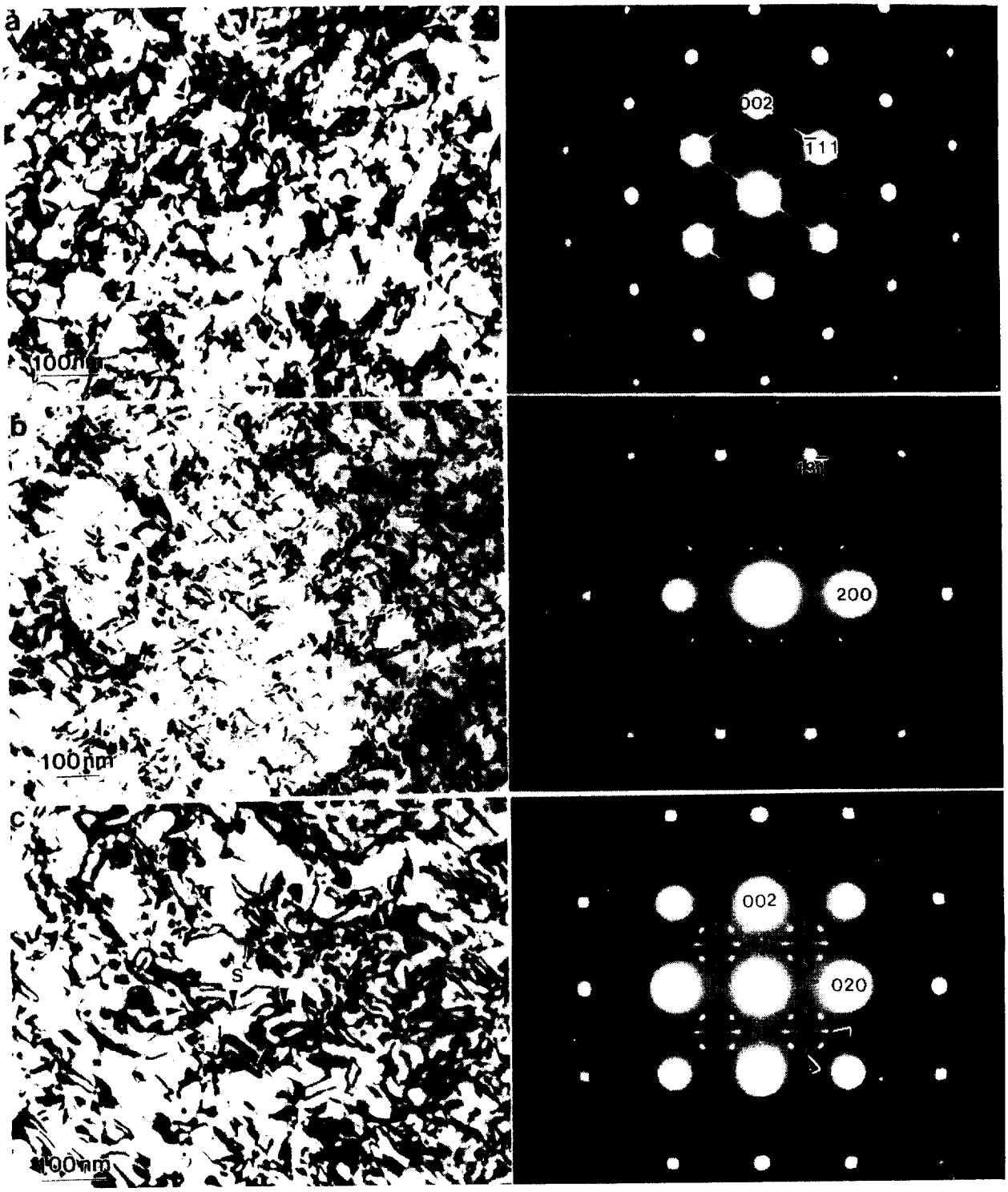

Figure 5. Bright-field TEM images and corresponding diffraction patterns from RX818-T8 alloy containing 0.7Mg and 0.4Ag (wt.%) in (a) <110>, (b) <112> and (c) <100> zone axis orientations.

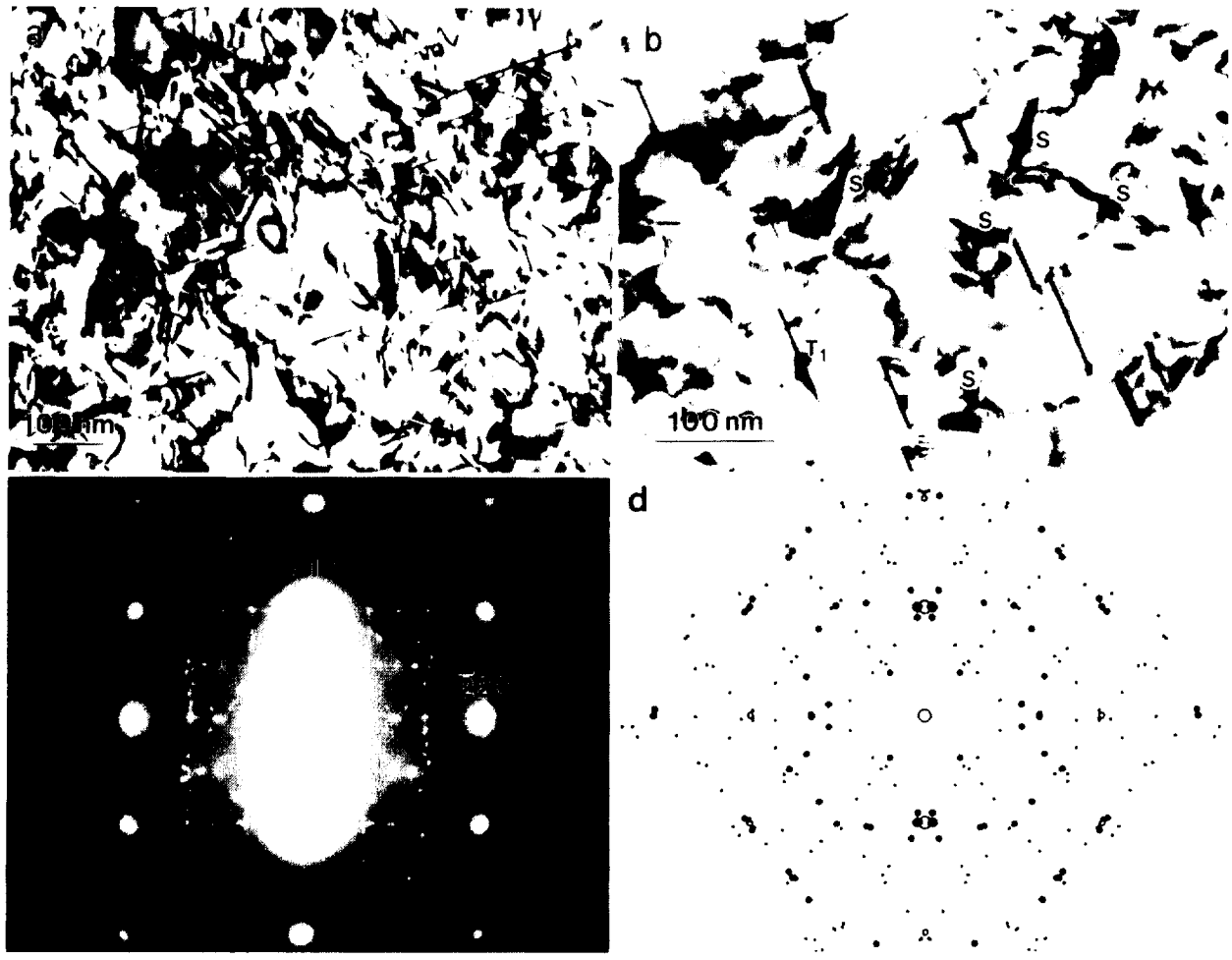

Figure 6. Bright-field TEM images and corresponding diffraction pattern from RX818-T8 alloy containing 0.8Mg and 0.8Ag (wt.%) showing (a) and (b) the S' precipitates, (c) a <112> diffraction pattern and (d) a corresponding calculated <112> diffraction pattern.

Subtask 2C. Al-Cu-Li-Mg-Ag Alloy Development (Boeing)

No progress to report to date. See Subtask 1A(i).

Subtask 2D. Al-Cu-Li-Mg-Ag Alloy Development (Douglas)

No progress to report to date.

TASK 3. P/M 2XXX ALLOY DEVELOPMENT

Principal Investigator:	Dr. L.M. Angers, Alcoa
Senior Engineer:	Dr. G. Dixon, Alcoa
Boeing Contact:	Dr. W.E. Quist
Douglas Contact:	Mr. R. Kahandal
UVa Contact:	Dr. E.A. Starke, Jr.

Objective. The primary objective of this task is to develop a damage tolerant aluminum based material for the lower wing and fuselage of a Mach 2.0 aircraft. This material must first meet preliminary strength and toughness targets at room temperature and then several criteria associated with elevated temperature service, (e.g., retention of room temperature properties after exposure, performance at the operating temperature and resistance to creep deformation).

The P/M 2XXX alloys are under consideration here for several reasons. Firstly, P/M processing provides rapid solidification rates, enabling one to introduce greater amounts of dispersoid forming elements into the aluminum solid solution than can be introduced using conventional ingot metallurgy methods. As a result, the wrought P/M products may be more resistant to recrystallization than I/M alloys with lower levels of these additions. Generally, unrecrystallized structures possess better strength/toughness combinations than recrystallized structures. Furthermore, if these additions are added in great enough amounts, modest dispersion strengthening may result. Finally, the refinement of constituent which is expected to accompany the rapid solidification will also have beneficial effects on toughness.

Background and Test Plans. P/M processing of the 2XXX alloys permits exploration of compositions which cannot be produced by conventional ingot metallurgy methods. High levels of

dispersoid forming elements can be introduced to increase the resistance to recrystallization. If high enough levels are appropriately introduced, there may also be modest strength improvements.

The P/M process also refines constituent particles which contain impurity elements and generally degrade fracture toughness. In the present study, however, we are addressing only the ability of the process to appropriately incorporate dispersoid forming elements. Since constituent particles could nearly be eliminated if high purity aluminum was used in conjunction with the ingot metallurgy process, this is considered to be a more cost effective option than P/M processing.

Alcoa data and Lockheed and NASA reports on the development of P/M 2XXX for high temperature aircraft structural applications were reviewed (1-4). These references summarize the NAS1-16048 program which represents the most extensive investigation of the P/M 2XXX alloys for high temperature applications.

During the first three iterations of that program, extrusions for damage tolerant applications were emphasized. Several were based on 2618, several on 2124 and one on 2219. Those based on 2618 had higher Cu levels than normal, e.g., 3.5 to 3.8 wt% instead of 2.3. One had high Fe and Ni (1.5 wt% each), one had typical Fe and Ni levels but higher Si than normal (1.2 Fe, 1.1 Ni and 0.2 Si), and one had no Fe or Ni. The four 2124 variants investigated higher levels of the dispersoid forming elements Mn and Zr: one had 1.5 Mn, another had 0.5 Mn, another had 0.2 Mn + 0.14 Zr and another had 0.2 Mn + 0.70 Zr. The 2219 variant contained 0.3 Mg. Figure 1 provides a summary of the strength/toughness combinations that were obtained. While the Zr-bearing variants of 2124 had the best combination, the 2219 variant was also very promising. None of the 2618 variants was particularly promising.

The high Zr variant of 2124 was chosen for fabrication to plate and sheet for investigation in the fourth iteration. In

this iteration, tensile and toughness testing was performed in two orientations. Measuring properties in two orientations was critical since it was important to show that the strength/toughness advantage over ingot metallurgy alloys was intrinsic rather than extrinsic, e.g., that the benefit in one orientation was not accompanied by a disadvantage in another orientation. Figure 2 shows that the strength/toughness combination was relatively isotropic in the plate but somewhat anisotropic in the sheet.

The NASA program also demonstrated that high room and elevated temperature strengths are associated with high levels of dispersoid forming elements like Mn (see Fig. 3). Whether this was due directly to dispersion strengthening or indirectly through the development of a highly textured grain structure was not established.

Because of the promising strength/toughness relationships, the P/M 2XXX alloys were pursued in the present investigation. Three alloys having high levels of dispersoid forming elements were selected.

1. Al-4.4 Cu-1.5 Mg-0.6 Mn-0.6 Zr-0.1 V
2. Al-5.85 Cu-0.5 Mg-0.3 Mn-0.5 Ag-0.6 Zr-0.1 V
3. Al-7.0 Cu-0.5 Mg-0.3 Mn-0.5 Ag-0.15 Zr-0.1 V.

Alloy 1 is essentially a high Zr version of 2124. Its composition is nearly identical to the alloy studied in the NASA program where excellent strength/toughness relationships were achieved. The effects of elevated temperature exposure on these materials were not carried out in that earlier study and will be done here.

Alloys 2 and 3 represent high Zr and Mn versions of the Ω phase alloy being considered in the ingot metallurgy portion of this program. Since the Ω phase alloy is expected to be our highest strength 2519 variant, it was chosen as a baseline into which excess Zr and Mn could be added. The Cu level in Alloy 3

was increased to account for the loss of Cu to formation of the $Al_{20}Cu_2Mn_3$ phase.

The addition of 0.1% V to all three alloys was made since all contain some Mn and Alcoa internal research has shown that V additions may refine the $Al_{20}Cu_2Mn_3$ phase which forms.

Material Fabrication. Powders have been gas atomized for this portion of the program. Nominal and actual compositions are compared in Table I.

Results and Discussion. None

Table I. Nominal and Actual Compositions of the P/M 2XXX Alloys of the Present Investigation

Alloy	Composition (wt. %)					
	Cu	Mg	Mn	V	Zr	Ag
655763						
nominal	4.4	1.5	0.6	0.1	0.6	-
actual	4.34	1.46	0.57	0.1	0.55	-
655765						
nominal	5.85	0.5	0.3	0.1	0.6	0.5
actual	5.72	0.54	0.31	0.10	0.57	0.51
655766						
nominal	7.0	0.5	1.8	0.1	0.15	0.5
actual	6.68	0.52	1.70	0.10	0.20	0.52

References.

1. D.J. Chellman, "Development of Powder Metallurgy Al Alloys for High Temperature Aircraft Structural Applications - Phase II," NASA Contractor Report 165965, November 1982.

2. D.J. Chellman, "Development of Powder Metallurgy 2XXX Series Al Alloys for High Temperature Aircraft Structural Applications," NASA Contractor Report 172408, November 1984.

3. D.J. Chellman, "Development of Powder Metallurgy 2XXX Series Al Alloy Plate and Sheet Materials for High Temperature Aircraft Structural Applications," NASA Contractor Report 172521, April 1985.

4. D.J. Chellman, T.B. Gurganus and J.A. Walker, "Development and Characterization of Powder Metallurgy (PM) 2XXX Series Al Alloy Products and Metal Matrix Composite (MMC) 2XXX Al/SiC Materials for High Temperature Aircraft Structural Application," NASA Contractor Report 187631, February 1992.

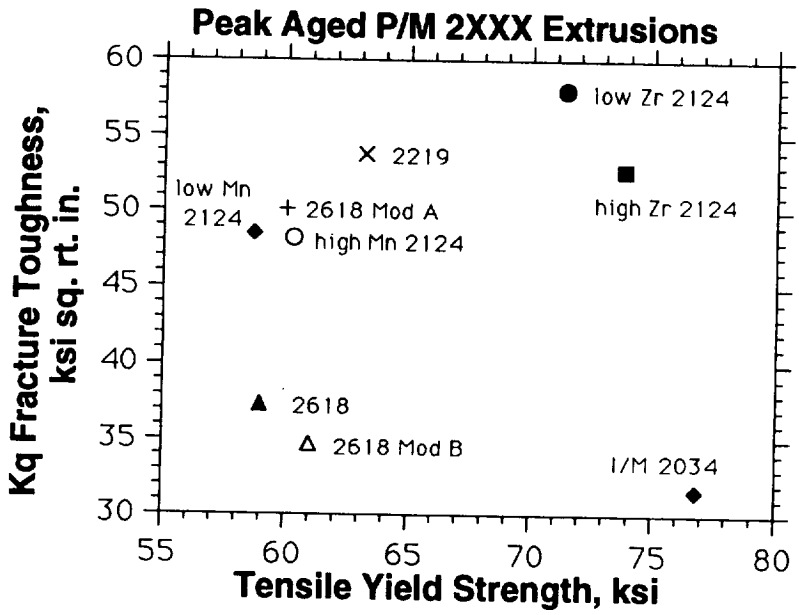

Figure 1. Summary of fracture toughness data K_q, as a function of tensile yield strength for the P/M extrusions studied in References 1 and 2.

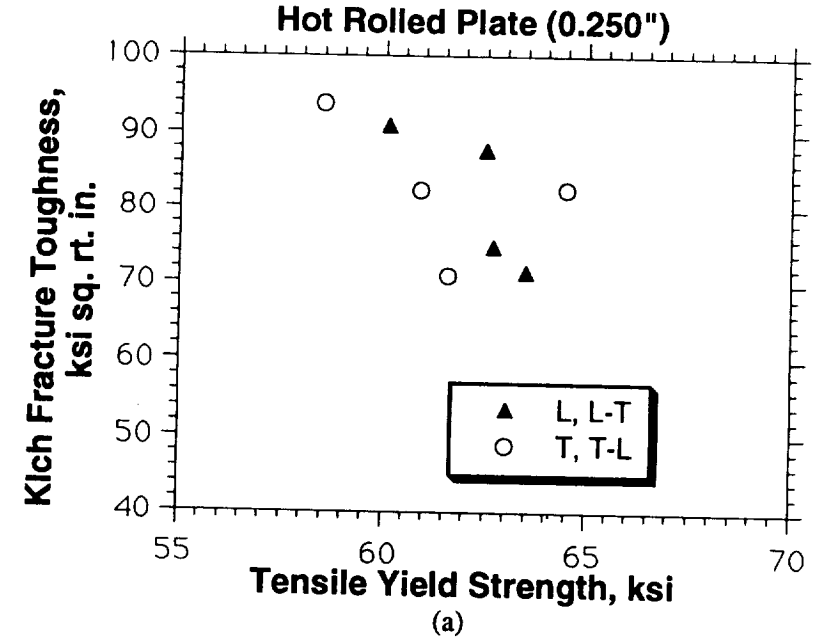

(a)

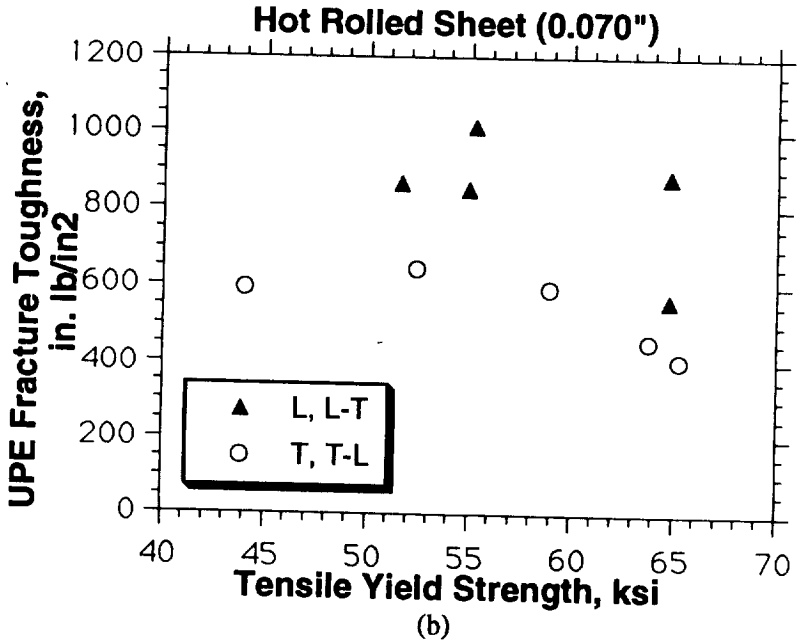

(b)

Figure 2. Measures of fracture toughness, L-T and T-L, as a function of tensile yield strength, L and T, for P/M versions of 2124 with high levels of Zr in (a) plate and (b) sheet. The measures of toughness were obtained from Charpy tests on plate, e.g., K_{ICH}, and from Kahn tear tests on sheet, e.g., U.P.E. or unit propagation energies.

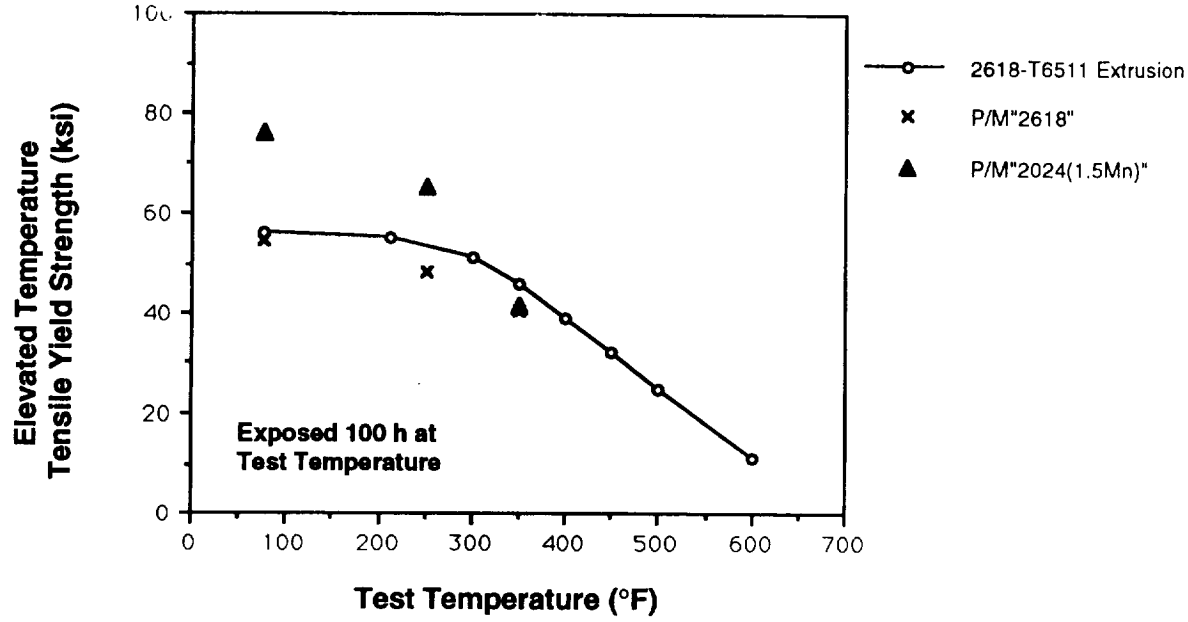

Figure 3(a). Elevated temperature tensile yield strength as a function of temperature for ingot metallurgy 2618-T6511 extrusions, P/M 2618 variant extrusion and P/M 2024 variant extrusion containing 1.5 wt.% Mn.

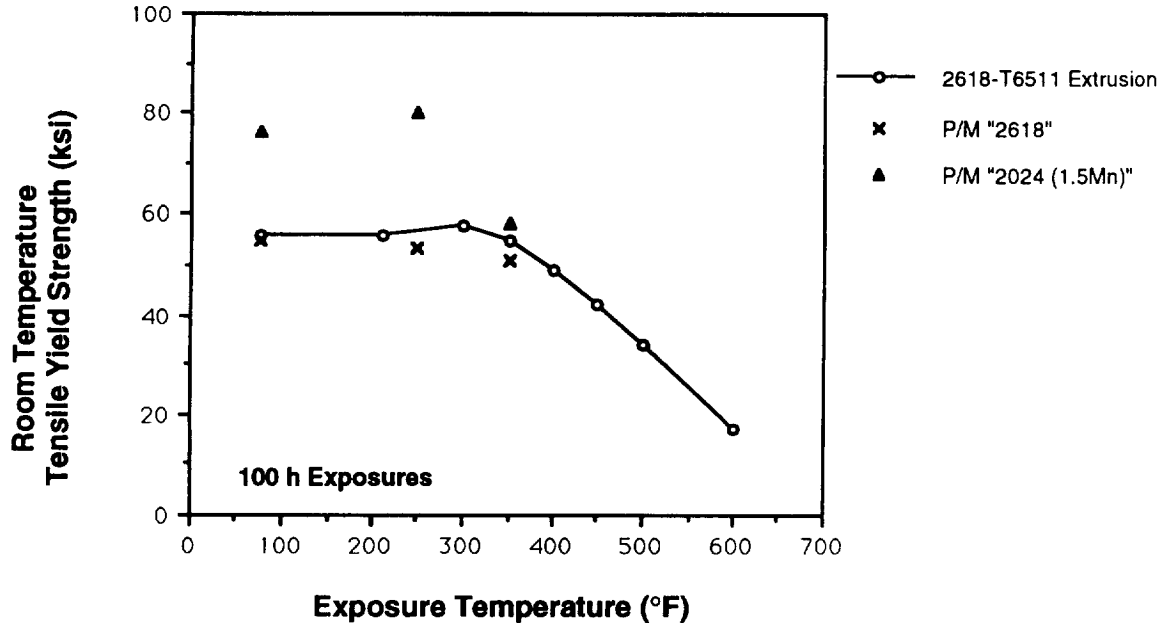

Figure 3(b). Room temperature tensile yield strength after exposure as a function of exposure temperature for ingot metallurgy 2618-T6511 extrusions, P/M 2618 variant extrusion and P/M 2024 variant extrusion containing 1.5 wt.% Mn.

Subtask 3A. P/M 2XXX Alloy Development (Boeing)

No progress to report to date. See Subtask 1A(i).

Subtask 3B. P/M 2XXX Alloy Development (Douglas)

No progress to report to date.

TASK 4. Al-Si-Ge ALLOY DEVELOPMENT (UVa)

Principal Investigator:	Dr. E.A. Starke, Jr.
Research Associate:	Dr. A.K. Mukhopadhyay
Graduate Student:	Mr. Holger Koenigsmann
Consultant:	Dr. E. Hornbogen
Alcoa Support:	Dr. R.W. Hyland

Task Objective. The objectives of this research are to determine the microstructural evolution and the concomitant property variations in a new class of experimental aluminum-based alloys that contain Si, Ge and Cu as the major alloying elements. The stability of the microstructures at moderate temperatures, and the critical dependence of hardness and strength on alloy composition and types of phases present are being investigated. This program uses theoretical concepts for selecting solute additions for an I/M age hardenable aluminum alloy that may have the strength and thermal stability necessary to meet the requirements for the proposed high speed civil transport (1-5).

Introduction. The mechanical properties of current precipitation hardenable aluminum alloys produced via the commercial ingot metallurgy (I/M) route deteriorate rapidly when exposed to aging temperatures between 100 and 200°C. The major reason for this behavior is due to the growth and coarsening of the strengthening phases. Most strengthening precipitates in these alloys are metastable and possess fully coherent or partially coherent interphase boundary structures. Long term exposure at intermediate temperatures (~100° - 200°C) leads to coarsening and gradual loss of full coherency together with a decrease in the particle number density. This is often accompanied by a change in the dislocation bypass mechanism from one of precipitate shearing to looping, and ultimately results in a decrease in alloy strength.

There are a few practical methods for reducing the critical diameter for the transition from the coherent or partially

coherent metastable phases to the less coherent equilibrium phases. For example, additions of suitable surface active elements can lower the interphase boundary energy (γ) and decrease the rate of particle coarsening. However, this may also lower the cohesive energy of the boundary and thus have an adverse effect on ductility. Alternatively, some trace additions may act to shift the e/a ratio and/or volume of the equilibrium precipitate more towards the ideal and thus encourage formation of a high number density of the stable phase (2,6,7). The utilization of such trace additions in multicomponent commercial Al alloys is, however, greatly hindered by the presence of a large number of solute additions in each alloy system which may form compounds with the trace additions and reduce their beneficial effects (2,8,9).

We have recently investigated a precipitation hardenable aluminum alloy in which a stable diamond cubic phase (Si,Ge) nucleates directly during the aging heat treatment (3,4). An important feature of both Si and Ge particles in an aluminum matrix is their extremely small critical size for the transition from shearing (S) to looping (L) by dislocations at the yield stress. Since Si and Ge have low solubility in Al and since the particles have an incoherent interface with the matrix, one would expect that they would have low coarsening rates at moderate temperatures. Unfortunately, precipitation hardening in binary Al-Si and Al-Ge alloys is insufficient for commercial utilization (10). The nucleation of the diamond cubic phase in the binary alloys is very vacancy sensitive and is affected by small variations in solutionizing temperature, quench rate and aging temperature (10,11). Even when these parameters are optimized, the microstructures are typically characterized by a heterogeneous distribution of Si or Ge precipitates that have a size and spacing too large for significant strengthening of the matrix.

Recent work (3,4) showed that the undesirable microstructural features in both binary alloys can be largely altered in ternary Al-Si-Ge alloys: the precipitate density is an order of magnitude

higher and the small equiaxed (Ge,Si) precipitates are much more evenly distributed. Also, there is no disturbance of this distribution by dislocations, and the PFZs around the grain boundaries are much less pronounced. The effects are based on the explanation that Si is smaller and Ge is larger than Al, and the atomic size misfit is compensated by the formation of pairs of Si and Ge (12,13). This effect is accentuated because of the similarities in the electronic structure between Si and Ge. The result is the attainment of the critical size by a large number of clusters containing the two elements which act as the nucleation centers for the diamond precipitates. Figures 1 (a)-(c) depict the typical microstructural features of binary Al-1at.%Si, binary Al-1at.%Ge and ternary Al-0.5at.%Si-0.5at.%Ge alloys obtained under identical heat treatment conditions. The variation in the degree of hardening in these alloys, as shown in Fig. 2, may also be compared with the corresponding changes in the degree of refinement and uniformity of the precipitates observed.

The level of hardening in the ternary alloys increases consistently with increasing (Si+Ge) content (cf. Fig. 2), and alloys containing Si and Ge in equal atomic concentrations maximize this effect. Metallographic evidence revealed that the use of the higher amounts of solute is, however, restricted to Si and Ge contents of 1 at% each owing mainly to the relatively low solid solubility of Si in Al as well as to the problem of segregation encountered in ingot casting and subsequent difficulties associated with the incomplete homogenization of the cast ingots within a practical homogenizing time and temperature.

Earlier studies further demonstrated that the strength level of the baseline alloy is inadequate for the targeted engineering applications. However, the microstructural stability of the ternary baseline alloy, as measured by hardness, is considerable at commercial aging temperatures and the level of hardening is appreciable for the small solute content. This report covers our NASA-sponsored research during the period January, 1992-June, 1992

on the effects of small Mg additions, trace element additions, selective alloying element additions, grain refining additions and thermomechanical treatments on the microstructure-property relationships of the baseline Al-1Si-1Ge alloy. Our primary objective is to achieve a higher strength level in the modified Al-Si-Ge-X alloys without negatively affecting the microstructural stability of the baseline alloy.

Experimental Procedure. The chemical compositions of the materials examined in the present investigation are given in Table 1. The alloys were prepared from high purity components in an induction furnace under argon atmosphere and in a copper mold. The 25 gm cylindrical cast ingots were of 12 mm diameter. Thermal analysis of the cast materials was undertaken in a Perkin Elmer DSC (differential scanning calorimeter) at a heating rate of 10°C/minute in order to select the optimum homogenization temperature for the cast ingots Figs. 3(a) and 3(b) represent the DSC traces for the cast baseline alloy (Al-1at.%Si-1at.%Ge) and the baseline + 3wt.%Cu + 0.4wt%Mn alloy, respectively. In the figures, the presence of broad endothermic reactions in the 500-540°C temperature range are evident; the endothermic reactions represent the melting of the eutectic phase mixtures present in the cast materials. Comparison of Fig. 3(a) with Fig. 3(b) further indicates that copper additions shift the endotherm in Fig. 3(a) to the left of the temperature axis. An optimum homogenization temperature of 480°C was, therefore, selected for all the alloys examined.

The materials were heated to the homogenization temperature at a heating rate of less than 50°C/hour followed by isothermal annealing at the homogenization temperature for 30 hours. Figures 4(a) and 4(b) show the as-cast microstructure of the baseline and the baseline + 3Cu + 0.4Mn alloys respectively; Fig. 4(c) shows the light micrograph of the homogenized baseline + 3Cu + 0.4Mn alloy. While Figs. 4(a) and 4(b) typically represent coring and

interdendritic segregation during solidification (the fine precipitates within the matrix being produced during cooling of the ingots), Fig. 4(c) shows that the homogenization treatment given to the cast ingots was appropriate. The widespread precipitation of the Mn-bearing precipitates in Fig. 4(c), on the other hand, is noteworthy, and the effects which these particles exert on the matrix nucleation of the (Ge,Si) precipitates in the heat treated samples are described later in this report. The homogenized materials were later either cold rolled (with intermediate annealing) or hot rolled to 2.5 mm sheet. All the materials were solution treated at 500°C for 1 hour followed by water quenching to room temperature. Materials were artificially aged at 160°C in an air circulating furnace to evaluate their aging response. The hardness data were obtained using a Vickers diamond indentor with a 10 kg load.

A combination of light microscopy and transmission electron microscopy was used to characterize the grain structure and the precipitation reactions which took place on subsequent heat treatments respectively. Specimens for light microscopy and thin foils for TEM were prepared using standard methods. The TEM studies were carried out on a Phillips 400T electron microscope operating at 120 kV.

Results and Discussion.

Effect of Small Amounts of Mg Additions:

Recent investigations (3) showed that Mg additions of 1 wt% to the baseline alloy result in the formation of a fine and uniform distribution of Mg_2Si precipitates and cause a coarse distribution of the (Ge,Si) precipitates. The present study was carried out to determine whether Mg, when present in reduced concentrations (i.e., 0.2-0.5 wt%), exerts a similar influence on the precipitation behavior of the baseline alloy. Figure 5 shows the TEM micrograph of the baseline alloy containing 0.5 wt% Mg,

when heat treated at 160°C for 10 hours after solution heat treatment and quenching. The micrograph shows a fine distribution of the Mg_2Si precipitates together with coarse (Ge,Si) precipitates in the matrix. A further reduction in the Mg content to 0.2 wt% did not prevent the formation of Mg_2Si precipitates and coarse (Ge,Si) precipitates in the matrix. Comparison of the precipitation behavior in the baseline alloy containing varying amounts of Mg up to 1 wt%, however, did show that decreasing the Mg content reduces the coarseness of the (Ge,Si) precipitates. The formation of the Mg_2Si precipitates, even in the material containing 0.2 wt% of Mg, is consistent with the strong electrochemical interaction between Mg and Si. These results indicate that the ternary baseline alloy cannot be further strengthened by Mg additions up to 1 wt.% (cf. see the age hardening curves in Fig. 6), and that Mg is unlikely to positively influence the mechanical behavior of the ternary Al-Si-Ge alloy.

Effect of Trace Additions of Sn, In and Ag:

Many researchers have shown that trace additions of Sn, In and Ag can have a beneficial effect on the precipitation of the strengthening phases in a wide variety of aluminum alloys (2). Consequently, we thought it worthwhile to investigate the effect of these trace additions on the precipitation in the baseline Al-(Si,Ge) alloy. The hardness versus time curves of Fig. 7 show the effects of trace additions of Sn, In and Ag on the hardness of the baseline alloy. The results indicate that trace additions of Sn and In produce an inferior age hardening response compared with the baseline alloy. We suggest that the high vacancy binding energy of Sn and In (measured in dilute binary Al alloys) results in a decrease in (Ge,Si) nucleus formation. Our TEM results support this interpretation. Ag, which has a negligible affinity to bind with a vacancy in an Al matrix, does not affect the normal aging behavior of the baseline alloy (cf. Fig. 7). These results

also suggest that trace elements having a strong affinity for vacancies in aluminum may not aid in the nucleation of precipitates which have a larger volume than the α-Al matrix.

Effect of Cu and Zn Additions:

Cu and Zn have adequate solid solubility in aluminum, a negligible affinity for vacancies in aluminum, and a minimal electrochemical affinity for Ge and Si. Hence, they were chosen as appropriate alloying additions for study. Varying amounts of each element were added to the baseline alloy in order to examine the effects of both the type and amount of additional solute on aging behavior. The results indicated that Zn additions had no influence, while Cu additions increased both the magnitude and rate of hardening (see Fig. 8). The aging curves in Fig. 8 also show that 2 wt% Cu additions do not accelerate the characteristic sluggish overaging of the baseline alloy. The results presented in Figure 9 indicate that increasing the Cu content to 2.5 wt% results in a peak hardness value of 108 VHN after 5 hours followed by negligible overaging even after 100 hours at 160°C. Figure 9 further indicates that Cu additions of ≤ 3 wt% increase the hardness of the alloys to about 132 VHN at 160°C; however, alloys containing this amount of copper do overage, i.e., lose hardness after 24 hours of aging.

TEM studies aided in explaining the aging curves for the Cu-containing alloys (cf. Fig. 10). It was found that in baseline alloys containing ≤ 2.5 wt% Cu a fine distribution of diamond cubic precipitates is the only one observed in the microstructure (Fig. 10a). On the other hand, for Cu contents ≥ 3 wt%, Θ'(Al_2Cu) precipitates also form in addition to (Ge,Si) precipitates having the diamond cubic structure. Θ' precipitates were found to nucleate heterogeneously on matrix dislocations and at the (Ge,Si) precipitate/α–Al interfaces (Fig. 10e). TEM studies showed that

coarsening of the Θ' precipitates with time at 160°C is responsible for the overaging observed in the Θ'-containing alloys. These results indicate that for moderate temperature applications the copper content must be appropriately adjusted so as not to allow Θ' nucleation to occur.

Compared to the baseline alloy, the quaternary alloy with 2 wt% Cu showed accelerated aging in addition to a 60% incremental hardening indicating that Cu additions aid in producing a higher number density of stable precursory clusters upon quenching. Fig. 11 shows the homogeneous distribution of small solute clusters in a naturally aged + 2 wt% Cu alloy. These clusters may act as the nucleation centers for the diamond precipitates at the aging temperature. X-ray EDS analyses of the diamond precipitates in TEM thin foils of the heat treated Al-Si-Ge-Cu alloys indicate that Si, Ge and Cu are associated with the diamond precipitates. However, given the dissimilarity in the electronic structure of Cu, Si, and Ge, together with the lack of solid solubility of Cu in either Si or Ge (14), the smaller Cu atoms most likely segregate to the (Ge,Si)/α-Al interfaces. The segregation may reduce the strain energy associated with the precipitates and their coarsening rates. This interpretation is consistent with that of Stewart and Martin (15) who investigated the role of Cu in an Al-Si-Cu alloy. However, our interpretation needs to be verified by further study.

Effect of Combined additions of Cu and Mg:

Mg additions are not recommended for the ternary alloys. However, earlier work of Brook and Hatt (16) demonstrated that combined additions of Mg and Si(/Ge) to an Al-4wt% Cu alloy have the effect of refining Θ' precipitates. Trace additions of Mg (0.15 wt%) were, therefore, made to the baseline + 4Cu alloy to

examine the (Si,Ge) and Θ' morphology as shown in Fig. 12. It may be noted that in the presence of this higher amount of Cu in the material, Mg additions do not have the adverse effect of producing coarse (Ge,Si) precipitates. Also, Fig. 12 shows that in the Mg modified high Cu alloy, all three phases, i.e., (Ge,Si), Θ' and Mg_2Si, can coexist uniformly. The hardness-time curve of the Mg modified baseline + 4Cu alloy at 160°C, however, showed that Mg additions do not bring about any beneficial change in the aging behavior; for example, Mg additions do not minimize or alter coarsening of the Θ'-containing alloy.

Effect of Mn additions:

Mn additions were made to the Cu-containing baseline alloy to form a dispersoid for grain structure control. Figure 13 shows the age hardening curves for the Al-Si-Ge-Cu-Mn alloys at 160°C. The results indicate that Mn additions reduce the aging response. It may be noted, however, that increasing the Cu content to compensate for the loss of Cu to the Mn dispersoid ($Al_{20}Cu_2Mn_3$) has the effect of restoring the hardness. The characteristic microstructural stability of the Θ' free Al-Si-Ge-Cu alloys remain undisturbed by Mn additions. Figure 14 is a TEM of an artificially aged baseline + 2.5 wt% Cu + 0.4 wt% Mn alloy. The micrograph shows that the coarse Mn-bearing precipitate (arrowed in the micrograph) has an associated small (Ge,Si) precipitate free zone. It may be that PFZs are formed due to the annihilation of vacancies at the interphase boundaries of the Mn-bearing particles.

Effect of Cold Work Prior to Artificial Aging:

The effect of cold work (15%) prior to artificial aging on the aging characteristics of the baseline + 2 wt% Cu alloy was investigated. Figure 15 shows the resultant age hardening curves.

The aging curves suggest that although the as-rolled hardness value was significantly higher than the as-quenched hardness value of the directly aged (T6) alloy, due to increased dislocation density in the former case, such differences in hardening were greatly reduced in the peakaged condition and only minimal differences in the hardness values could be detected beyond the peakaged condition. These results reconfirm those earlier (3,4) that (Ge,Si) precipitate nucleation in Al-Si-Ge alloys remain undisturbed by the presence of dislocations, and that even in the binary Al-(Si,Ge) alloys precipitation does not appear to be enhanced by dislocations. Clusters of Ge and Si atoms which form during, or immediately after quenching, are sufficient to nucleate the diamond cubic phase. On the other hand, the strain energy reduction offered by dislocations is insufficient to lower ΔG^* enough to permit nucleation to occur.

Summary and Conclusions.

1. Mg additions (ranging from 0.2 to 1 wt%) to the ternary baseline alloy have the effect of forming fine and uniformly distributed Mg_2Si precipitates and coarser (Ge,Si) precipitates. Mg additions provide almost no additional hardening to the baseline alloy.
2. Trace additions of In and Sn to the baseline alloy give rise to poor age hardening response of the materials. Both In and Sn interact strongly with the vacancies, slow down the normal (Ge,Si) nuclei formation, and cause a reduction in both the precipitate density and hardening ability.
3. The ternary alloy can be strengthened by Cu additions. The hardness increment in the baseline alloy containing up to 1.1 at% (~2.5 wt%) copper is about 60%. The hardness increment is associated with the refinement of the (Ge,Si) precipitates within the microstructure.
4. Cu additions up to 2.5 wt% to the baseline alloy do not alter

the superior microstructural stability of the baseline alloy when aged at 160°C. It is proposed that the segregation of the smaller Cu atoms at the (Si,Ge)/α-Al interfaces facilitates structural accommodation with the matrix, thus maximizing precipitate density, as well as providing stability to the precipitates during aging. (However, very recent work in our laboratory has shown that Cu may have just the opposite effect, i.e., it may aid in coarsening).

5. Cu contents equal to or greater than 3.0 wt% in the baseline alloy cause Θ' nucleation to occur. Θ' nucleation occurs on matrix dislocations as well as at the (Ge,Si)/α-(Al) interfaces. Θ' coarsens during aging at 160°C and there is an associated drop in hardness.

6. The presence of up to 0.2 wt% Mg in the Al-Si-Ge-Cu alloys containing 4 wt% Cu does not affect the distribution of the (Ge,Si) diamond cubic phase in the matrix.

7. Cold work prior to artificial aging does not affect the precipitation behavior of the Θ' free Al-Si-Ge-Cu alloys, and provides minimal additional hardening to these alloys in the peakaged or in the overaged conditions.

8. Mn additions to the Al-Si-Ge-Cu alloys decreases the age hardening response. The hardness may be increased by increasing the Cu content to compensate for that which is lost in the Mn dispersoid ($Al_{20}Cu_2Mn_3$). Formation of (Ge,Si) precipitate free zones occurs around the coarse Mn-bearing particles.

References

1. E. Hornbogen and E.A. Starke, Jr., "Theory Assisted Design of High Strength Low Alloy Aluminum," Overview No. 102, *Acta Met. Mater.* 41, 1993, p. 1-16.

2. A.K. Mukhopadhyay, G.J. Shiflet and E.A. Starke, Jr., *Proc. Morris E. Fine Symp.*, ed. P.K. Liaw, et al., TMS-AIME, Warrendale, PA (1991), p. 283.

3. E. Hornbogen, A.K. Mukhopadhyay and E.A. Starke, Jr., "An Exploratory Study of Hardening in Al-(Si,Ge) Alloys, *Z. Metallkunde* 83, 1992, p. 577-584.

4. E. Hornbogen, A.K. Mukhopadhyay and E.A. Starke, Jr., "Precipitation Hardening of Al-(Si,Ge) Alloys," *Scripta Met. Mater.* 27, 1992, p. 733-738.

5. E. Hornbogen, A.K. Mukhopadhyay and E.A. Starke, Jr., *Proc. 3rd Int. Conf. "Aluminum Alloys - Their Physical and Mechanical Properties,"* Vol. 1, eds. L. Arnberg, O. Lohne, E. Nes, and N. Ryum, The Norwegian Institute of Technology, Trondheim, Norway (1992), p. 199-207.

6. I.J. Polmear and M.J. Couper, "Design and Development of an Experimental Wrought Aluminum Alloy for Use at Elevated Temperatures," *Met. Trans.* 19A (1988), p. 1027.

7. I.J. Polmear, "Role of Trace Elements in Aged Aluminum Alloys," *Mater. Sci. Forum*, 13-14 (1987), p. 195.

8. L.B. Blackburn and E.A. Starke, Jr., in *Proc. Al-Li 5th Conf.*, eds. T.H. Sanders, Jr., and E.A. Starke, Jr., MCE Publications Ltd., Birmingham, United Kingdom (1989), p. 751.

9. I.J. Polmear and R.J. Chester, "Abnormal Age Hardening in an Al-Cu-Mg Alloy Containing Silver and Lithium," *Scripta Met. Mater. 23*, 1989, p. 1213.

10. L.F. Mondolfo, *Aluminum Alloys*, Butterworths, London (1976), p. 292,368.

11. G.W. Lorimer, "Precipitation Process in Solids," eds. K.C. Russel and H.I. Aaronson, AIME Conf. Proc., Warrendale, PA, 1978, p. 87.

12. H.K. Hardy and T.J. Heal, "Report on Precipitation," *Progress in Mat. Sci.*, New York, 1954, p. 268.

13. N. Ryum, *Aluminum Alloys, Their Physical and Mechanical Properties*, eds. E.A. Starke, Jr. and T.H. Sanders, Jr., EMAS, West Midlands, England, 1968, p. 1511.

14. M. Hansen, *Constitution of Binary Alloys*, McGraw Hill Book Company, Inc., 1958, p. 585, 629.

15. A.T. Stewart and J.W. Martin, "A Note on the Effect of 0.45 Wt.% Copper on the Precipitation of Silicon in an Aluminium-0.5 Wt.% Silicon Alloy," *J. Inst. Metals 98*, 1970, p. 62.

16. G.B. Brook and B.A. Hatt, *The Mechanism of Phase Transformation in Crystalline Solids*, Inst. Met. London, p. 82 (1969).

17. W. Balluffi and P.S. Ho, *Diffusion*, ed. H.I. Aaronson, ASM, Metals Park, OH, 1973, p. 83.

TABLE I. Chemical Composition (at%) of the Alloys

	SYMBOL	Si	Ge	Cu	Zn	Sn	In	Ag	Mg	Mn	Cr
1	Al-1.06Si	1.0	1.0	-	-	-	-	-	-	-	-
2	Al-2.6Ge										
3	Al-1.06Si-2.6Ge										
4	Baseline + 2Cu	1.0	1.0	0.85	-	-	-	-	-	-	-
5	Baseline + 2.5Cu	1.0	1.0	1.06	-	-	-	-	-	-	-
6	Baseline + 3Cu	1.0	1.0	1.3	-	-	-	-	-	-	-
7	Baseline + 4Cu	1.0	1.0	1.75	-	-	-	-	-	-	-
8	Baseline + 0.2Mg	1.0	1.0	-	-	-	-	-	0.23	-	-
9	Baseline + 0.5Mg	1.0	1.0	-	-	-	-	-	0.55	-	-
10	Baseline + 2Zn	1.0	1.0	-	0.85	-	-	-	-	-	-
11	Baseline + 0.5Ag	1.0	1.0	-	-	-	-	0.13	-	-	-
12	Baseline + 0.10Sn	1.0	1.0	-	-	0.025	-	-	-	-	-
13	Baseline + 0.10In	1.0	1.0	-	-	-	0.025	-	-	-	-
14	Baseline + 2.5Cu +0.4Mn	1.0	1.0	1.06	-	-	-	-	-	0.2	-
15	Baseline + 3.0Cu +0.4Mn	1.0	1.0	1.3	-	-	-	-	-	0.2	-

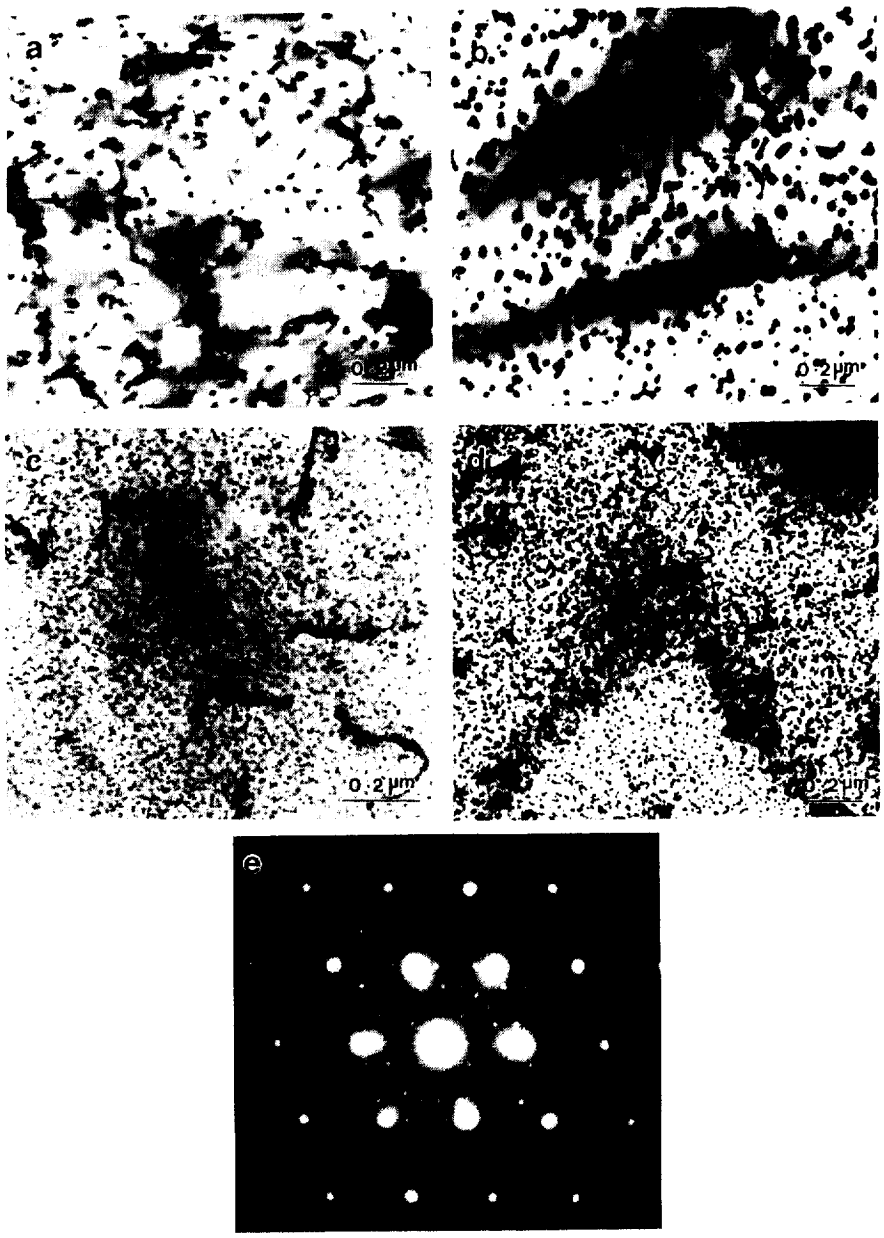

Figure 1. TEMs showing Si, Ge and (Ge,Si) precipitation in (a) Al-Si (b) Al-1Ge (c) Al-0.5Si-0.5 Ge and (d) Al-1Si-1at%Ge alloys. <011> Al orientation. Fig.1(e) represents a typical electron diffraction pattern corresponding to the Fig. 1(c).

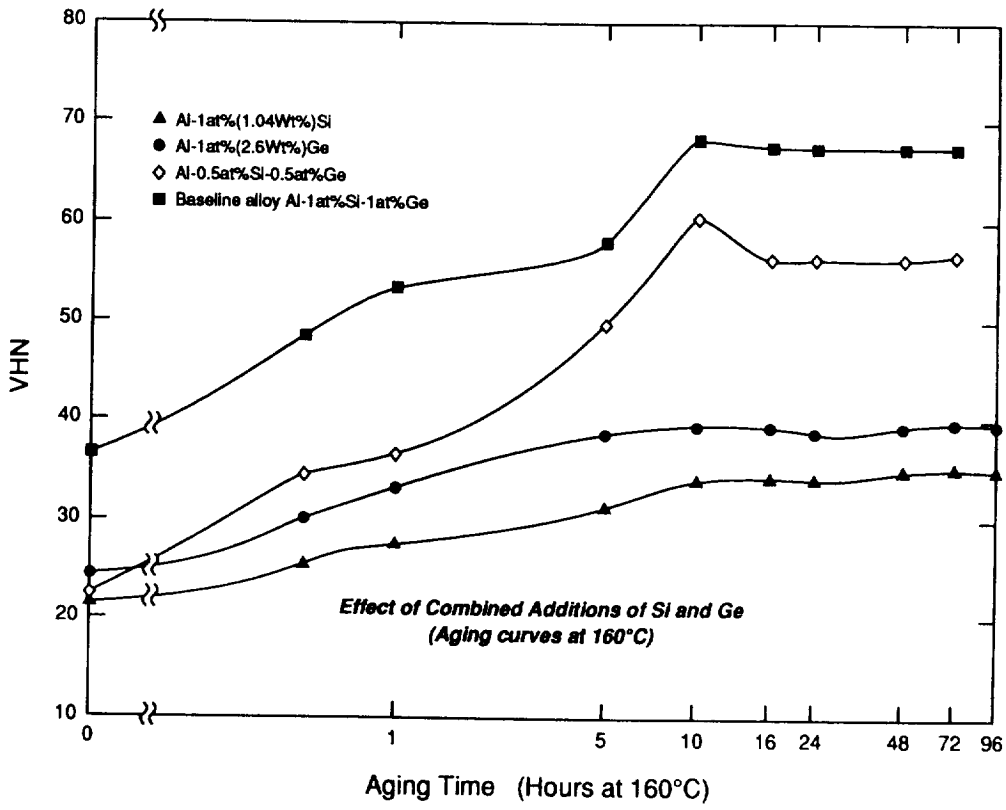

Figure 2. Hardness-time curves at 160°C showing the effect of combined additions of Si and Ge to aluminum.

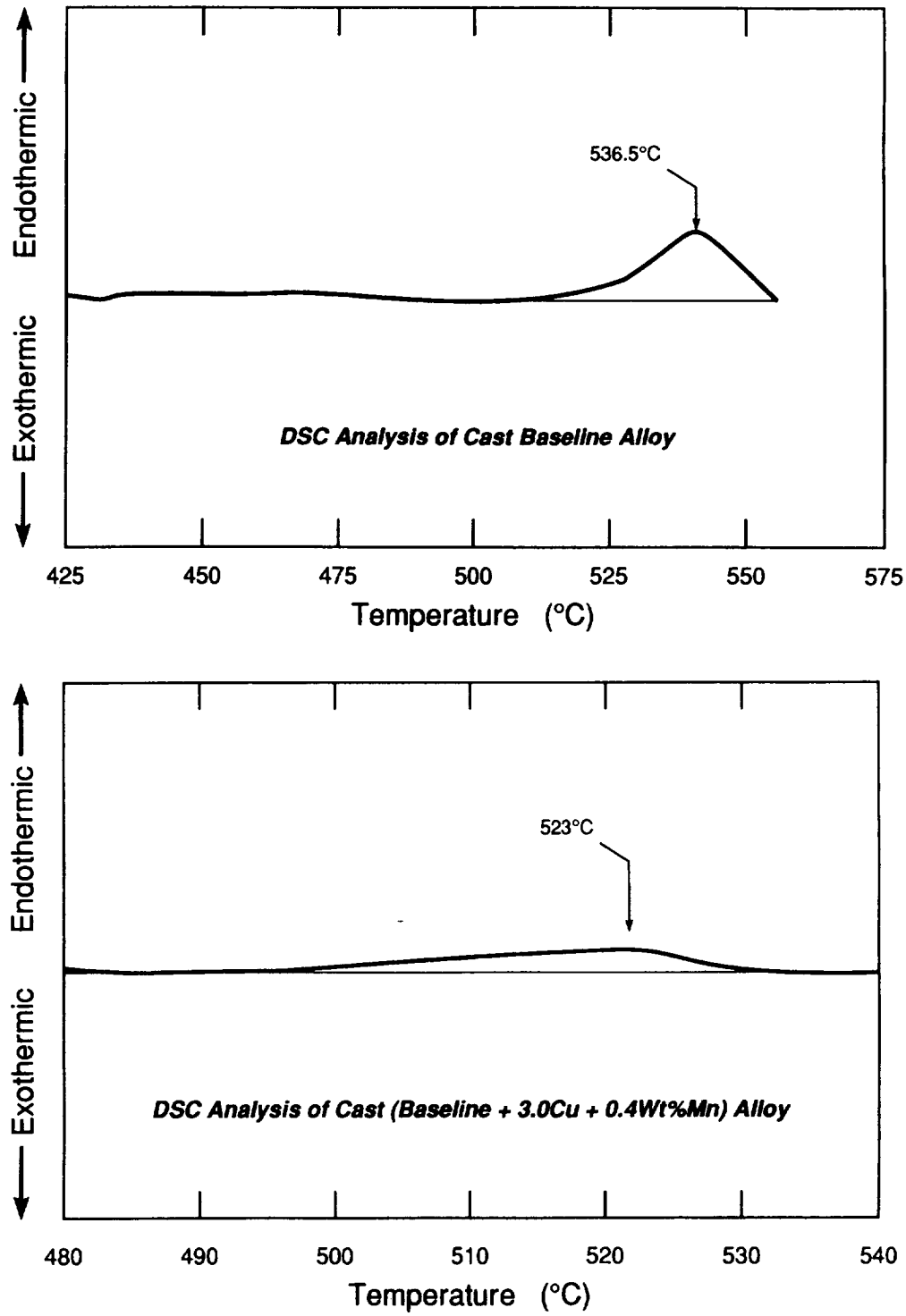

Figure 3. DSC thermograms revealing the presence of low melting eutectics in the as-cast (a) baseline and (b) baseline + 3Cu + 0.4wt% Mn alloys.

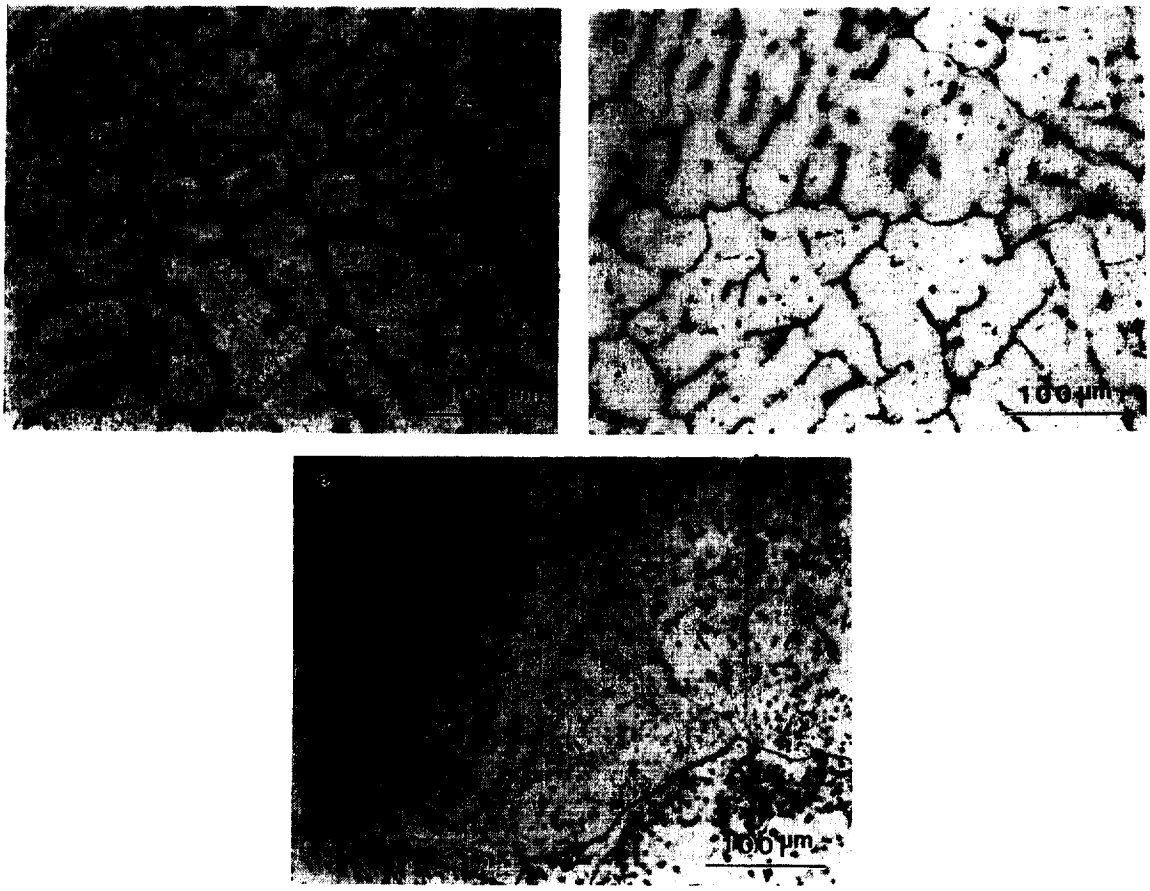

Figure 4. Light micrographs showing the as-cast microstructure of the (a) baseline and the (b) baseline + 3Cu + 0.4Mn alloys and the (c) homogenized microstructure of the baseline + 3Cu + 0.4wt% Mn) alloy.

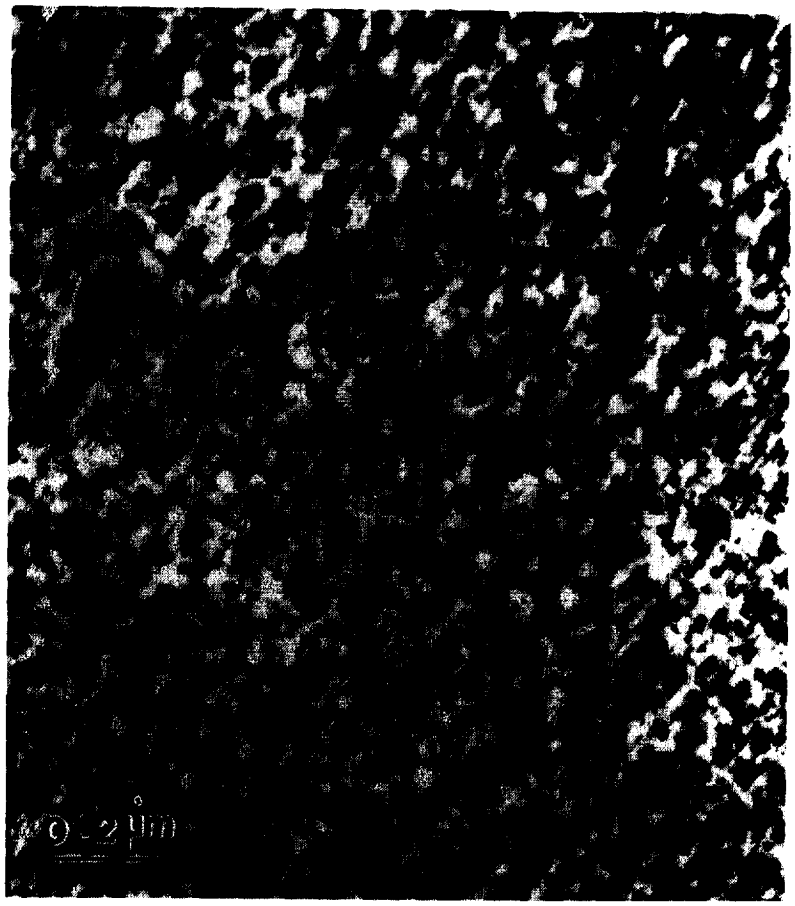

Figure 5. TEM showing the formation of fine Mg_2Si precipitates (viewed end on) and coarse (Ge,Si) precipitates in baseline + 0.5wt% Mg alloy when solution treated, water quenched and aged at 160°C for 10 hours. <001> Al orientation.

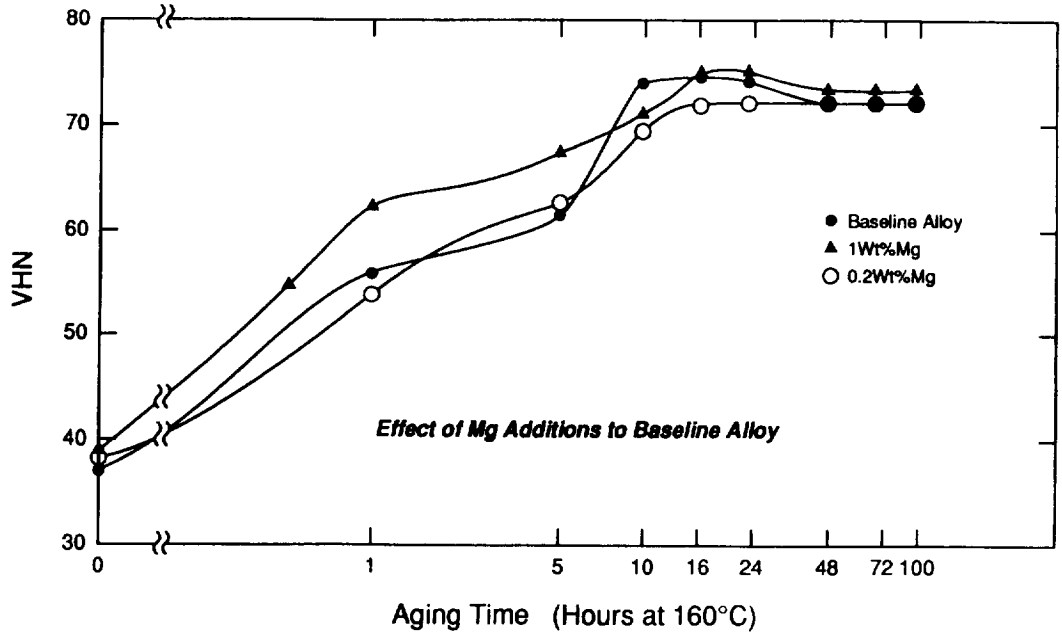

Figure 6. Hardness-Time curves at 160° C showing the effect of varying amounts of Mg additions to the baseline alloy.

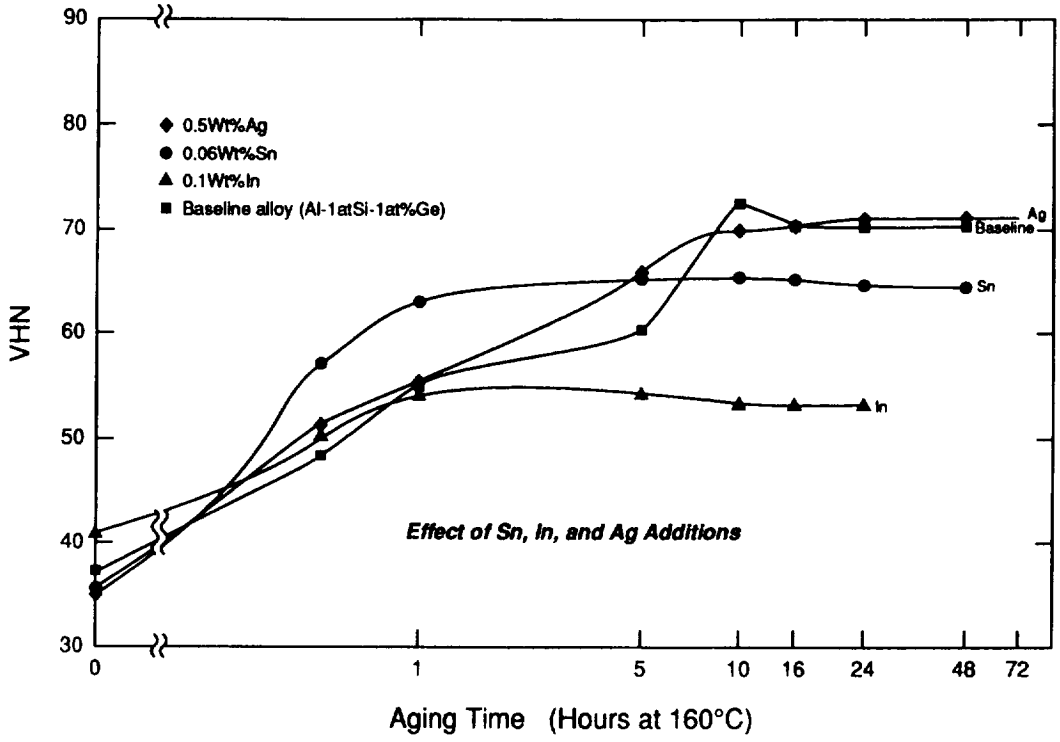

Figure 7. Hardness-Time curves at 160°C showing the effects of Sn, In and Ag to the baseline alloy.

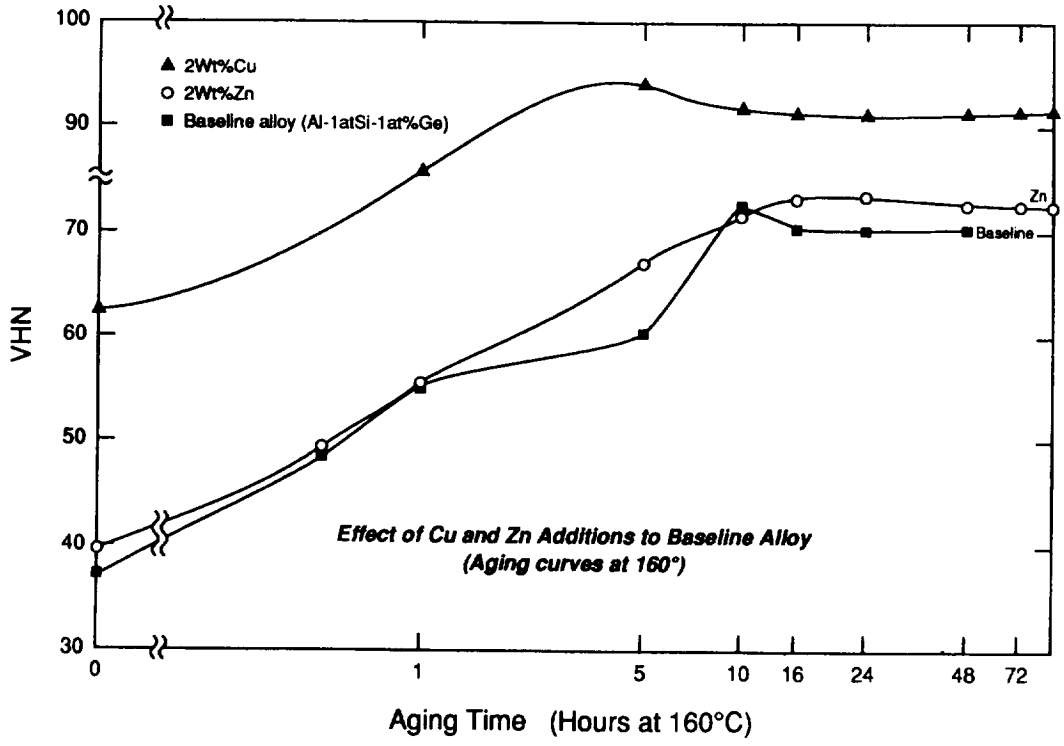

Figure 8. Hardness-Time curves at 160°C showing the effects of Zn and Cu additions to the baseline alloy.

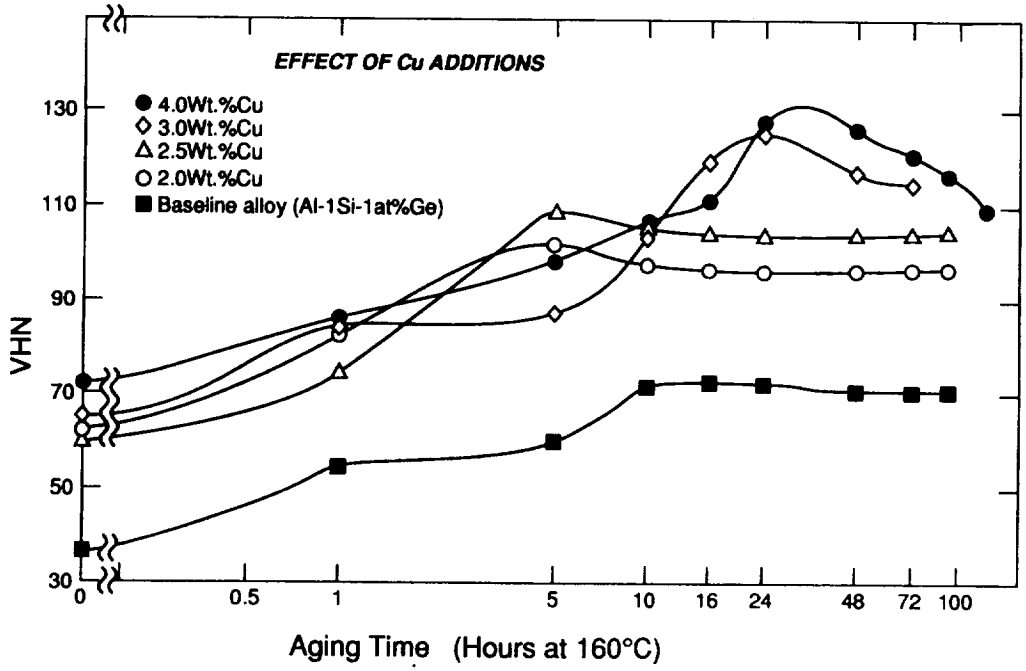

Figure 9. Hardness-Time curves at 160°C showing the effects of varying amounts of Cu additions to the baseline alloy.

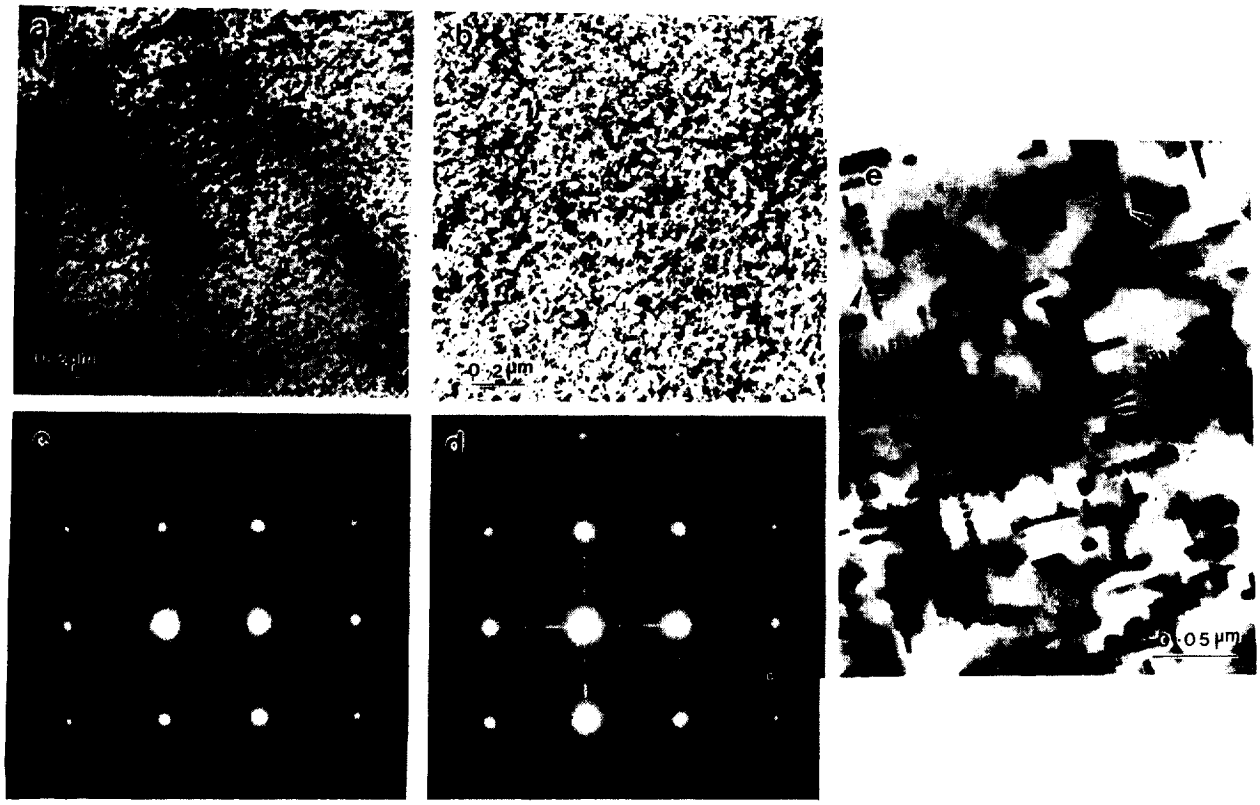

Figure 10. TEM's showing the (a) (Ge,Si) precipitates in baseline + 2 wt% Cu alloy aged at 160°C for 5 hours and (b) (Ge,Si) and Θ' nucleation in the baseline + 4 wt% Cu alloy aged at 160°C for 18 hours. Figs. 10(c) and 10(d) represent the electron diffraction patterns corresponding to the Figs. 10(a) and 10(b), respectively. Fig. 10(e) is a high magnification image of Fig. 10(b) showing Θ' nucleation (arrowed) at the (Ge,Si)/α-Al interface. <001> Al orientation.

Figure 11. TEM showing spherical (Si+Ge) clusters developed in the baseline + 2wt% Cu alloy, when solution treated, water quenched and naturally aged for two weeks. <011> Al orientation.

Figure 12. TEM showing coexistence of (Ge,Si), Θ' and Mg_2Si in a baseline + 4Cu + 0.15Mg alloy, when solution treated, water quenched and aged at 160°C for 32 hours. <001> Al orientation.

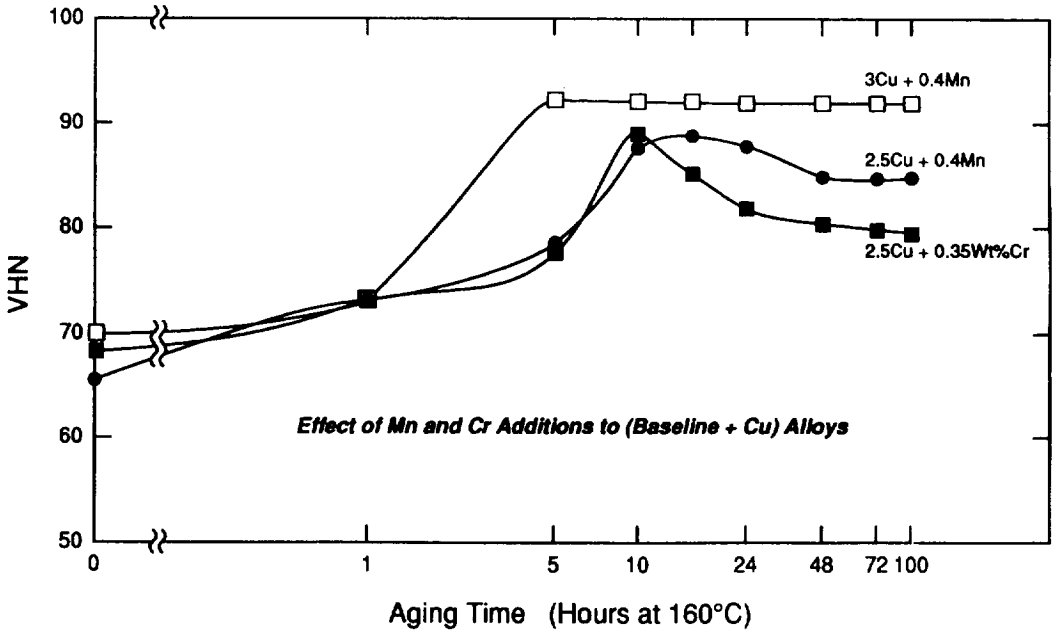

Figure 13. Hardness-Time curves at 160°C showing the effect of Mn additions to the baseline + Cu alloys.

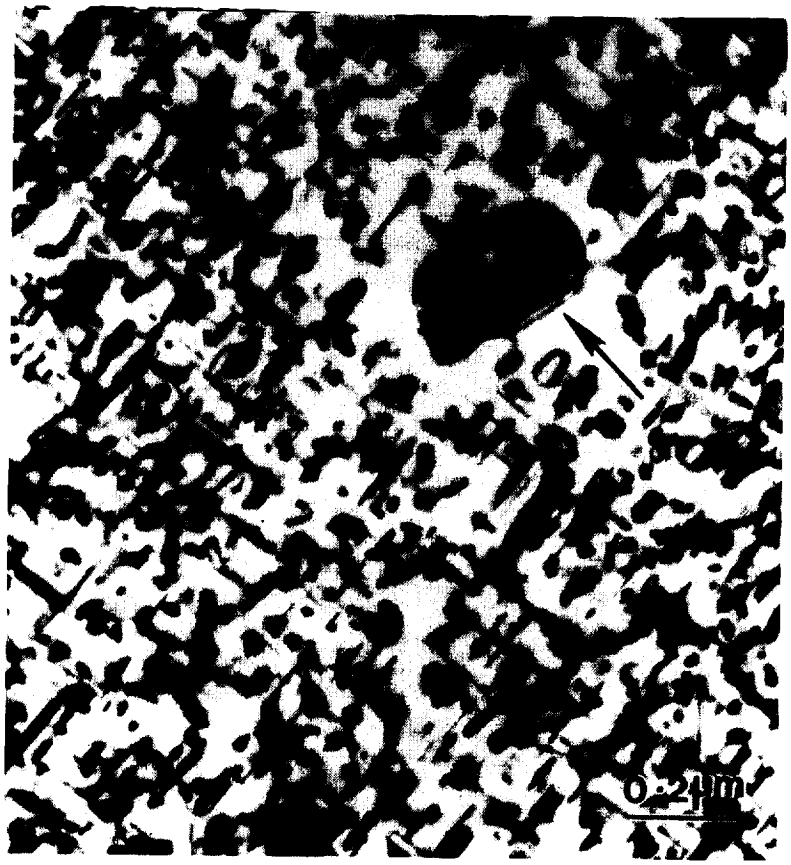

Figure 14. TEM showing coarse (Ge,Si) dispersion together with the PFZs around the coarse Mn-bearing particles in a baseline + 2.5wt% Cu + 0.4wt% Mn alloy. <001> Al orientation.

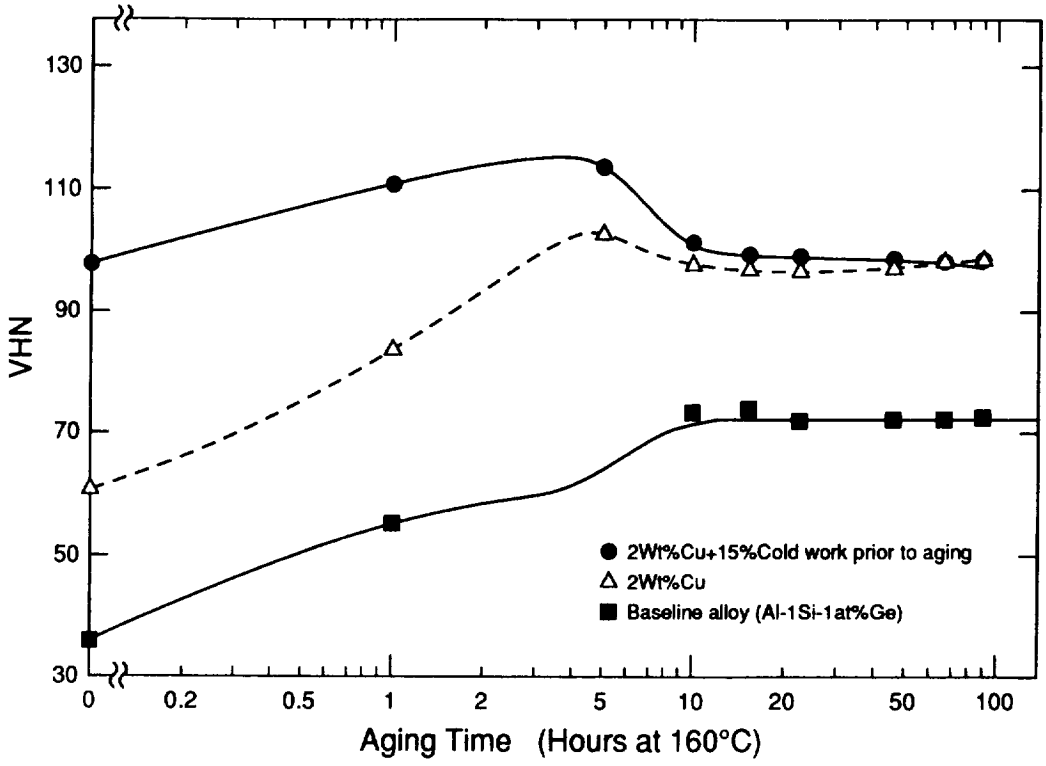

Figure 15. Hardness-Time curves at 160°C showing the effect of preaging cold work on the baseline + 2 wt% Cu alloy.

TASK 5. TOUGHNESS STUDY OF P/M Al-Fe-X SYSTEM

Principal Investigator: Dr. L.M. Angers
Boeing Contact: Mr. P.G. Rimbos
Douglas Contact: Mr. R. Kahandal

Toughness & Ductility Minima in Al-Fe-Ce:

Objective. The objective of this task is to gain a greater understanding of the ductility and fracture toughness reductions that occur in the dispersion strengthened alloys as temperature is increased into the range of interest for High Speed Civil Transport. If the phenomena are understood, it may be possible to propose methods for reducing or eliminating the effect.

Background & Test Plans. A review of tensile and toughness data generated at Alcoa on Al-Fe-Ce and a review of the literature on the toughness/ductility minima in Al-Fe-X alloys were initiated.

The rapidly solidified Al-Fe-X alloys and mechanically alloyed materials exhibit a "ductility minima" at elevated temperatures. Figure 1a shows this phenomenon in a plot of elevated temperature elongation (%) as a function of test temperature for a number of Al-Fe-Ce extrusions produced during an AFWAL contract (1). Here, Process A denotes data obtained from extrusions seeing the least amount of thermal exposure, Process B denotes data obtained from extrusions seeing an intermediate amount of thermal exposure and Process C denotes data obtained from extrusions seeing the greatest amount of thermal exposure. This figure shows that the ductility minima occurs around the service temperatures expected for HSCT.

Theories put forth to explain the ductility/toughness minima in these alloys were examined and existing data analyzed (2-4). Numerous theories on this subject are based on the concept that the loss in ductility is due to a dynamic strain aging phenomenon.

In rapidly solidified alloys, slowly diffusing elements are introduced to avoid rapid coarsening of the dispersoids. Some researchers believe that dynamic strain aging in these alloys, therefore, occurs at higher temperatures and is enhanced by the extension of solid solubility during rapid solidification.

Data generated from strain rate change tests performed on Al-Cr-Zr and Al-Fe-V-Si support the occurrence of dynamic strain aging. In addition, the temperature range at which dynamic strain aging is believed to occur in these alloys has been correlated to the solute element in solid solution and the strain rate of the test. In Al-Fe-V-Si, Fe is the most likely cause of the ductility dip and in Al-Cr-Zr, the ductility dip is believed to be due to the migration of chromium.

There are some indications that there may also be a reduction in room temperature ductility (and possibly fracture toughness) after exposures of these materials to intermediate temperatures. Figure 1b, which is a plot of room temperature elongation as a function of exposure temperature for the Al-Fe-Ce extrusions of the early AFWAL studies, also shows a ductility minima for samples exposed at the service temperatures expected for HSCT. Again, Process A denotes data obtained from extrusions seeing the least amount of thermal exposure, Process B denotes data obtained from extrusions seeing an intermediate amount of thermal exposure and Process C denotes data obtained from extrusions seeing the greatest amount of thermal exposure.

It has been suggested that the fracture toughnesses of these materials may be reduced as a result of elevated temperature exposure. Alcoa data on F-temper material shows that the plane stress toughness of the Al-Fe-Ce alloy X8019 is excellent when compared to ingot metallurgy alloys although plane strain fracture toughness data show X8019 to be inferior. Unfortunately, little plane stress or plane strain toughness data are available for material exposed to elevated temperatures. Furthermore, any plane stress toughness data that are available are from Kahn tear tests,

and therefore, are not considered to be as reliable as wide panel data.

Much attention has been paid to the minima that occurs at elevated temperatures, however, very little work has been done to explore what effect the elevated temperature exposures have on microstructures and room temperature properties. Therefore, the primary goal of this portion of the investigation is to generate ductility and toughness data at room temperature before and after elevated temperature exposures and determine possible mechanisms for the observed behavior.

An experimental test plan has been developed for Al-Fe-Ce. R-curve data will be generated on straight notched compact fracture type R-curve specimens taken from extrusions and sheet. By testing both extrusions and sheet, the questions regarding plane stress and plane strain behavior will be addressed. Two sample thicknesses will be tested from the extruded material: 1" and 0.1". Sheet samples will also be tested at 0.1" in thickness. In this way, it will be possible to test the same microstructure at two thicknesses and to test two different microstructures at the same thickness.

Fracture toughness tests will be performed at different strain rates and some test specimens will be exposed to elevated temperatures prior to the room temperature fracture toughness tests. These tests will establish whether the fracture toughness is reduced during elevated temperature exposure and whether this phenomenon is related to the ductility dip. An accelerated exposure of 600 hr at 300°F was selected to simulate Mach 2.0 exposure. In addition to the fracture toughness tests, tensile tests on comparable material will be performed.

The overall toughness study for X8019 will include microstructural analysis and fractography on Al-Fe-Ce for each condition tested.

Material Fabrication. Atomization of Al-8.3 wt% Fe-4.0 wt% Ce powder was initiated; however, furnace problems necessitated termination of that run. The furnace could not be fixed immediately and support personnel were re-assigned to another activity. Since that time, the facility has been fixed. Atomization will begin as soon as support personnel are available.

Results and Discussion. None

References.

1. S. L. Langenbeck et. al., "Elevated Temperature Aluminum Alloy Development," AFWAL Contract F33615-81-C-5096, Interim Technical Report for Period 1981 October-1982 March.

2. E. Bouchard, L. Kubin and H. Octor, "Ductility and Dynamic Strain Aging in Rapidly Solidified Aluminum Alloys," *Met. Trans. 22A*, p. 1021-1028 (1990).

3. D. J. Skinner, M. S. Zedalis, and P. Gilman, "Effect of Strain Rate on Tensile Ductility for a Series of Dispersion-Strengthened Aluminium-Based Alloys, *Mat. Sci. and Eng. A119*, p. 81-86 (1989).

4. P. Krawczyk and K. V. Jata, "Influence of Strain Rate on the Fracture Toughness of Al-8Fe-1V-2Si at 315°C," *Scripta Met. 24*, p. 1009-1013 (1990).

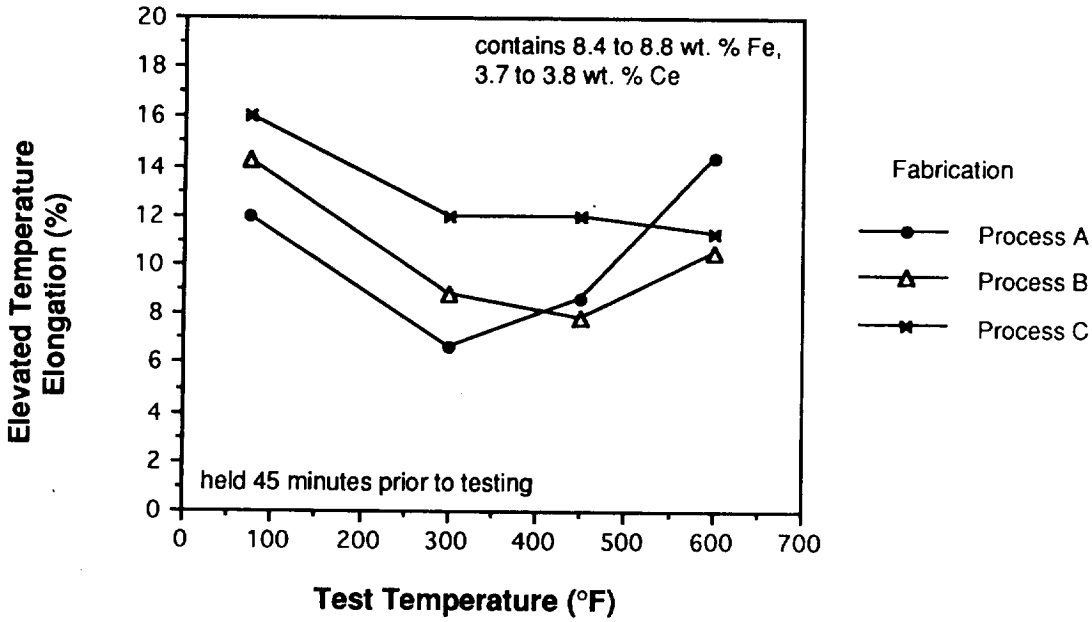

Figure 1(a). Elevated temperature tensile elongation as a function of test temperature for P/M Al-Fe-Ce alloys containing 8.4 to 8.8 wt.% Fe and 3.7 to 3.8 wt.% Ce. Here, Process A denotes data obtained from extrusions seeing the least amount of thermal exposure, Process B denotes data obtained from extrusions seeing an intermediate amount of thermal exposure and Process C denotes data obtained from extrusions seeing the greatest amount of thermal exposure.

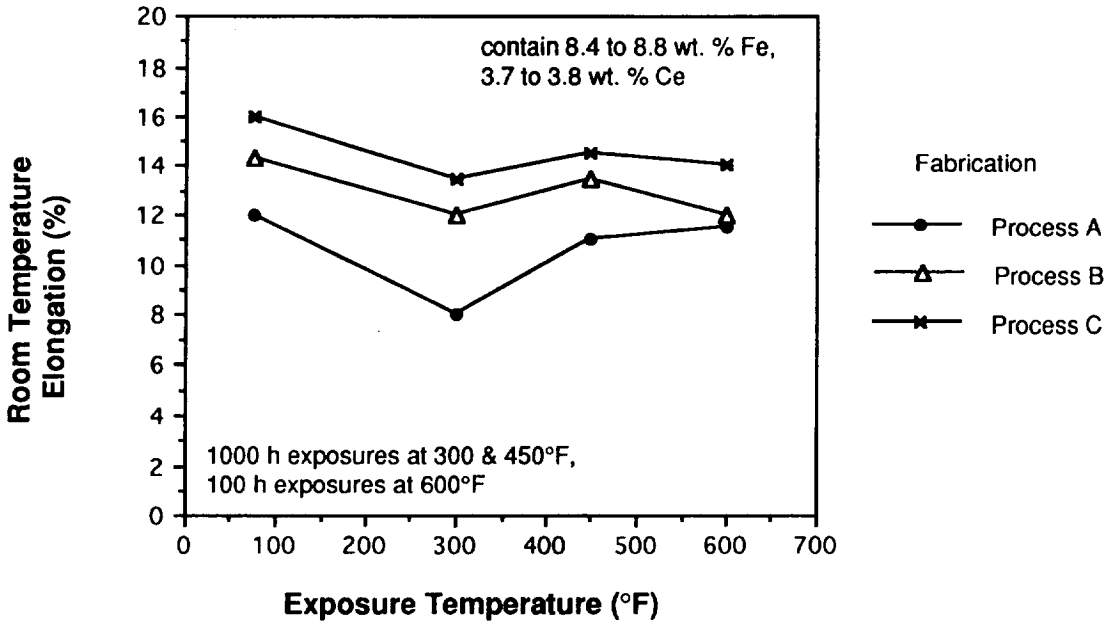

Figure 1(b). Room temperature tensile elongation as a function of exposure temperature for P/M Al-Fe-Ce alloys containing 8.4 to 8.8 wt.% Fe and 3.7 to 3.8 wt.% Ce. Here, Process A denotes data obtained from extrusions seeing the least amount of thermal exposure, Process B denotes data obtained for extrusions seeing an intermediate amount of thermal exposure and Process C denotes data obtained from extrusions seeing the greatest amount of thermal exposure.

Subtask 5A. Toughness Study of the P/M Al-Fe-X System (Boeing)

No progress to report to date. See Subtask 1A(i).

Subtask 5B. Toughness Study of the P/M Al-Fe-X System (Douglas)

No progress to report to date.

TASK 6. PROCESSING-BASED IMPROVEMENTS IN THE MECHANICAL ISOTROPY AND INTERMEDIATE TEMPERATURE DAMAGE TOLERANCE OF Al-Fe-V-Si ALLOY 8009

Principal Investigator, UVa: Dr. R.P. Gangloff
Principal Investigator, Allied Signal: Dr. M.S. Zedalis

Background and Problem Statement. Among the emerging light aluminum alloys and composites for future high speed civil transportation systems, rapid solidification and powder metallurgy (RS/PM) processed Al-Fe-X alloys have received significant attention (1,2). The high volume fraction of dispersoids and ultra-fine grain size, which are stable to 425°C, and good specific strength and stiffness properties, make these dispersion-strengthened alloys particularly attractive for elevated temperature applications.

Previous research, funded by NASA (3-6) and at Allied Signal (7-9), demonstrated that the initiation fracture toughness, crack growth resistance and tensile ductility of RS/PM Al-Fe-Si-V alloy 80009 are each significantly reduced at temperatures between 175 and 200°C. While the room temperature crack initiation fracture toughness (K_{IC} for plane strain) of rolled and extruded 8009 is well above the value for ingot metallurgy wrought 2618, a reverse ranking is observed at 175°C. Additionally, the ductility and toughness of 8009 significantly decrease with decreasing strain rate at both elevated and ambient temperatures. The ductility and fracture toughness of 8009 are anisotropic, at least for extruded product. This unique time-temperature fracture behavior is probably universal to elevated temperature aluminum alloys which contain submicron grain size and a high volume fraction of 50 nm diameter dispersoids (2,3,10,11). None-the-less, intermediate temperature fracture damage tolerance must be improved and property aniostropy must be reduced in order to employ 8009-type alloys in elevated temperature HSCT structures.

Accordingly, a Task was initiated in the 1992 NASA-UVA HCST program to investigate "Processing-Based Improvements in the Mechanical Isotropy and Intermediate Temperature Damage Tolerance of Al-Fe-V-Si Alloy 8009" (12). This work is being jointly conducted by Drs. M.S. Zedalis and S.K. Das of Allied Signal Incorporated, by Professor R.P. Gangloff and Dr. S.S. Kim at UVa, and by Mr. J.K. Donald at Fracture Technology Associates.

Task Objective. The objectives of this research are to: (a) reduce the extent of fracture toughness anisotropy and dynamic strain aging (DSA) by optimizing the processing of the 8009 alloy composition for high speed airframe applications, (b) improve intermediate temperature and prolonged-time fracture resistance of 8009 by microstructural modifications through processing, (c) establish micromechanical mechanisms for time-temperature dependent deformation and fracture of 8009-type alloys, and (d) provide initial characterization of the long-term damage tolerant properties of an optimized microstructure of HTA 8009.

The first two objectives are emphasized during this reporting period and are being accomplished by: (a) reducing the oxide content at prior particle boundaries, (b) improving metallurgical bonding between powder particles, and (c) reducing the concentration of Fe and V in the Al-solid solution matrix. The approach involves modifications to planar flow casting, powder degassing and consolidation practices conventionally employed by Allied Signal to manufacture HTA 8009. Consolidated billets are subjected to various hot and cold rolling schedules. The fracture toughnesses of a variety of process-dependent microstructures, processed in Task 6A, are characterized in Task 6B by a J-integral fracture mechanics R-curve method, as a function of elevated temperature and loading rate.

Subtask 6A. HTA 8009 Processing (Allied-Signal)

Principal Investigator: Dr. M.S. Zedalis

Background. Commercially available high temperature Al-Fe-V-Si (HTA) alloy 8009 has emerged as a leading candidate Al-base material for aerospace applications with service temperatures approaching 600K (1-4). HTA 8009 (formerly designated FVS0812) is processed utilizing rapid solidification/powder metallurgy technologies and combines the room temperature strength, ductility and fracture toughness of conventional 2000 and 7000 series aerospace aluminum alloys with greatly improved elevated temperature strength and stability. HTA 8009 derives its excellent mechanical and physical properties from a uniform dispersion of $Al_{13}(Fe,V)_3Si$ particles dispersed in an aluminum solid solution matrix. The silicide dispersoids typically range from 50-80 nm in diameter after consolidation (e.g., extrusion, forging, and rolling) and are extremely resistant to particle coarsening at elevated temperatures. As a result, no measurable material degradation occurs even after exposure for 1000 hours to temperatures approaching 725K (5,6). HTA 8009 also exhibits approximately a 25% increase in Young's modulus over conventional Al-base alloys and, on a specific stiffness basis, is superior to Ti-6Al-4V and 17-4 PH steel to temperatures approaching 750K (7). This combination of properties makes HTA 8009 extremely attractive for applications which have been previously restricted to heavier titanium or steel alloys, and superior to polymer composites at elevated temperatures. HTA 8009 is presently being evaluated for wing skins, aircraft landing wheels, missile bodies and fins as well as a variety of gas turbine engine components which operate at slightly elevated temperatures.

While the benefits of using HTA 8009 over titanium and steel alloys for certain applications are clearly recognized, extensive mechanical characterization of the alloy has identified two (2)

potential areas of concern to high eed aircraft and engine designers:

i) mechanical anisotropy as a function of product form; and,

ii) reduced plasticity in the 450-550K temperature range.

Anisotropy in the mechanical behavior of HTA 8009 is most apparent in variation in toughness and ductility for samples tested in directions orthogonal to the rolling/extrusion directions. Porr et al. (8) have recently shown for HTA 8009 flat bar extrusions that values of plane strain fracture toughness, K_{IC}, could vary from as high as about 36.6 MPa$\sqrt{m}$ for samples tested in the L-T orientation to as low as about 16.1 MPa$\sqrt{m}$ for samples tested in the T-L orientation. Fractography performed by Chan (9,10) and later confirmed by Porr et al. (8) indicates that the variation in toughness is related to the extent of delamination occurring along oxide decorated prior particle boundaries. Based on these observations, Chan (9) concluded that K_{IC} values measured for samples tested in the L-T orientation are enhanced as a result of a loss in through-thickness constraint associated with delamination. The mechanism of "thin sheet toughening" is viewed as contributing substantially to L-T toughness, while leading to lower toughness in orthogonal orientations.

Reduced plasticity in the 450-550K temperature range in HTA 8009, on the other hand, has been attributed to the phenomenon of dynamic strain aging (DSA) occurring in the alloy (11). DSA is not uncommon to conventional aluminum alloys, but typically occurs below ambient temperatures due to the higher diffusivity of the more traditional alloying constituents, (e.g., Cu, Mg, Si). For HTA 8009, Skinner et al. (11) has observed that DSA occurs at intermediate temperatures due to the more sluggish diffusivity of Fe and V present in the matrix. Solute levels of these two (2) elements in the Al-base matrix have been measured to be greatly in excess of equilibrium levels and, at present, do not appear to be affected by hot working or static thermal exposure. While DSA is

known to reduce ductilit ›ughness in HTA 8009 (6,11), the effect becomes significa ›re serious when it is combined with the mechanical anisotrop› the material. For example Porr et al. (8) measured that K_{IC} ılues for samples tested in the L-T orientation decreased to a minimum of about 15 MPa$\sqrt{m}$ over this intermediate temperature range compared to a minimum of about 9.5 MPa$\sqrt{m}$ for samples tested at similar temperatures in the T-L orientation.

Task Objectives and Approach. The objectives of this research are to improve the mechanical isotropy and elevated temperature damage tolerance of high temperature aluminum (HTA) alloy 8009 plate and sheet by modifying the current processing parameters and practice. Specifically, these objectives will be accomplished by:

(i) improving the metallurgical bonding between prior powder particles by reducing the oxide layer thickness at the particle interfaces; and,

(ii) reducing the concentration of solute Fe, V and Si in the Al matrix as well as modifying the alloy's grain/sub-grain structure via thermo-mechanical processing.

In practice, the oxide layer present at the prior powder particle boundaries will be reduced by casting and comminuting the planar flow cast 8009 ribbon in a protective atmosphere. Moreover, supersaturated solute atoms as well as grain/sub-grain structure in 8009 plate and sheet will be affected by employing a thermo-mechanical process which involves modifications to current hot/cold rolling practices. Each of these process modifications will be performed on commercial scale quantities of material, and hence, may be directly implemented into current manufacturing specifications. Milestones for the present program are shown in Fig. 1.

Progress During Report Period.

A. Planar Flow Casting

Two (2) approximately 100 kg batches of HTA 8009 were initially planar flow cast (pfc) into approximately 40 μm x 5 cm ribbon. Two (2) processing modifications were employed during casting to reduce the hydrate layer which is known to form on the surface of the pfc ribbon, Fig. 2. Casting Modification "A" involved shrouding the melt puddle and as-cast ribbon with dry Ar gas. Casting Modification "B" incorporated similar inert gas shrouding; however, a mechanical device was also placed behind the nozzle to obstruct the gas boundary layer known to be present along the surface of the casting wheel. The rationale behind these casting modifications was based on previous data which indicated that the hydrate layer, which forms on the surface of the pfc ribbon, could be substantially reduced by casting in a dry Ar environment. Based on known dehydration and oxidation sequences for aluminum, Table 1, a thinner overall oxide layer would be manifest by reducing this surface hydrate layer (12). Moreover, the H2 concentration would also be reduced in consolidated HTA by minimizing the hydrate surface layer.

To evaluate the effect of these two (2) casting modifications on hydrate layer formation, the surfaces of ribbon cast in the present investigation were examined by scanning electron microscopy (SEM), Auger electron spectroscopy (AES) as well as x-ray photoelectron spectroscopy (XPS or ESCA). To evaluate the microstructure of the pfc ribbon, transmission electron microscopy (TEM) was also performed. For comparison, data was also compiled for pre-program vintage HTA 8009 ribbon that was planar flow cast in moist laboratory air (i.e., cast without a dry Ar shroud).

TABLE 1

Decomposition Sequence for Al Hydrate Present on PFC 8009 Ribbon Surface as a Function of Degassing Temperature (12)

Above 373K:	$Al(OH)_3.nH_2O \Rightarrow Al(OH)_3 + nH_2O$
Less than 420K:	$Al(OH)_3 \Rightarrow AlO(OH) + H_2O$
From 580 - 773K	$2AlO(OH) \Rightarrow Al_2O_3 + H_2O$
At ALL Temperatures:	$2/3\ Al + H_2O \Rightarrow 1/3\ Al_2O_3 + H_2$

Al_2O_3 Remains Stable @ T > 820K

Scanning Electron Microscopy (SEM)

Scanning electron microscopy (SEM) was performed on a JEOL 840 electron probe microanalyzer equipped with energy (EDS) and wavelength dispersive (WDS) spectroscopy capabilities. The accelerating voltage used as well as the working distances and magnifications are indicated on the SEM micrographs.

The results of SEM analyses performed on the surfaces of the ribbon samples indicate little or no difference between casting modification A versus modification B, or for that matter, pre-program vintage pfc ribbon samples. Large differences, however, were apparent between the wheel-side surface and the air-side surface for all of the ribbon samples examined, Figs. 3 & 4. In general, the wheel-side surface of the ribbon is much smoother than the air-side surface and clearly reflects the surface of the casting wheel. Surface asperities are apparent and may be attributed to localized sticking of the molten metal/ribbon to the casting wheel, Fig. 3b.

The ribbon's air-side surface provides very different information on the solidification mechanics and specifically, the formation of the hydrate layer on the ribbon's surface. Two (2) distinctly different regions are apparent on the air-side surface

of the ribbon, Fig. 4a. The striated bands scattered across the surface of the ribbon indicate a thicker hydrate layer which initially forms on the surface of the molten metal puddle during casting. Based on information in the literature (13,14), these hydrate layers are suggested to have a pseudo-boehmite structure [i.e., AlO(OH)]. As casting proceeds, these layers break apart and are carried away with the planar flow cast ribbon.

In between these coarse striated regions, very small ($\approx$ 0.5 μm) particles may also be observed, Fig. 4b. Based on the fact that they appear slightly clustered, it is suggested that they reflect microcellular and/or discrete $Al_{13}(Fe,V)_3Si$ particles present in the HTA alloys. Based on their relative size, it is also suggested that these particles are likely coated with Al and a AlO(OH) layer. Clearly, the presence of such particles, (and associated porosity), indicates that the ribbon's actual surface area is much greater than a calculated value for the surface area based on the ribbon's overall dimensions. Hence, the importance of controlling the casting atmosphere and specifically, minimizing surface hydration is further magnified.

Auger Electron Spectroscopy (AES)

Auger electron spectroscopy (AES), combining scanning Auger microprobe (SAM) with secondary ion mass spectroscopy (SIMS) was performed for submicron analysis of the composition of the surface layers of the planar flow cast ribbon. AES analysis was performed using a PHI 595 SAM. The accelerating voltage was 10 keV and the beam current was typically about 80 nA. The beam was rastered at television rates at 10 kx magnification in order to minimize contamination and desorption problems. Chemical depth profiling of the ribbon's surfaces was performed at a 2x2 mm raster size at a beam voltage of 4 keV to a depth of 1 to 3 nm.

AES analysis was performed on both the wheel- and air-sides of planar flow cast ribbon samples from casting modifications A

and B. On the air-side surface of the ribbon, AES was only performed on areas corresponding to the clustered particles previously observed by SEM, Fig. 4b. In general, survey scans indicate very similar results for both the air- and wheel-sides of the pfc ribbon samples even though the surface morphologies were very different. Survey scans of the as-cast surfaces, Figs. 5a & 6a, indicate that the surfaces are enriched with oxygen (representative of the hydrate layer) and have lesser amounts of C and Al. Very small amounts of Fe are also evident. Comparison of the C peaks indicates a slight enrichment of C on the wheel-side of the pfc ribbon from casting modification B. (Note: All of the peaks heights are normalized to the peak intensity for oxygen; hence, direct comparison of peak intensities may be made.) The slightly enriched C level on the wheel-side surface of the pfc ribbon is suggested to be due to a graphite coating applied to the mechanical device employed to obstruct the gas boundary layer along the surface of the casting wheel. It is speculated that this graphite coating was eroded away during casting by the rapidly rotating casting wheel. Further information on the magnitude of C coating present on the wheel side surface of the pfc ribbon from modification B is presented below in the results of x-ray photoelectron spectroscopy.

AES depth profiling was also performed to evaluate the sub-surface composition of the pfc ribbon. Chemical profiles as a function of sputtering time (i.e., sputtering depth) for the air- and wheel- sides of the pfc ribbon are shown in Figs. 5b & 6b, respectively. In general, the variation of sub-surface composition as a function of sputtering depth were very similar for both sides of the ribbon. Bulk compositions for O_2, Al, Fe and Si appear to be reached after approximately 90 seconds of Ar ion sputtering. Based on these data, the hydrate layer thickness may be estimated to be about 4 nm on both sides of the ribbon. Interestingly, there appears to be minor sub-surface segregation of Si. The Si intensity as a function of sputtering depth for all

of the surfaces examined by AES reaches a maximum after about 1 minute of sputtering and then decays to a bulk composition. Survey scans of a clustered region on the air-side surface of the ribbon clearly indicate that the Si signal is more intense after 45 seconds of Ar ion sputtering than after 90 seconds of sputtering, Figs. 7a and b, respectively.

X-ray Photoelectron Spectroscopy (XPS)

X-ray photoelectron spectroscopy (XPS) was specifically employed to quantify the hydrate layer thickness on the air- and wheel- side surfaces of the planar flow cast ribbon. XPS involves the energy analysis of photoelectrons ejected from the surface of a material under x-ray bombardment. Unlike AES, XPS requires only a single measurement per sample and does not require any ion etching (i.e., depth profiling) or separate calibration procedures. Moreover, XPS derives its chemical information from a much larger spatial area than AES; hence, the data is not susceptible to chemical inhomogeneities in the material. For the present investigation, a VG ESCALAB MARK II photospectrometer equipped with a triple channeltron detection system was employed. Standard Al K-alpha x-rays were used at an energy of 1486.6 eV. General survey scans were recorded between 100 and 1500 eV kinetic energy to show the relative intensities of the elements present. The binding energy was calibrated to the adventitious C 1s peak at a binding energy of 285.0 eV.

Survey scans indicating the intensities of all of the elements on the air- and wheel-side surfaces of pfc ribbon from casting modifications A and B are shown in Figures 8-11 a and b. The major peak in all of the scans is obviously oxygen, which is assumed to correspond to the surface hydrate layer (14). Smaller peaks corresponding to Fe, C and Al are also observed. The most noticeable difference between the scans is the higher C level present on the wheel-side surface of pfc ribbon cast following modification B. These results confirm the earlier AES data which

indicated that the wheel-side surface of pfc ribbon from casting modification B had an enriched C content. It may also be concluded that the C coating is spread over the majority of the wheel-side surface of the ribbon since XPS analyzes a much larger area than AES. Presently, the effect of the C coating and potential graphite contamination in the consolidated material is unknown. The presence of graphite in casting modification B HTA material has been conveyed to Prof. R. Gangloff at the University of Virginia (UVa). Its potentially deleterious effects will be monitored during testing and by subsequent microscopy performed on consolidated HTA plate and sheet samples. If necessary, the testing matrix at both UVa and Allied will be modified to concentrate characterization of only material from casting modification A.

Comparison of the relative intensities of the oxidic and metallic Al 2p peak intensities allow the determination of the relative oxide (or hydrate) thickness among the sample examined, Figs. 8-11 b (14). In general, the greater the oxide (or hydrate) to metal intensity ratio, the thicker the oxide (or hydrate). Calculated values of hydrate thickness for both the air-and wheel-sides of the ribbon samples examined as well as for some pre-program vintage ribbon are summarized in Table 2. In comparison to pre-program vintage ribbon which had hydrate thicknesses on both the air- and wheel-side surfaces ranging from about 4.0-5.0 nm, the hydrate thicknesses for both the modification A and B ribbon are on the order of about 3.1 nm. This ≈25-40% reduction in hydrate layer thickness may be directly attributed to casting the HTA 8009 ribbon in a protective, dry Ar atmosphere. Of all of the ribbon samples examined, the wheel-side surface of the pfc ribbon cast following modification B exhibited the thinnest hydrate layer, 2.8 nm. These results indicate that obstruction of the gas boundary layer present along the surface of the casting wheel does minimize the hydration of the pfc ribbon due to the influx of moist air. Unfortunately, the mechanical device employed

in the present program will require modification to eliminate the source of C.

TABLE 2
Hydrate Layer Thickness on Planar Flow Cast HTA 8009 Ribbon Based on Comparison of the Relative Intensities of the Metallic and Oxidic Al 2p Peak Intensities from XPS Survey Scans.

Sample ID	Hydrate Thickness (nm)
Pre-Program Ribbon	4.0 - 5.0
Modification A	
Wheel Side	3.2
Air Side	3.3
Modification B	
Wheel Side	2.8
Air Side	3.0

Transmission Electron Spectroscopy (TEM)

Transmission Electron Spectroscopy (TEM) was performed on pfc ribbon from casting modifications A and B to evaluate the as-cast microstructure. TEM foils were mechanically thinned and electropolished in a 20% HNO_3 - 80% CH_3OH solution at 223K. Microscopy was performed on a Philips EM400T microscope equipped with STEM and EDS capabilities.

TEM analysis performed on pfc ribbon cast following modification A indicates a microcellular structure which is typical of pre-program vintage and standard cast HTA 8009 ribbon, Fig. 12. The cell walls have a chemistry similar to that of the primary dispersion strengthening phase, $Al_{13}(Fe,V)_3Si$. During subsequent thermal treatments, (e.g., degassing, compaction, extrusion), discrete silicide particles nucleate and form in place of the cellular network. Comparison of dispersoid size to cell wall thickness indicates that minimal growth is experienced during

this decomposition sequence. The cell size in the as-cast pfc ribbon basically corresponds to the sub-grain size in the consolidated material. The sub-grain size remains stable since its boundaries are pinned with thermally stable $Al_{13}(Fe,V)_3Si$ dispersoids. The light gray intracellular regions represent the supersaturated Al-solid solution. Preliminary EDS analysis indicates supersaturated levels of Fe, V and Si well in excess of equilibrium concentrations.

TEM analysis of pfc HTA 8009 ribbon cast following modification B indicates a grossly different microstructure than ribbon from casting modification A, Fig. 13. The microstructure is composed of large "O" phase islands (15) present in an Al-solid solution matrix. The "O" phase is a quasicrystalline icosahedral phase which forms in HTA 8009 typically when very high undercooling of the melt puddle is achieved (5-7). Since casting modification B involves obstructing the gas boundary layer present at the surface of the casting wheel, it is suggested that increased wetting of the melt puddle to the casting wheel does in fact occur, which in turn results in higher undercooling of the melt puddle prior to solidification. During subsequent thermal treatments (as actually observed by hot stage microscopy), discrete silicide particles nucleate and grow within each of these "O" phase islands. In general, the size of the silicide particles produced from this decomposition/nucleation and growth event are typically coarser than silicide particles formed from a microcellular structure, typical of casting modification A ribbon, Fig. 12. In turn, slightly lower strengths are anticipated for casting modification B material.

B. Ribbon Comminution, Degassing and Vacuum Hot Compaction

The planar flow cast ribbon from modifications A and B were then comminuted in separate batches to -40 mesh powder under a dry, protective atmosphere following Process Specifications HTAPS A114. The separate batches of -40 mesh HTA 8009 powder after

pulverization were then dynamically degassed following Process Specification HTAPS A120. Gas chromatography performed during the degassing cycle indicates that the primary gas liberated during vacuum degassing is water vapor. Water vapor is present on the HTA powder as adsorbed water molecules and is also the decomposition product of the dehydration sequence outlined in Table 1 for the aluminum hydrate layer present on the surface of the pfc ribbon/powder.

Following Process Specifications HTAPS A120, the degassed powder was directly fed into a 1650 ton vacuum hot press for compaction into ~30 cm diameter X ~ 60 cm long billets. The overall density of the consolidated billets was approximately 93% and each billet weighed approximately 100kg. Billet number 92A022 was comprised of powder from casting modification A, while billet number 92A024 was comprised of powder from casting modification B. The compacted billets were then machined and inspected following Process Specifications HTAPS A121 and A150 prior to being released for extrusion.

C. Extrusion and Preparation of Rolling Preforms

The two (2) approximately 100 kg vacuum hot pressed HTA 8009 billets, 92A022 and 92A024, were extruded at Spectrulite Consortium Inc. (SCI), Madison, IL, into approximately 4.0 cm X 20.3 cm rectangular bar. Extrusion conditions for both billets were nearly identical and fell within the requirements of Process Specification HTAPS 221. Both extrusions were approximately 2.75 meters in length and exhibited an excellent surface finish. Each of the extrusions were inspected and sectioned into approximately 30 cm preforms following Process Specifications HTAPS 222 and 223 prior to being released for rolling.

Oxygen and hydrogen analyses were measured by LECO Corporation on the nose and tail of extrusions 92A022 and 92A024 to evaluate the effect of casting modifications A and B on the hydrogen and oxygen contents in the extruded product, Table 3.

Hydrogen contents was measured by thermal conductivity on 5 gram pin samples using a LECO RH402 hydrogen analyzer. Oxygen content was measured by infrared spectroscopy on 0.25 gram pin samples using a LECO 416DR oxygen analyzer.

TABLE 3

Gas Contents for HTA 8009 Extrusions Composed of Powder from Casting Modifications A and B Compared to Pre-Program Vintage HTA 8009 Material

Billet I.D.	Modification	Position	Percent Oxygen	Total Hydrogen (ppm)
Pre-Program Vintage		Nose/Tail	0.120-0.130	3.50-4.50
92A022	A	Nose	0.084	1.61
"	"	Tail	0.090	2.51
		Avg.	0.087	2.06
92A024	B	Nose	0.076	1.73
"	"	Tail	0.082	1.29
		Avg.	0.079	1.51

Examination of the data in Table 3 indicates that shrouding the melt puddle and pfc ribbon with a dry Ar gas does result in a significant reduction in oxygen and hydrogen contents in extruded HTA 8009 in comparison to pre-program vintage extrusions. In general, the casting modifications employed for this program resulted in a 25-35% reduction in total oxygen content and a 50-60% reduction in total hydrogen content in comparison to pre-program vintage material. Extrusion 92A024, composed of ribbon/powder from casting modification B, indicated approximately a 9% reduction in total oxygen and approximately a 25% reduction in total hydrogen in comparison to extrusion 92A022, comprised of ribbon/powder from casting modification A. This reduction in gas content is consistent with the results of AES and XPS performed on the as-cast ribbon from these two casting modifications, and

further supports the original premise of the program that the oxide (and hydrogen) content in consolidated HTA 8009 may be significantly reduced by: (i) controlling the environment in which planar flow casting is performed; and, (ii) minimizing the hydrate layer that forms on the surface of the planar flow cast ribbon. While the benefits of reduced oxide and hydrogen contents will be highlighted in subsequent mechanical testing performed during the second half of this program, an immediate benefit from the above mentioned casting modifications is that HTA 8009 with hydrogen levels in the 1.5-2.0 ppm range is weldable with little or no porosity depending on the fusion welding technique employed. In turn, the ability to weld HTA has a significant impact on the number of potential applications where the alloy may be utilized.

D. Plate and Sheet Fabrication

Rolling of the HTA 8009 extruded preforms was performed at Kaiser Aluminum's Center for Technology (CFT) in Pleasanton, CA. The rolling campaign was designed to evaluate the major objectives of the program, namely:

(i) to evaluate the effects of rolling direction and total reduction in gauge on mechanical isotropy in HTA 8009 plate and sheet; and,

ii) to evaluate the application of thermo-mechanical processing to improve elevated temperature ductility and toughness by modifying the grain/sub-grain structure in HTA 8009 sheet as well as by reducing the solute content in the Al matrix.

Based on mechanical and microstructural testing and evaluation performed on material fabricated during this campaign, modifications to current rolling procedures and specifications will be recommended.

The specific rolling schedules designed to meet the aforementioned objectives are summarized in Fig. 14. To evaluate the effects of rolling direction and total reduction in gauge on

mechanical isotropy in HTA 8009 plate and sheet, one-half of the pre-forms from each casting modification received only cross-rolling (i.e., rolled normal to the extrusion direction), while the balance received only straight-rolling (i.e., rolled parallel to the extrusion direction). An identical pass schedule (i.e., reduction per pass and the number of passes per rolling heat) was practiced for all lots of material. Plate and sheet having respective gauges of 0.64 cm (0.25"), 0.22 cm (0.090") and 0.10 cm (0.040") were produced during this phase of the program.

To evaluate the application of thermo-mechanical processing (TMP) to improve elevated temperature ductility and toughness, HTA 8009 sheet was initially hot rolled to approximately 0.22 cm (0.090") gauge. Three (3) different rolling practices were then employed to fabricate 0.10 cm (0.040") gauge sheet. The first rolling practice involved only hot rolling to the final gauge. Here the sheet was soaked at approximately 673K (750°F) prior to being rolled. During the campaign, the sheet was reheated if it's temperature ever fell below about 500K (450°F).

The second rolling practice involved only cold rolling to the final gauge. Here the sheet was allowed to cool to approximately 298K (77°F) prior to being cold rolled to its final gauge. Work induced adiabatic heating of the sheet was experienced during cold rolling; however, the sheet temperature never exceeded about 340K (150°F).

The third rolling practice also involved only cold rolling [298K (77°F)] to the final gauge; however, after approximately every 30% reduction in gauge, the sheet was subjected to an annealing treatment at approximately 673K (750°F) for 0.5 hrs. This TMP was selected in hopes of reducing the concentration of Fe, V and Si in the HTA 8009 matrix by enhancing heterogeneous nucleation of precipitates in the matrix as well as by maximizing the "sweeping" action of glissile dislocation through the matrix without creating cavitation or the formation of micro-cracks.

E. Initiation of Testing at Allied and the UVA

In total, approximately 150 kg of sheet were rolled at Kaiser Aluminum - CFT for the present program. Prior to being shipped back to Allied, all of the sheet was trimmed to remove edge cracks and sectioned into approximately 250 cm (100") lengths. Approximately one-third of this HTA 8009 plate and sheet was further sectioned for subsequent testing and evaluation by Allied's Metals Laboratory. The balance of material from casting modifications A and B were supplied to the University of Virginia for their testing matrix. Material supplied to the UVa is summarized in Tables 4 and 5.

Summary Standard processing parameters and practices employed to manufacture rapidly solidified high temperature Al-Fe-V-Si (HTA) alloy plate and sheet were systematically modified to evaluate their effect(s) on mechanical isotropy (as a function of product form) and elevated temperature damage tolerance. Initially, two [2] approximately 100 kg batches of HTA 8009 were planar flow cast following two [2] modified casting practices selected to minimize the hydrate/oxide layer present on the surface of the as-cast ribbon. Reduced oxide thickness has been determined to result in improved better metallurgical bonding between prior powder particles which in turn enhances the mechanical isotropy of the wrought product. Reduced oxide content has also been found to mitigate the ductility decrease previously measured for HTA at elevated temperatures. In comparison to conventionally cast HTA 8009 ribbon, which exhibits a hydrate layer (as measured by XPS) ranging from 4.0-5.0 nm, ribbon produced from the two [2] modified casting practices exhibited hydrate layer thicknesses ranging from 2.8-3.3 nm. SEM and TEM analyses performed on the as-cast ribbon indicated that the casting modifications did not adversely affect the ribbon's as-cast microstructure and that the structure was consistent with as-

TABLE 4

Material Supplied to the UVa for Testing

Casting Modification A

ID	Dimensions (cm)	Comments
92A022-1C	0.63 x 36.80 x 88.90	Hot, Cross Rolled
92A022-1A	0.63 x 22.90 x 139.70	Hot, Straight Rolled
92A022-2A	0.26 x 35.60 x 114.30	Hot, Cross Rolled
92A022-2A	0.25 x 35.60 x 162.60	Hot, Cross Rolled
92A022-2B	0.26 x 22.90 x 167.60	Hot, Straight Rolled
92A022-2B	0.26 x 21.60 x 241.30	Hot, Straight Rolled
92A022-2C1	0.07 x 21.60 x 198.10	Hot, Straight Rolled
92A022-2C1	0.07 x 21.60 x 223.50	Hot, Straight Rolled
92A022-1B1	0.10 x 35.60 x 203.20	Hot, Cross Rolled
92A022-2C2	0.10 x 10.20 x 245.10	Cold, Straight Rolled
92A022-1B2	0.10 x 34.30 x 207.00	Cold Cross Rolled
92A022-2C3	0.10 x 17.10 x 124.50	Cold/Anneal, Straight Roll
92A022-2C3	0.10 x 15.90 x 124.50	Cold/Anneal, Straight Roll
92A022-1B3	0.10 x 35.60 x 204.50	Cold/Anneal, Cross Roll

TABLE 5

Material Supplied to the UVa for Testing

Casting Modification B

ID	Dimensions (cm)	Comments
92A024-1C	0.64 x 29.20 x 78.70	Hot, Cross Rolled
92A024-1A	0.64 x 23.50 x 83.80	Hot, Straight Rolled
92A024-1B	0.27 x 23.50 x 108.00	Hot, Straight Rolled
92A024-1B	0.27 x 23.50 x 185.40	Hot, Straight Rolled
92A024-1D	0.22 x 27.90 x 121.30	Hot, Cross Rolled
92A024-1D	0.22 x 27.90 x 182.90	Hot, Cross Rolled
92A024-2A1	0.08 x 24.10 x 125.70	Hot, Straight Rolled
92A024-2A1	0.08 x 25.40 x 73.70	Hot, Straight Rolled
92A024-2B1	0.10 x 29.80 x 175.30	Hot, Cross Rolled
92A024-2A2	0.10 x 10.10 x 160.00	Cold, Straight Rolled
92A024-2A2	0.09 x 10.80 x 80.00	Cold, Straight Rolled
92A024-2B2	0.10 x 26.70 x 171.50	Cold, Cross Rolled
92A024-2A3	0.09 x 15.20 x 63.90	Cold/Anneal, Straight Rolled
92A024-2B3	0.10 x 27.30 x 40.60	Cold/Anneal, Cross Rolled
92A024-2B3	0.11 x 27.30 x 177.80	Cold/Anneal, Cross Rolled

cast ribbon, which after consolidation, demonstrated an excellent combination of mechanical properties.

The rapidly solidified, planar flow cast ribbon from the two [2] casting modifications was then comminuted to -40 mesh powder under a dry, protective atmosphere and consolidated into billets having an approximate dimension of 30 cm in diameter X 60 cm in length. The overall density of the consolidated billets was approximately 93% and each billet weighed approximately 100 kg. The billets were then extruded into 4.0 cm X 20.3 cm rectangular bars which, after sectioning, were rolled into plate and sheet. Oxygen and hydrogen analyses performed on the extruded bars indicated a significant reduction in both oxygen and hygrogen in comparison to conventionally cast and processed HTA extrusions. In general, the casting modifications employed for this program resulted in a 25-35% reduction in total oxygen content and a 50-60% reduction in total hydrogen content in comparison to pre-program vintage material. Oxygen and hydrogen data for both extrusions were consistent in ranking to that of XPS analysis previously performed on the as-cast ribbon to determine hydrate layer thickness.

Rolling of the extruded HTA 8009 rectangular bar was successfully completed following a pass schedule specifically designed to evaluate the effects of rolling direction and total reduction in gauge on mechanical isotropy and to improve the elevated temperature damage tolerance in HTA plate and sheet. Application of a thermo-mechanical treatment may improve elevated temperature ductility and toughness by modifying the grain/sub-grain structure in HTA 8009 sheet as well as by reducing the solute content in the Al-solid solution matrix by enhancing precipitate nucleation and growth. In total, approximately 150 kg of sheet were rolled for the present program. Approximately one-third of the plate and sheet was kept by Allied-Signal's Metals Laboratory for subsequent testing and evaluation. The balance of material was supplied to the University of Virginia for the

ambient and elevated temperature toughness testing.

References.

1. U.S. Air Force Contract F33615-85-R-5160, "900°F Aluminum-Base Materials Research", Awarded to the University of Virginia, 1985.
2. U.S. Air Force Contract F33615-87-R-3206, "Elevated Temperature Aluminum Program", Awarded to Lockheed - California Company, 1987.
3. Naval Air Development Center Contract N62269-88-C-0255, "Elevated Temperature Aluminum Base Alloys for Applications in Advanced Turbofan Jet Engines", Awarded to Allied-Signal Inc., January 1989.
4. E.Y. Ting and J.R. Kennedy, NASA CR-181849, "Superplastic Forming and Diffusion Bonding of Rapidly Solidified, Dispersion Strengthened Aluminum Alloys for Elevated Temperature Structural Applications", 181-198 (1989).
5. D.J. Skinner, "The Physical Metallurgy of Dispersion Strengthened Al-Fe-V-Si Alloys", in *Dispersion Strengthened Aluminum Alloys*, Y.W. Kim and W.M. Griffith, eds., TMS, (1988).
6. P.S. Gilman, M.S. Zedalis, J.M. Peltier and S.K. Das, "Rapidly Solidified Aluminum-Transition Metal Alloys for Aerospace Applications", AIAA/AHS/ASEE Aircraft Design, Systems and Operations Conference, Atlanta, GA, Sept. 1988.
7. M.S. Zedalis and D.J. Skinner, "Young's Moduli of Al-Fe-X-Si Alloys and Al-Fe-V-Si -Base Metal Matrix Composites", in *Lightweight Alloys for Aerospace Applications*, E.W. Lee, E.H. Chia and N.J. Kim, eds., TMS, 335-344 (1989).
8. W.C. Porr, Y. Leng and R.P. Gangloff, "Elevated Temperature Fracture Toughness of P/M Al-Fe-V-Si", in *Low Density, High Temperature P/M Alloys*, W.E. Frazier, M.J. Koczak, and P.W. Lee, eds., TMS-AIME, Warrendale, PA, 129-155 (1991).

9. K.S. Chan, "Evidence of Thin Sheet Toughening Mechanism in Al-Fe-X Alloys", *Met. Trans.*, **20A**, 155-164 (1989).
10. K.S. Chan, "Confirmation of Thin Sheet Toughening Mechanism and Anisotropic Fracture in Al-Fe-X Alloys", *Met. Trans.*, **20A**, 2337-2344 (1989).
11. D.J. Skinner, M.S. Zedalis and J.M. Peltier, "Anomalous Ductility Variation at Intermediate Temperatures in Rapidly Solidified Al-Base Alloys", in *Lightweight Alloys for Aerospace Applications*, eds., E.W. Lee, E.H. Chia and N.J. Kim, TMS, 71-78 (1989).
12. A.I. Litvintsev and L.A. Arbuzova, *Sov. P/M Met. Cer.*, **1**, 1 (1967).
13. W.M. Mullins and B.L. Averback, "The Electronic Structure of Anodized and Etched Aluminum Alloy Surfaces", *Surf. Sci.*, **206**, 52 (1988).
14. B.R. Strohmeier, "An ESCA Method for Determining the Oxide Thickness on Aluminum Alloys", *Surf. and Interface Anal.*, **15**, 51 (1990).
15. D.J. Skinner, K. Okazaki and C.M. Adam, "Physical Metallurgy and Mechanical Properties of Aluminum Alloys Containing Eight to Twelve Percent Iron", in *Rapidly Solidified Powder Al Alloys*, eds., M.E. Fine and E.A. Starke, ASTM, 211-236 (1986).
16. C.M. Adam, V.R.V. Ramanan and D.J. Skinner, in *Undercooled Alloy Phases*, eds., E.W. Collings and C.C. Koch, TMS, 59 (1987).
17. D.J. Skinner, V.R.V. Ramanan, M.S. Zedalis and N.J. Kim, "Stability of Quasicrystalline Phases in Al-Fe-V Alloys", *Mat. Sci. Eng.*, **99**, 407-411 (1988).
18. M.S. Zedalis, V.R.V. Ramanan and D.J. Skinner, "Thermal Analysis of Rapidly Solidified Al-Fe-V Alloys, and SiCp Reinforced Al-Li-Cu-Mg-Zr Composites" in Thermal Analysis in Metallurgy, eds., R.D. Shull and A. Joshi, TMS, 279-295 (1992).

Acknowledgements. The authors (M.S.Z & S.K.D) would gratefully like to acknowledge the members of Allied-Signal's High Performance Alloy Products group for manufacturing of HTA 8009 for the present program, especially P. Chipko, J.M. Peltier and E. Rainal. The expert assistance of W. Moore, W. Duncan and D. Timmons of Spectrulite Consortium Inc. and Kaiser Aluminum-CFT during the extrusion and rolling of HTA 8009, respectively, is also acknowledged. Finally, the authors would like to personally thank M. Rodriguez, P.Jeges, A. Townsend and R. Toscano of the Metals Laboratory as well as E. Leone of Allied's Analytical Laboratory for performing TEM, light microscopy and surface analyses on HTA 8009 ribbon and sheet samples.

Program Schedule

Aluminum Based Materials for High Speed Aircraft

Sub-Contract No. 5-28407

Date: 7-15-92

No.	Milestone	Month 1	2	3	4	5	6	7	8	9	10	11	12
1	8009 Casting & Pulverization		▲										
2	Degassing and Compaction			▲									
3	Extrusion & Sectioning					▲							
4	Hot Rolling					▲							
5	Cold Rolling / Annealing					▲							
6	Supply Material to UVa							▲					
7	Characterization												
a	Gas Analyses								△				
b	Tensile Testing										△		
c	Microscopy, EDS/WDS											△	
8	Reporting								△				△

Figure 1.

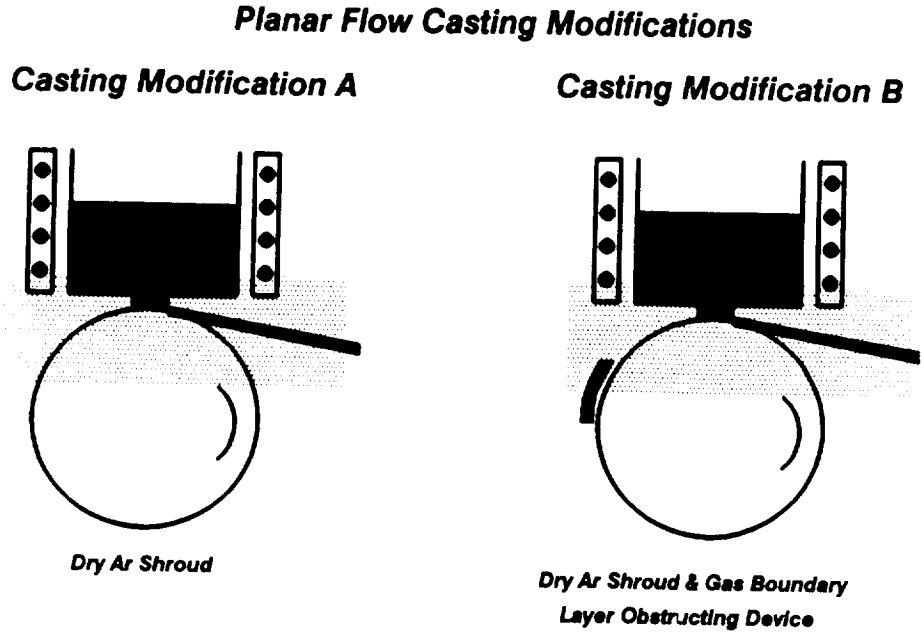

Figure 2. Two (2) planar flow casting modifications were employed to minimize hydration of the melt puddle and as-cast HTA 8009.

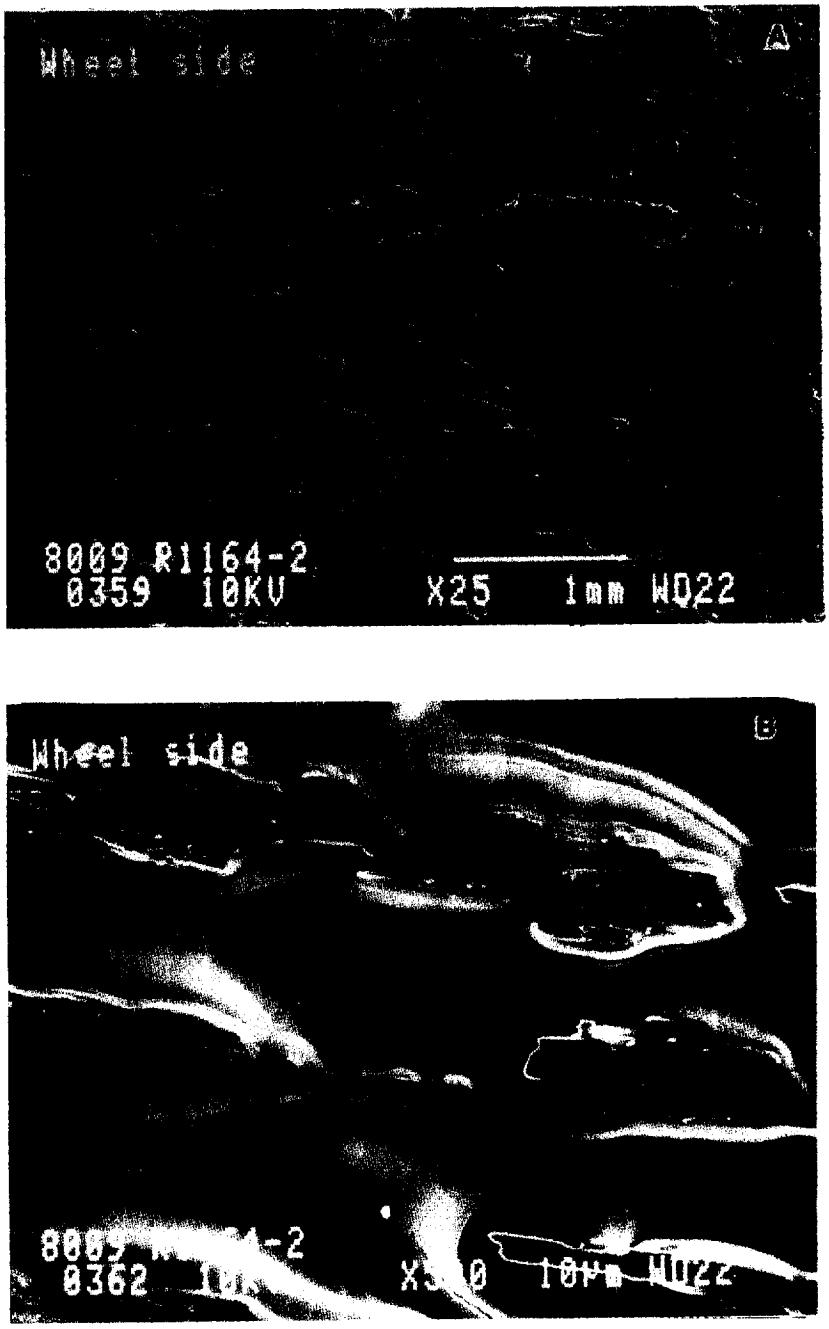

Figure 3. The wheel-side surface of planar flow cast HTA 8009 ribbon as characterized by this low magnification SEM micrograph (a) reflects the surface of the casting wheel. Asperities as noted at higher magnifications (b) are the result of localized sticking of the molten metal to the wheel surface after solidification.

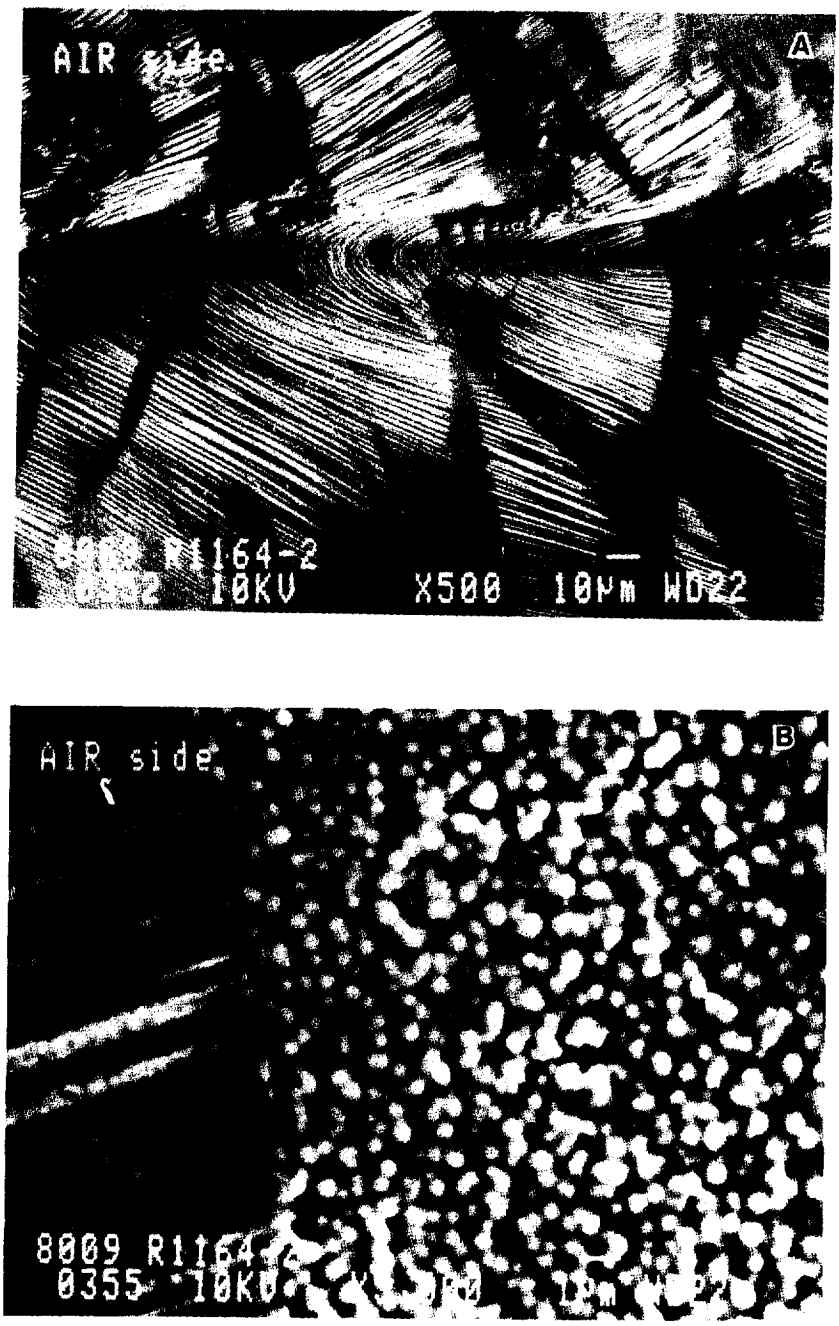

Figure 4. (a) The air-side surface of planar flow cast HTA 8009 ribbon is comprised of striated hydrate regions as noted at low magnifications. (b) Higher magnification microscopy indicates a substructure composed of very fine $Al_{13}(Fe,V)_3Si$ particle cluster enveloped in the Al-solid solution matrix.

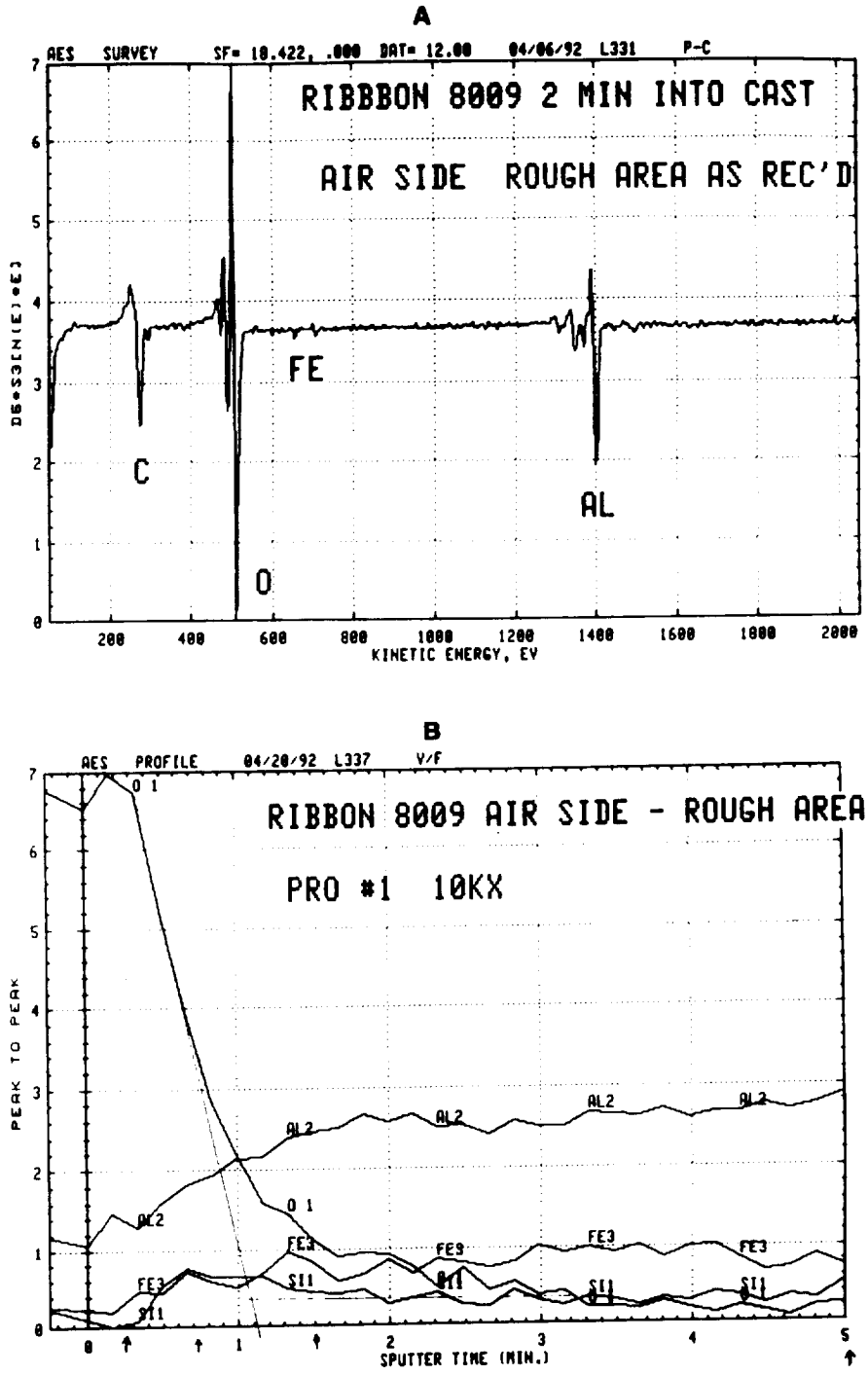

Figure 5. (a)Overall AES survey scan for air-side surface of pfc ribbon; (b) Compositional variation as a function of sputtering time (depth) for the same ribbon.

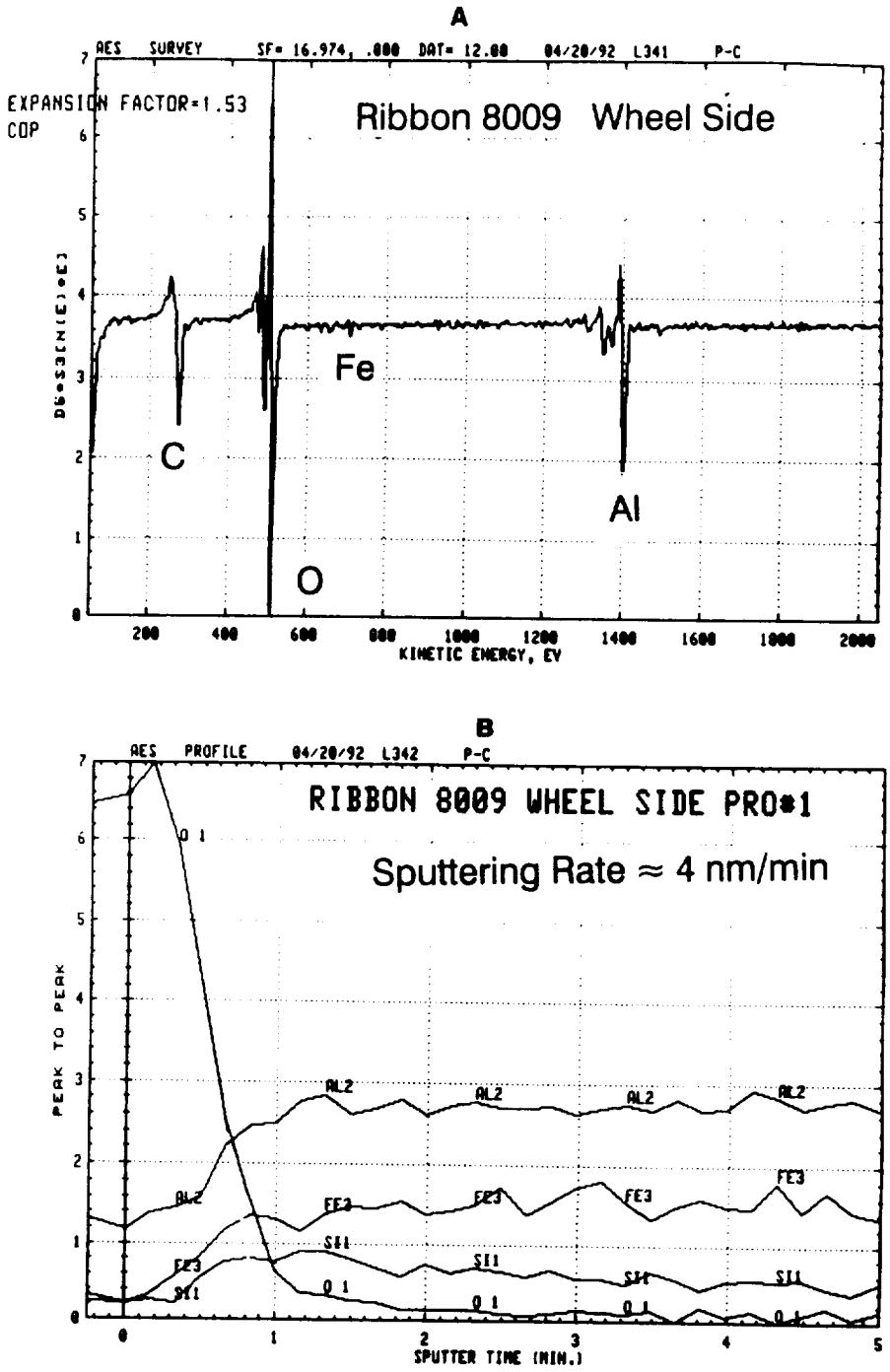

Figure 6. (a) AES survey scan for wheel-side surface of pfc ribbon; (b) Compositional variation as a function of sputtering time (depth) for the same ribbon.

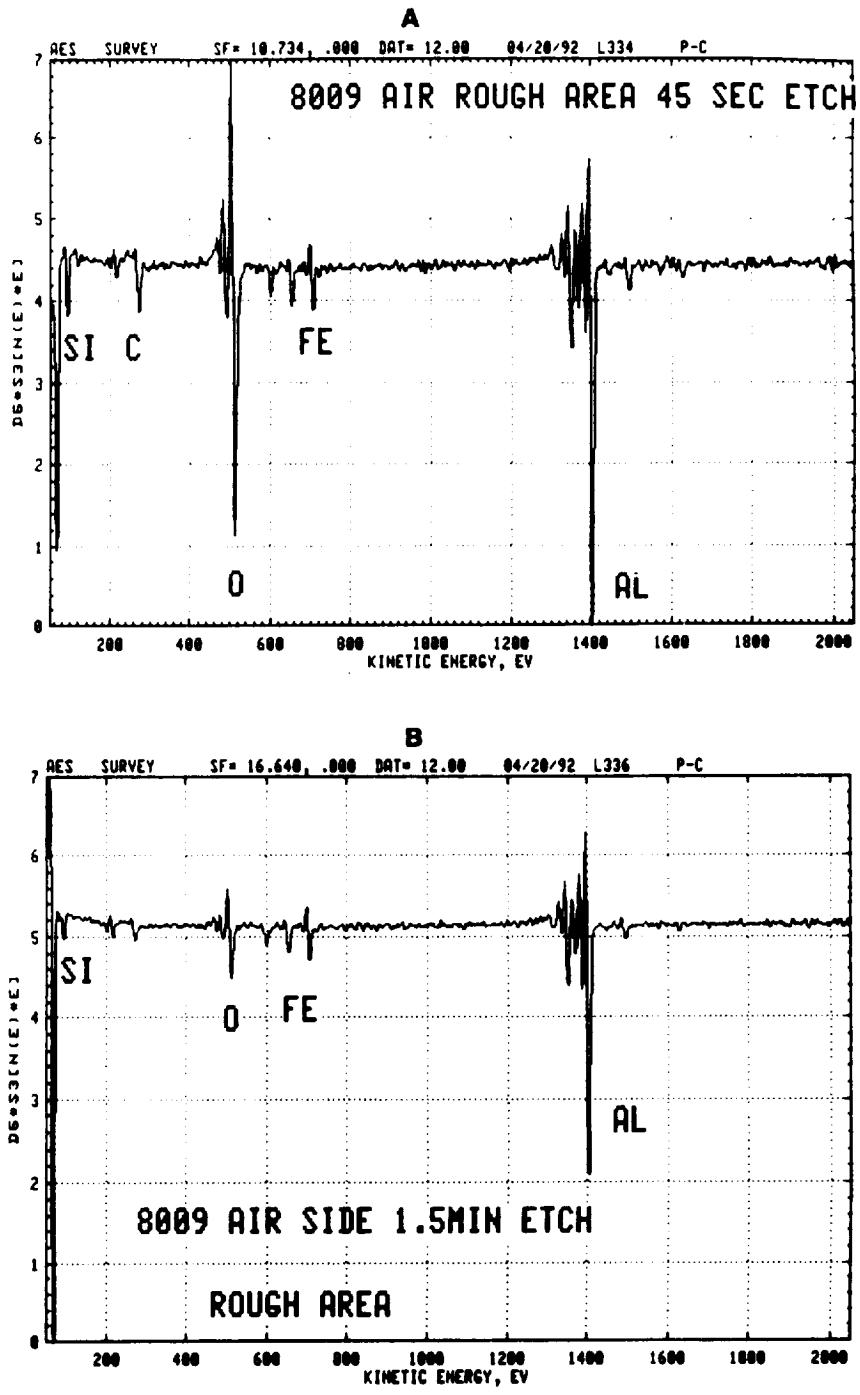

Figure 7. Si sub-surface segregation is clearly obvious in these AES survey scans of the clustered regions on the air-side surface of the ribbon after Ar ion sputtering for 45 and 90 seconds, respectively.

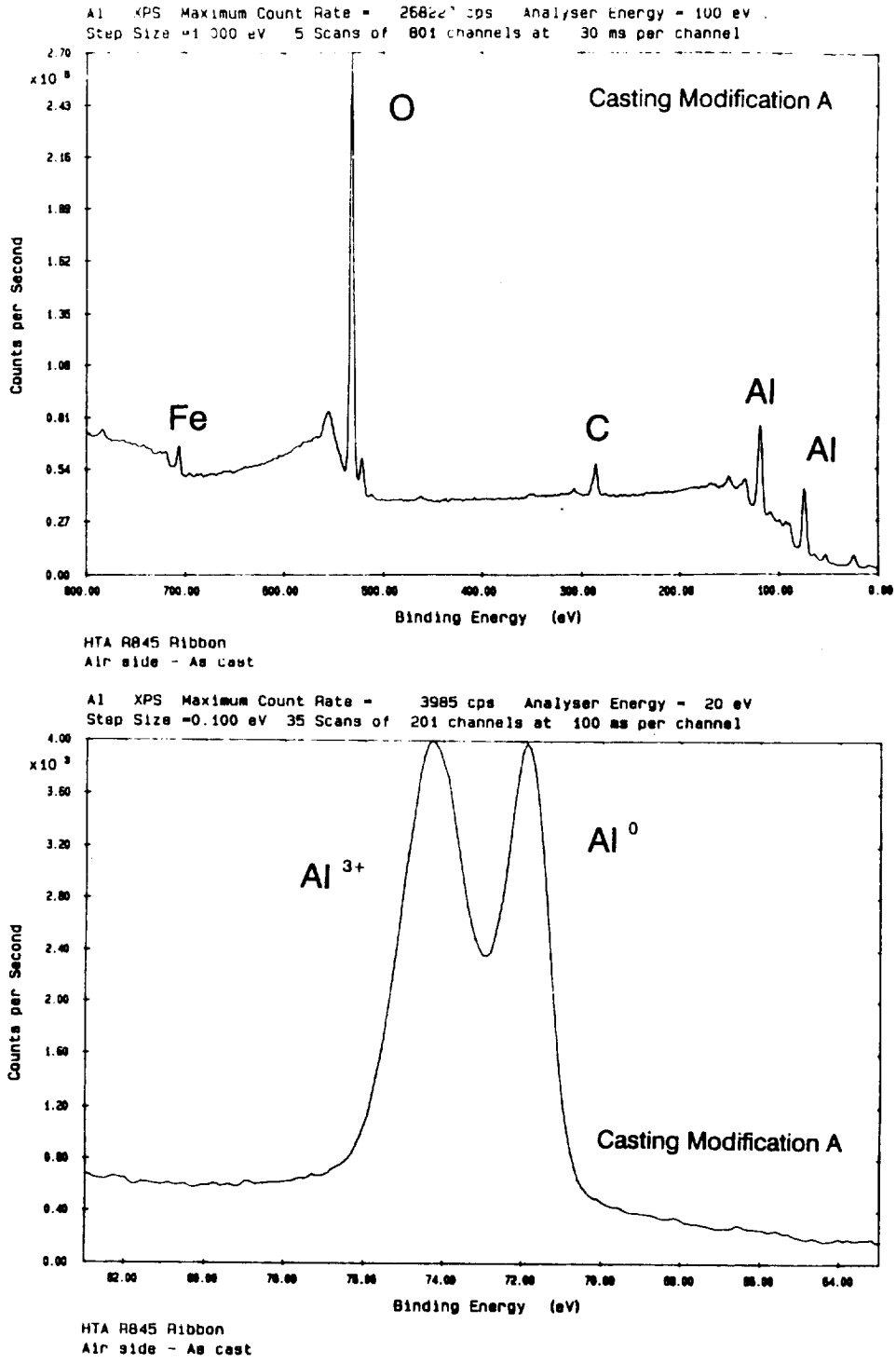

Fig. 8. (a) XPS survey scan of the air-side surface of as-cast modification A ribbon; (b) oxidic and metallic Al 2p peaks used to determine hydrate layer thickness.

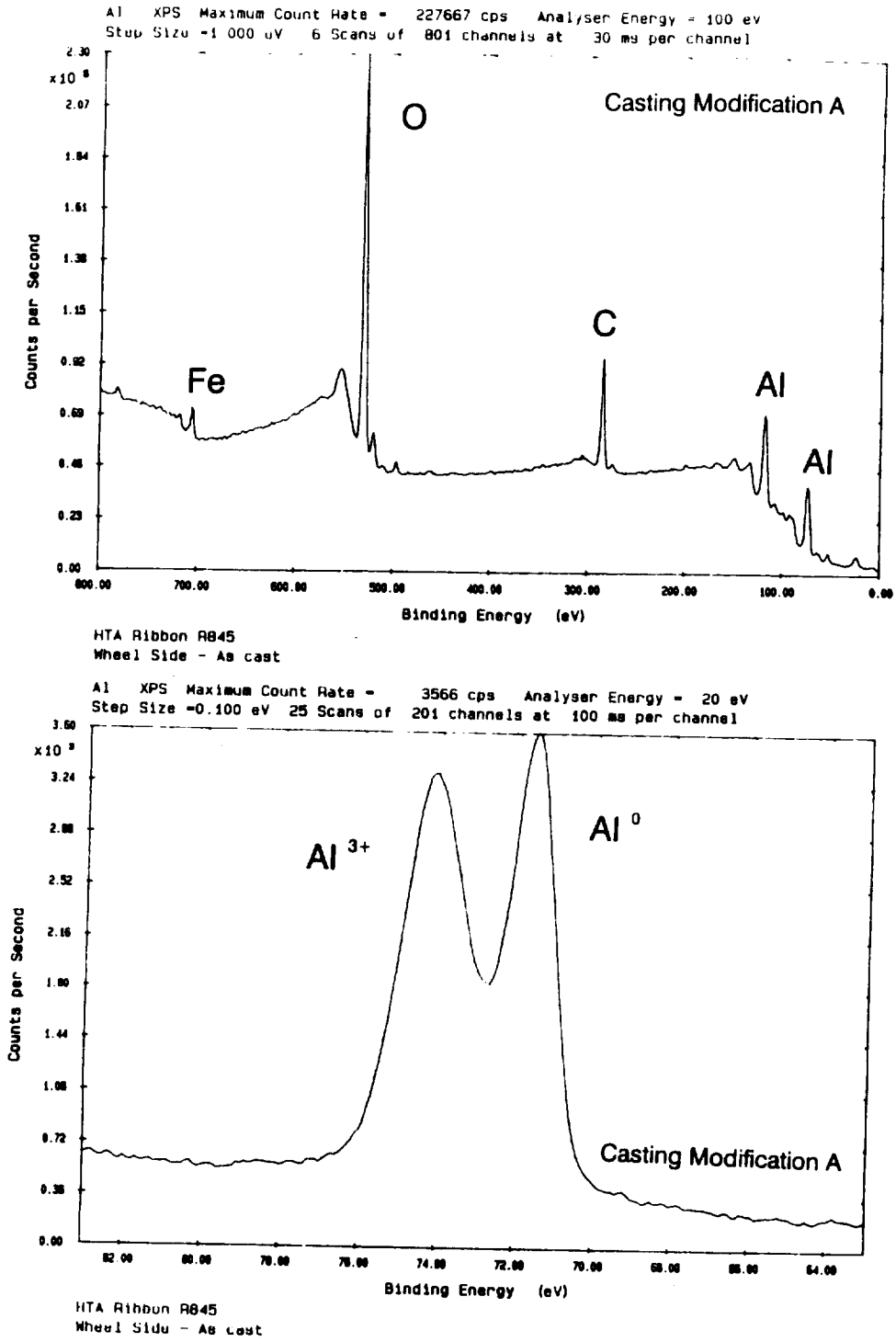

Fig. 9. (a) XPS survey scan of the wheel-side surface of as-cast modification A ribbon; (b) oxidic and metallic Al 2p peaks used to determine hydrate layer thickness.

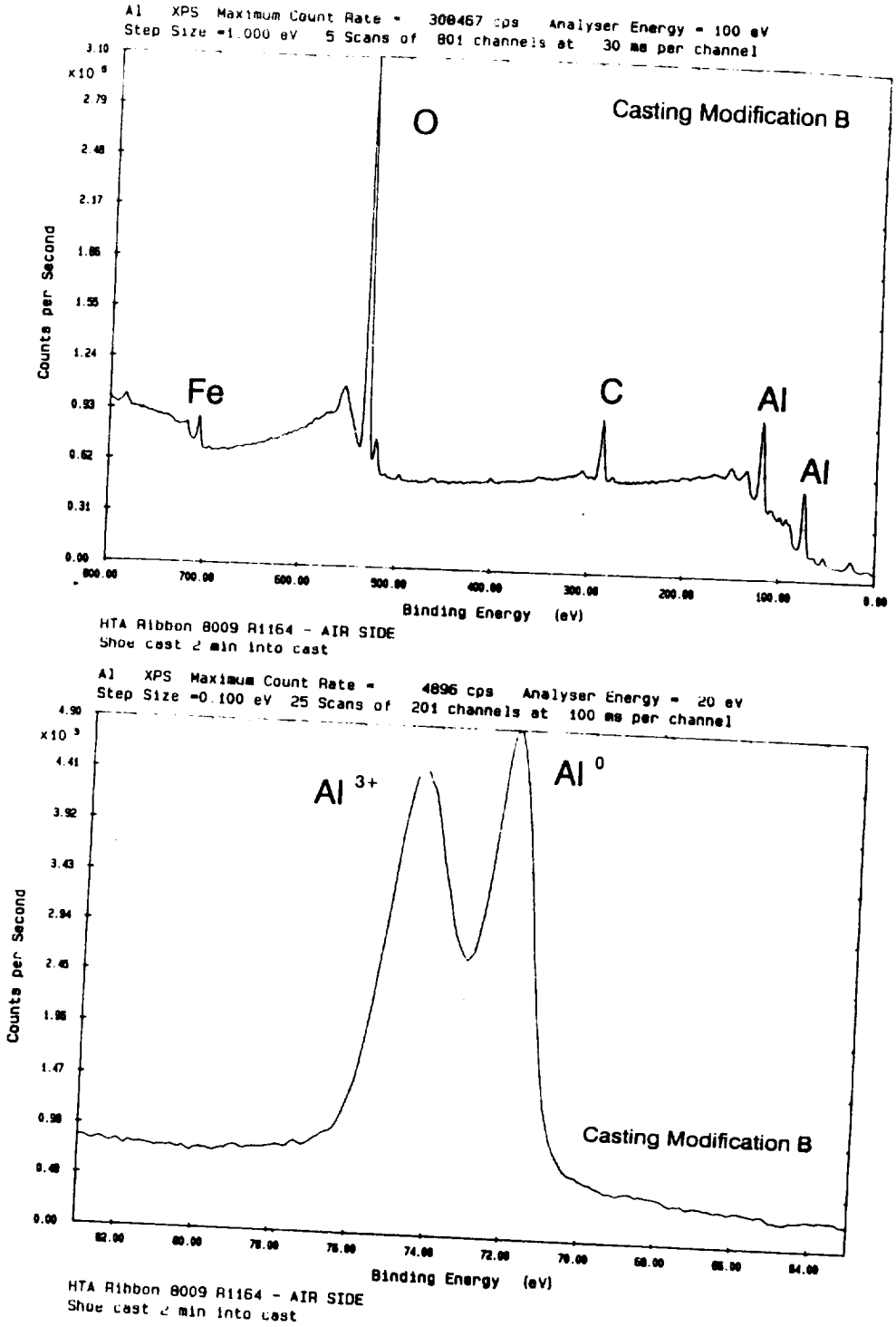

Fig. 10. (a) XPS survey scan of the air-side surface of as-cast modification B ribbon; (b) oxidic and metallic Al 2p peaks used to determine hydrate layer thickness.

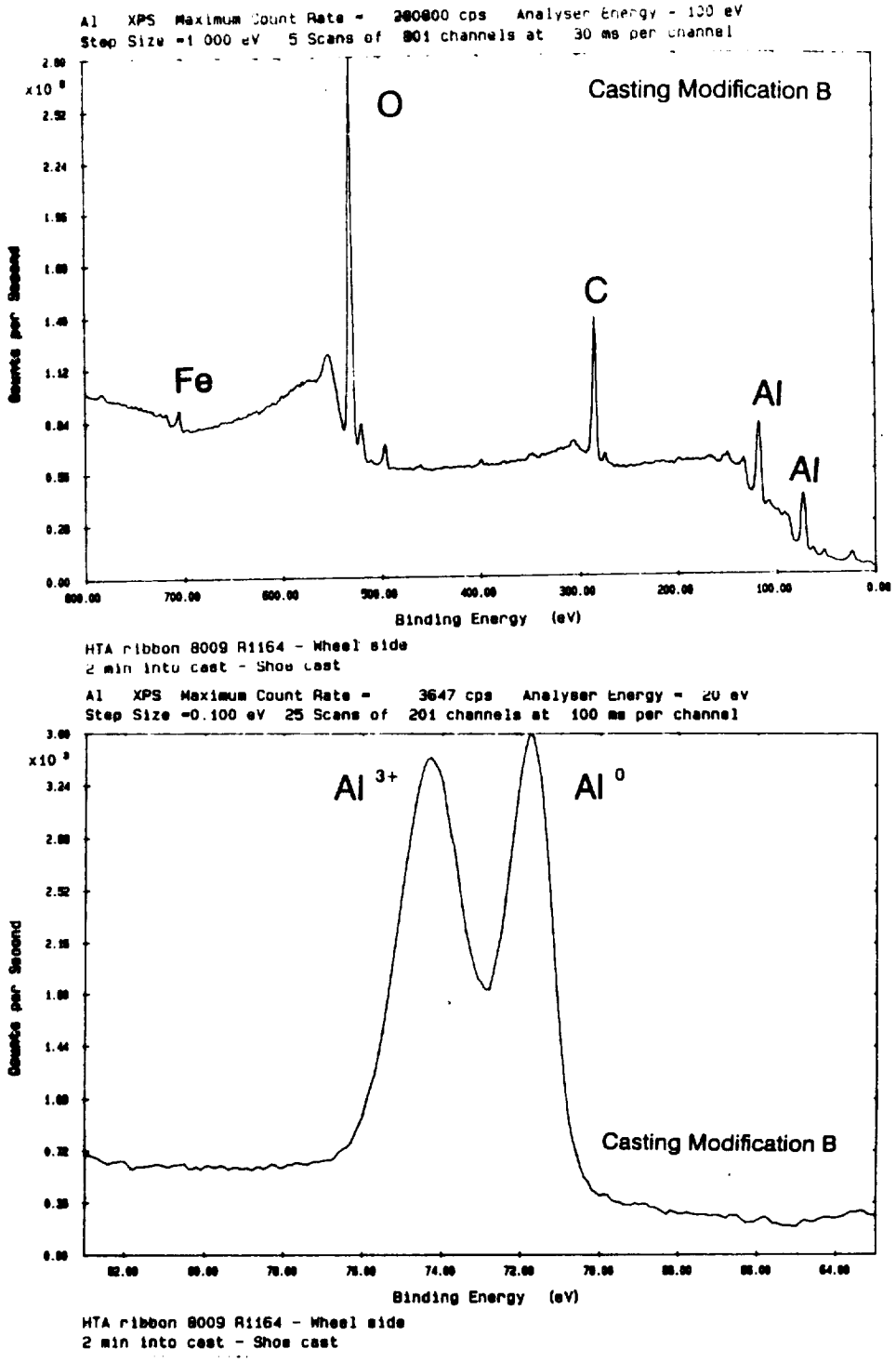

Fig. 11. (a) XPS survey scan of the wheel-side surface of as-cast modification B ribbon; (b) oxidic and metallic Al 2p peaks used to determine hydrate layer thickness.

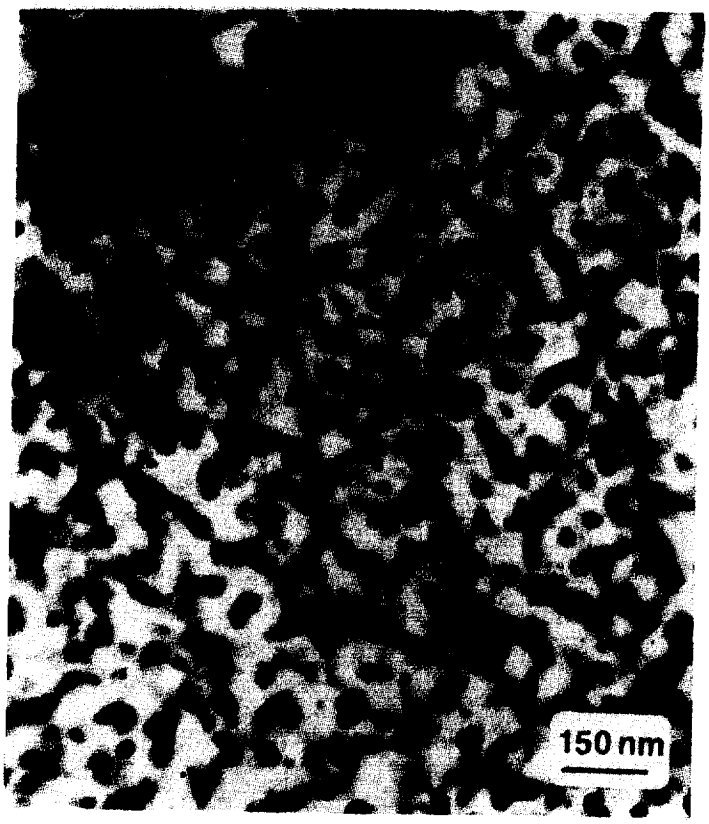

Figure 12. TEM micrograph of pfc HTA 8009 ribbon cast following modification A indicating a microcellular structure.

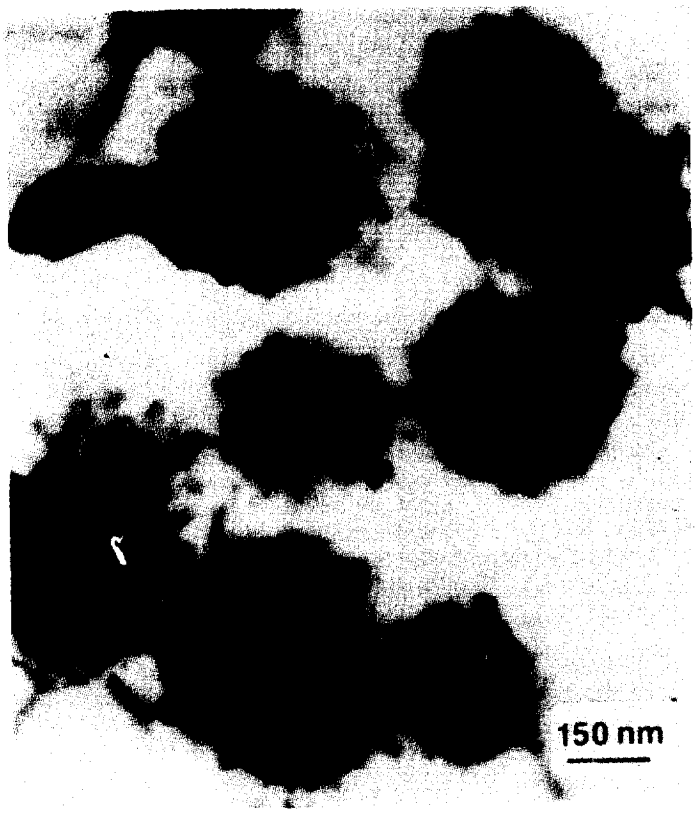

Figure 13. TEM micrograph of pfc HTA 8009 ribbon cast following modification B indicating coarse quasicrystalline icosahedral particles ("O" phase) in an Al-solid solution matrix.

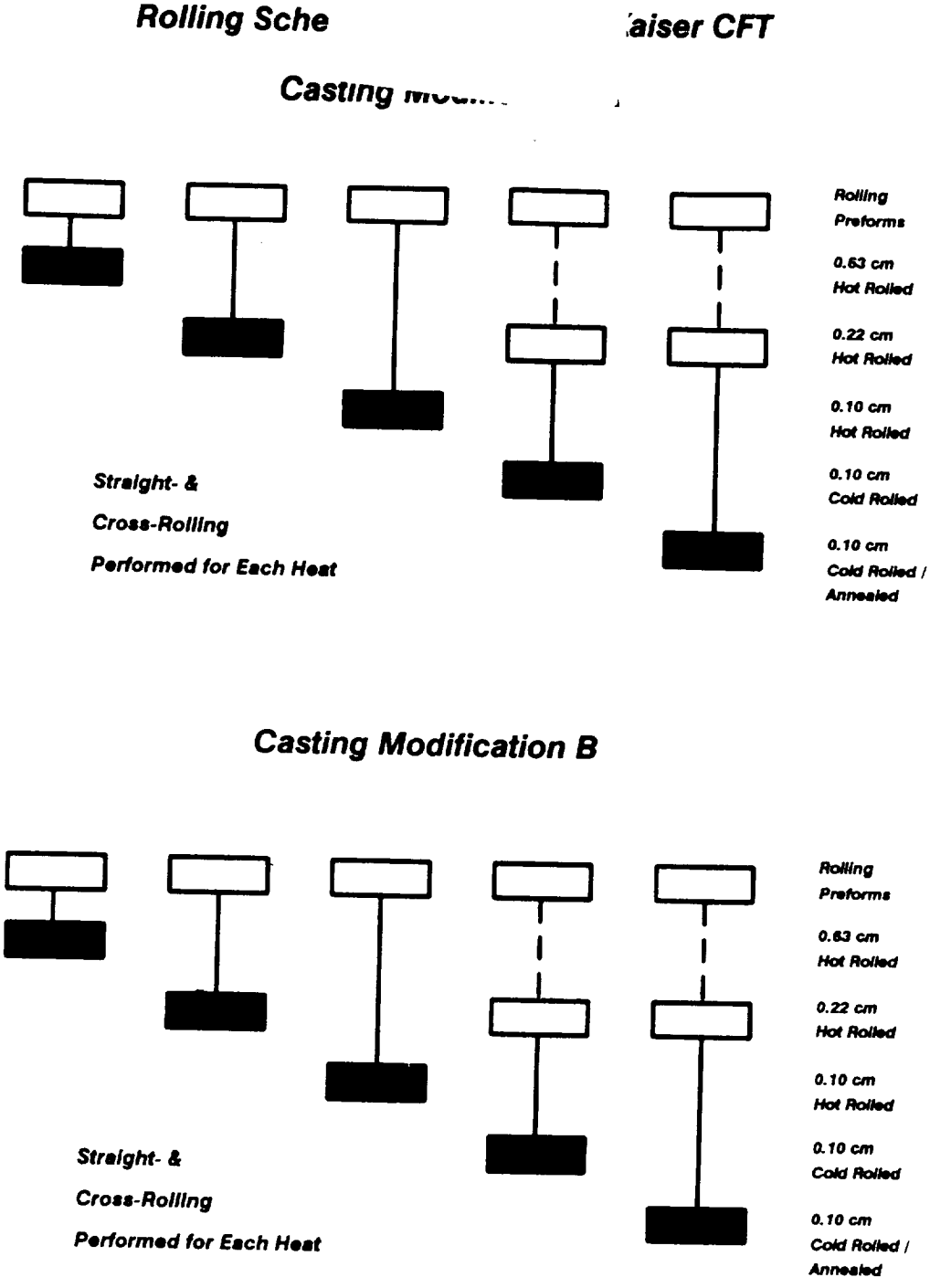

Figure 14. Pass schedules were designed to evaluate the effects of rolling direction and thermo-mechanical processing on ambient and elevated temperature mechanical properties of HTA 8009 plate and sheet.

Subtask 6B. Fracture Toughness Evaluations (UVa)

Principal Investigator: Dr. R.P. Gangloff
Research Associate: Dr. Sang-Shik Kim
Visiting Scholar: Professor Y.B. Xu

Progress During the Reporting Period. During the reporting period, fracture toughness experiments were conducted on various 8009 sheet and plate, either conventionally or inert-gas processed, and on Exxon DS Aluminum extrusion, including:

- 8009 sheet, autoclaved after conventional ribbon solidification, compaction and rolling to produce a low dissolved hydrogen content with no variation in oxide content.
- Conventionally processed HTA 8009 (preprogram vintage), hot and cold rolled to three different thicknesses of 6.3, 2.3 and 1.1 mm.
- Modified 6.3 mm thick 8009 plate; ribbon was melt spun in a dry inert gas atmosphere, then compacted according to conventional processes.
- Solute free, ultra-fine grain size dispersion strengthened aluminum, produced by cryogenic milling and extrusion compaction at Exxon Research and Engineering Co.

Nominal compositions and processing histories are summarized in Table 1.

Tensile tests were performed at UVa on 6.3 mm and 2.3 mm thick 8009, and Exxon DS Aluminum at various temperatures. Microstructures of the three gauges of conventionally cast HTA 8009 were examined by Phillips EM 400T transmission electron microscopy (TEM). Crack growth resistance was measured by R-curve procedures discussed elsewhere (3). Fracture surfaces were documented using a JEOL JSM-35 scanning electron microscope (SEM).

Microstructural Characterization. The microstructures of preprogram vintage HTA 8009[1] (Al-8.5Fe-1.3V-1.7Si) were characterized by TEM. This alloy was rapidly quenched from the melt into ribbons using the planar flow casting process. The ribbons were mechanically comminuted to an average powder particle size of 200 μm, and consolidated into bulk compacts by vacuum hot pressing followed by hot extrusion. Extruded product was hot or cold cross-rolled into plate or sheet with thicknesses of 6.3, 2.3 and 1.1 mm.

Figures 1, 2 and 3 show TEM micrographs of HTA 8009 in thicknesses of 6.3, 2.3 and 1.1 mm, respectively. Nearly spherical $Al_{12}(Fe,V)_3Si$ dispersoids (average size of 80 nm) are observed to be unaffected by the thermomechanical processing. Silicide particles are present within grains and at grain boundaries; clustered dispersoids are often observed. Selected area electron diffraction and convergent beam diffraction reveal that some of the silicide particles can have a specific orientation relationship with the surrounding aluminum matrix as follows:

$$\{110\}_{\text{Al-matrix}} \;//\; \{110\}_{\text{phase}}$$

$$\langle 111\rangle_{\text{Al-matrix}} \;//\; \langle 110\rangle_{\text{phase}}$$

High resolution Electron Microscope (HREM) studies indicate that an amorphous layer, about 5 nm in thickness, exists at the interface between silicide particles and the aluminum matrix, as shown in Fig. 4. The silicide lattice parameter was measured by electron diffraction to equal 1.211 nm and by x-ray diffraction to equal 1.256 nm. The latter value is more accurate. Subgrain size is approximately equal for the different thicknesses of HTA 8009, as illustrated in Figs. 5, 6 and 7. Average grain size ranges

[1]This material was processed by state-of-the-art procedures in 1992.

from 0.2 to 0.5 μm. Optical and SEM metallography is in progress to define oxide morphologies. Detailed microstructural characterizations are being conducted in Task 6A.

Tensile Experiments. Uniaxial tensile experiments were performed on 6.3 and 2.3 mm thick 8009, and on Exxon DS Aluminum, along the longitudinal direction and within the temperature range of 25 to 300°C. Tensile results are summarized in Tables 2 and 3 as a function of temperature for 8009 and DS Aluminum, respectively. The data indicate that both yield and ultimate tensile strengths decrease with increasing temperature for each material. Unlike conventional ingot metallurgy processed aluminum alloys,such as 2618, reduction of area decreases with increasing temperature. A "ductility minimum" is only observed for 2.3 mm thick 8009.

HTA 8009 thin foil specimens were taken within 2 mm of the tensile fracture surface and were characterized by TEM. Results are shown in Fig. 8 for experiments at: (a) 25°C and (b) 200°C. Notably, at room temperature, dislocations are mainly pinned by $Al_{12}(Fe,V)_3Si$ particles. At 200°C, however, dislocations are dominant along grain boundaries and do not show any sign of interaction with particles. Due to dislocation pile-ups along grain boundaries at elevated temperatures, grain boundary cracking is often observed, as illustrated in Fig. 9 for a specimen deformed at 200°C. The implications of these results on temperature-dependent fracture in 8009 will be considered during the next reporting period.

Fracture Toughness Experiments.

A. Experimental Method

Fracture toughness experiments were conducted both at Fracture Technology Associates (FTA), employing the ASTM-standard

unloading compliance method to define J-Δa[2], and at the University of Virginia (UVa), employing direct current electrical potential measurements of Δa and computed unloading compliance to determine J-integral values. Compact tension (CT) specimens were prepared with a width of 38.1 mm. CT specimens of 6.3 mm thick HTA 8009, modified HTA 8009 and Exxon DS Aluminum have a 6.3 mm gross thickness with sidegrooves of 19.8% of the gross specimen thickness (5.05 mm net thickness). CT specimens were prepared from HTA 8009 sheets with thicknesses of 2.3 and 1.1 mm, without sidegrooves. In order to understand the effect of specimen thickness on toughness, 2.3 mm thick CT specimens were machined without sidegrooves from the center portion of a 6.3 mm thick HTA plate. Tables 4 to 10 summarize the fracture toughness data obtained during this reporting period.

Considering Tables 4 to 9, J_i represents the initiation toughness which is determined by the first nonlinearity in direct current electric potential versus load line displacement data. Measurements illustrating such a nonlinearity in DCPD are shown in Fig. 10. As reported by Porr (3), this is a sensitive measure of the first stage of crack tip process zone damage, probably at the center of the specimen under plane strain constraint. J_{IC} is defined by the intersection of an arbitrarily offset (Δa = 0.2 mm) blunting line ($J = 2\sigma_{ys}\Delta a$) with the crack resistance curve, defined by either electric potential or unloading compliance. Plain strain fracture toughnesses (K_{IC} and K_{JIC}) are calculated from J_i and J_{IC}, respectively, according to:

$$K = (JE/1-\nu^2)^{1/2} \qquad (1)$$

---

[2]Δa is the increment of stable crack growth, ahead of the fatigue precrack, during increasing load.

where E is the elastic modulus and ν is Poisson's ratio. Tearing modulus, T_R, is determined from the slope of the applied J versus crack extension (Δa) relationship, according to:

$$T_R = (E/\sigma_o^2)(dJ/d\Delta a) \quad (2)$$

where σ_o is flow stress and $dJ/d\Delta a$ is the slope of the J-R curve determined by linear regression of Δa values from 0.15 to 1.5 mm. Figure 11 schematically illustrates the analysis of J_i and J_{IC} along with the crack tip morphology after the initiation of the crack between K_{IC} and K_{JIC}. Figure 12 illustrates the J-R curve determined from the data shown in Fig. 10.

All data presented in this study satisfy the J-controlled stable crack growth criterion:

$$\Delta a < 0.1\ (W-a) \quad (3)$$

where (W-a) is the uncracked ligament length. J-integral plane strain thickness requirements were satisfied for each alloy, temperature and thickness based on the approximate criterion:

$$\text{Thickness} \geq 25\ J/\sigma_o \quad (4)$$

B. Effect of Temperature

1. Conventionally Processed and Autoclaved 8009

Fracture toughness results for low hydrogen HTA 8009 are presented in Table 4 and are compared to the behavior of conventionally processed plate 8009 of 1989 vintage. The data in Table 4 were obtained by Porr (3). It is clear that the total dissolved hydrogen content of HTA 8009, in the range of 4 ppm for conventionally processed alloy and 1 ppm for the autoclaved materials, does not critically affect toughness.

2. Preprogram Vintage 8009: Conventionally Processed

The effects of temperature on the initiation fracture toughness (K_{IC} and K_{JIC}) of conventionally processed HTA 8009 plate, with thicknesses of 6.3, 2.3 and 1.1 mm, are shown in Figs. 13 through 18. The results in Figs. 16, 17, and 18 were obtained by FTA employing the unloading compliance method. These figures clearly establish that the initiation fracture toughness for HTA 8009 decreases with increasing temperature, regardless of product form and fatigue precrack orientation. Compared to the results for 8009 extrusion (3), HTA 8009 plate and sheet products exhibit a significantly reduced effect of precrack orientation on fracture toughness. For the fracture experiments at 25°C, some toughness anisotropy is observed; the TL orientation in cross rolled product is of higher toughness compared to the LT case for both 6.3 mm plate and 1.1 mm sheet. This is reasonable because the TL orientation for cross rolled plate and sheet involves crack initiation and growth in a direction perpendicular to the original extrusion direction. The important point is that both the LT and TL toughnesses are relatively high at 25°C for cross rolled 8009; the remaining anisotropy is measurable, but of secondary engineering importance compared to the behavior of extrusions (3). The alternate perspective is that additional processing may further increase the LT toughness of 8009 to very high levels. Porr (3) demonstrated isotropic toughness for 8 mm cross rolled plate of 8009. The difference between this result and the data in Figure 16 is not understood.

Figures 19 to 21 compare the toughness data obtained by UVa and FTA for HTA 8009 with three different thicknesses of 6.3, 2.3 and 1.1 mm, respectively. The toughness data from UVa and FTA are generally in good agreement, and equivalently demonstrate the deleterious effect of increasing test temperature for each product form of 8009. Given the definitions of K_{IC-UVA}, $K_{JIC-UVA}$, and $K_{JIC-FTA}$ (3), the expectations are that the latter two quantities should be equal for a given temperature and microstructure, and that K_{IC-UVA}

should be less than either of the latter two values. While such behavior is observed for the experiments at 175°C, $K_{JIC-FTA}$ is consistently less than K_{IC-UVA}. Since the compact tension specimens were machined from the same lots of 8009, the explanation for this behavior is most likely associated with subtle differences in experimental measurements and data analysis. An ASTM standard governs J-R curve determinations; however, experience to date has largely been with steels rather than ductile aluminum alloys. Work at UVa and FTA during the next reporting period will systematically examine methods of J analysis, the accuracy of crack length detection, the precise definition of the onset of crack initiation, and specimen gripping. Additionally, future work will report the complete K-Δa data set for each experiment; single values of K_{IC} and T_R may magnify interlaboratory variability. A workshop will be convened at NASA-LaRC to discuss issues associated with fracture toughness measurements for advanced aluminum alloys.

Figures 22 and 23 show the tearing modulus, which represents crack growth resistance, for HTA 8009 with various thicknesses and as a function of temperature obtained from UVa and FTA, respectively. T_R sharply decreases with increasing temperature to 175°C; at 300°C, however, an increase in T_R is observed. Additionally, considering 6.3 mm thick HTA 8009 plate at 25°C, two out of three specimens showed unstable crack growth after initiation; T_R approaches zero.

Figure 24 shows power law curve fits representing J-Δa data as a function of temperature for 6.3 mm thick HTA 8009. The effect of thickness on the R-curve is presented in Fig. 25 for HTA 8009 at 25°C. It is clear that the R-curve at 25°C is much higher than those observed at 175 and 300°C. The R-curves are similar for three different products of HTA 8009 at 25°C.

3. Modified-Process 8009

Figures 26 and 27 show the fracture toughness and tearing modulus, respectively, for modified 8009 plate as a function of temperature. This 8009 plate was produced from powder that was planar flow cast using a modified practice which involved inert gas shrouding of the melt puddle and ribbon exiting the casting wheel (Task 6A). Although this practice has been determined to be beneficial in reducing the hydrated oxide and hydride layer formed on the surface of the planar flow cast ribbon, modified HTA 8009 does not show any improvement of fracture toughness within the temperature range studied. Compared to the results for conventionally processed HTA 8009, modified HTA 8009 has a slightly reduced toughness and tearing modulus at room temperature. Additional experiments are required to test the recently produced plate and sheet of 8009.

4. Cryogenically Milled Aluminum

In order to understand the effect of dynamic strain aging on elevated temperature fracture toughness in HTA 8009, the fracture behavior of Exxon DS Aluminum was examined. This material consists of submicron aluminum grains, stabilized by about 5 volume percent of Al_2O_3 and AlN dispersoids, and presumably contains a low solute content. Fracture toughness and tearing modulus data for Exxon DS Aluminum are presented in Figs. 28 and 29, respectively. DS Aluminum shows a decrease in fracture toughness with increasing temperature, suggesting that metastable solute such as Fe, Si and V do not govern the temperature dependent fracture toughness of 8009.

5. Summary of Temperature Dependent Fracture Toughness

Initiation fracture toughness (K_{IC}) values for HTA 8009, from different process techniques and thicknesses, are plotted as a function of temperature in Fig. 30 along with 8009 extrusion, Al/SiC_p composite and ingot metallurgy wrought 2618-T851 data that

were previously measured at UVa (3,13).

C. Effect of Displacement Rate/Crack Tip Strain Rate

The effects of displacement rate on the initiation and growth fracture toughnesses were examined for 6.3 mm thick 8009 plate at 25 and 175°C. Initiation toughness results are presented in Figs. 31 and 32. Tearing moduli for 6.3 mm thick HTA 8009 as a function of displacement rate at 25°C and 175°C, respectively, are shown in Figs. 33 and 34. At both temperatures, fracture toughnesses decrease with decreasing displacement rate. It also appears that the critical displacement rate for the rapid decrease in fracture toughness depends on the testing temperature. Although limited, the data indicate that the fracture toughness of Exxon DS Aluminum also decreases with decreasing displacement rate at 25°C.

D. Effect of Specimen Thickness

In order to understand the effect of specimen thickness on toughness, 2.3 mm CT specimens were machined from the center portion of 6.3 mm thick HTA 8009 without sidegrooves. The results of fracture toughness experiments are presented in Figs. 35 and 36, along with the data for 6.3 mm thick HTA 8009 plate with sidegrooves. Despite the significantly reduced CT specimen thicknesses, similar K_{JIC} values are obtained at 25 and 175°C, consistent with the very small requirement for thickness-independent J_{IC}. Tearing modulus, however, increases with decreasing specimen thickness, as illustrated in Figs. 37 and 38.

E. SEM Fractography

Figure 39 shows low magnification SEM fractography of 6.3 mm thick 8009 plate for experiments at: (a) 25°C, (b) 175°C and (c) 300°C. Unlike extruded 8009 which shows significant delaminations at 25 and 300°C (3), HTA 8009 plate does not exhibit delaminations within the temperature range studied. At 300°C, however, some delaminations occurred. Thinner HTA 8009 sheet products do not

show noticeable delaminations, regardless of test conditions.

Figures 40 to 44 show SEM fractographic results for HTA 8009 tested with various thicknesses, displacement rates and fracture temperatures. The fracture surface for Exxon DS Aluminum is shown in Fig. 45. Regardless of product form and test conditions, HTA 8009 fails by what appears to be microvoid coalescence. At 25°C, the fracture surface for HTA 8009 is covered with spherical dimples with the size ranging from 2 to 5 μm. At 175°C, a uniform size distribution of shallow voids is observed and the average void diameter appears to decrease from 4 to 1 μm with decreasing gauge thickness from 6.3 to 1.1 mm. Notably, slowly deformed HTA 8009 at 25°C has a fracture surface similar to the specimen deformed at high temperature. The fracture surface appearance of Exxon DS Aluminum shows fine microvoid coalescence, without exhibiting notable change in morphology with increasing temperatures. Detailed SEM studies are in progress at UVa.

Conclusions. Several conclusions are drawn based on the experiments conducted during this reporting period.

- TEM shows that subgrain size, silicide particle size, and particle distribution in 8009 are unaffected by thermomechanical processing from rolled plate to sheet.
- Selected area electron diffraction and convergent beam diffraction indicate that silicide particles have a specific orientation relationship with the surrounding aluminum matrix:

$$\{110\}_{\text{Al-matrix}} \;//\; \{110\}_{\text{phase}}$$

$$\langle 111\rangle_{\text{Al-matrix}} \;//\; \langle 110\rangle_{\text{phase}}$$

- HREM studies indicate that a 5 nm thick amorphous layer exists at the interface between silicide particles and the aluminum matrix.
- Both yield strength and ultimate tensile strength for HTA

8009 and Exxon DS Aluminum decrease with increasing temperature. Tensile ductility (% RA) decreases with increasing temperature; only 6.3 mm thick 8009 shows a ductility minimum at 175°C

- TEM studies on HTA 8009, tensile deformed at 25 and 200°C, indicate that a particle-dislocation interaction transition occurs with increasing temperature. At 25°C, dislocation motion is hindered by $Al_{12}(Fe,V)_3Si$ particles. At 200°C, however, dislocations accumulate at grain boundaries, indicating a loss of particle-dislocation interaction, and promote boundary cracking.
- The initiation fracture toughness (K_{IC} and K_{JIC}) of conventionally processed HTA 8009 decreases with increasing temperature, regardless of product form and fatigue precrack orientation. Notably, the intermediate temperature toughness reduction occurs in both 1.1 mm and 2.3 mm thick rolled sheet, analogous to the well-established behavior of thicker plate and extrusion of 8009. The decrease in fracture toughness, however, is negligible after 175°C and a minimum in K_{IC} is never observed.
- The tearing modulus, T_R decreases with increasing temperature, exhibiting a minima at 175°C, regardless of product form and process condition. Unlike the initiation fracture toughness, T_R shows a significant increase with increasing temperature above 175°C perhaps due in part to delamination.
- Compared to the results for 8009 extrusion, HTA 8009 plate and sheet products exhibit a significantly reduced effect of precrack orientation on fracture toughness. The toughness anisotropy problem for extruded 8009 is largely eliminated by rolling to plate and sheet. Residual anisotropy may be removed by additional processing.
- The total dissolved hydrogen content of HTA 8009, in the range of 4 ppm for conventionally processed alloy and 1 ppm

for autoclaved and inert gas cast materials, has no effect on fracture toughness and does not explain the reduction in K_{IC} with increasing temperature. This result is consistent with previous experiments which demonstrated a lack of moist air-reaction produced or process-dissolved hydrogen embrittlement of 8009.

- Limited experiments indicate that the fracture toughness of modified 8009 plate, involving ribbon melt spun in an inert gas atmosphere, decreases significantly with increasing temperature, exhibiting the similar toughness trend as conventionally processed HTA 8009 plate. At 25°C, the fracture toughness modified HTA 8009 is slightly lower than that of conventional HTA 8009.
- Both K_{IC} and tearing modulus increase significantly with increasing displacement rate for 6.3 mm thick HTA 8009 at both 25 and 175°C. The critical displacement rate for rapid degradation of fracture toughness appears to increase with increasing temperature.
- The initiation fracture toughness of solute-free, ultra-fine grain size Exxon DS Aluminum decreases with increasing temperature up to 250°C, without exhibiting toughness minimum. Tearing modulus decreases sharply with increasing temperature. The decrease in fracture toughness of this low solute alloy indicates that dynamic strain aging does not necessarily play the principal role in "intermediate temperature embrittlement".
- The fracture toughness results from UVa and FTA are generally in good agreement, and equivalently demonstrate the deleterious effect of increasing test temperature for each product form of 8009. Differences in electrical potential J_i and J_{IC} from the arbitrarily offset blunting line can be significant, and further test development work is required.
- Considering initiation toughness at both 25°C and 175°C, similar K_{IC} and K_{JIC} values are obtained for significantly

varying compact tension specimen thickness, consistent with the small requirement for thickness-independent J-integral toughness. Tearing modulus increases with decreasing specimen thickness, at least for tougher 8009 at 25°C.

- Unlike extruded 8009 which delaminates significantly at 25 and 300°C, HTA 8009 plate and sheet products do not exhibit significant delamination. At 300°C, 6.3 mm thick plate exhibits some delamination.
- Regardless of product form and test conditions, HTA 8009 apparently fails by microvoid coalescence. The size and distribution of voids, however, exhibit complex dependencies on temperature, displacement rate and gauge thickness.

Current and Potential Problem Areas. None

References.

1. W.M. Griffith, R.E. Sanders, Jr. and G.J. Hildeman, in *High Strength Powder Metallurgy Aluminum Alloys*, eds. M.J. Koczak and G.J. Hildeman, TMS-AIME, Warrendale, PA (1982), pp. 209-224.

2. S.L. Langenbeck et al., in *Rapidly Solidified Powder Aluminum Alloys, ASTM STP 890*, eds. M.E. Fine and E.A. Starke, Jr., ASTM, Philadelphia, PA (1986), pp. 410-422.

3. W.C. Porr, Jr., "Elevated Temperature Fracture of Advanced Powder Metallurgy Aluminum Alloy 8009", PhD Dissertation, University of Virginia (1992).

4. W.C. Porr, Jr., Y. Leng and R.P. Gangloff, in *Low Density, High Temperature P/M Alloys*, eds. W.E. Frazier, M.J. Koczak and P.W. Lee, TMS-AIME, Warrendale, PA (1991), pp. 129-156.

5. Y. Leng, W.C. Porr, Jr. and R.P. Gangloff, "Time Dependent Crack Growth in P/M Al-Fe-V-Si at Elevated Temperatures," *Scripta Met. Mater. 25* (1991), pp. 895-900.

6. W.C. Porr, Jr., A.P. Reynolds, Y. Leng and R.P. Gangloff, "Elevated Temperature Cracking of RSP Aluminum-Alloy 8009 - Characterization of the Environmental Influence," *Scripta Met. Mater. 25* (1991), pp. 2627-2632.

7. D.J. Skinner, M.S. Zedalis and P. Gilman, "Effect of Strain Rate on Tensile Ductility for a Series of Dispersion-Strengthened Aluminium-Based Alloys," *Mat. Sci. and Engr., A119* (1989), pp. 81-86.

8. D.J. Skinner, M.S. Zedalis and J. Peltier, in *Light Weight Alloys for Aerospace Applications*, eds. E.W. Lee, E.H. Chia and N.J. Kim, TMS-AIME, Warrendale, PA, pp. 71-78 (1989).

9. D.J. Skinner, R.L. Bye, D. Raybould and A.M. Brown, "Dispersion Strengthened Al-Fe-V-Si Alloys," *Scripta Met. 20* (1986), pp. 867-872.

10. H. Westengen, in *Strength of Metals and Alloys*, ed. R.C. Gifkins, ICSMA 6, Melbourne, Australia (1982), pp. 461-466.

11. J.A. Hawk, P.K. Mirchandani, R.C. Benn and H.G.F. Wilsdorf, in *Dispersion Strengthened Aluminum Alloys*, eds. Y.W. Kim and W.M. Griffith, TMS, Warrendale, PA (1988), pp. 517-537.

12. R.P. Gangloff, E.A. Starke, Jr., J.M. Howe and F.E. Wawner, Jr., "Aluminum Based Materials for High Speed Aircraft", University of Virginia, Proposal No. MS-NASA/LaRC-5215-92, October (1991).

13. B.P. Somerday, Yang Leng, F.E. Wawner and R.P. Gangloff, "Elevated Temperature Fracture Toughness of a SiC Particulate Reinforced 2009 Aluminum Composite", in *Advanced Metal Matrix Composites for Elevated Temperatures*, ed. M.N. Gungor, ASM International, Metals Park, Ohio, pp. 167-182 (1992).

Table 1
Chemical Compositions and Processing Details for the Materials Studied.

Alloy	Chemical Composition (wt.%)	Thick. (mm)	Processing Details
Al 8009	Al-8.5Fe-1.3V-1.7Si	6.3	Autoclaved after solidification, compaction and rolling
Al 8009* (90A438-B)	"	6.3	Standard planar flow casting, hot cross rolled
Al 8009* (90A677-1S)	"	2.3	Standard planar flow casting, cold cross rolled
Al 8009* (91A693-1A)	"	1.1	Standard planar flow casting, cold cross rolled
Al 8009 (92A024-1C)	"	6.3	Melt spun ribbon in dry inert gas, hot cross rolled
Exxon DS Aluminum	High purity Al + 3 wt.% Al_2O_3	6.3	Cryogenic milling for 5 hrs at -196°C and extrusion compaction at 460°C

* Preprogram vintage

Table 2
Tensile Properties of 6.3 and 2.3 mm Thick HTA 8009 as a Function of Temperature.*

Thick. (mm)	Temp. (°C)	Orient.	Str.Rate+ (/sec)	Y.S (MPa)	U.T.S (MPa)	R.A. (%)
2.3	25	L	$5x10^{-4}$	478	490	43.9
2.3	175	L	$5x10^{-4}$	345	350	24.9
2.3	300	L	$5x10^{-4}$	189	200	36
6.3	25	L	$3.2x10^{-4}$	410	450	49.4
6.3	175	L	$3.2x10^{-4}$	370	410	42
6.3	300	L	$3.2x10^{-4}$	300	320	37.3

* Data obtained by UVa.
+ Strain rate = v/L_o where v is cross head speed and L_o is gauge length.

Table 3
Tensile Properties of Exxon DS Aluminum as a Function of Temperature.*

Temp. (°C)	Orient.	Str.Rate+ (/sec)	Y.S (MPa)	U.T.S (MPa)	R.A. (%)
25	L	$5x10^{-4}$	260	274	34.4
175	L	$5x10^{-4}$	230	240	15.6
250	L	$5x10^{-4}$	200	210	15.0

* Data obtained by UVa.
+ Strain rate = v/L_o where v is cross head speed and L_o is gauge length.

Table 4

Fracture Toughness of 6 mm Thick HTA 8009 (1991 Vintage), Conventionally Processed and Autoclaved, as a Function of Temperature.*

Temp. (°C)	Orientation	J_i (kN/m^2)	K_{IC} (MPa$\sqrt{m}$)	T_R
25	LT	8.3	27.9	5.3
25	LT	9.0	29.0	8.3
25	LT	7.3[a]	26.1[a]	7.4[a]
25	LT	8.2[b]	27.7[b]	17.7[b]
25	LT Low H[c]	13.8	36.0	0.0
25	TL	7.5	26.5	6.8
175	LT	1.3	10.0	1.8
175	LT	1.3	10.2	1.3
175	LT	1.7[b]	11.5[b]	1.5[b]
175	LT Low H[c]	2.0	12.5	4.6
175	TL	1.3	10.1	1.4
316	LT	1.0	8.2	5.7
316	LT Low H[c]	1.2	9.1	4.3
316	TL	1.1	8.7	2.8

* Data obtained by UVa.

+ Fracture toughness tests were conducted with CT specimens with sidegrooves (net thickness = 5 mm), if not specified.

a Heat treated at 175°C for 100 hours prior to testing.

b No sidegrooves.

c Total dissolved hydrogen content estimated to equal 1 ppm.

Table 5

Fracture Toughness of 6.3 mm Thick HTA 8009 (90A438-B) as a Function of Temperature and Displacement Rate.*

Temp. (°C)	Gross Thick. (mm)	Net Thick. (mm)	Disp. Rate+ (mm/sec)	J_i (kJ/m^2)	J_{IC} (kJ/m^2)	K_{IC} (MPa$\sqrt{m}$)	K_{JIC} (MPa$\sqrt{m}$)	dJ/da (MPa)	T_R
25	6.3	5.06	$2.54x10^{-3}$	15.9	-#	38.3	-	-	-
25	6.3	5.06	$2.54x10^{-3}$	9.7	-#	29.9	-	-	-
25	6.3	5.06	$2.54x10^{-3}$	15.2	40	37.4	60.7	39.7	19.4
25	6.3	5.06	$5.08x10^{-6}$	2.5	7.5	15.2	26.3	8.2	4.0
25	6.3	5.06	$2.54x10^{-2}$	19.9	35.5	42.8	57.2	51	24.9
175	6.3	5.06	$2.54x10^{-3}$	1.2	2.7	9.6	14.4	4.9	2.2
175	6.3	5.06	$5.08x10^{-6}$	0.22	0.52	4.1	6.3	0.44	0.2
175	6.3	5.06	$5.08x10^{-6}$	0.58	-	6.7	-	0.7	0.4
175	6.3	5.06	$2.54x10^{-2}$	3.0	7.5	15.2	24.1	10.1	4.6
300	6.3	5.06	$2.54x10^{-3}$	0.8	2.2	7.7	12.6	6.3	4.2
25	2.3	2.3	$2.54x10^{-3}$	7.0	40.5	25.4	61	72.5	35.4
175	2.3	2.3	$2.54x10^{-3}$	1.5	6.2	10.7	21.9	12.8	6.5

* Data obtained by UVa.

+ Displacement rate = actuator speed.

Table 6

Fracture Toughness of 2.3 mm Thick HTA 8009 (90A677-1S) as a Function of Temperature.*

Temp. (°C)	Thick (mm)	Disp. Rate (mm/sec)	J_i (kJ/m^2)	J_{IC} (kJ/m^2)	K_{IC} (MPa$\sqrt{m}$)	K_{JIC} (MPa$\sqrt{m}$)	dJ/da (MPa)	T_R
25	2.3	$2.54x10^{-3}$	4.3	27	20	49.8	62.7	21.9
25	2.3	$2.54x10^{-3}$	3.2	30	17.2	52.5		
175	2.3	$2.54x10^{-3}$	0.38	2.0	5.4	12.4	6.1	3.5
175	2.3	$2.54x10^{-3}$	0.2	1.5	3.9	10.8	7.6	4.4
300	2.3	$2.54x10^{-3}$	0.51	2.1	6.1	12.3	11.5	19.5

* Data obtained by UVa.

Table 7

Fracture Toughness of 1.1 mm Thick HTA 8009 (91A693-1A) as a Function of Temperature.*

Temp. (°C)	Thick (mm)	Disp. Rate (mm/sec)	J_i (KJ/m^2)	J_{IC} (KJ/m^2)	K_{IC} (MPa$\sqrt{m}$)	K_{JIC} (MPa$\sqrt{m}$)	dJ/da (MPa)	T_R
25	1.1	$2.54x10^{-3}$	4.04	36.4	19.3	57.9	81.9	29.4
175	1.1	$2.54x10^{-3}$	0.38	1.7	5.4	11.5	8.04	4.7
300	1.1	$2.54x10^{-3}$	0.51	1.7	6.1	11.2	8.2	14.7

* Data obtained by UVa.

Table 8

Fracture Toughness of Exxon DS Aluminum as a Function of Temperature and Displacement Rate.*

Temp. (°C)	Thick (mm)	Disp. Rate (mm/sec)	J_i (kJ/m^2)	J_{IC} (kJ/m^2)	K_{IC} (MPa$\sqrt{m}$)	K_{JIC} (MPa$\sqrt{m}$)	dJ/da (MPa)	T_R
25	6.3	2.54×10^{-3}	3.0	7.5	13.6	24.1	22.8	22.1
25	6.3	5.08×10^{-6}	1.6	2.7	11.0	14.5	4.6	4.7
80	6.3	2.54×10^{-3}	2.2	5	12.7	19.1	13.7	14.5
125	6.3	2.54×10^{-3}	1.3	2.9	9.5	14.3	5.6	6.1
175	6.3	2.54×10^{-3}	0.75	1.5	7.1	10.0	3.0	3.3
215	6.3	2.54×10^{-3}	0.65	1.1	6.5	8.4	1.4	1.64
250	6.3	2.54×10^{-3}	0.48	0.93	5.0	6.9	1.1	1.25

* Data obtained by UVa.

Table 9

Fracture Toughness of Modified 6.3 mm Thick HTA 8009 (92A024-1C) as a Function of Temperature.*

Temp. (°C)	Thick (mm)	Disp. Rate (mm/sec)	J_i (KJ/m^2)	J_{IC} (KJ/m^2)	K_{IC} ($MPa\sqrt{m}$)	K_{JIC} ($MPa\sqrt{m}$)	dJ/da (MPa)	T_R
25	6.3	2.54×10^{-3}	13.5	24.1	35.2	47.1	18.1	8.8
175	6.3	2.54×10^{-3}	1.5	4.5	10.8	18.7	5.6	2.8
300	6.3	2.54×10^{-3}	0.8	3.5	7.6	15.9	7.3	5.2

* Data obtained by UVa.

Table 10
Fracture Toughness of HTA 8009 as a Function of Temperature and Orientation.*

Temp. (°C)	Thick. (mm)	Orient.	Disp. Rate (mm/sec)	J_{IC} (kJ/m^2)	K_{JIC} (MPa$\sqrt{m}$)	T_R
25	6.3[1]	LT	$2.54x10^{-3}$	9.5	28.1	-
25	6.3	TL	$2.54x10^{-3}$	19.3	40.2	41.3
25	2.3[2]	LT	$2.54x10^{-3}$	12.4	32.2	30.7
25	1.1[3]	LT	$2.54x10^{-3}$	15.8	36.3	20.2
25	1.1	TL	$2.54x10^{-3}$	39.8	57.7	14.1
175	6.3	LT	$2.54x10^{-3}$	2.7	13.5	3.0
175	6.3	TL	$2.54x10^{-3}$	3.0	14.4	3.6
175	2.3	LT	$2.54x10^{-3}$	2.3	12.6	3.4
175	2.3	TL	$2.54x10^{-3}$	1.6	10.7	2.9
175	1.1	LT	$2.54x10^{-3}$	4.1	16.8	2.7
175	1.1	TL	$2.54x10^{-3}$	3.9	16.5	2.1

* Data obtained by FTA.
1 90A438-B
2 90A677-1S
3 91A693-1A

Fig. 1. TEM micrograph of 6.3 mm thick HTA 8009.

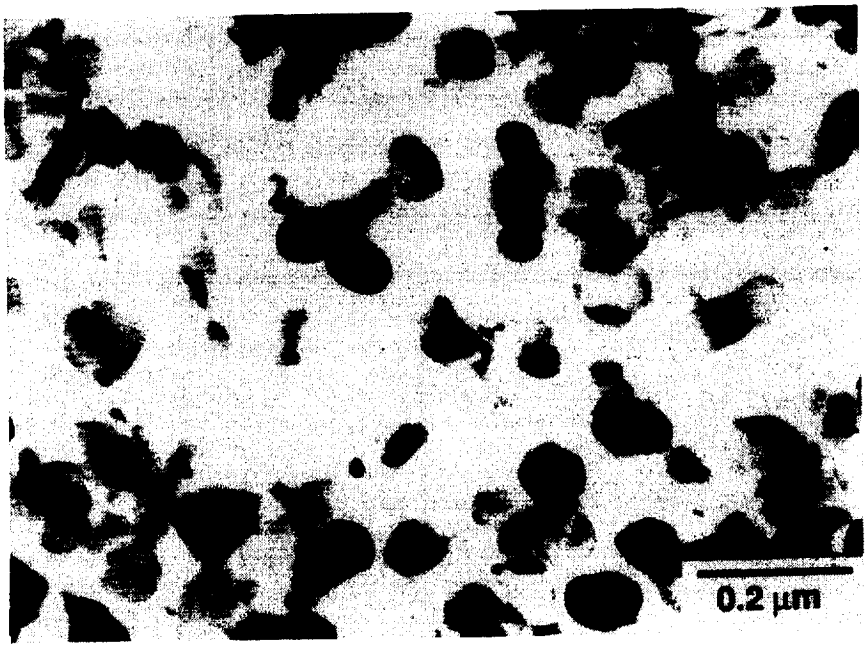

Fig. 2. TEM micrograph of 2.3 mm thick HTA 8009.

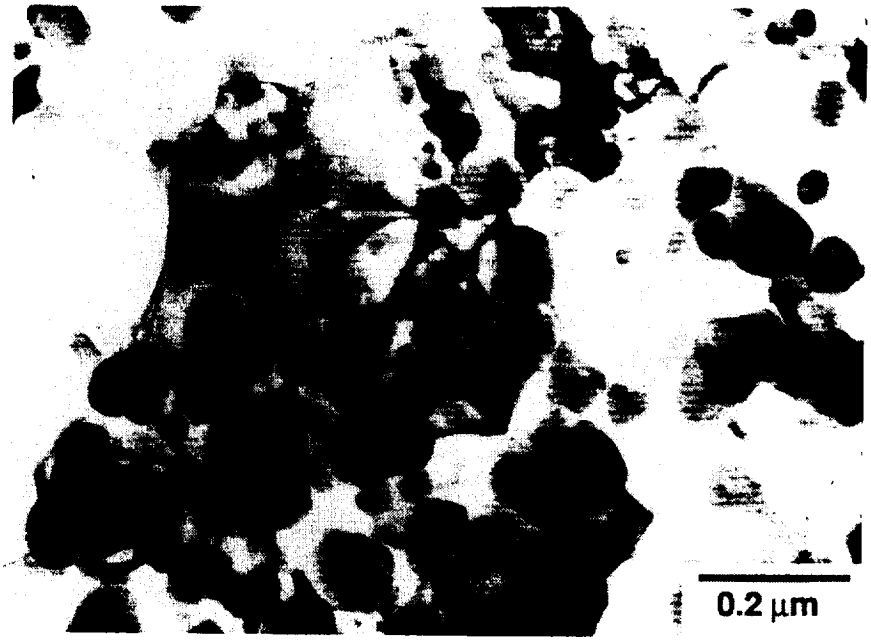

Fig. 3. TEM micrograph of 1.1 mm thick HTA 8009.

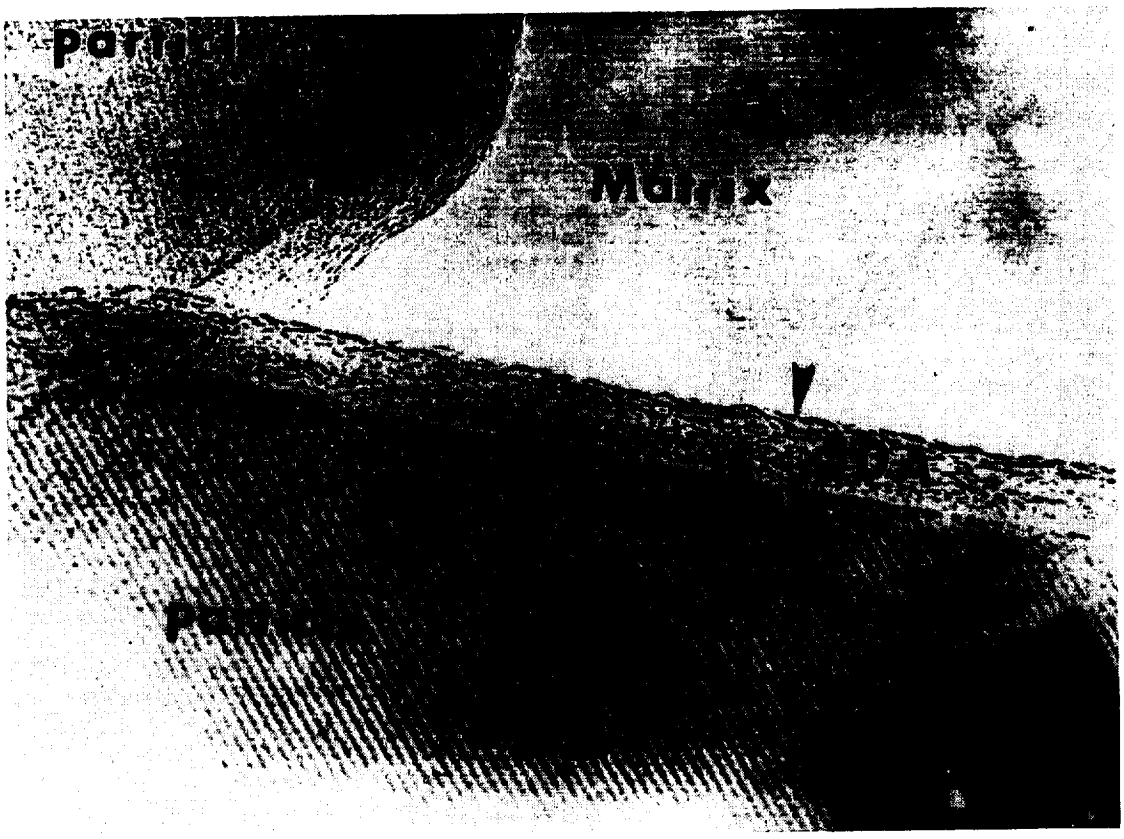

Fig. 4. HREM micrograph of 6.3 mm thick HTA 8009.

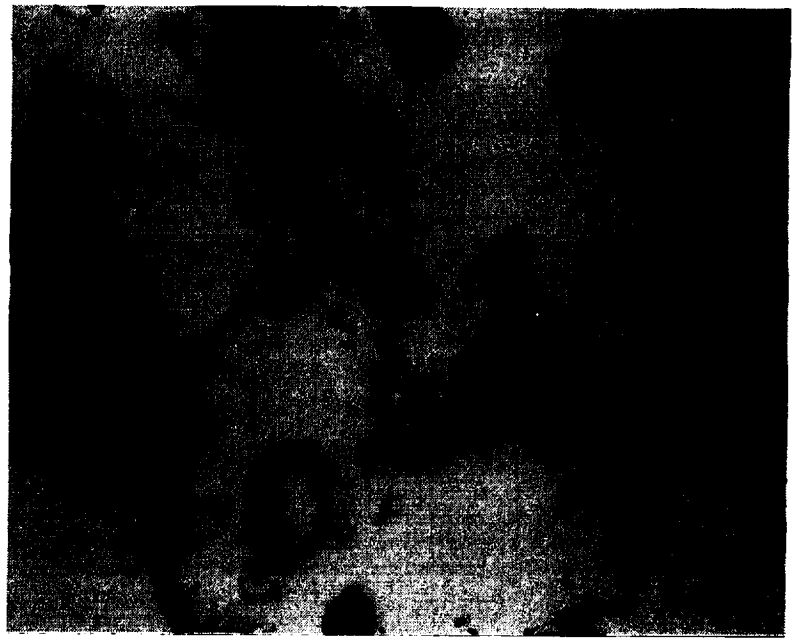

Fig. 5. TEM micrograph of 6.3 mm thick HTA 8009.

Fig. 6. TEM micrograph of 2.3 mm thick HTA 8009.

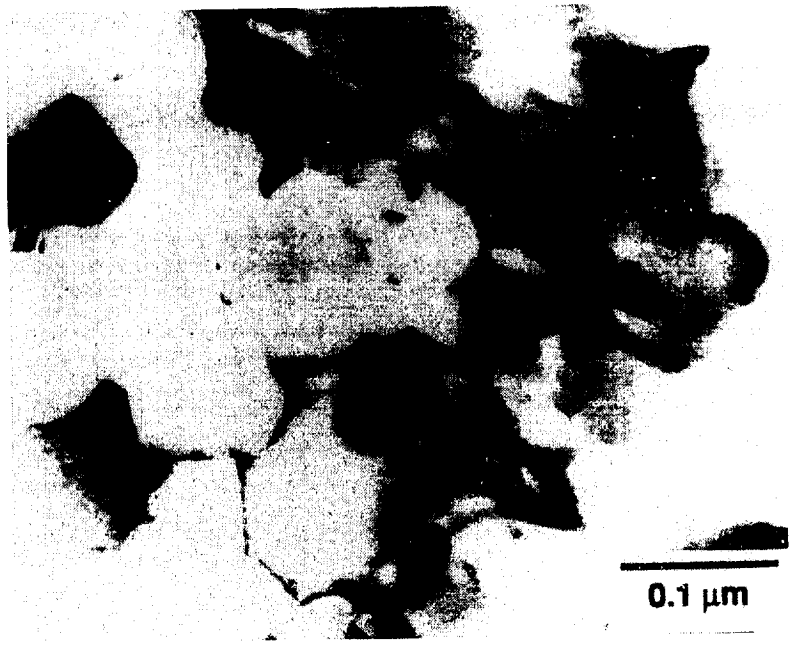

Fig. 7. TEM micrograph of 1.1 mm thick HTA 8009.

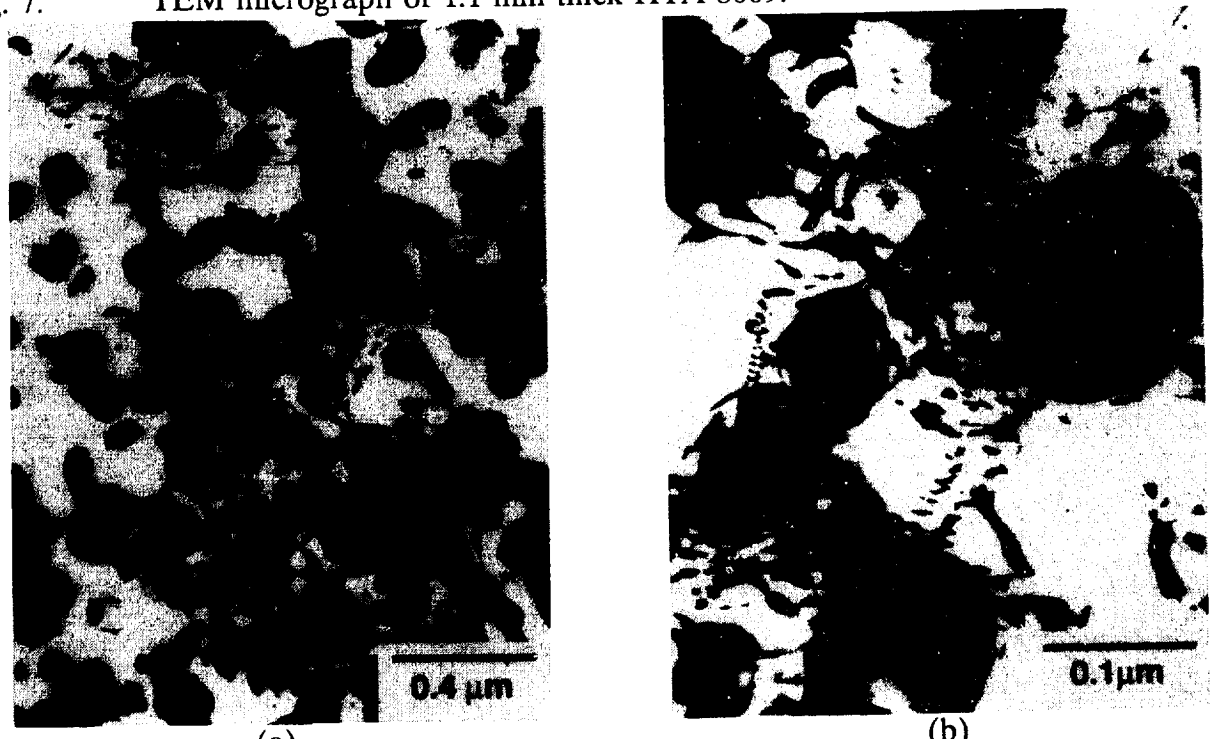

(a) (b)

Fig. 8. TEM micrograph of tension deformed HTA 8009 at (a) 25°C and (b) 200°C.

Fig. 9. TEM micrograph of tension deformed HTA 8009 at 200°C showing grain boundary cracking.

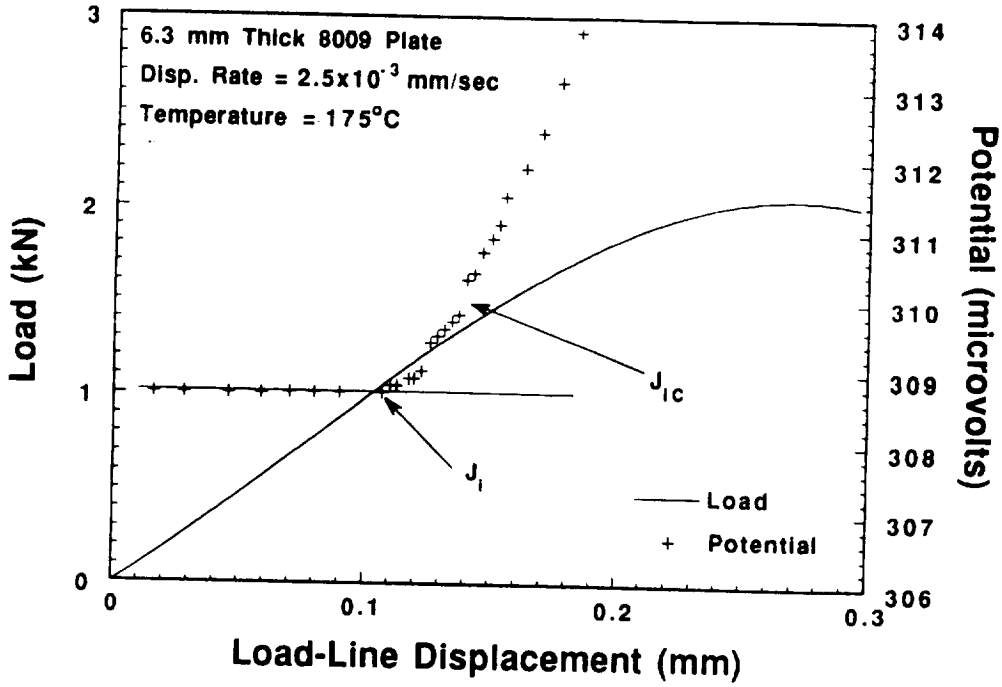

Fig. 10. Load versus load-line displacement and direct current electric potential data from a monotonic increasing displacement fracture toughness experiment with a CT specimen of 8009 at 175°C.

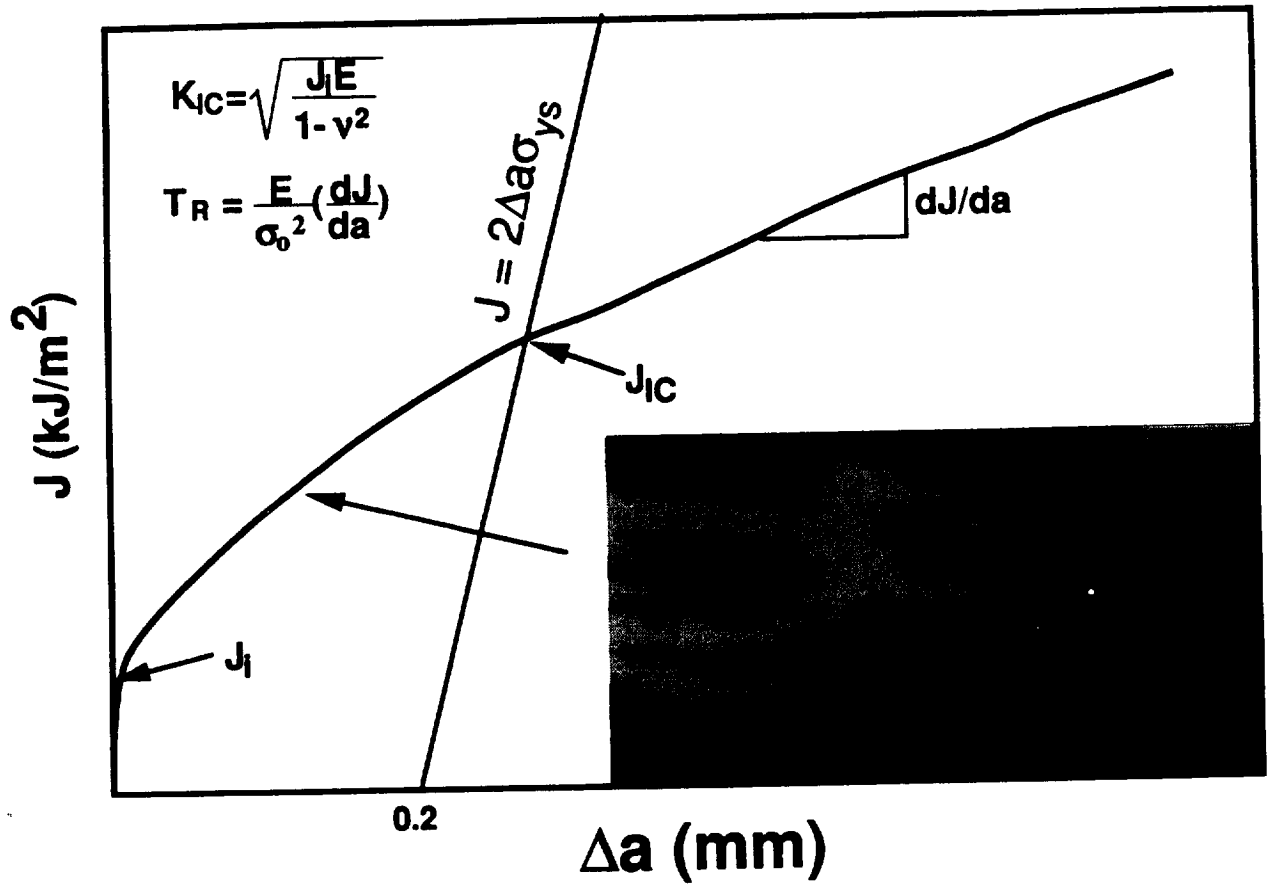

Fig. 11. Schematic illustration of the analysis of J_i and J_{IC}.

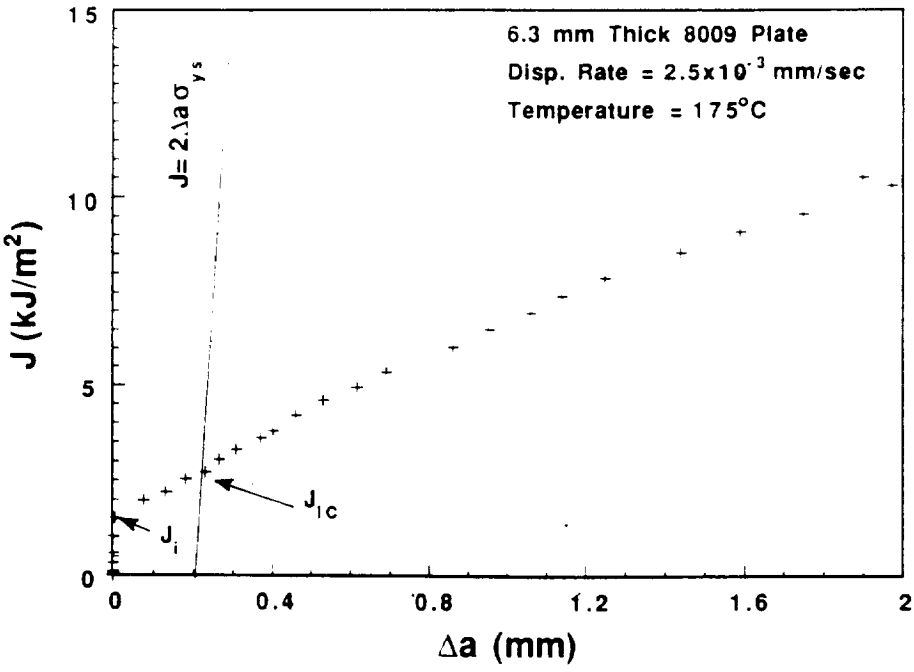

Fig. 12. J-R results determined from data shown in Fig. 10.

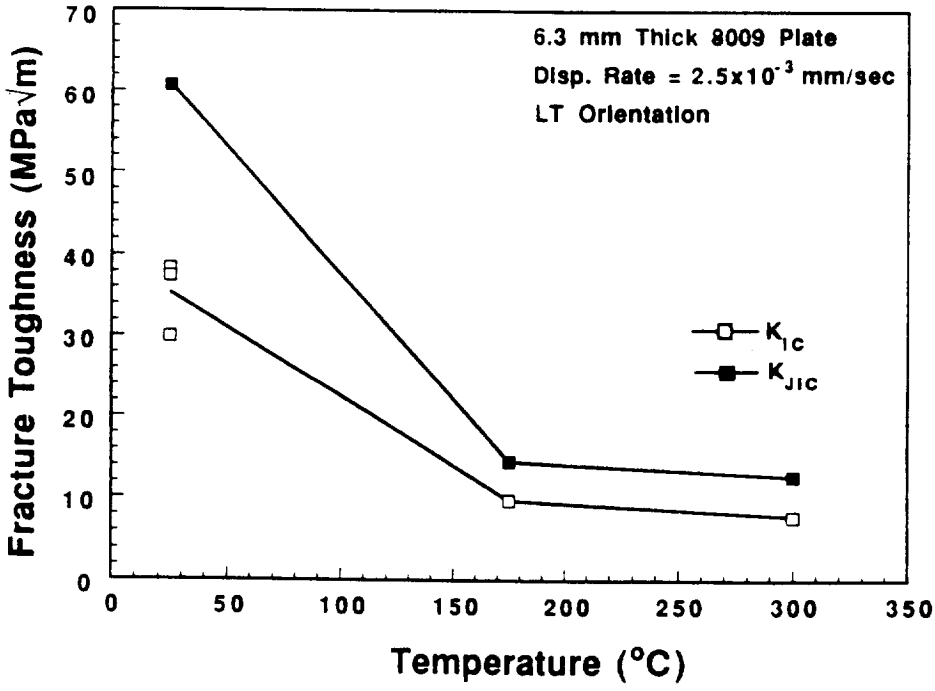

Fig. 13. Initiation fracture toughness of 6.3 mm thick HTA 8009 plate as a function of temperature.

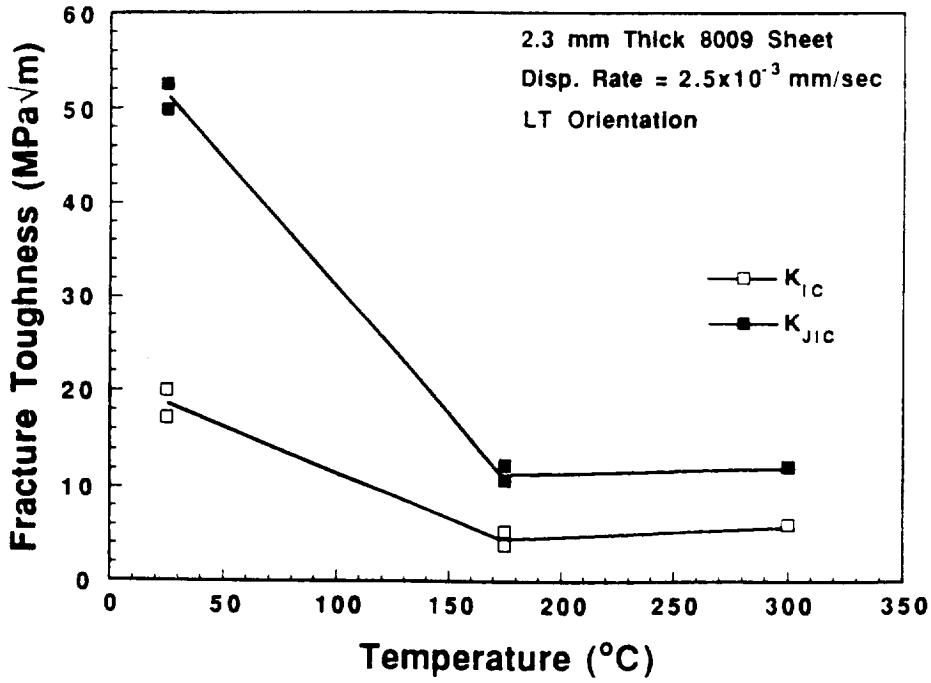

Fig. 14. Initiation fracture toughness of 2.3 mm thick HTA 8009 sheet as a function of temperature.

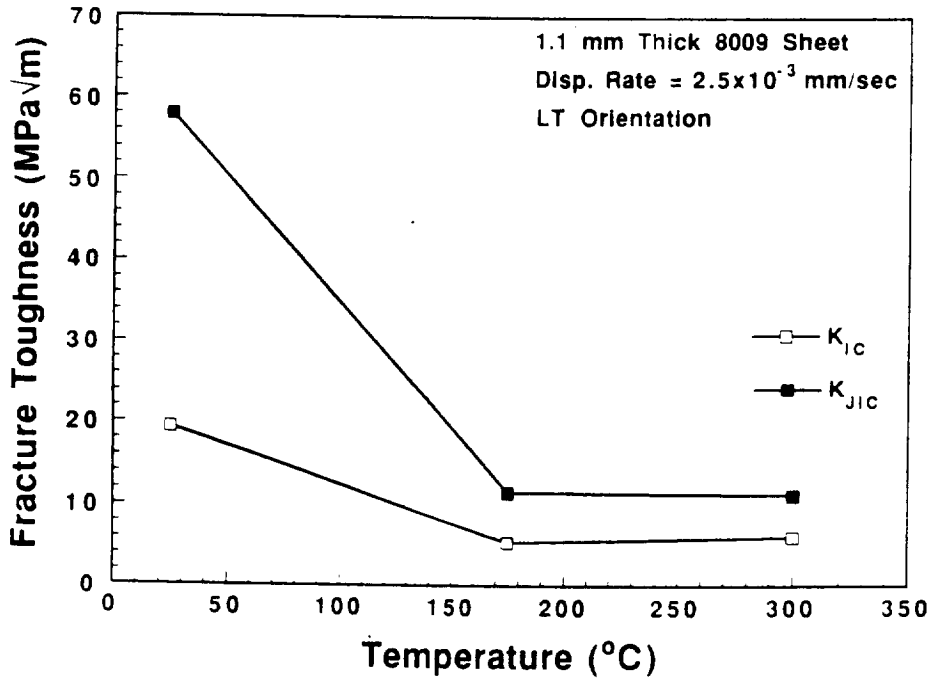

Fig. 15. Initiation fracture toughness of 1.1 mm thick HTA 8009 sheet as a function of temperature.

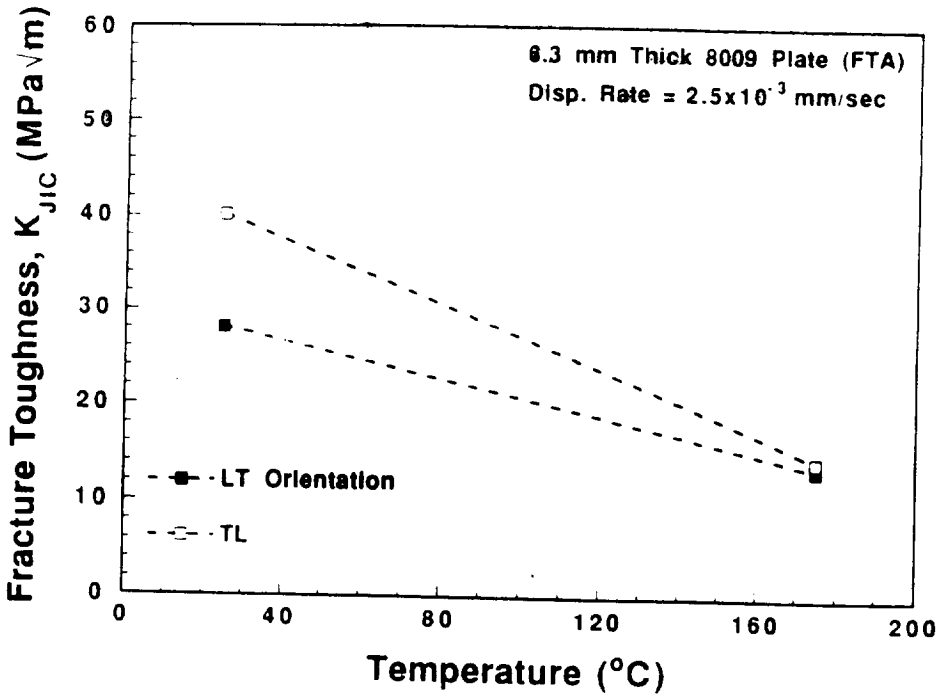

Fig. 16. Initiation fracture toughness of 6.3 mm thick HTA 8009 plate as a function of temperature. These data were obtained by FTA.

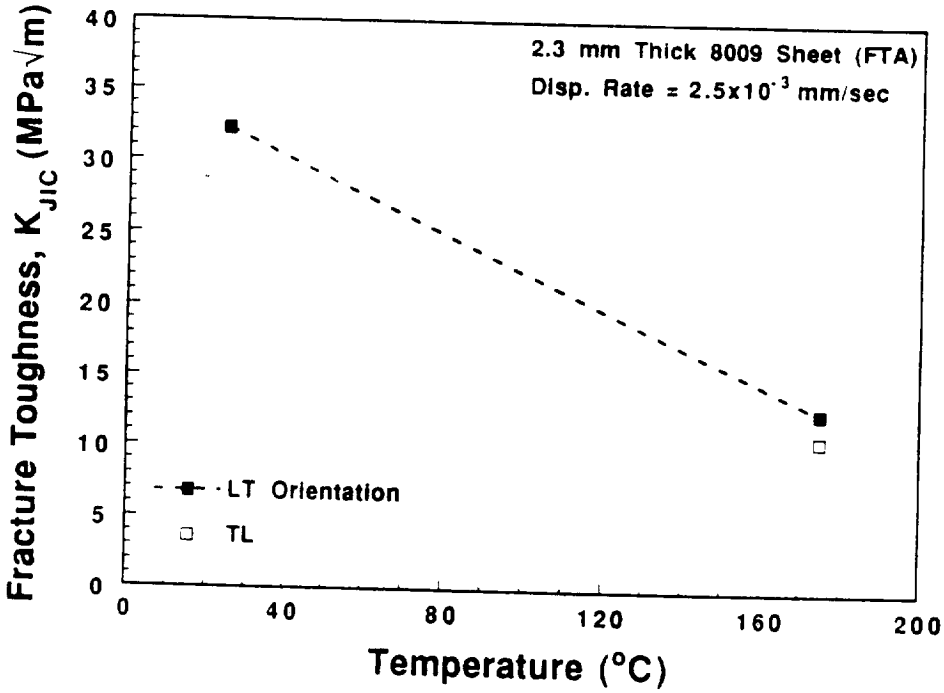

Fig. 17. Initiation fracture toughness of 2.3 mm thick HTA 8009 sheet as a function of temperature. These data were obtained by FTA.

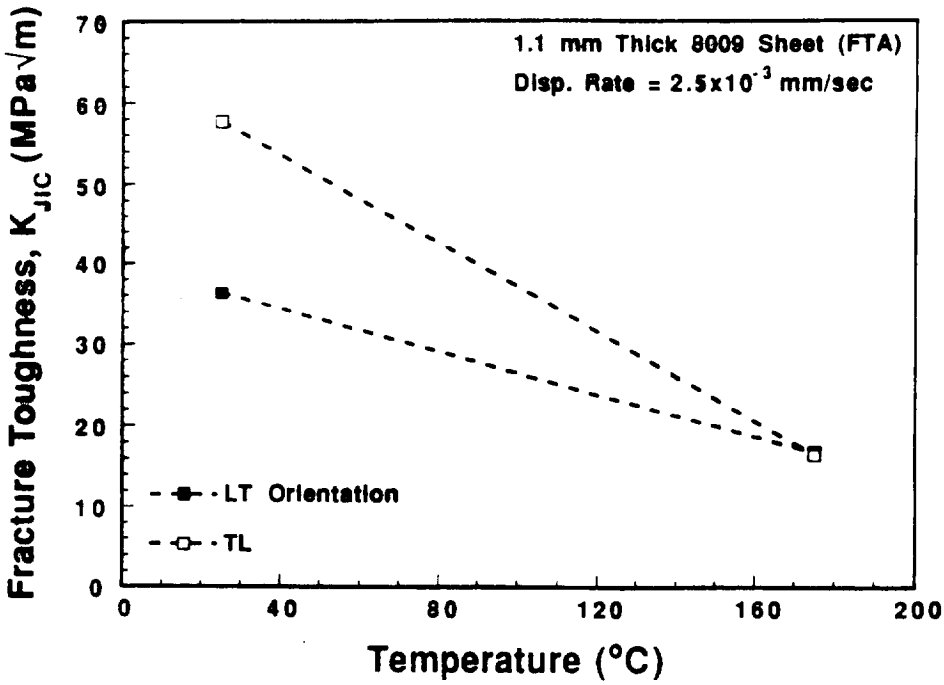

Fig. 18. Initiation fracture toughness of 1.1 mm thick HTA 8009 sheet as a function of temperature. These data were obtained by FTA.

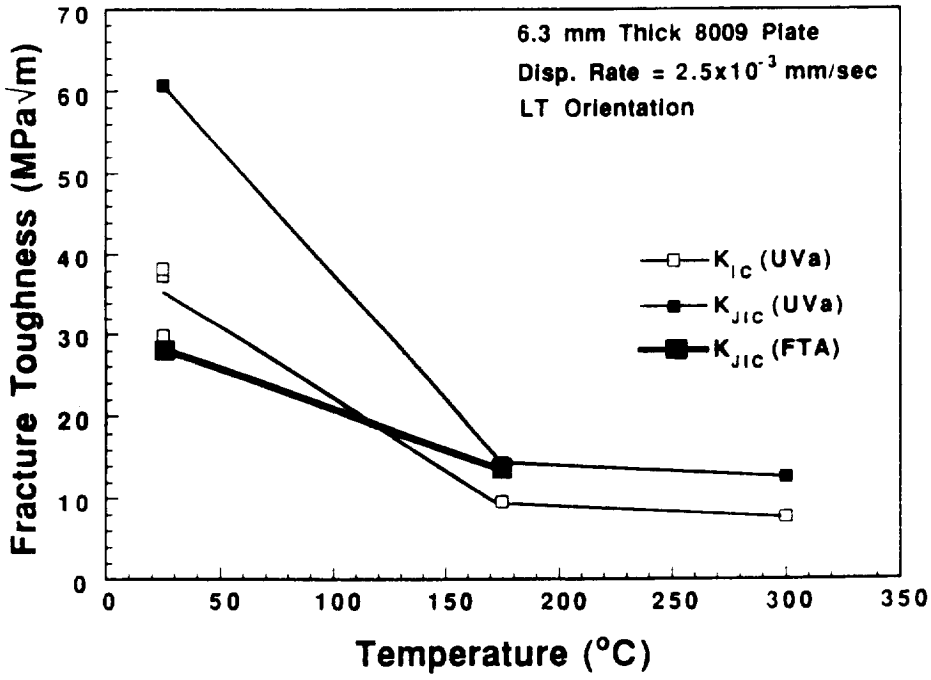

Fig. 19. Comparison of initiation fracture toughness obtained by UVa and FTA for 6.3 mm thick HTA 8009 as a function of temperature.

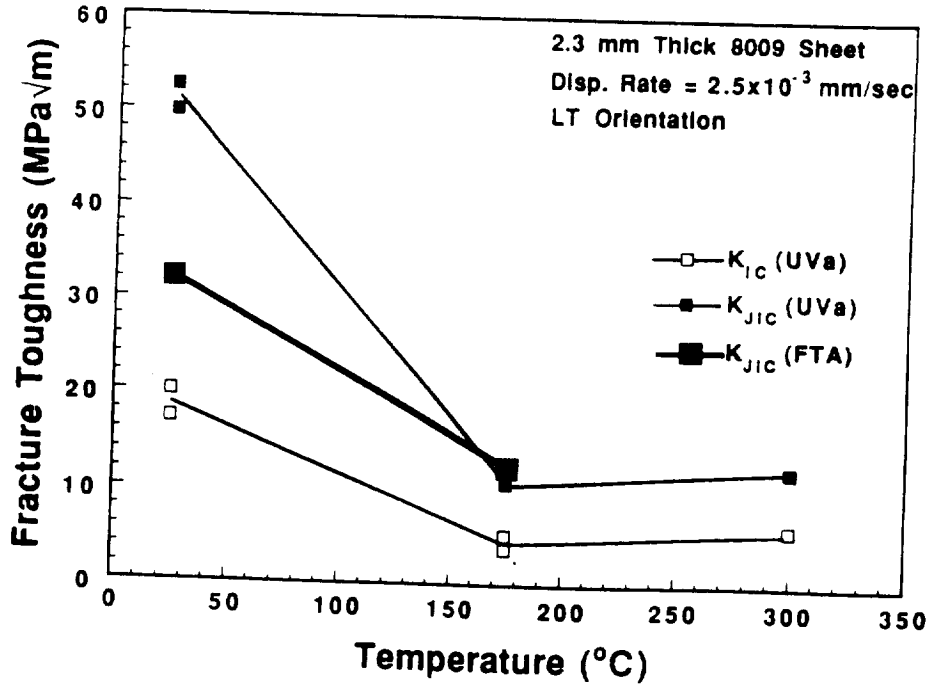

Fig. 20. Comparison of initiation fracture toughness obtained by UVa and FTA for 2.3 mm thick HTA 8009 as a function of temperature.

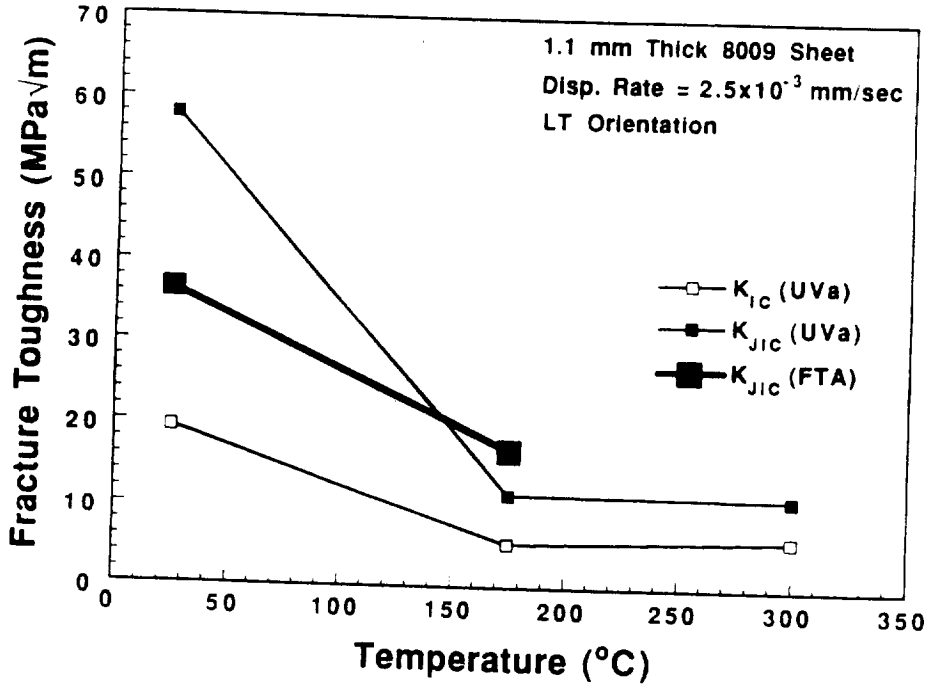

Fig. 21. Comparison of initiation fracture toughness obtained by UVa and FTA for 1.1 mm thick HTA 8009 as a function of temperature.

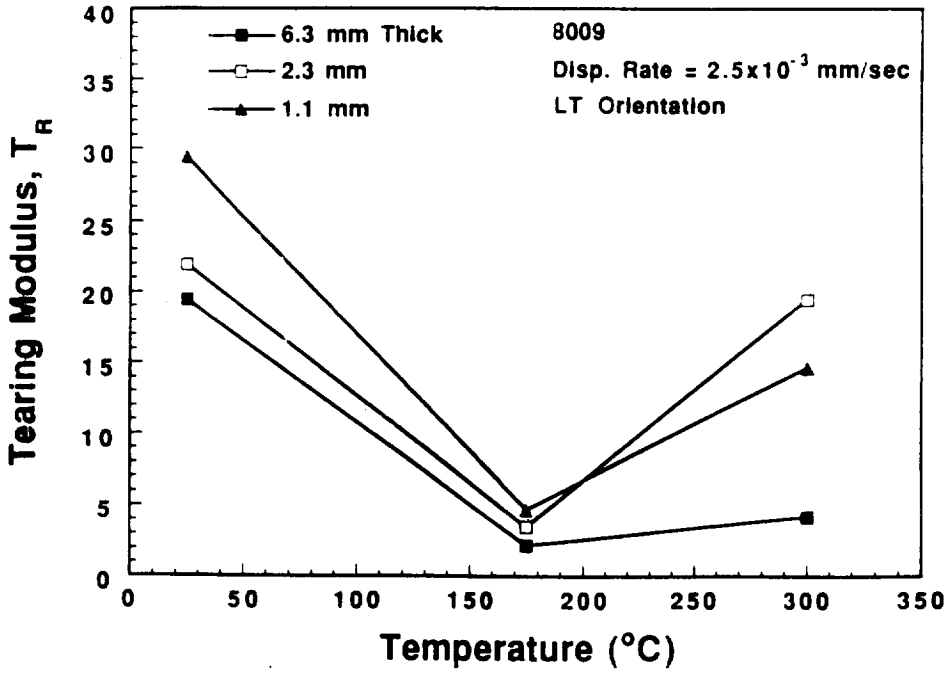

Fig. 22. Tearing modulus for HTA 8009 as a function of temperature.

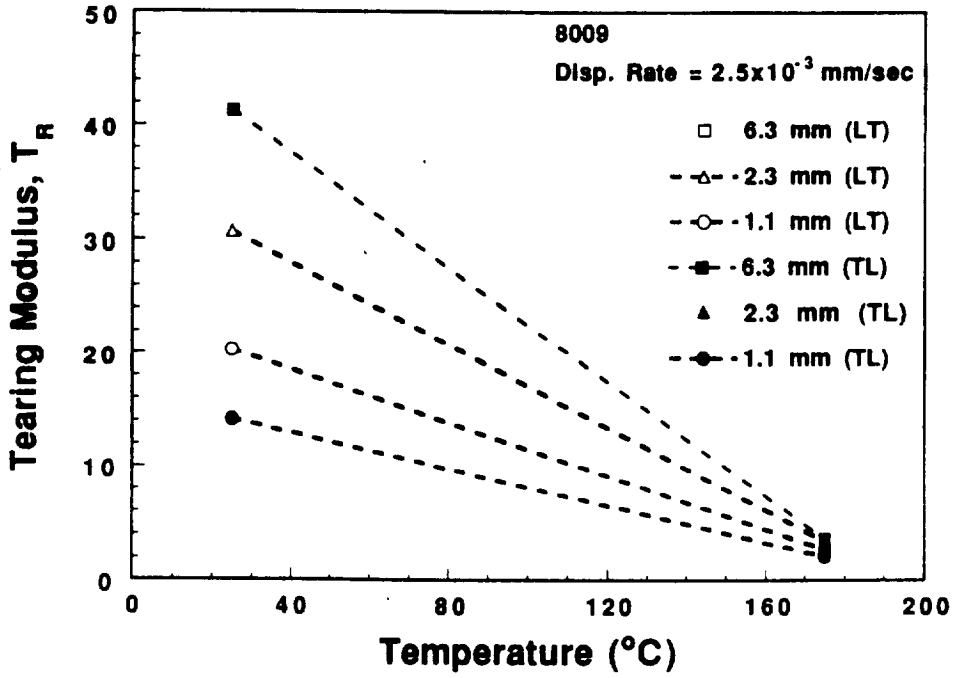

Fig. 23. Tearing modulus for HTA 8009 as a function of temperature. Data were obtained by FTA.

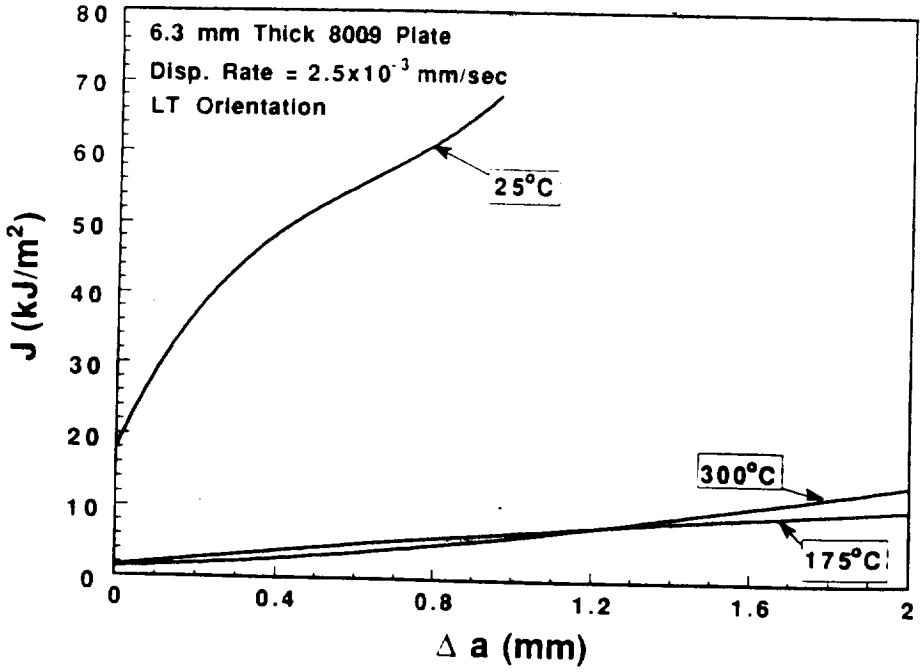

Fig. 24. Power law curve fits representing J-Δa data as a function of temperature for 6.3 mm thick HTA 8009.

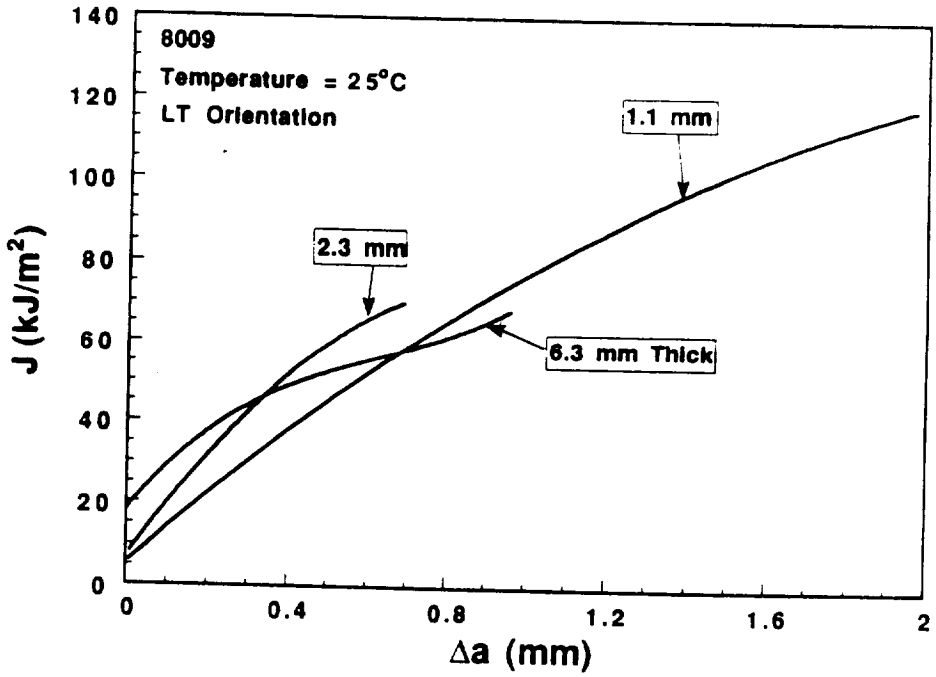

Fig. 25. Power law curve fits representing J-Δa data as a function of thickness for HTA 8009 at 25°C.

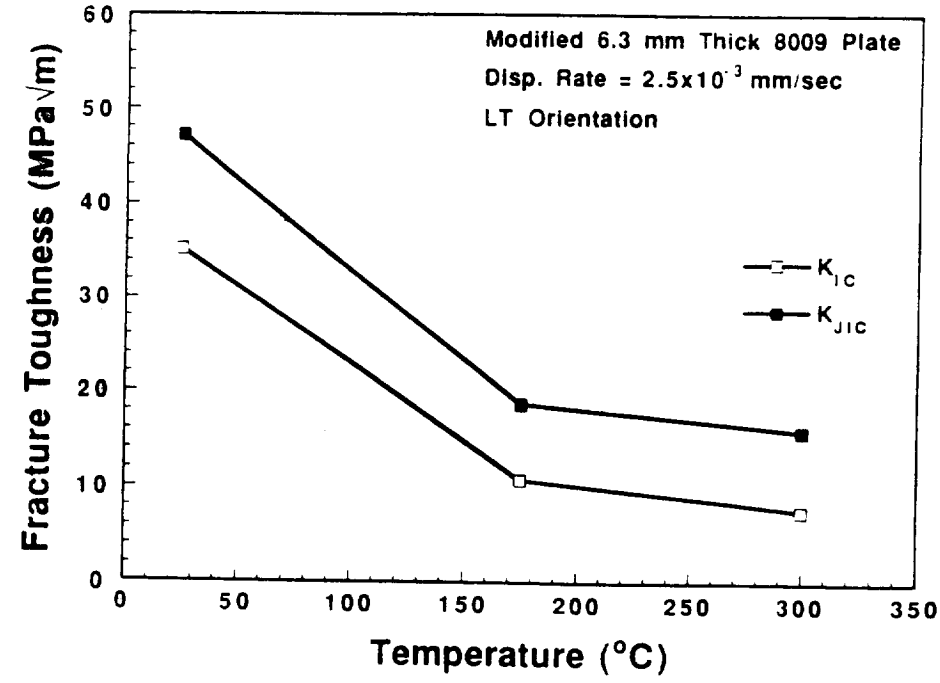

Fig. 26. Fracture toughness of modified 6.3 mm thick HTA 8009 as a function of temperature.

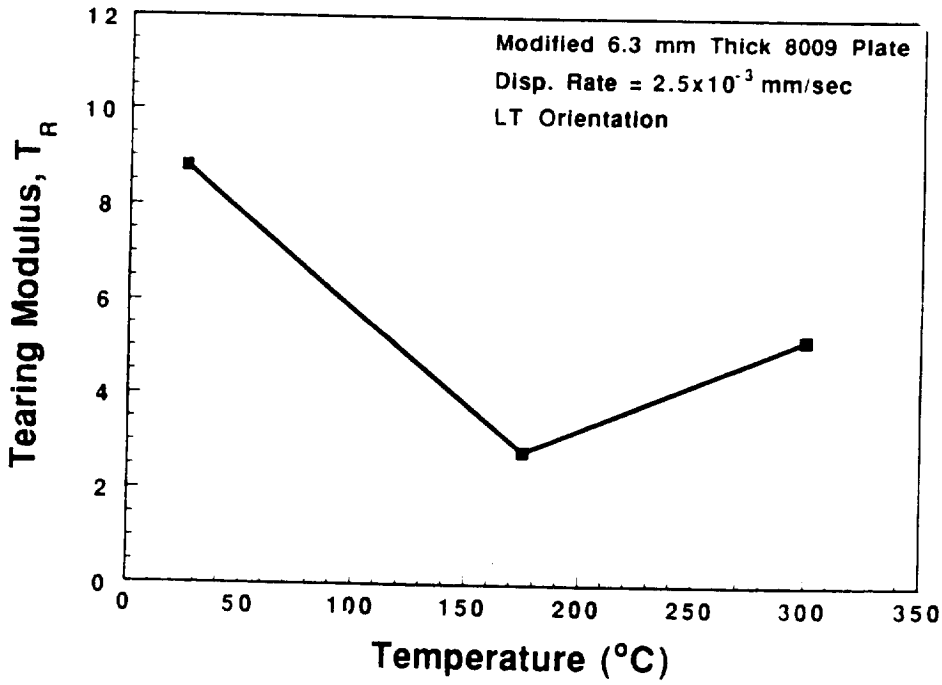

Fig. 27. Tearing modulus for modified HTA 8009 as a function of temperature.

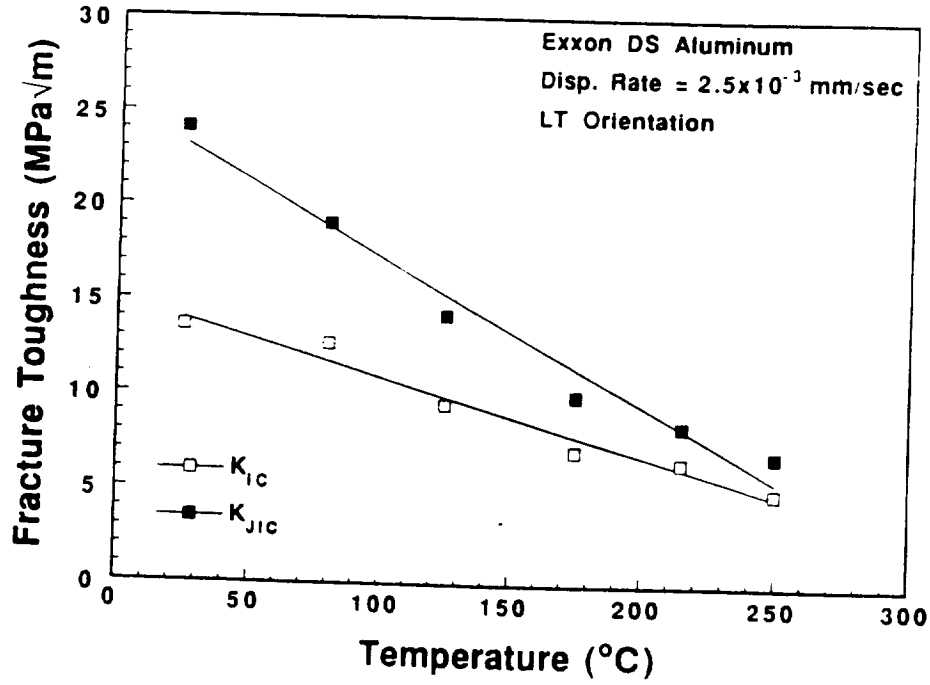

Fig. 28. Fracture toughness of Exxon DS Aluminum as a function of temperature.

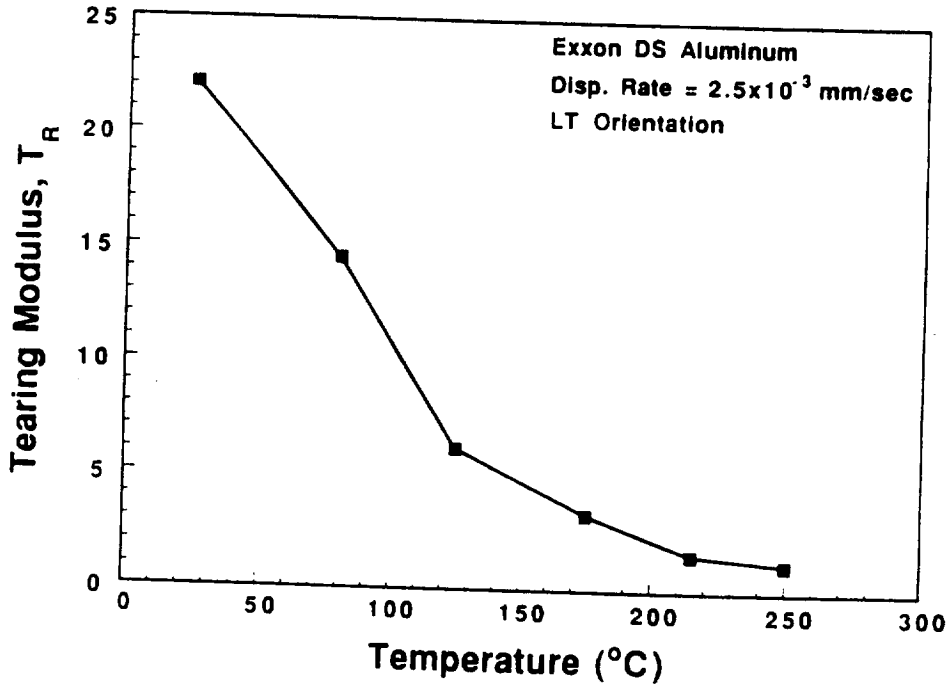

Fig. 29. Tearing modulus for Exxon DS Aluminum as a function of temperature.

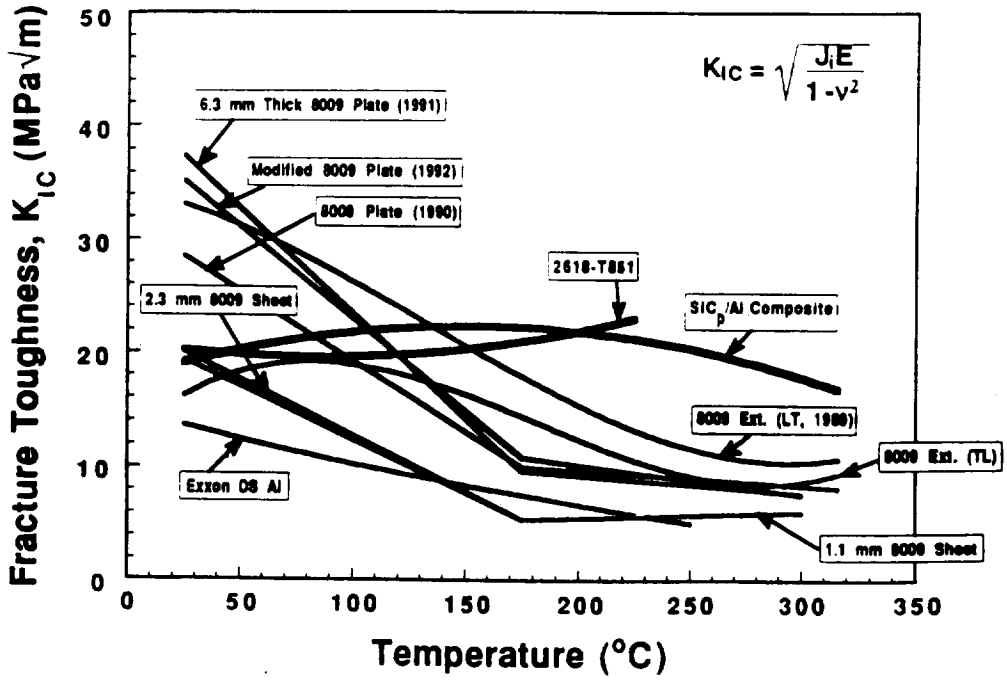

Fig. 30. Fracture toughness of modified and conventionally processed HTA 8009 as a function of temperature at a constant displacement rate of 2.5×10^{-3} mm/sec.

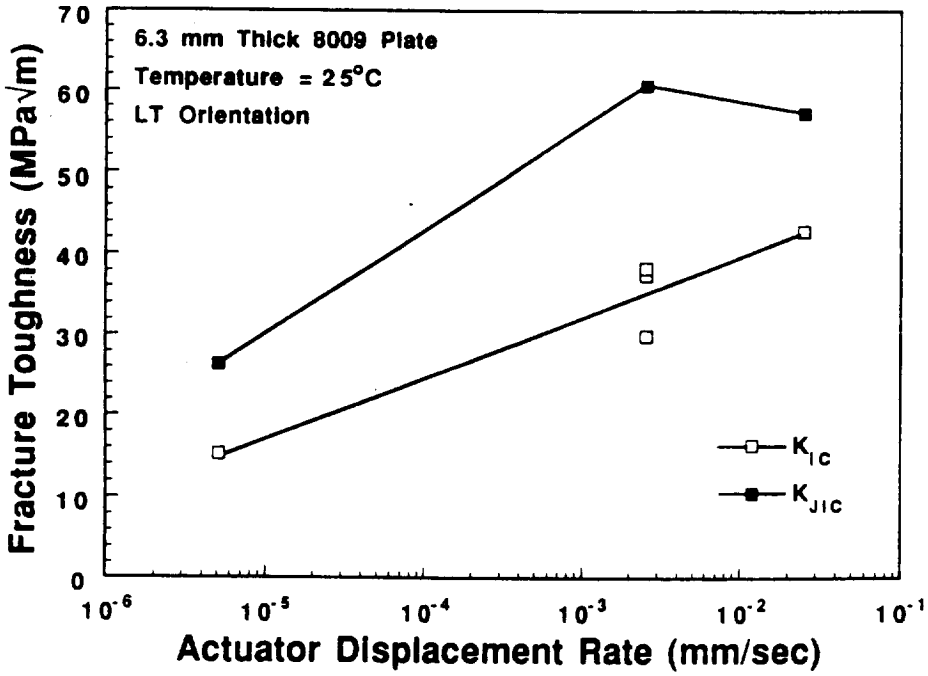

Fig. 31. Fracture toughness for 6.3 mm thick HTA 8009 plate as a function of actuator displacement rate at 25°C.

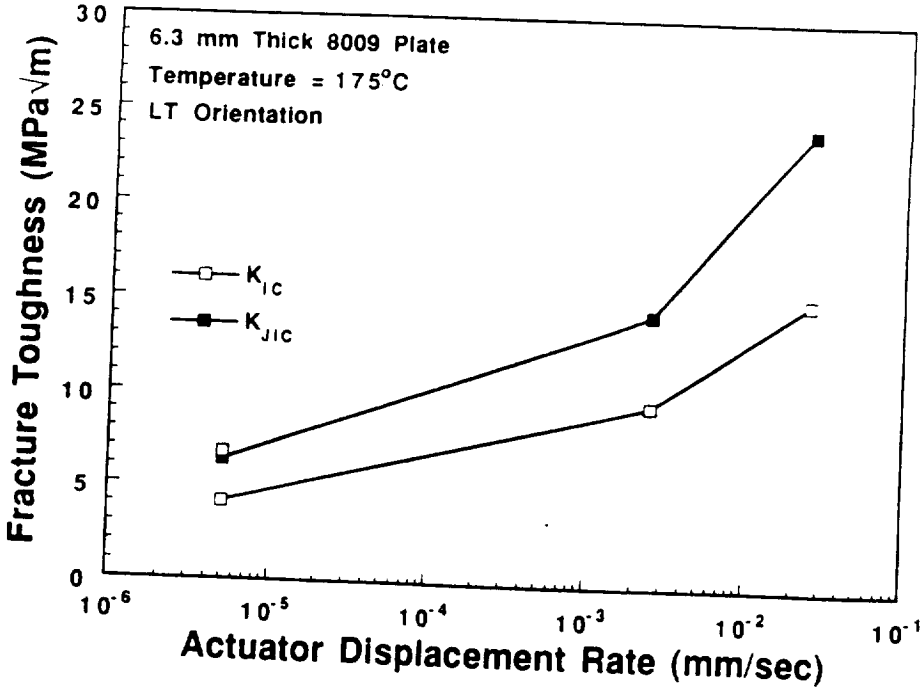

Fig. 32. Fracture toughness for 6.3 mm thick HTA 8009 plate as a function of actuator displacement rate at 175°C.

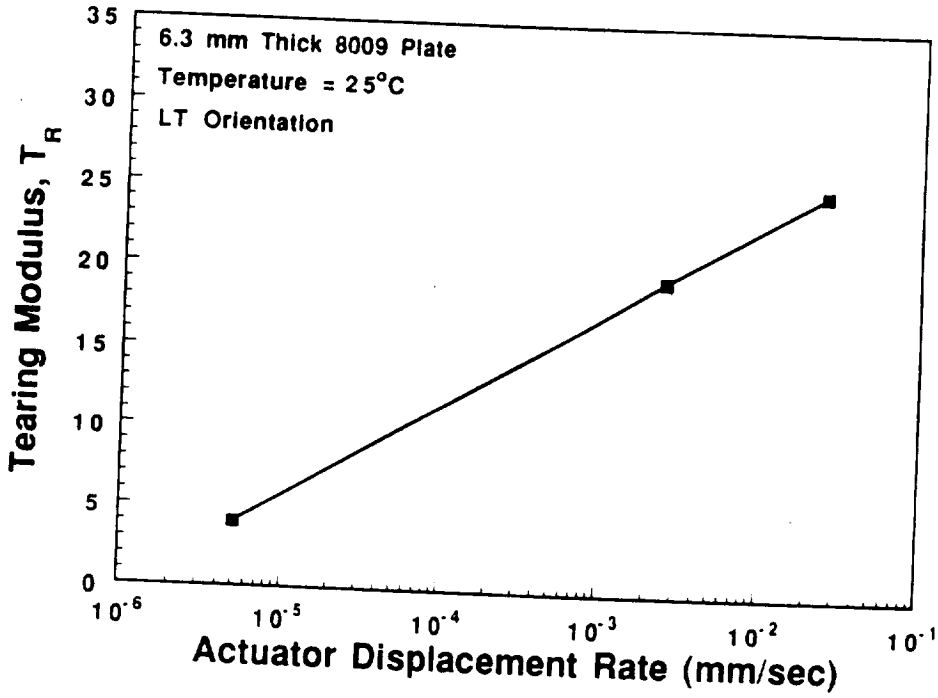

Fig. 33. Tearing modulus for 6.3 mm thick HTA 8009 as a function of displacement rate at 25°C.

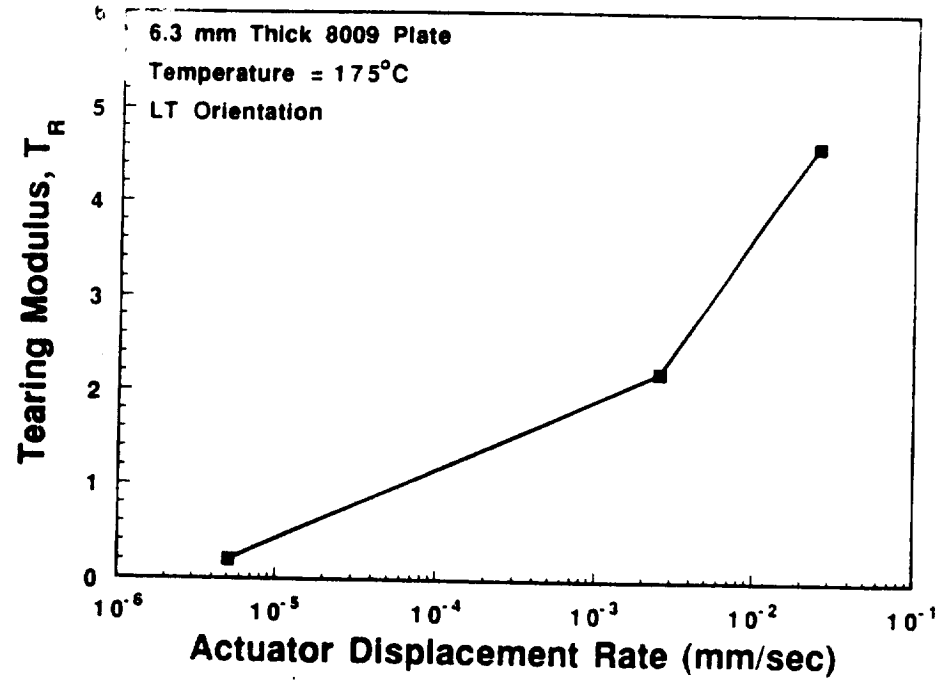

Fig. 34. Tearing modulus for 6.3 mm thick HTA 8009 as a function of displacement rate at 175°C.

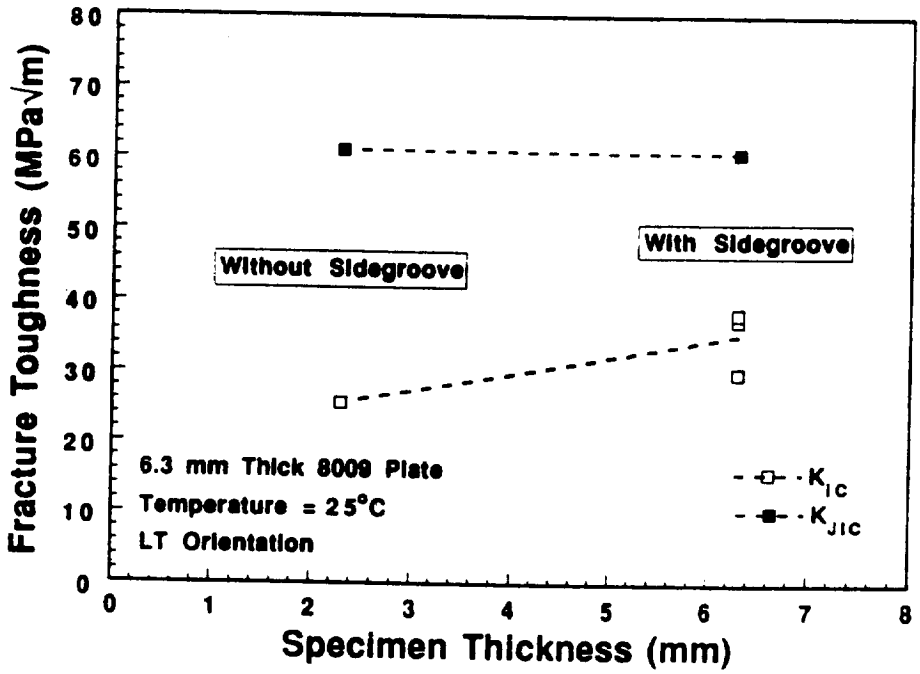

Fig. 35. Effect of specimen thickness on initiation fracture toughness for HTA 8009 at 25°C.

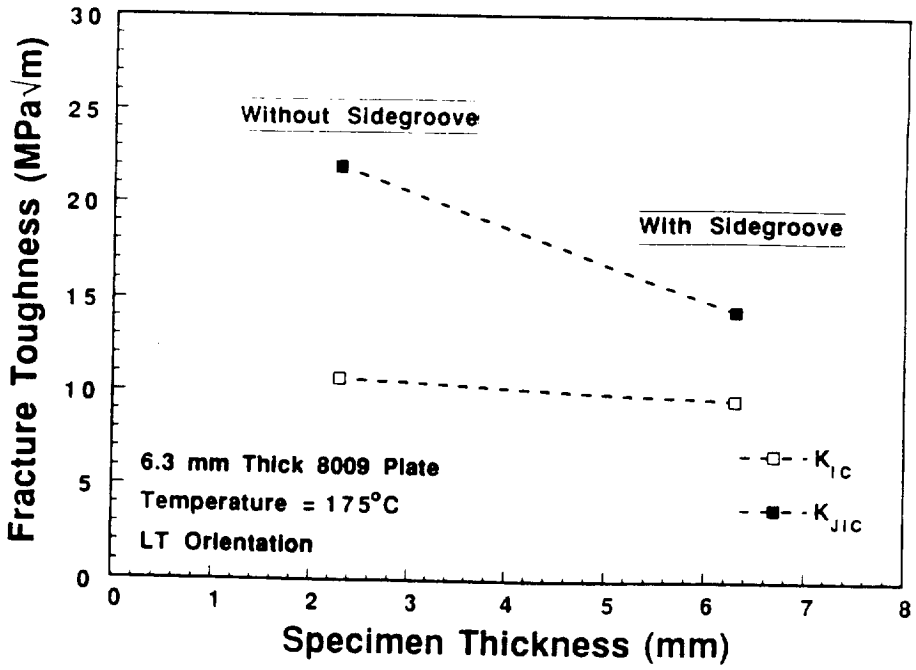

Fig. 36. Effect of specimen thickness on initiation fracture toughness for HTA 8009 at 175°C.

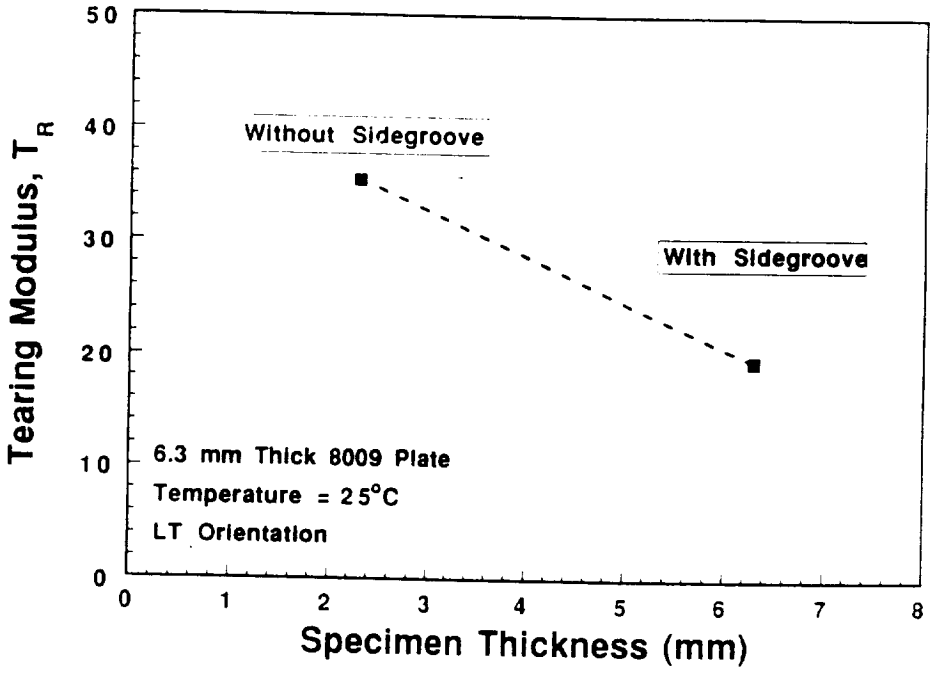

Fig. 37. Effect of specimen thickness on tearing modulus for HTA 8009 at 25°C.

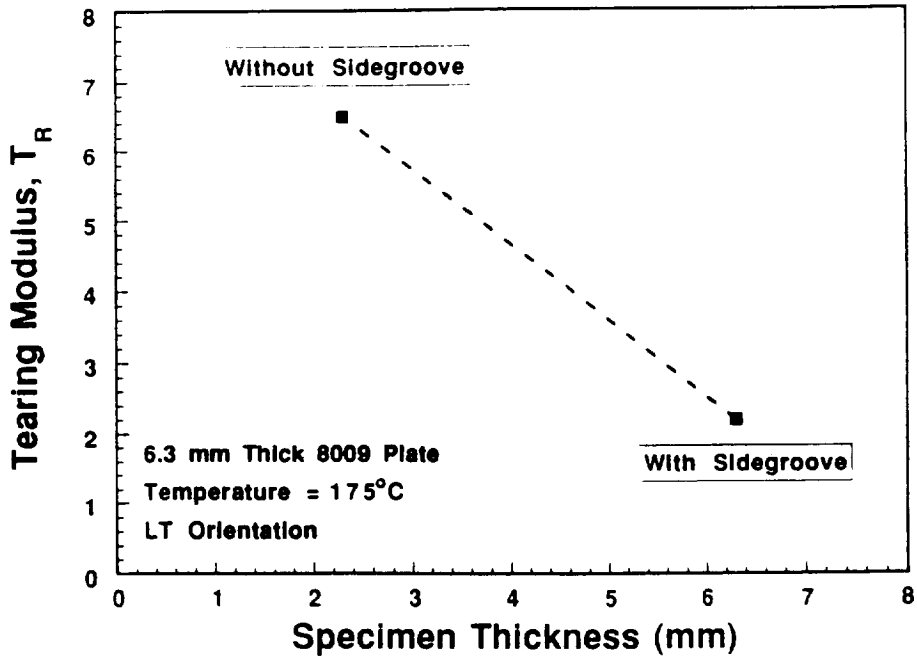

Fig. 38. Effect of specimen thickness on tearing modulus for HTA 8009 at 175°C.

(a)

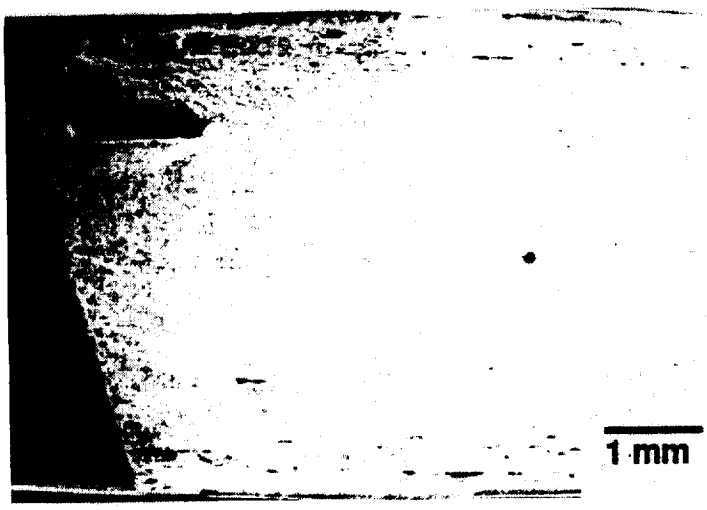

(b)

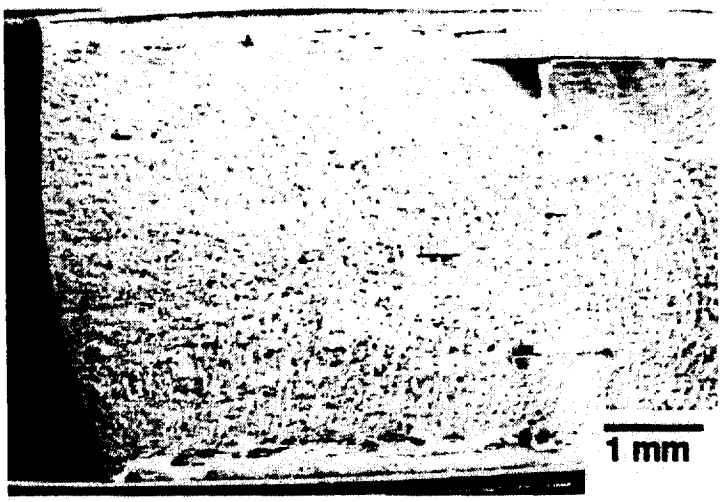

(c)

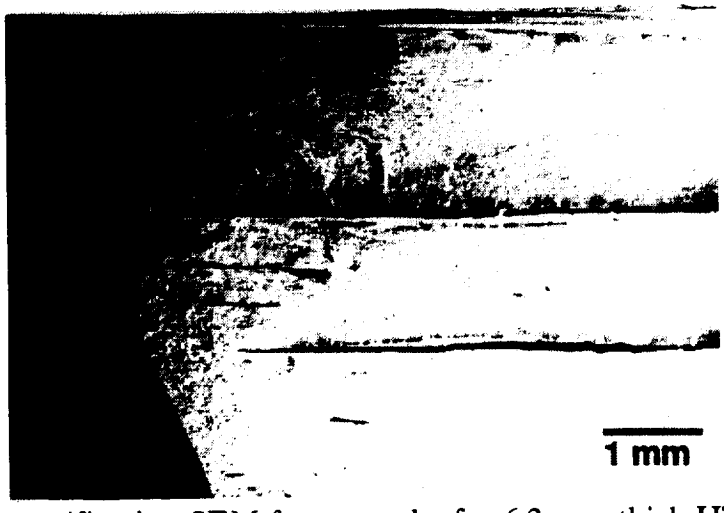

Fig. 39. Low magnification SEM fractography for 6.3 mm thick HTA 8009 fractured at: (a) 25°C, (b) 175°C and (c) 300°C; displacement rate of 2.54×10^{-3} mm/sec.

(a)

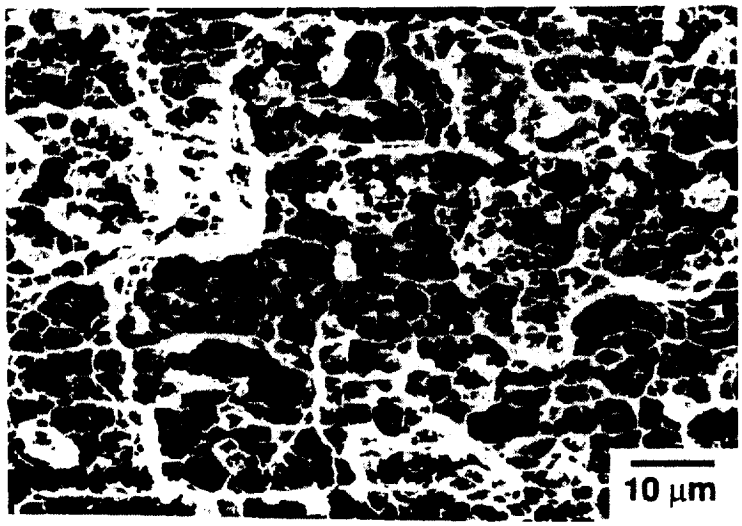

(b)

Fig. 40. SEM fractography for 6.3 mm thick HTA 8009 fractured at: (a) 25°C and (b) 175°C; displacement rate of 2.54×10^{-3} mm/sec.

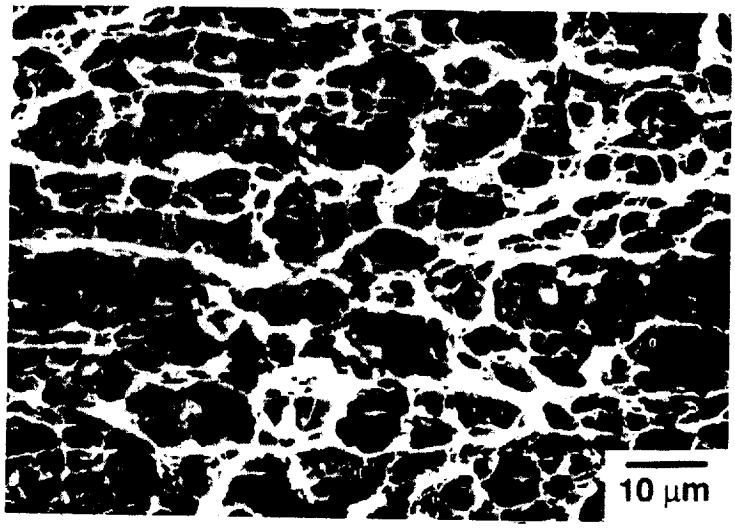

(a)

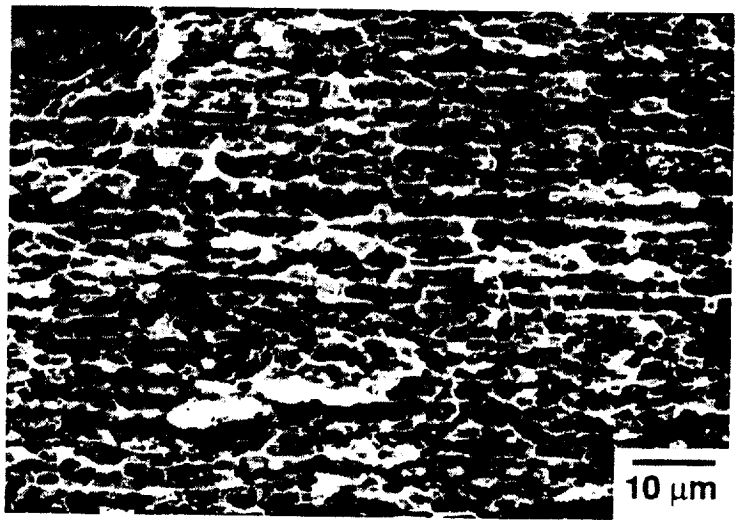

(b)

Fig. 41. SEM fractography for 2.3 mm thick HTA 8009 fractured at: (a) 25°C and (b) 175°C; displacement rate of 2.54×10^{-3} mm/sec.

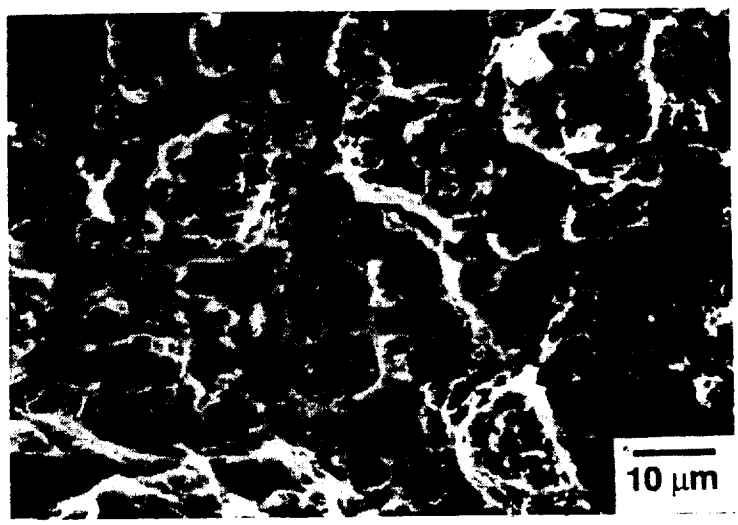

(a)

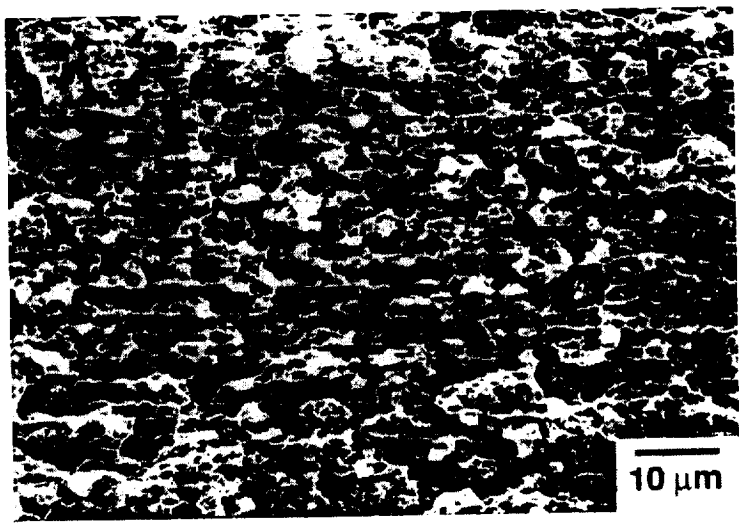

(b)

Fig. 42. SEM fractography for 1.1 mm thick HTA 8009 fractured at: (a) 25°C and (b) 175°C; displacement rate of 2.54×10^{-3} mm/sec.

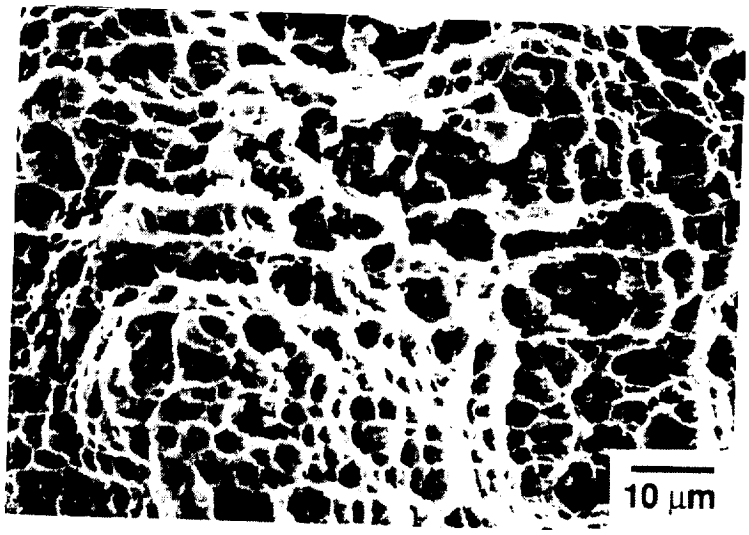

(a)

(b)

Fig. 43. SEM fractography for 6.3 mm thick HTA 8009 fractured at 25°C and displacement rates of: (a) 5.08×10^{-6} mm/sec and (b) 2.54×10^{-2} mm/sec.

(a)

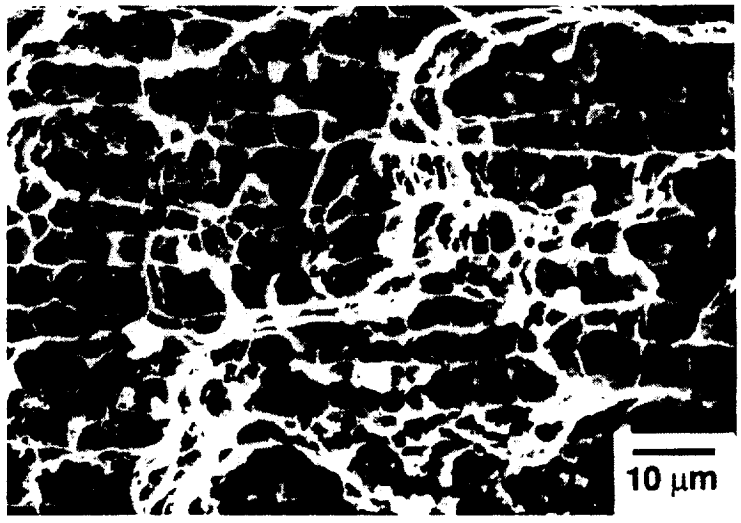

(b)

Fig. 44. SEM fractography for 6.3 mm thick HTA 8009 fractured at 175°C and displacement rates of: (a) 5.08×10^{-6} mm/sec and (b) 2.54×10^{-2} mm/sec.

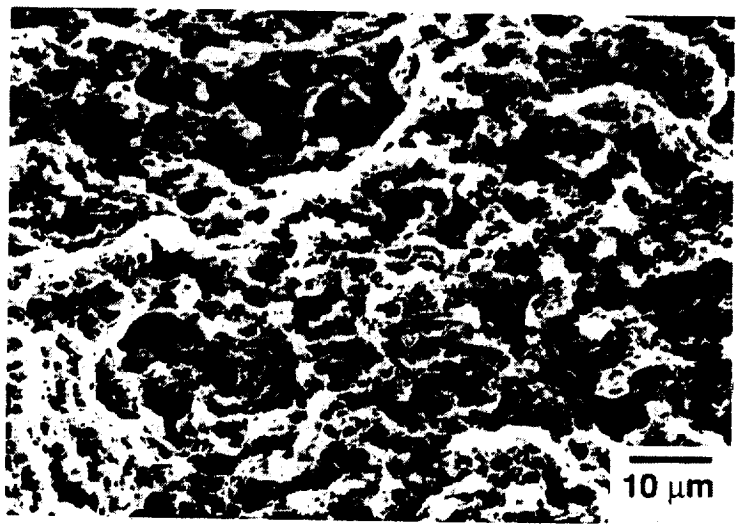

(a)

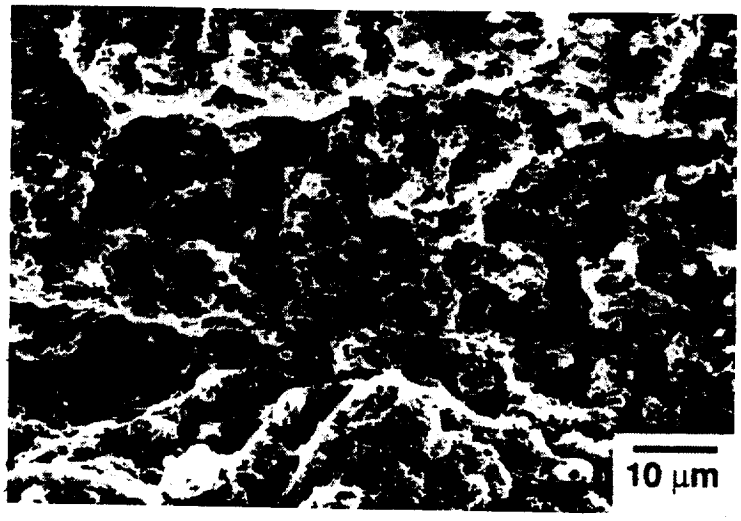

(b)

Fig. 45. SEM fractography of Exxon DS Aluminum fractured at a displacement rate of 2.54×10^{-3} mm/sec at: (a) 25°C and (b) 175°C.

TASK 7. STRENGTH/TOUGHNESS COMBINATION IN DMMCs

Principal Investigator:	Dr. L. M. Angers, Alcoa
Senior Engineer:	Dr. G. Dixon, Alcoa
Boeing Contact:	Mr. P.G. Rimbos
Douglas Contact:	Mr. R. Kahandal

Objective. The objective of this task is to characterize sheet produced from discontinuously reinforced metal matrix composites. Room temperature tensile and plane stress fracture toughness tests will be conducted on materials aged to peak strengths and on materials given Mach 2.0 simulations.

Background and Test Plans. An experimental plan to establish the strength/plane stress toughness relationship which can be achieved in aluminum based composites reinforced with 20% SiC has been developed and initiated.

Three materials were identified for use in this task: 2080/SiC/20_p, MB85/SiC/20_p and 6113/SiC/20_p. MB85 is a higher Zr version of 2080, e.g., 0.35% Zr. The 2080/SiC/20_p and MB85/SiC/20_p will be fabricated using two different rolling practices in an attempt to produce two different grain structures: one with a large grain size (roughly ASTM grain size of 2) and one with a small grain size (roughly ASTM grain size of 9). The effects of grain structure, product thickness and Zr level on the strength/toughness relationship will be studied here.

Material Fabrication. Atomized powders of 2080, MB85 and 6113 and SiC reinforcement powders were donated to the University of Virginia Subcontract No. 5-28406 so that fabrication, consolidation and characterization could occur without unnecessary delay.

The aluminum powders were blended with SiC and cold isostatically pressed to produce compacts approximately 75% of theoretical density. The compacts were vacuum degassed, hot

pressed and extruded.

The 2080/SiC, MB85/SiC and 6113/SiC materials are awaiting rolling. Rolling conditions have been determined for 2080/SiC and MB85/SiC to produce the desired coarse (~ASTM 2) and fine (~ASTM 9) grain size. The 6113/SiC composite material will be rolled via a standard rolling practice.

Since plane stress fracture toughness data are needed, enough material will be rolled to produce 16" x 44" panel.

Results and Discussion. None

Subtask 7A. DMMC Development (Boeing)

No progress to report to date. See Subtask 1A(i).

Subtask 7B. DMMC Development (Douglas)

No progress to report to date.

TASK 8. INVESTIGATION OF THE FORMATION OF THE Ω PHASE IN MODIFIED 2009 AND CHARACTERIZATION OF THE MODIFIED ALLOYS' THERMOMECHANICAL PROPERTIES (UVa)

Principal Investigator: Dr. F.E. Wawner
Graduate Student: Mr. Qiong Li
Consultant: Dr. E.A. Starke, Jr.

Objective and Technical Approach. The objective of this investigation is to modify 2009 (a product of Advanced Composite Materials Corporation) with Ag to enhance the formation of the Ω phase in the SiC particulate reinforced Al-Cu-Mg matrix composite in order to increase the composites elevated temperature stability.

The technical approach initially being taken is to fabricate potential matrix alloys at UVA to determine optimum Cu/Mg ratio and optimum amount of Ag in order to generate a maximum volume fraction of the coherent Ω phase. Initial composite samples will be produced by compocasting at UVA, incorporating SiC into the alloy composition determined to be best. Microstructural studies of these composites will be made to ascertain if the Ω phase is retained after introduction of the ceramic particles. If it is not, other iterations of matrix composition will be made to achieve maximum Ω in the composite. After establishing the optimum composition, ACMC will produce a P/M sample for evaluation of the material's thermomechanical properties and stability at UVA.

Experimental. Initial experimental alloys are being produced using an induction heater to melt the metal charge in a glove box containing an argon atmosphere. The composition of the alloys investigated thus far are listed in Table 1.

TABLE 1

Sample	Cu wt%	Mg wt%	Ag wt%	Al wt%
A11M	3.2	0.45	0.4	bal
A11MM	3.2	0.45	0.5	bal
A12M	4.0	0.45	0.4	bal
A13M	2.6	0.45	0.4	bal

After casting, all alloys were hot rolled and then homogenized for 24 hours at 495°C, solutionized for 19 hours at 525°C, quenched in ice water, and artificially aged at different times and temperatures. Hardness tests were made on an Indentron Rockwell hardness tester to establish peak aging conditions. A Perkin Elmer DSC7 differential scanning calorimeter was used to investigate the precipitation process and melting temperature in the alloys. For the microstructural investigations a Philips EM 400T with EDS and a JEOL 4000EX high resolution transmission electron microscope were utilized. Determination of shear strength was made using the blanking shear test technique.

Results and Discussion.

1. Hardness Tests:

Hardness tests were made on all alloys produced to determine peak aging conditions. Figure 1 shows the results. The data shows that peak hardness is achieved after 3 hours at 200°C and after approximately 26 hours at 150°C. In general the higher ratios of Cu/Mg tended to produce harder alloys. Sample A12M which has the highest hardness retained approximately 90% of the peak value after 26 hours at 200°C. At 150°C the peak hardness is reached at 26 hours and this value is maintained after 200 hours aging at this temperature (Fig. 1b). Based on the hardness data sample A13M, which demonstrated inferior hardness at both temperatures, was dropped from consideration for a detailed study and effort was concentrated on alloys A11M and A12M.

2. Differential Scanning Calorimetry

The DSC investigation was conducted using the isothermal mode at 200°C. The reason for using the isothermal mode is that it is more realistic with regard to actual application, i.e. ability to detect reactions during prolonged exposure. A qualitative comparison of the exotherms or endotherms can generate some feeling for the thermal stability of the alloy. Figure 2 shows the results of the isothermal scan at 200°C. Samples A11M and A11MM show large exothermal peaks after the initial peak (nucleation) implying precipitation of phases out to approximately 24 hours. The A12M demonstrates much smaller exotherms implying better thermal stability. TEM studies are being made after each precipitation peak to quantify the microstructure. Based on electron micrographs, to be shown later, the A12M sample contains predominately Ω phase after 30 hours while the A11M sample shows mostly σ with some Ω.

DSC was also used to determine the melting temperature of the alloys which was documented at 622°C.

3. Microstructure

Analytical and high resolution transmission electron microscopy have been utilized to define the microstructure in the alloys. Typically in the aluminum alloys of Al-Cu-Mg compositions, the predominate precipitate phases are Θ' (Al_2Cu) and S (Al_2CuMg). However, recently two additional coherent phases Ω (Al_2Cu) and σ ($Al_2Cu_6Mg_2$) have been detected in these alloys (1,3,9,10).

The S phase (Al_2CuMg) is a needle-shaped precipitate in Al-Cu-Mg alloys with low Cu/Mg ratio and has an orthorhombic crystal structure. The [100], [010], and [001] directions of S are parallel to the [100], [021], and [012] directions of the matrix. The S precipitates normally nucleate on dislocations and grow as lath on [210] along the [100] direction (1).

The Θ' phase (Al_2Cu) is a plate-shaped precipitate which is a well-known metastable phase in Al-Cu alloys. It is fully coherent with the matrix along the broad faces, and the (001) planes and [001] directions of the Θ' are parallel to the (001) planes and [001] direction of the matrix. Θ' often nucleates directly on dislocations since dislocations can act to relieve the misfit associated with the precipitate (1).

It was shown by Polmear et al. (2-4) that adding small amounts of Ag to Al-Cu-Mg alloys with proper Cu/Mg ratio would promote precipitation of a coherent phase designated Ω. The Ω phase (Al_2Cu) forms on the {111} Al matrix planes as a uniform dispersion of large but very thin hexagonal-shaped plates. The structure of this phase has been the subject of considerable controversy (6-8) but is presently thought to be tetragonal and a variant of Θ' (Al_2Cu). The crystallography orientation relationship between Ω and the matrix has been determined to be (001) of Ω is parallel to [111] of Al, [010] of Ω is parallel to [101] of Al and [100] of Ω is parallel to [121] of Al (6-8). There is a large negative strain of 9.3% normal to the face of the precipitate plate. A significant increase in the age-hardening characteristics of Al-Cu-Mg-Ag alloys is observed due to the presence of this phase (2,7,8). In addition, the phase remains stable at relatively high temperatures and is more resistant to coarsening than Θ' or S, the other common strengthening precipitates in these alloys.

Recently a cubic shaped precipitate has been observed and identified in Al-Cu-Mg alloys (9,10). This phase appears to result from small amounts of Si in the alloy which offers a site for its nucleation and growth. This phase has been designated σ. The σ phase ($Al_5Cu_6Mg_2$) has a cubic structure and is coherent and coplanar with the Al matrix, i.e. {100} of σ is parallel with

{100} of Al and <100> of σ is parallel with <100> of Al and the habit plane is {100}. A coherent-coplanar interface is an ideal structure for high temperature stability. The coherent-coplanar correspondence means that the precipitate-matrix interface is a low energy interface and there is little tendency for coarsening, and if the interfacial energy is low, there is little driving force for coalescence (11,12). A good example of a coherent-coplanar precipitate is γ′ (Ni_3Al) in the Ni-based superalloys. These alloys, which are used at very high temperatures (up to 0.75 T_m) depend on the presence of γ′ precipitates which are coherent and coplanar with the matrix. These precipitates are thermodynamically stable at high temperatures. Hence obtaining an Al alloy with coherent-coplanar precipitates could lead to a functionable material for long term elevated temperature use.

Figure 3 shows the general microstructure of sample A12M (Cu/Mg=9) after one hour at 200°C. Θ′ and Ω are present along with some σ phase. The high aspect ratio of the Ω phase is obvious. A dark field micrograph of an Ω reflection shows the high density of Ω after this limited thermal treatment (Fig. 4). Heat treating at 200°C for 3 hours, which corresponds to peak aging, shows a higher density of Ω phase (Fig. 5), as shown by the bright field-dark field pair of micrographs of the same region in the sample. Figure 6 depicts a region in sample A12M, peak aged, containing Θ′, S, and σ phases.

In sample A11M, all four precipitate phases are observed after peak aging conditions (3 hours, 200°C) however there appears to be a higher density of the S phase (see Figs. 7 and 8, a bright field-dark field pair). The orientation of the S phase is such that it appears as dots (the needle ends) in Fig. 7. The Ω phase, while present, does not appear to be as abundant as in sample A12M (see Fig. 5 for comparison). After aging this sample for 19 hours

the Θ' and S phases coarsen while the σ and Ω phases remain about the same size (Fig. 9). Interfacial misfit dislocations are obvious on the coherent-coplanar σ phase.

Further aging at 200°C for 26 hours shows the development of more of the σ phase (Fig. 10). It was occasionally observed the Ω and the σ phase formed in a segregated manner, as shown in Fig. 11. This could be due to local variation in alloy chemistry which could affect the nucleation and growth of the specific phases. It was also noted that, after 26 hours at 200°C, precipitation, presumably Θ', occurs along grain boundaries (Fig. 12). This creates a "partial" precipitate free zone along the GB. Although the Θ' and σ phases are inhibited from precipitation in this region, the Ω phase appears to be unaffected. This effect must be monitored carefully with prolonged thermal exposure since PFZ's are deleterious to mechanical properties when and if localized yielding occurs.

High resolution TEM demonstrates the coherency, the large aspect ratio, and the absence of ledges on the Ω phase in sample A11M heated to 200°C for 26 hours (Fig. 13). Nucleation and early stages of growth can be seen in Fig. 14. Occasionally the Ω plates intersected one another and exhibited a small ledge (Fig. 15).

The coherent-coplanar nature of the cubic σ phase is also shown by HRTEM in Fig. 16. Virtually none of these precipitates showed ledges, which are quite common in the S phase (Fig. 17) and lead to rapid coarsening (11,12). Consequently the lower interfacial energy and the lack of ledges in the Ω and σ phases implies a more stable structure and a lower coarsening rate with thermal exposure.

4. Coarsening Study on the σ Phase

A statistical analysis was carried out on the growth of the σ phase aged at 200°C for various times. Figure 18 shows the size distribution of the precipitate after three different times. The narrow size distribution of this phase is impressive and important from a strengthening standpoint. The mean diameter of the precipitates is plotted against aging time in Fig. 19. This graph shows that the σ phase coarsens very slowly which is consistent with the prediction that precipitates with coherent interfaces (low energy) and small ledges have a lower coarsening rate.

More coarsening studies at longer times are presently in progress for the σ phase and similar studies are being initiated on the Ω phase.

5. Composite Fabrication

Since the objective of this study is to modify 2009 (a Al-Cu-Mg/SiC particulate material) it is necessary to evaluate composite samples to determine if the introduction of ceramic particles alters the type of phases that precipitate in the matrix. To expedite determination of the optimum matrix composition for maximum Ω phase, composite samples are being produced at UVA by compocasting. Two castings have been attempted thus far without complete success. In the first the SiC particulate (4.5 microns in diameter) was completely rejected by the melt. This was determined to result from inadequate surface treatment of the particulate before introduction into the melt and due to the low amount of Mg in the alloy which aids wetting and incorporation.

The second approach was to melt some of ACMC 2009 material (with SiC particles already incorporated) and add the appropriate amount of Al, Cu, and Ag to give the composition of A11M, agitate the melt, then cast. This approach will yield a composite with a lower volume fraction of particulate but that is not of importance in the present study as mechanical properties are not of concern,

only matrix microstructure. Examining this casting showed that there was not sufficient agitation to obtain complete mixing and dispersion of the particles hence a mechanical stirrer will be used in the next attempt.

6. Shear Strength Determination on Experimental Alloys

In order to get an early indication of mechanical properties (to supplement hardness data) for the experimental alloys, blanking shear tests were performed on alloy A12M in the peak aged condition and after 100 hours at 200°C. For comparison, P/M 2124 (produced by ACMC in the manner that 2009 is prepared) was also tested after similar conditions. Table 2 shows the results.

TABLE 2

SAMPLE	# TESTS	CONDITION	SHEAR STRENGTH
P/M2124	2	peak aged	43.8 ksi
A12M	2	peak aged (200°C,3hrs)	44.8 ksi
P/M2124	2	heated 100 hrs at 200°C	33.2 ksi
A12M	2	heated 100 hrs at 200°C	35.9 ksi

In the peak aged condition the experimental alloy had a slightly higher strength (albeit with only 2 tests this may not be significant) than the 2124 and appeared to exhibit greater ductility (qualitatively determined from the load-elongation curve). After aging for 100 hours at 200°C, the A12M sample showed approximately a 20% shear strength decrease while the P/M 2124 sample showed approximately a 25% decrease.

7. Discussion of Results

Of the four alloy compositions that have been produced during

the program A11M (Cu/Mg=7) and A12M (Cu/Mg=9) appear promising to pursue as a matrix composition for 2009. Both alloys contained Ω and σ precipitates in combination; the lower ratio alloy gives more σ phase and the higher ratio material gives more Ω. The Ω phase is coherent (or partially coherent, 8.3% misfit) with the Al (111) planes, while the σ phase has a higher degree of coherency with Al (3.1% misfit). Because of the lower interfacial energy associated with coherent phases they will coarsen more slowly when exposed to elevated temperatures. The fact that two coherent phases coexist in these alloys is of extreme interest and could have strong implications with respect to a material with good thermal stability.

Calculations have been made for estimating strengthening effects of the σ phase and suggest that a maximum increase of 45 ksi in yield strength can be obtained if the particles can be precipitated with a diameter of 2.7 nm (9). A diameter of 20 nm would generate an 11 ksi increase (this size may be more practically attainable). This potential strength increase from coherency hardening, Orowan strengthening and modulus hardening combined with the thermal stability (σ has been shown to resist coarsening for 350 hours at 250°C (9)) of this phase implies a reasonable material for HSCT applications. The Ω phase, with its coherency and high aspect ratio should exhibit similar potential.

References.

1. E.A. Starke, Jr., *Aluminum Alloys - Contemporary Research and Applications, Treatise on Materials Science and Technology*, Vol 31, eds. A. Vasudevan and R. Doherty, 1989, pp. 35-63.

2. I. Polmear and M. Couper, "Design and Development of an Experimental Wrought Aluminum Alloy for Use at Elevated Temperature," *Met. Trans. 19A*, 1027 (1988).

3. I. Polmear, "The Effects of Small Additions of Silver on the

Aging of Some Aluminum Alloys," *Trans. Met Soc., AIME 230,* 1331 (1964).

4. J. Vietz and I. Polmear, "The Influence of Small Additions of Silver on the Ageing of Aluminum Alloys," *J. Inst. Met. 94,* 410 (1966).

5. N. Sano, K. Hono, T. Sakurai and K. Hirano, "Atom-Probe Analysis of Ω and Θ' Phase in an Al-Cu-Mg-Ag Alloys," *Scripta Met. Mat. 25,* 491 (1991).

6. K. Knowles and W. Stobbs, "The Structure of {111} Age-Hardening Precipitates in Al-Cu-Mg-Ag Alloys," *Acta Cryst. B44,* 207 (1988).

7. A. Garg and J. Howe, "Nucleation and Growth of Ω Phase in Al-4.0Cu-0.5Mg-0.5Ag Alloy - an in-situ Hot-Stage TEM Study," *Acta Met. 39,* 1925 (1991).

8. A. Garg and J. Howe, "Convergent-Beam Electron Diffraction Analysis of Ω Phase in Al-4.0Cu-0.5Mg-0.5Ag Alloy," *Acta Met. 39,* 1331 (1991).

9. R. Schueller, "Identification and Analysis of a Unique 'Cubic Phase' in an Al-Cu-Mg/SiC Composite," Ph.D. Dissertation, University of Virginia, 1992.

10. R. Schueller, A. Sachdev, and F. Wawner, "Identification of a Cubic Precipitate Observed in an Al-4.3Cu-2Mg/SiC," *Scripta Met. Mat. 27,* 617 (1992).

11. M. Fine D. Bourell, Z. Eliezer, C. Persad, and H. Marcus, "Basic Principles for Selecting Phase for High Temperature Metal Matrix Composites: Interfacial Considerations," *Scripta Met. Mat. 22,* 907 (1988).

12. M. Fine, *Dispersion Strengthened Aluminum Alloys,* eds. Y. Kim and W. Griffith, The Minerals, Metals and Materials Society, 1988, pp. 103-121.

Figure 1. Hardness Test on Al-Cu-Mg-Ag alloys

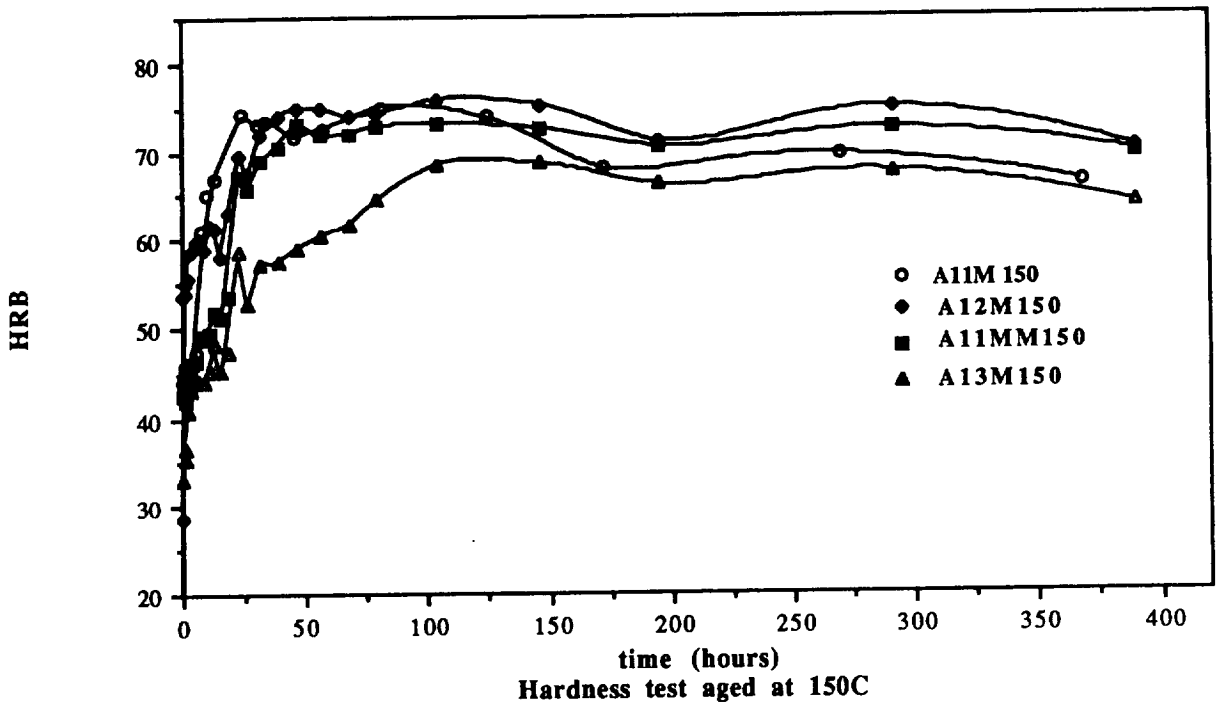

Hardness test aged at 150C

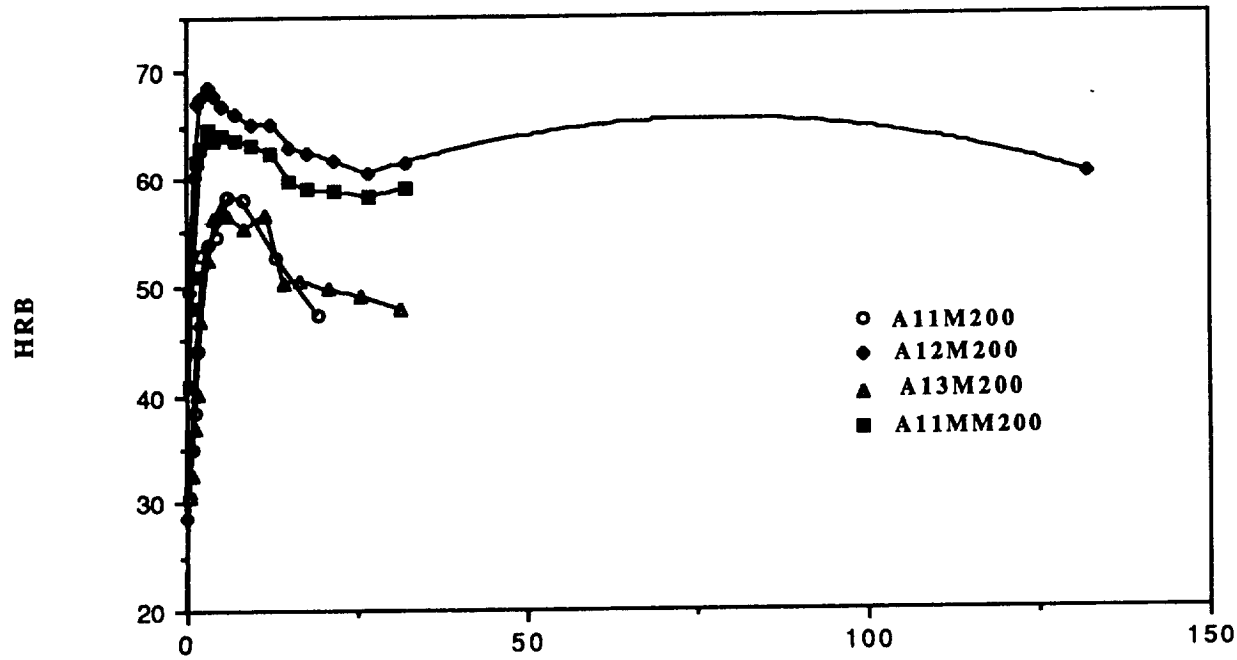

Hardness test aged at 200C

Figure 2. Isothermal DSC Plot for Al-Cu-Mg-Ag Alloys at 200°C

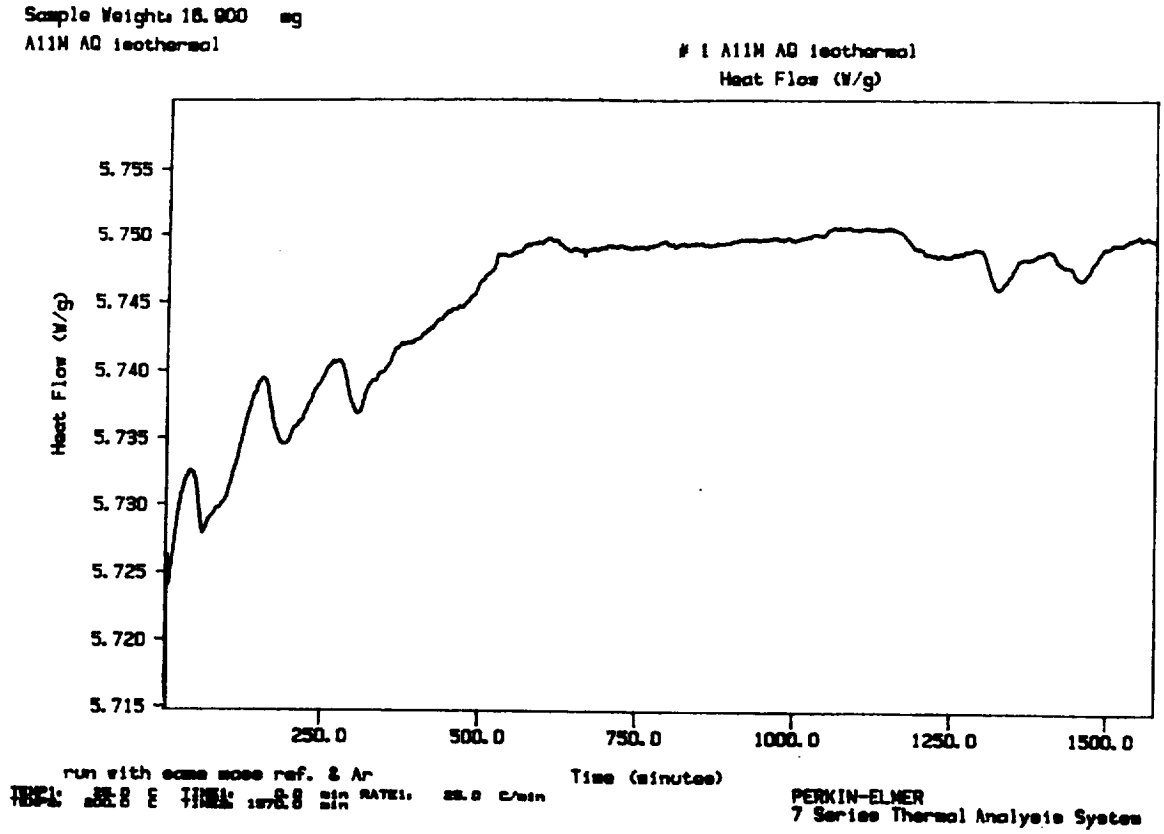

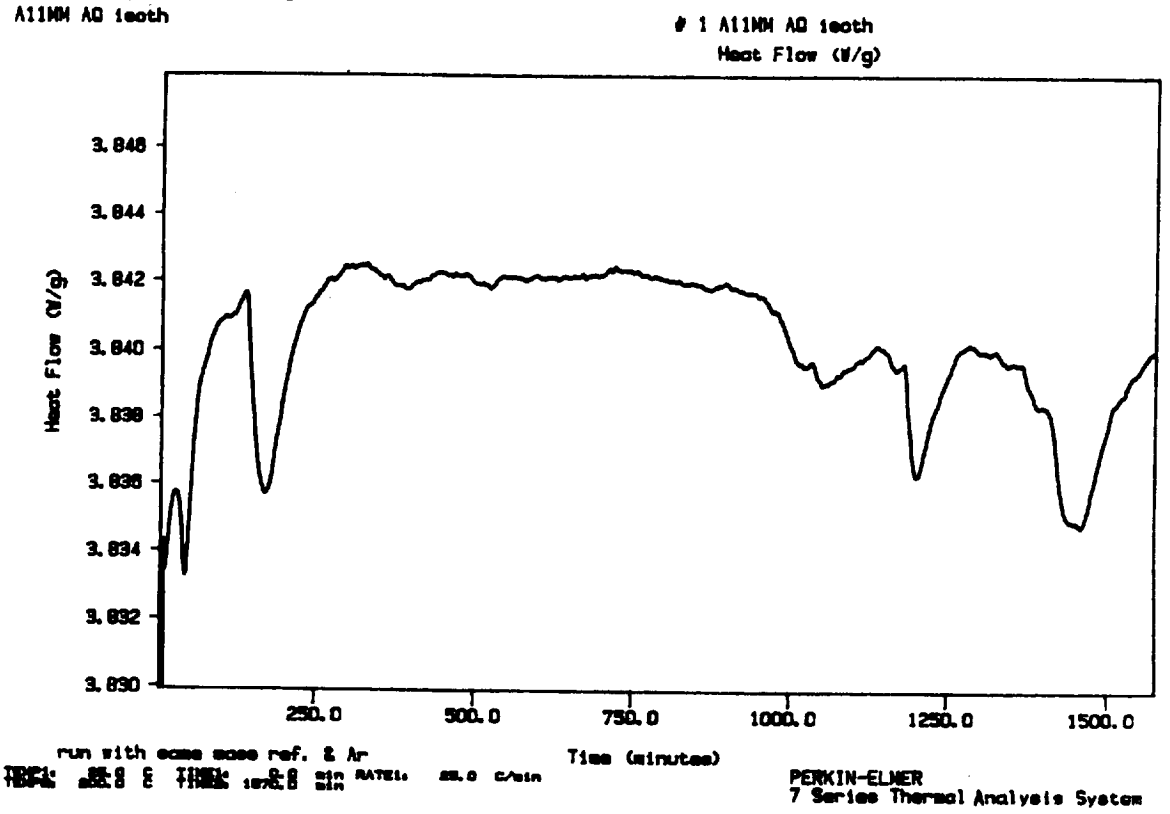

Figure 2. Isothermal DSC Plot for Al-Cu-Mg-Ag Alloys at 200°C

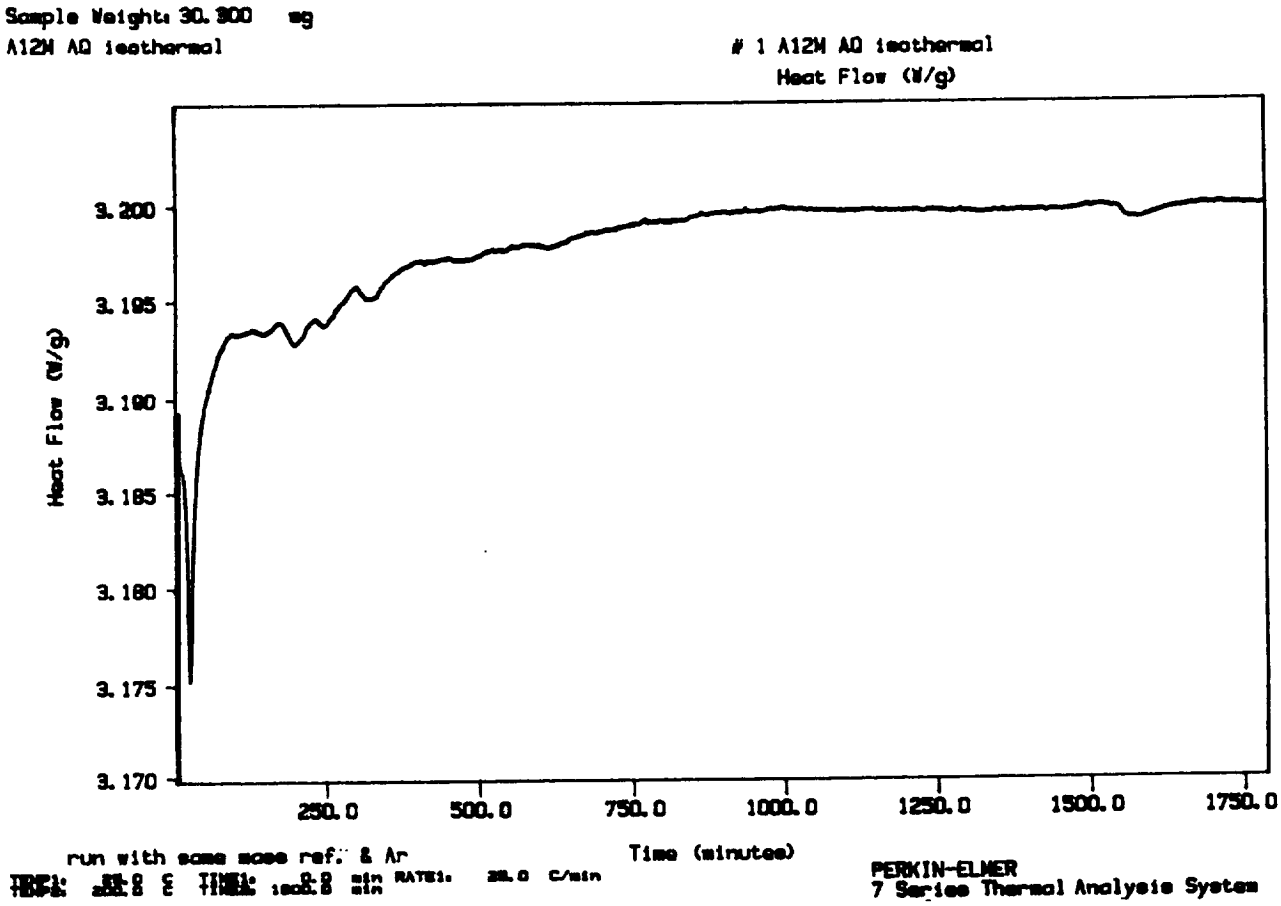

Figure 3. Microstructure of sample A12M, heat treated for one hour at 200°C, showing precipitate phase.

Figure 4. Dark field micrograph of sample A12M, heat treated for one hour at 200°C, showing Ω platelets .

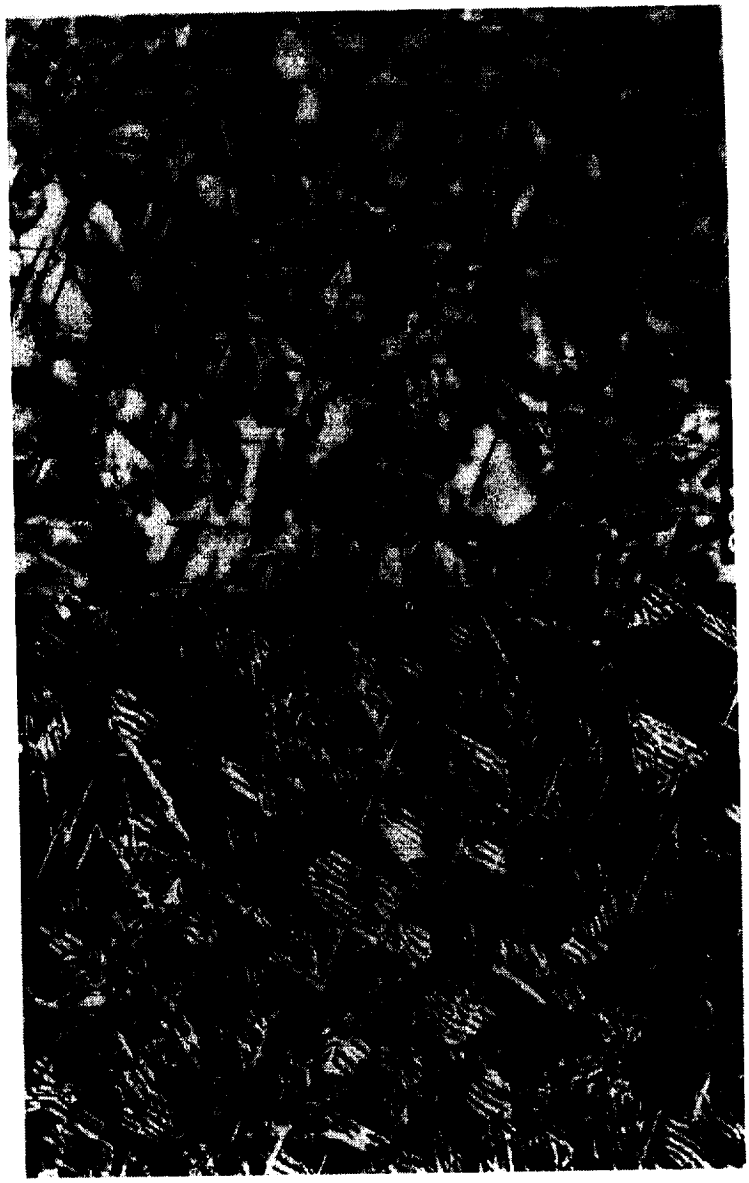

Figure 5. Bright field-dark field pair of same area on sample A12M, heat treated for three hours at 200°C, showing high density of Ω phase.

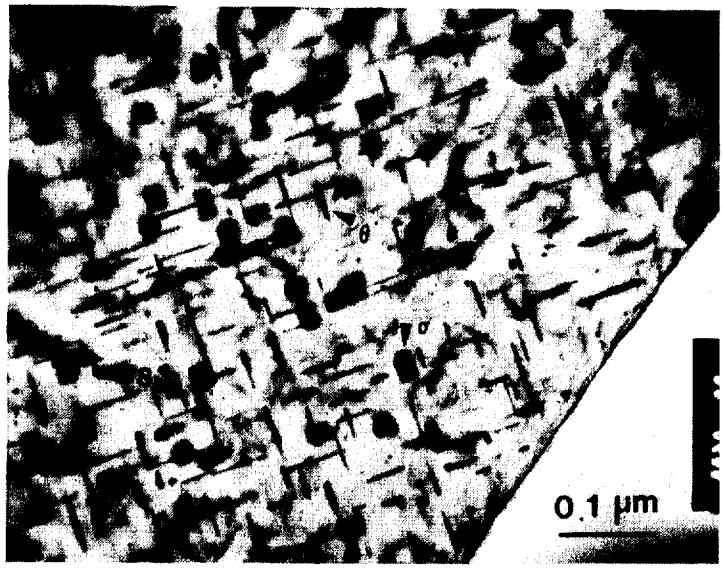

Figure 6. Micrograph of sample A12M, heat treated for three hours at 200°C showing θ', S and the σ precipitates.

Figure 7. TEM micrograph of sample A11M, heat treated for 3 hours at 200°C, showing all four precipitate phases.

Figure 8. Dark field of area in Figure 7 using Ω reflection.

Figure 9. Microstructure of sample A11M after 19 hours at 200°C.

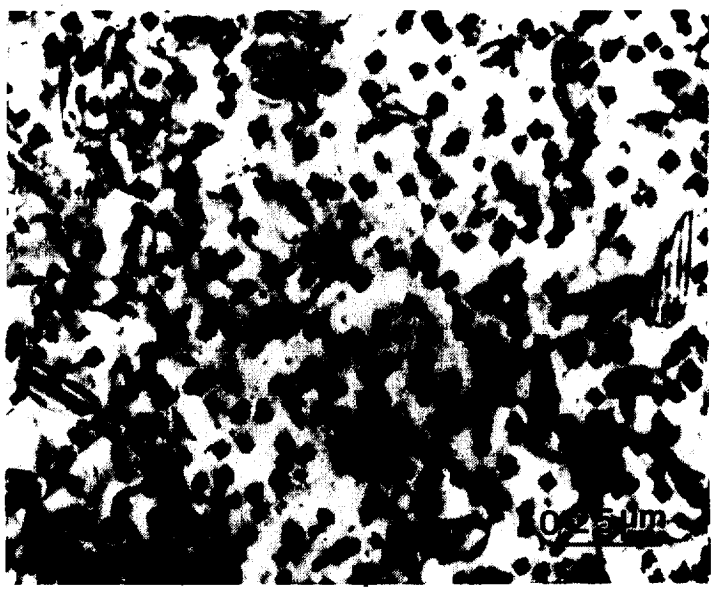

Figure 10. Sample A11M, heat treated 26 hours at 200°C, showing a higher density of the σ phase.

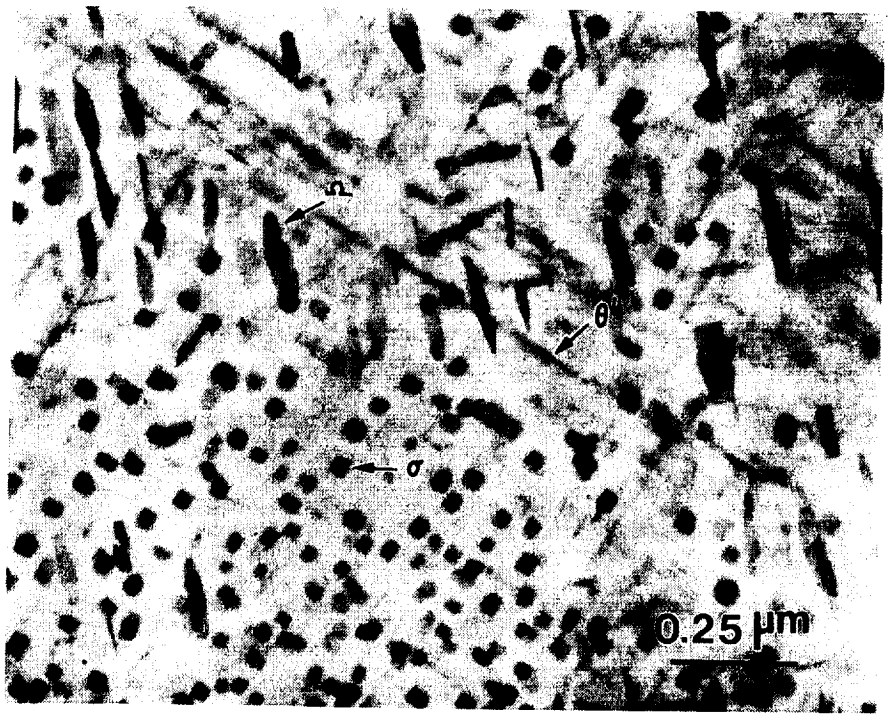

Figure 11. Segregated region in A11M between the Ω and σ phases.

Figure 12. PFZ in sample A11M after 26 hours at 200°C.

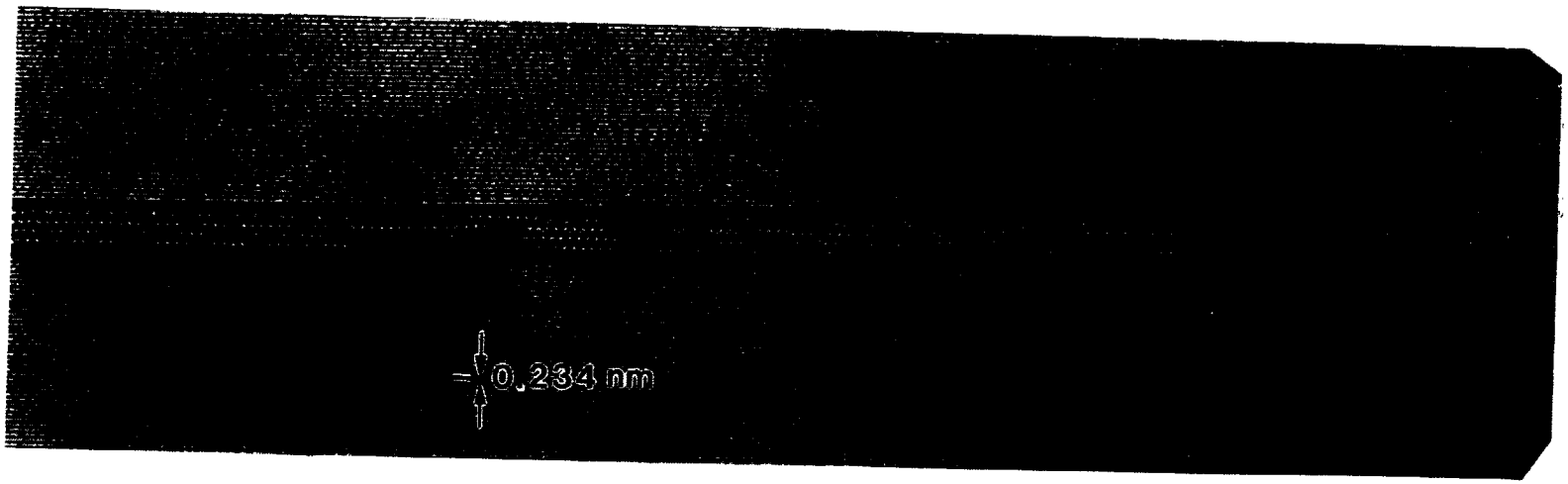

Figure 13. HRTEM of Ω phase showing high aspect ration coherent interface and lack of ledges B=[112].

Figure 14. HRTEM of Ω phases nucleation.

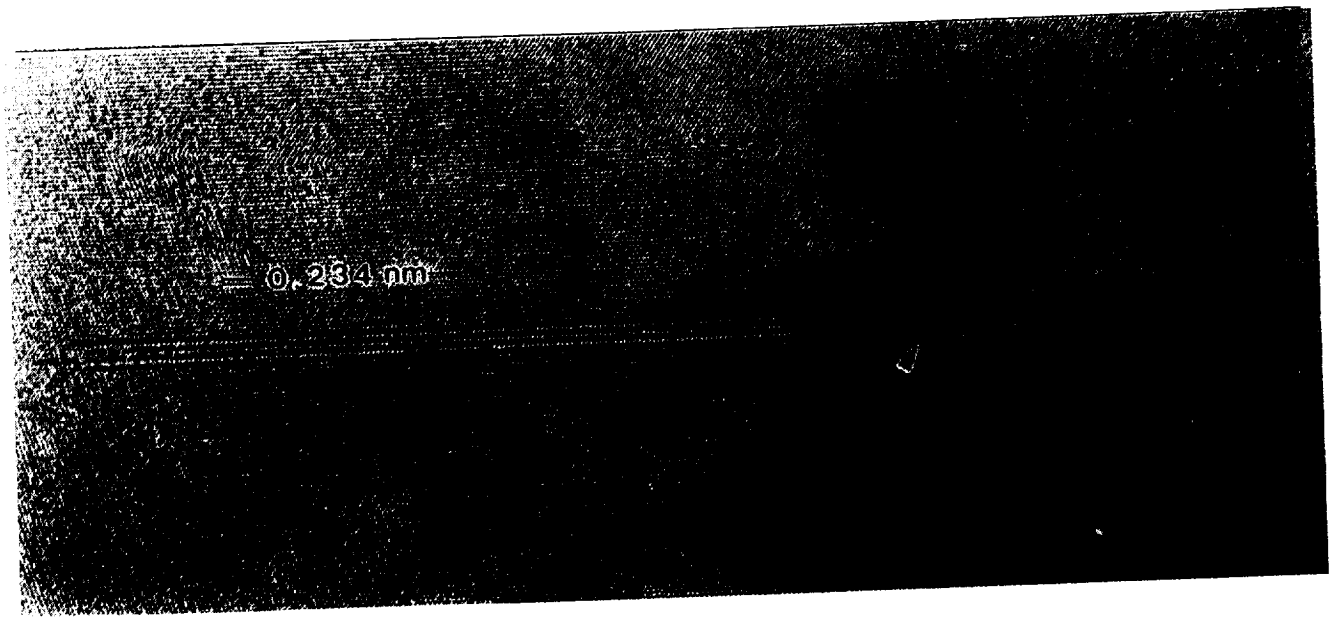

Figure 15. HRTEM of Ω platelets intersecting and exhibiting a ledge, the arrows point out the ledge.

Figure 16. HRTEM of σ phase B=[001], showing coherent interface, arrows pointing out the growth ledges.

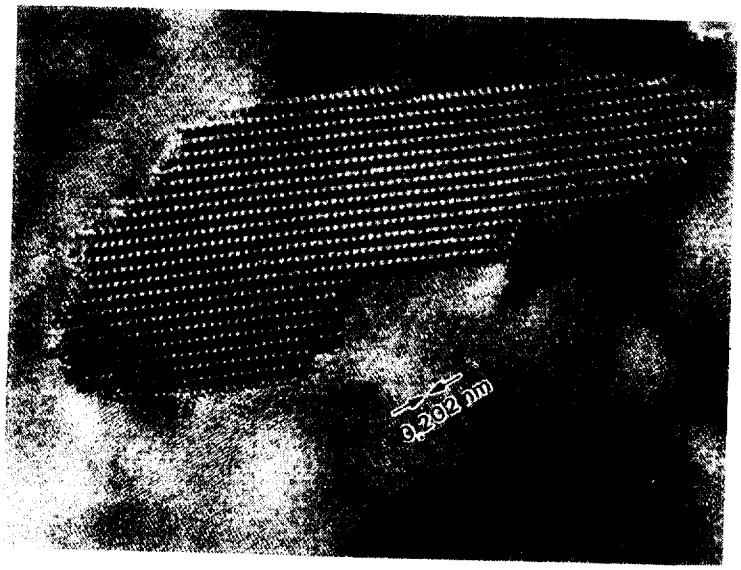

Figure 17. HRTEM of S phase showing large ledges and incoherent interface.

Figure 18. Size distribution of σ phase precipitates after thermal exposure.

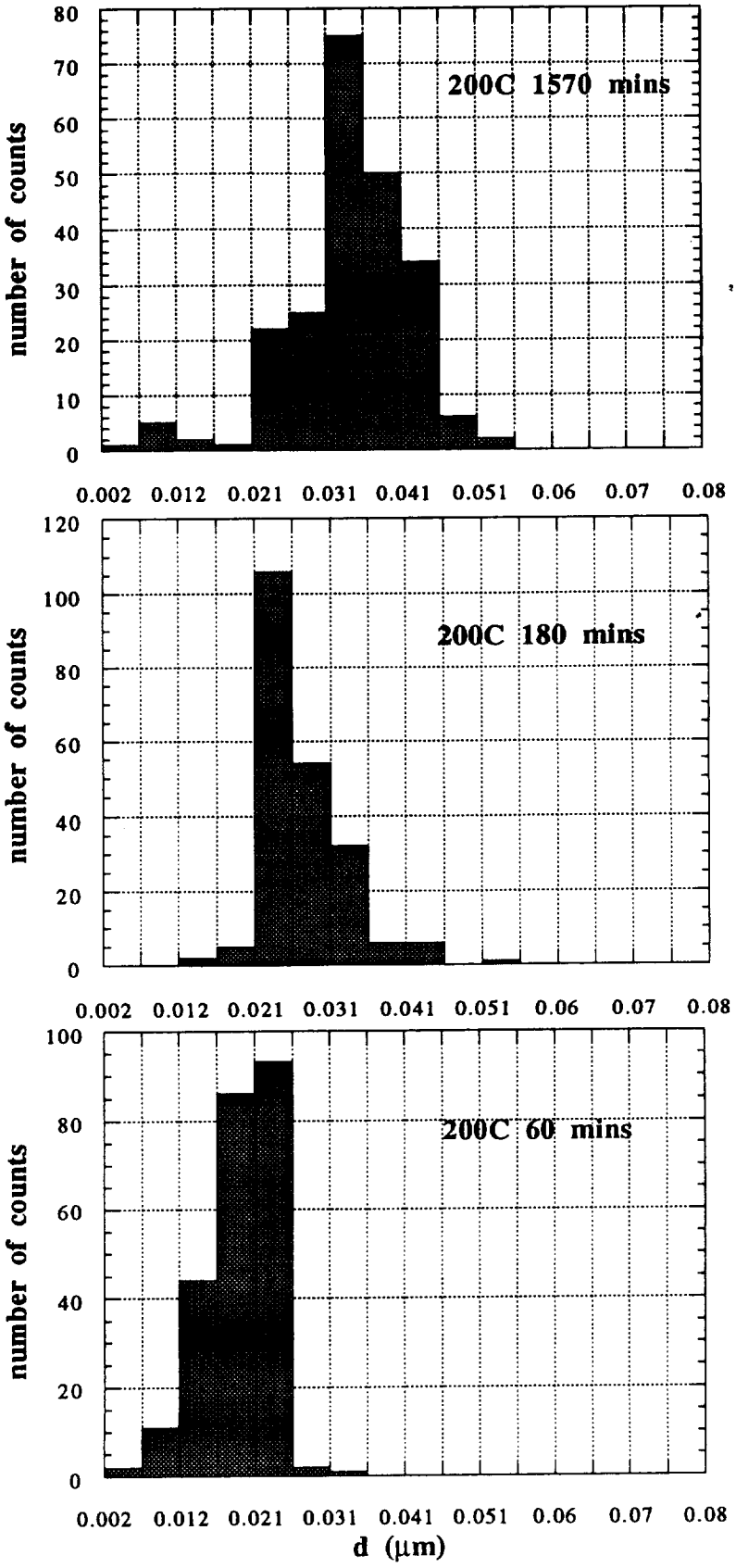

Figure 19. Coarsening of σ precipitates at 200°C

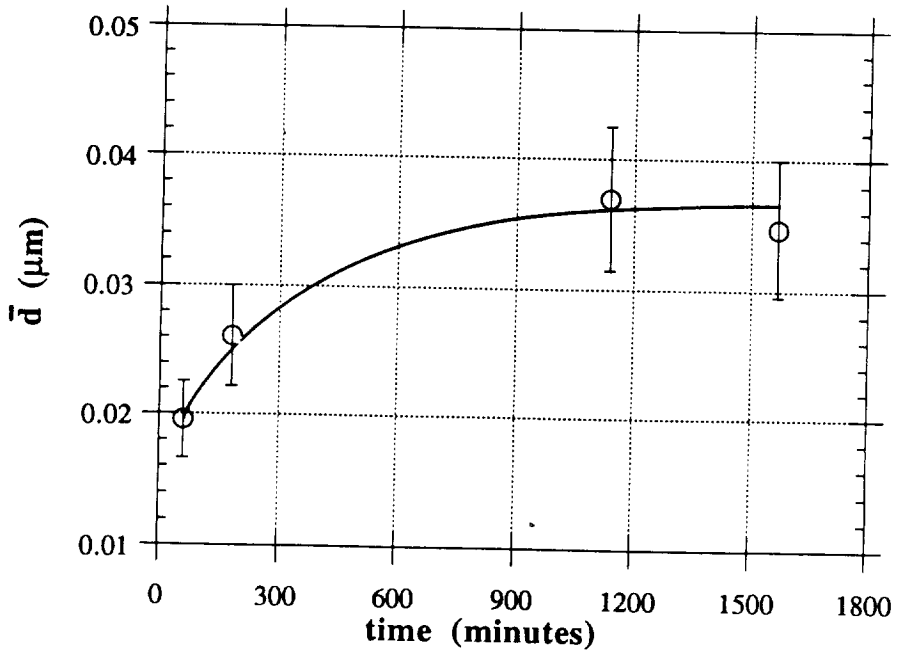

TASK 9. ACCELERATED EXPOSURE STUDY (Alcoa)

Principal Investigator: Dr. L.M. Angers
Senior Engineer: Dr. G. Dixon

Objective. The objective of this task is to develop a philosophy for simulating high speed aircraft service using accelerated exposures. The importance of incorporating a stress will also be investigated.

Background and Test Plans. A spring fixture has been developed for creep aging materials for the HSCT program (see Fig. 1). A spring, loaded in compression, imparts a tensile load to the specimen located in the center of the spring. This fixture has been designed to load 1/8" diameter tensile specimens. After aging the specimen under load, the specimen is removed from the fixture and tested to determine the residual tensile strength of the material.

The current fixture can be used at temperatures up to 400°F and will load specimens to stresses of up to 20 ksi. Stiffer springs can be obtained which will permit loading specimens to 60 ksi. The major difference between this fixture and the fixture used in alternate immersion testing is that the former provides a constant stress while the latter provides a constant displacement. This difference is important when exposure temperatures are high enough and times are long enough that significant creep deformation occurs. The fixture is quite compact, e.g., 2" in diameter and approximately 7" long, permitting a large number of specimens to be aged in a single oven.

Three materials were identified for accelerated exposures in these constant-stress aging fixtures. These materials are:

2080/SiC/20_p, 2519-T87 and 6013-T6. These materials were chosen since they represent three different candidates for a Mach 2.0 aircraft: a discontinuously reinforced metal matrix composite for use on the upper wing and two different precipitation strengthened monolithic alloys for use in the fuselage and lower wing. Exposure temperatures of 300°F and 215°F will be used. The temperature of 300°F is considered a reasonable temperature for accelerated tests intended to simulate Mach 2.0 service. To simulate 120,000 h at 215°F, exposures of 600 to 1000 h at 300°F will be considered. Tensile specimens will be taken out at various time intervals and tested for residual strength and elongation. Some test specimens will be stressed and others will be unstressed. An 18 ksi stress will be used for the first iteration of stressed specimens.

Experimental Details. Initial tests to verify the fixture performance were performed on 2519-T87 specimens. Specimens were strain gaged prior to loading and aging to verify the loads applied to the specimens, determine the amount of bending present and to determine whether any significant decrease in load occurred during aging. These tests were performed at a stress of 18 ksi for 100 hr at 400°F. Another set of tests were run at a lower temperature, e.g., 300°F, where the effects of stress might be emphasized and the effects of temperature minimized.

Results and Discussion. A summary of the data generated from the tests at 400°F is given in Table I. As shown in Table I, test conditions included a standard creep test under 18 ksi stress for 100 hr-400°F, an accelerated exposure (AE) at 18 ksi stress in the aging fixture for 100 hr-400°F, an accelerated exposure (AE) at 0 stress for 100 hr-400°F and unexposed material. Since there was no difference between the residual tensile properties of the sample exposed in the fixture and the sample exposed with no stress and there was some difference between the

residual tensile properties of the sample exposed in the fixture and the sample exposed in the creep machine, further examination of the fixture was required.

Preliminary data generated at 300°F after 250 and 500 hr exposures for 2519-T87 are shown in Table II. Some specimens were stressed by exposing in the spring fixture and others were not stressed. A comparison of the unstressed specimens for the 250 and 500 hr exposure show that slight reductions in residual tensile yield and ultimate tensile strengths occur. Similarly, a comparison of residual tensile properties of specimens stressed in the fixture shows the same trend. However, a comparison of stressed and unstressed specimens reveals a reduced rate of strength loss for the stressed specimens rather than the accelerated rate of overaging which was anticipated.

Several test development issues were then addressed:

Concern	Modification
Bending in the spring	A sleeve was designed to minimize any bending once the load was in place.
Creeping of the spring during long exposure times	The spring was pre-aged to eliminate stage I creep.
Constant load maintained during long exposure times	Plan to measure load at room temperature and re-measure load after exposure.
Touching of spring-coils	No modifications needed; load - displacement curves for the spring showed no significant increase in the spring rate.
Specimen alignment	Results are preliminary; more data are needed to determine what modifications are needed.

All test specimens for this task have been machined and are awaiting testing.

Table I Residual Tensile Properties of 2519-T87 Samples Exposed at 400°F

Exposure Condition	TYS (ksi)	UTS (ksi)
in Creep Machine, 18 ksi, 400°F-100 hr.	46.1	58.6
AE in fixture, 18 ksi, 400°F-100 hr.	47.3	59.0
AE in oven, 400°F-100 hr.	47.2	58.8
As Received	61.0	67.2

Table II Residual Tensile Properties of 2519-T87 Samples Exposed at 300°F

Exposure Time (hours)	Stress (ksi)	TYS (ksi)	UTS (ksi)
250	0	59.8	67.1
250	18	61.0	68.4
500	0	58.2	66.0
500	18	59.3	67.4

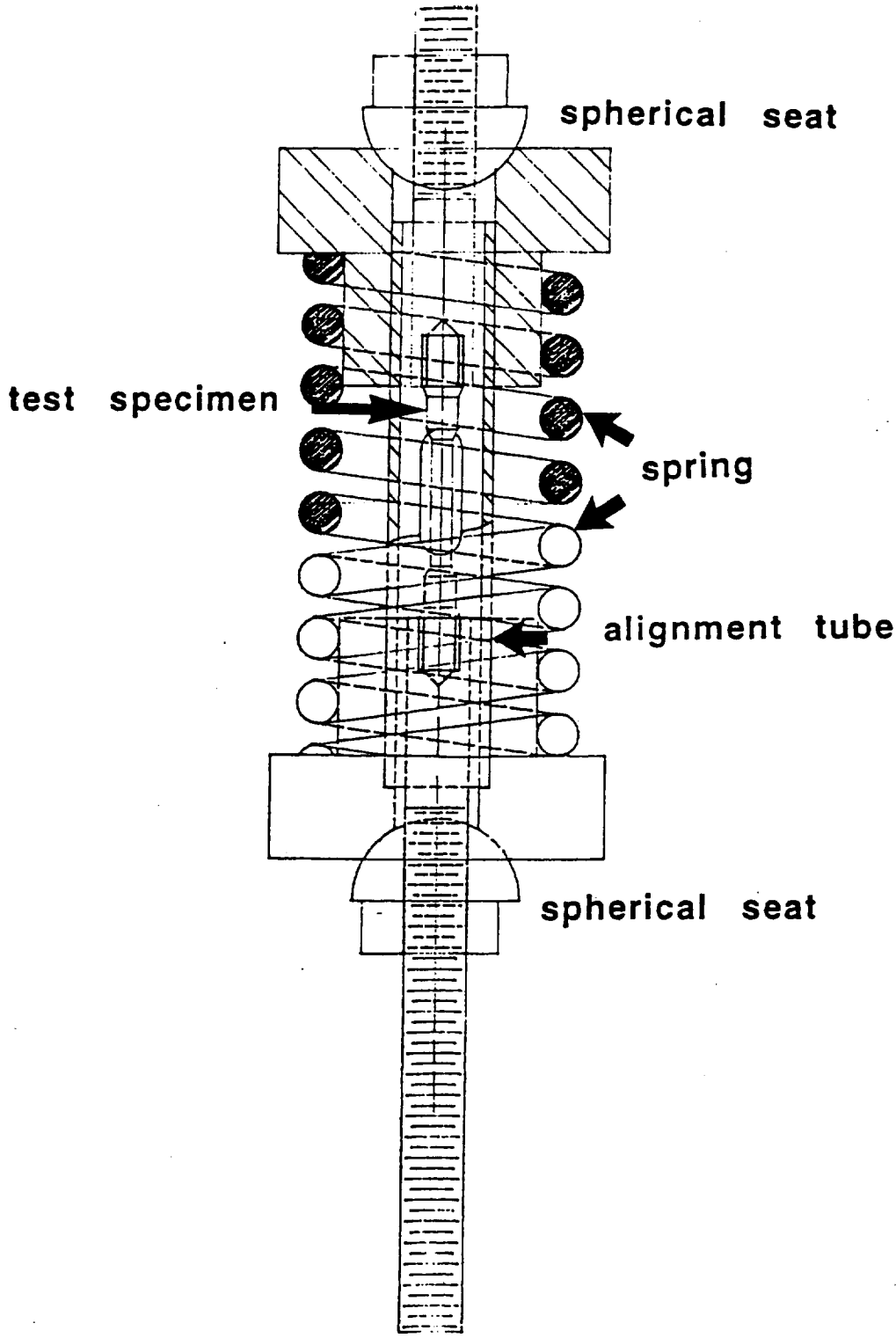

Figure 1

Spring Test Fixture-Accelerated Exposures

TASK 10A. MATERIALS TECHNOLOGY TRADE-OFF STUDIES FOR THE AIRFRAME (Boeing)

No progress to report to date. See Subtask 1A(i).

TASK 10B. MATERIALS TECHNOLOGY TRADE-OFF STUDIES FOR THE AIRFRAME (Douglas)

No progress to report to date.

REPORT DOCUMENTATION PAGE

Form Approved
OMB No. 0704-0188

1. AGENCY USE ONLY (Leave blank)	2. REPORT DATE	3. REPORT TYPE AND DATES COVERED
	June 1993	Contractor Report 1/1/92 - 6/30/92

4. TITLE AND SUBTITLE

NASA-UVa Light Aerospace Alloy and Structure Technology Program Supplement: Aluminum-Based Materials for High Speed Aircraft

5. FUNDING NUMBERS

G NAG1-745

WU 763-23-45-86

6. AUTHOR(S)

E. A. Starke, Jr.

7. PERFORMING ORGANIZATION NAME(S) AND ADDRESS(ES)

School of Engineering and Applied Science
University of Virginia
Thornton Hall
Charlottesville, VA 22903

8. PERFORMING ORGANIZATION REPORT NUMBER

9. SPONSORING/MONITORING AGENCY NAME(S) AND ADDRESS(ES)

National Aeronautics and Space Administration
Langley Research Center
Hampton, VA 23681-0001

10. SPONSORING/MONITORING AGENCY REPORT NUMBER

NASA CR-4517

11. SUPPLEMENTARY NOTES

Langley Technical Monitor: Dennis L. Dicus

12a. DISTRIBUTION/AVAILABILITY STATEMENT

Unclassified-Unlimited

Subject Category: 26

12b. DISTRIBUTION CODE

13. ABSTRACT *(Maximum 200 words)*

This report on the NASA-UVa Light Aerospace Alloy and Structure Technology Program Supplement: Aluminum-Based Materials for High Speed Aircraft covers the period from January 1, 1992 to June 30, 1992. The objective of the research is to develop aluminum alloys and aluminum matrix composites for the airframe which can efficiently perform in the HSCT environment for periods as long as 60,000 hours (certification for 120,000 hours) and, at the same time, meet the cost and weight requirements for an economically viable aircraft. Current industry baselines focus on flight at Mach 2.4. The research covers four major materials systems: (1) Ingot metallurgy 2XXX, 6XXX, and 8XXX alloys, (2) Powder metallurgy 2XXX alloys, (3) Rapidly solidified, dispersion strengthened Al-Fe-X alloys, and (4) Discontinuously reinforced metal matrix composites. There are ten major tasks in the program which also include evaluation and trade-off studies by Boeing and Douglas aircraft companies.

14. SUBJECT TERMS	15. NUMBER OF PAGES
Aluminum Alloys High speed aircraft Composites	228
	16. PRICE CODE A11

17. SECURITY CLASSIFICATION OF REPORT	18. SECURITY CLASSIFICATION OF THIS PAGE	19. SECURITY CLASSIFICATION OF ABSTRACT	20. LIMITATION OF ABSTRACT
UNCLASSIFIED	UNCLASSIFIED		

NSN 7540-01-280-5500

Standard Form 298 (Rev. 2-89)
Prescribed by ANSI Std. 239-18
298-102